Università Ca'Foscari Venezia

ISP Istituto di Scienze Polari
Consiglio Nazionale delle Ricerche

PhD in Polar Sciences

37° cycle

Photodegradation processes of natural and anthropogenic compounds in icy matrices

---

PhD candidate:
Frassati Stefano

Supervisor:
Prof. Marco Roman

Abstract

Traditionally, snow and ice have been considered chemically inert environments in which crustal and oceanic emissions accumulate. However, over the last two decades, a new view has emerged, according to which chemical compounds can undergo transformation processes in the cryosphere, particularly through photochemical processes. Although, according to Arrhenius' law, reaction rates decrease at low temperatures, several studies have shown that some photoinduced reactions in ice are faster than in the aqueous phase. This is attributed to the concentration effect of species in the quasi-liquid layer at the ice-air interface, which favours interaction between the molecules present. Although the reaction rates of many species have been studied, the nature of the degradation products, their reactivity and their environmental fate remain poorly explored.

In this work, the focus was on an organic compound, bisphenol A (BPA), and an inorganic species, bromine. For BPA, its photoreactivity in ice, snow and sea ice was studied, identifying degradation products and assessing their potential toxicity in silico. For bromine, in relation to oxidative processes in snow, a sensitive method for the speciation and quantification of ultra-traces of Br^- and BrO_3^- has been developed and applied to samples collected in Svalbard to Understand photo-oxidative processes and bromine mobilisation in polar environments.

List of acronym

QLL	Quasi-liquid Layer
$\mathbf{G}_{QLL}$	Free energy of quasi-liquid layer
T	Temperature
P	Pressure
d	Thickness of quasi-liquid layer
$\boldsymbol{\rho}$	Density of different phase
$\boldsymbol{\mu}$	Chemical potential of different phase
l	Liquid phase
s	Solid phase
v	Gas phase
i	Impurities
$\mathbf{F}_{tot}\mathbf{(d)}$	Excess free energy per unit area
$\boldsymbol{\gamma}$	interfacial energy
f(d)	Van de Waals energy interactions
T(m)	Melting temperature
q(m)	Latent heat
$\mathfrak{F}(\boldsymbol{d})$	Total effective interfacial free energy
$\mathbf{F}_{VdW}\mathbf{(d)}$	Van der Waals force
$\mathbf{F}_{DH}\mathbf{(d)}$	Debye-Huckel force
$\boldsymbol{\Phi_{H_2O}(T)}$	Portion of free water in ice
$\boldsymbol{\Delta H_f^0}$	Enthalpy of water

List of variables: Optical properties

$\mathbf{E}$	Electromagnetic field
$\mathbf{t}$	Time
$\boldsymbol{\omega}$	Angular frequency
$\boldsymbol{\mu}$	Magnetic permeability
$\boldsymbol{\epsilon}$	Permittivity of the material
$\boldsymbol{\lambda}$	Wavelength
$\mathbf{n}$	Refractive index
$\mathbf{k}_a$	Absorption coefficient
$\mathbf{k}_{scat}$	Scattering coefficient
$\mathbf{I}$	Absorbed radiation intensity
$\mathbf{I}_0$	Incident intensity
$\mathbf{K}$	Extinction coefficient
$\mathbf{z}$	Optical path
$\mathbf{SSA}$	Specific surface Area
$\mathbf{r}$	Radius

Contents

Aim and structure of the work

Traditionally, snow and ice systems have been considered passive, chemically inert environments in which crustal and oceanic emissions accumulate. Over the past two decades, however, the view of the cryosphere as a dynamic compartment, capable of influencing the transformation of chemical compounds, in particular through photochemical processes, has gradually become established. Although low temperatures seem to hinder chemical reactions according to Arrhenius' law, numerous studies have shown that some photoinduced reactions in ice occur more rapidly than in the aqueous phase. This apparent paradox is attributed to a concentration effect of the reactants within a quasi-liquid layer located at the ice-air interface, which favours molecular interaction and thus reactivity. Although numerous studies have investigated how the reaction rates of organic and inorganic compounds vary under different environmental conditions, there remains a significant knowledge gap regarding the degradation products generated by these processes. In particular, the chemical identity, reactivity, and environmental fate of such products in icy environments remain poorly explored.

Herin, the focus was on the study of an organic pollutant, bisphenol A (BPA), and an inorganic species, bromine. With regard to BPA, its photoreactivity was investigated in different cryospheric matrices, including freshwater ice, snow, and sea ice, with the aim of identifying the degradation products generated upon irradiation. To complement these analyses, an *in silico* evaluation of the potential toxicity of the identified secondary compounds was carried out. In the context of the photochemical processes and oxidative reactions that occur in the snow cover, particular attention was paid to bromate (BrO_3^-), the end product of bromide oxidation (Br^-) by ozone (O_3). In light of this, a highly sensitive analytical method was developed for the speciation and ultratrace quantification of Br^- and BrO_3^-. This method was successfully applied to the analysis of snow samples collected in the Svalbard archipelago, to further our understanding of oxidative processes and bromine mobilization in polar environments. These results aim to fill a gap in the knowledge regarding the effect of the matrix on the development of photo-oxidation products in frozen matrices with respect to organic compounds. On the other hand, the study of bromide oxidation to bromate in snow, a reaction also induced by photochemistry, has filled an important gap relating to the fact that models relating to the study of bromine reactions in the cryosphere (known as bromine explosions) undergo significant variations in the spring period compared to the measured data, so much so that the authors themselves point out that a pool of non-reactive bromine, namely bromate, is possible.

This PhD thesis is a compilation of scientific papers that have already been published or submitted to international specialist journals. The first two chapters provide a comprehensive overview of the chemical and physical properties of different ice matrices (ice, snow and sea ice), with a specific focus on chemical reaction sites and their interactions with solar radiation. The second chapter, in particular, analyses in detail the photochemical reactions and chemical species involved in these processes.

The experimental results of this research are presented in the following chapters, dedicated respectively

to investigations conducted on BPA and bromine. Each chapter begins with an introduction providing a comprehensive overview of the relevant state of the art. Subsequently, the individual scientific articles that make up this work are presented and analysed, each introduced by a brief descriptive section summarising its objectives and main results. Finally, each chapter concludes with a section of specific conclusions, summarising the main results obtained and discussing their impact and significance in the context of the research. Finally, the concluding chapter provides an overview of the results obtained and discusses their implications.

Chapter 1

Ice, snow and sea ice: physical and chemical properties

List of variables: ice

QLL	Quasi-liquid Layer
$\mathbf{G}_{QLL}$	Free energy of quasi-liquid layer
T	Temperature
P	Pressure
d	Thickness of quasi-liquid layer
$\boldsymbol{\rho}$	Density of different phase
$\boldsymbol{\mu}$	Chemical potential of different phase
l	Liquid phase
s	Solid phase
v	Gas phase
i	Impurities
$\mathbf{F}_{tot}\mathbf{(d)}$	Excess free energy per unit area
$\boldsymbol{\gamma}$	interfacial energy
f(d)	Van de Waals energy interactions
T(m)	Melting temperature
q(m)	Latent heat
$\boldsymbol{\Im(d)}$	Total effective interfacial free energy
$\mathbf{F}_{VdW}\mathbf{(d)}$	Van der Waals force
$\mathbf{F}_{DH}\mathbf{(d)}$	Debye-Huckel force
$\boldsymbol{\Phi_{H_2O}(T)}$	Portion of free water in ice
$\boldsymbol{\Delta H_f^0}$	Enthalpy of water

List of variables: Optical properties

$\mathbf{E}$	Electromagnetic field
$\mathbf{t}$	Time
$\boldsymbol{\omega}$	Angular frequency
$\boldsymbol{\mu}$	Magnetic permeability
$\boldsymbol{\epsilon}$	Permittivity of the material
$\boldsymbol{\lambda}$	Wavelength
$\mathbf{n}$	Refractive index
$\mathbf{k}_a$	Absorption coefficient
$\mathbf{k}_{scat}$	Scattering coefficient
$\mathbf{I}$	Absorbed radiation intensity
$\mathbf{I}_0$	Incident intensity
$\mathbf{K}$	Extinction coefficient
$\mathbf{z}$	Optical path
SSA	Specific surface Area
$\mathbf{r}$	Radius

The cryosphere (from the Greek "*krios*", meaning ice or cold) refers to the portion of the Earth's surface where water exists in solid form [1]. During the 1972 Human Environment Conference, organized by the World Meteorological Organization (WMO) in Stockholm, it was proposed to include the cryosphere as the fifth terrestrial sphere, alongside the atmosphere, lithosphere, hydrosphere, and biosphere [2]. Currently, approximately 10% of the earth's land surface is covered by glaciers, while 70% of the planet is occupied by oceans, 5% of which are periodically covered by ice in polar regions. The cryosphere includes glaciers, permafrost, icebergs, polar ice caps, sea ice, snow cover, frozen rivers, lakes, seas, and seasonally frozen ground [3]. Historically, the cryosphere has been regarded as an inert system, functioning only as a final receptor for terrestrial and oceanic emissions and atmospheric particles, with its primary function being the reflection of solar radiation (albedo) by snow cover. However, in the past two decades, it has become evident that the cryosphere actively interacts with the atmosphere and other environmental components, thus playing a more complex role in the Earth system [4–8]. In recent years, scientific literature has increasingly highlighted the chemical-physical processes that occur within ice matrices, recognizing their impact on other ecological and environmental compartments [9, 10]. Among the most studied phenomena there are photochemical processes, which involve the initiation of chemical reactions through a part of the solar radiation spectrum [11–14]. These processes, well known in aquatic environments, play a crucial role in stratospheric ozone balance in polar regions through reactions with bromine [15–17].However, there is a scarcity of research on the degradation mechanisms of both natural and anthropogenic compounds within ice matrices. However, in the study of (photo)chemical reactions, particularly for ice and snow, but with less focus on sea ice (a matrix chemically distinct from the others), there is often a tendency to concentrate on one specific matrix and then make generalizations about the others. This methodological approach fails to recognize that the formation and chemical characteristics of each matrix – ice, snow, or sea ice – differ significantly, thereby influencing the chemical processes occurring within. To understand how these photoinduced processes are influenced by the matrix in which the reaction takes place, it is essential to describe the various types of ice matrices found in nature and their interaction with the solar spectrum.

1.1 Physical and chemical properties of ice

1.1.1 Quasi-liquid layer

Ice represents the crystalline solid phase of water and can assume different forms depending on temperature and pressure conditions. However, the predominant structure found in nature is ice Ih. The hexagonal structure of ice was first proposed by Pauling in 1935, describing each oxygen atom as part of a tetrahedral arrangement, where it is surrounded by four neighboring oxygen atoms, forming a lattice known as "wurtzite"[18] . A fundamental characteristic of Pauling's model is the absence of long-range order in the orientation of H_2O molecules or hydrogen bonds. According to Pauling: "*Under normal conditions, the interaction between non-adjacent molecules is not sufficient to stabilize any of the many configurations that satisfy the ice rules*" [3]. This observation implies that the disorder of hydrogen atoms is required to adhere to two fundamental principles, termed ice rules. The first principle states that each oxygen atom must be bonded to two adjacent hydrogen atoms. The second principle asserts that each hydrogen atom is capable of forming only a single bond. Ice occurs predominantly in polycrystalline forms or as aggregates of grains, the size of which can vary significantly depending on the thermodynamic or deposition processes that led to its formation. [19]. Qualitative analysis of this polycrystalline matrix can be conducted using microscopy techniques based on optical anisotropy, i.e. the variation in the polarisation of light due to the hexagonal

crystal structure of the ice (Fig 1.1) [20]. During warming processes, the molecular disorder of grains tends

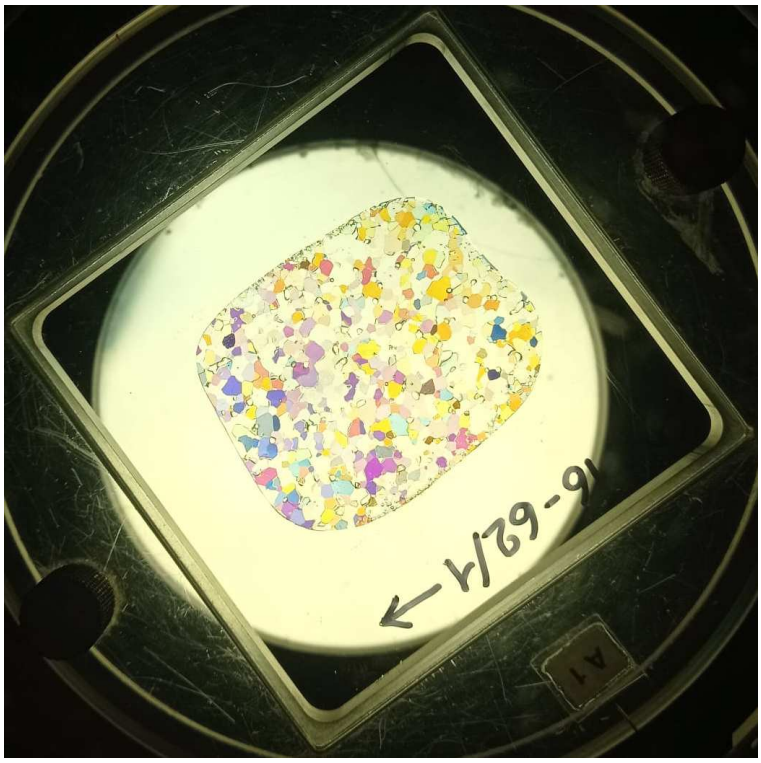

Figure 1.1: Effect of the different reflection of polarised light by a section of ice core

to increase in areas of discontinuity between them. Specifically, the intersection of two grains constitutes a grain boundary; the intersection of three grains forms a vein; and the intersection of four or more grains constitutes a node [21]. In these areas, the addition of thermal energy causes an increase in the agitation of the particles, leading to greater molecular disorder. In previous theorizing, it was assumed that ice melt is solely influenced by two intensive variables: pressure and temperature [22, 23]. However, these two factors have been shown to be insufficient in explaining certain phenomena, for example why ice is slippery even at temperatures below zero, forming a thin liquid layer on the surface. The explanation for this phenomenon lies in other contributing factors, such as surface melting and frictional melting, which play an important role in the formation of the lubricating layer that reduces friction [24]. In the ideal case of water that is free from impurities, the thickness of the quasi-liquid layer (QLL) is determined by the reduction of interfacial energy. Under equilibrium conditions with its own vapour at a given pressure (P) and temperature (T), and with a surface wetted by the QLL, the free energy of the liquid film (G_{qll}) can be expressed as reported in (1.1) [24]:

$$G_{\mathrm{qll}}(T, P, d) = [\rho_l \mu_l(T, P)]d + F_{\mathrm{tot}}(d) \tag{1.1}$$

Where ρ_l and μ_l represent, respectively, the density and the chemical potential of the liquid phase, d is the film thickness, and $F_{\mathrm{tot}}(d)$ denotes the excess free energy per unit area, which is proportional to the interfacial energy γ (1.2):

$$F_{\mathrm{tot}}(d) = \Delta\gamma f(d) + \gamma_{\mathrm{sv}} \tag{1.2}$$

$\Delta\gamma$ is the difference between wet and dry interfacial free energy for different interface types (s, solid; l, liquid; v, vapor; $\Delta\gamma = \gamma_{\mathrm{sl}} + \gamma_{\mathrm{lv}} - \gamma_{\mathrm{sv}}$), while $f(d)$ represents a decrease in energy due to Van der Waals

interactions as a function of d. Theoretical models have been developed to facilitate the calculation of the thickness of ice surfaces and interfacial melting in relation to temperature. These models utilise van der Waals forces, the long-range potential of which falls quadratically with distance [25–27]. Appropriate substitutions can be made to calculate the thickness $d(T)$ as function of the operating temperature in relation to the melting temperature T_m (1.3):

$$d = \left(\frac{2\Delta\gamma\sigma^2}{\rho_l q_m}\right)^{1/3} \left(\frac{T_m - T}{T_m}\right)^{-1/3} \tag{1.3}$$

where q_m is the latent heat of transformation, and σ is a constant on the order of a molecular diameter. This theoretical discussion is applicable to ice in the absence of impurities; however, it is well-established that impurities are invariably present in real environments. Impurities have been shown to significantly enhance pre-melting through a phenomenon referred to as the colligative effect, also known as the solute effect [24]. This effect reduces the chemical potential of the liquid phase. Furthermore, during the process of freezing, impurities are expelled from the solid phase and tend to accumulate at the interface, forming highly concentrated solutions [24, 28].Consequently, equation (1.1) can be reformulated to incorporate factors that depend on the dissolved species and their concentration (1.4):

$$G_{\mathrm{qll}}(T, P, d, N_i) = \rho_l \mu_l(T, P) + \mu_i(T, P) N_i + RTN_i \left[\frac{\ln N_i}{\rho_{ld}}\right] + \mu_s(T, P) N_s + \Im(d) \tag{1.4}$$

where the subscript l represents the components (chemical potential μ and number of moles N) in the liquid phase, s in the solid, and i refers to impurities. In addition, the term $\Im(d)$ is the total effective interfacial free energy, which is a function of equation (1.5), which takes into account both the Van der Wall (F_{vdw}) and Debye-Hückel (F_{DH}) forces.

$$\Im(d) = F_{\mathrm{vdw}}(d) + F_{\mathrm{DH}}(d) \tag{1.5}$$

Knowing that $F_{\mathrm{DH}} \propto e^{-\frac{1}{\lambda_{\mathrm{D}}}}$, with λ_{D} is the the Debye length which is itself $\propto \sqrt{\frac{T}{N_i}}$. This implies that when the impurity concentration is high, the Debye forces dominate, that is, the Coulomb interactions screened between the charges in the liquid film. This leads to a thinning of the film due to the electrostatic repulsion between the ice surfaces ($d \propto T^{-1}$). In contrast, when the impurity concentration is low, van der Waals forces, which are attractive, dominate and promote the thickening of the film until it completely disappears at a certain temperature ($d \propto T^{-\frac{1}{3}}$). Conversely, at constant impurity concentration, at higher temperatures, Coulombic effects dominate, while at lower temperatures, van der Waals effects dominate. This means that the overall behavior of the film depends not only on the impurity concentration but also on the temperature, which modulates the competition between these forces [29].

Specifically, one of the preferred techniques for studying the thickness of the quasi-liquid layer (QLL) is Atomic Force Microscopy (AFM), which examines the variation in capillary force between a solid and the quasi-liquid structure on the surface. Using this technique, a thickness range of 11 nm at 263 K and 32 nm at 272 K has been measured [30]. However, Pittenger et al. [31] studied the behavior of the tip during its interaction with ice at different temperatures, finding that the presence of a quasi-liquid layer is influenced by both temperature and the hydrophobic properties of the tip. They suggested that AFM measurements could be compromised at temperatures below $-10°$C. However, by using appropriate probes and working in specialized chambers, it is still possible to measure the thickness of the QLL, which has been found to be on the order of a few nanometers[32]. Another widely used technique is ellipsometry. Using this method, it was possible to distinguish two different structures of the QLL. The study conducted by Sazaki et al. [33], which focused on the formation of the liquid film within a temperature range of 258 to 272.9 K, particularly

examining the interval from 271 to 272.9 K, demonstrated the existence of two completely distinct liquid films that can coexist in the same space. At temperatures below 272 K, the presence of droplets, known as $\alpha - QLL$, was observed. As the temperature increased, the droplets tended to aggregate into a uniform structure with greater wettability to ice than α-QLL; this structure was identified as β-QLL (Fig.1.2). These results were confirmed by studies conducted at the same temperatures using AFM.

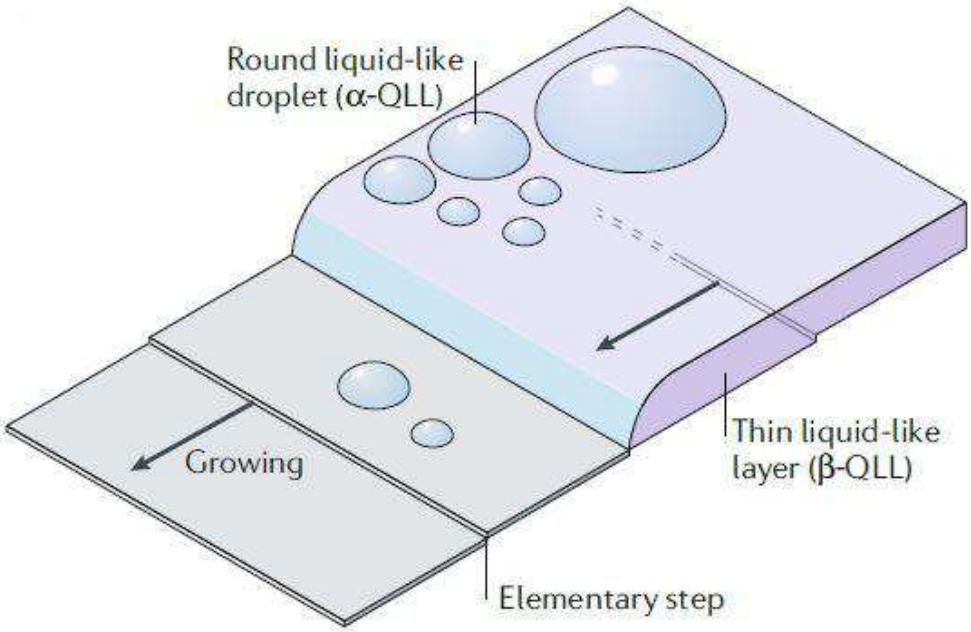

Figure 1.2: Schematic existence of $\alpha-$ and $\beta-$ QLL on ice crystals [32].

Other techniques that can be used to analyze the thickness of the QLL include NMR (Nuclear Magnetic Resonance), ATR-FTIR (Attenuated Total Reflection- Fourier Transform Infrared Spectroscopy), proton scattering, and Low Energy Electron Diffraction (LEED) [32]. The results obtained using these methods are consistent in terms of thickness measurements, which, of course, depend on both the temperature and, in part, the specific measurement technique used. When working with ultrapure water, the thickness ranges from approximately fifty nanometers (at temperatures close to 0°C) to just a few angstroms, eventually disappearing at temperatures below −70°C [34].

Exist an empirical relationship between the total concentration of solutes ($C_t^o = \sum_{i=1}^{n} C_i$) and the portion of free water in ice ($\Phi_{\mathrm{H_2O}}(T)$), which in turn is proportional to the thickness of QLL (1.6) [35]:

$$\Phi_{\mathrm{H_2O}}(T) = \frac{m_{\mathrm{H_2O}} RT}{1000 \Delta \mathbf{H}_f^o} \frac{T}{T - \mathrm{T}_f} \mathrm{C}_t^o \tag{1.6}$$

where the molecular weight of the water ($m_{\mathrm{H_2O}}$) is related to the temperature at which it operates (T), minus the gas constant (R), the enthalpy and melting temperature of the water, $\Delta \mathbf{H}_f^o$ and T_f, respectively.

1.1.2 Location of impurities

The chemical-physical discussion of the QLL presented thus far has aimed to provide insight into the possible reaction environment in which chemical processes can occur. However, as previously mentioned, during the

process of solidification, dissolved species tend to be expelled from the ice crystal lattice. Consequently, a comprehensive understanding of the distribution of chemical species in ice is crucial, as it has significant implications for: (*i*) the movement of deposited chemical species during post-depositional processes [36]; (*ii*) variations in the ice's conductivity [37, 38]; (*iii*) changes in the chemical reactivity between species depending on their location, potentially influencing photoinduced reactions [13, 39–41]. Ions such as Cl^- and NO_3^- can become entrapped within the ice lattice during crystallization are in the form of HCl and HNO_3 respectively [42, 43]. Once incorporated, their mobility is reduced, effectively rendering them chemically inactive under stable conditions and also altering the crystal structure ice lattice. This discussion of ion inclusion in the crystal lattice applies to all species that can originate from ice nuclei, i.e. the ice nucleation centres in the atmosphere. For example, there is a close relationship between NO_3^- and Na^+in coastal areas (R^2=0.92), which gradually decreases as one moves inland (R^2=0.12), as seen in the case of the Antarctic plateau or the Greenland ice sheet [44].

In the coastal case, the high correlation can be explained by the trapping of species during solidification. However, as one moves inland, the uptake of NO_3^- is driven by gaseous HNO_3 or dissolved species in the atmosphere, which then partition onto the grain surface (across the QLL), and thus the reactivity increases. Furthermore, in the coastal uptake scenario, at temperatures above the eutectic point, these particles are expected to form liquid droplets that preferentially accumulate in the grooves at the grain boundaries. Below the eutectic temperature, the sea salt will remain as individual particles, where NO_3^- may exhibit a very different reactivity than in highly concentrated brines [13].

Regarding organic compounds, formaldehyde (HCHO) has been identified as a key component in the chemistry of snow and the polar atmosphere. It influences the chemical reactivity of the snowpack, ozone depletion and the preservation of climate archives in ice. This is due to its photolysis, which produces reactive oxygen species (ROS, e.g. OH·, $HO_2^\bullet$), characteristic of snow and ice as reactive environments [11, 41, 45, 46]. However, it has been demonstrated that formaldehyde can be entrapped within the ice crystal lattice, bind to the surface through hydrogen bonds, or dissolve in the liquid-like region [41]. Studies conducted on the dynamics of formaldehyde exchanges between snow and the atmosphere have shown that this process is relatively slow and that the main variable influencing it is the size of the snow crystals, and thus their surface area [47, 48]. Consequently, the exchange of formaldehyde between snow and atmosphere can be adequately explained without necessarily invoking the processes occurring in the QLL [13]. Concerning larger organic molecules, these have been demonstrated to play a significant role as photosensitisers. This aspect has been extensively researched in the context of aqueous solutions (see section 3). Of particular note are macromolecules such as Humic-Like Substances (HULIS), which are of crucial importance as they act as chromophores, absorbing solar radiation and triggering photochemical reactions in the snowpack. It has been reported that large molecules with low polarity and high vapor pressure, such as Polyciclic Aromatic Hydrocarbons (PAHs) and other Persistent Organic Pollutants (POPs) [14], do not form solid solutions with ice but tend to adsorb onto the surface of snow crystals. Due to their low vapor pressure, they also bind to organic aerosols in the atmosphere [49]. However, it should be noted that adsorption alone does not fully explain all the observed phenomena, indicating the presence of some molecules embedded into organic particles [50]. The presence of organic particles in snow can be attributed to their entry via precipitation or atmospheric transport. These particles undergo chemical transformations, such as oxidation and the formation of new functional groups [51]. The interaction between these particles and the ice surface remains a subject of limited research, but it is hypothesized that a significant portion of organic molecules undergo self-association rather than diffusion onto the ice surface [52]. While some organic acids may migrate to

the ice surface, their interactions are limited. The current state of understanding is incomplete, but it is known that some molecules dissolve in the ice, while others remain in the organic particles or adsorb onto the surface. The effect of the brine formed on the photochemistry of snow appears to be limited [13]. In conclusion, the current state of knowledge does not allow for a definitive conclusion to be drawn on the manner in which organic molecules arrange themselves on the ice, whether they cover the surface uniformly or create agglomerates, and how these may impact (photo)chemical reactions. Furthermore, the behaviour of these species once in contact with the ice remains to be elucidated, for example whether their structure or their ability to absorb solar radiation do change. It has been established that some phenolic compounds may undergo a batochromic shift when in cold environments and in agglomerated form [53].

1.1.3 Optical properties

This section presents an overview of the optical properties of pure ice. Based on this foundation, specific parameters relevant to the investigated environment are introduced in the description of the various types of naturally occurring ice. However, it is first essential to understand the phenomena occurring in pure ice. To that end, the equation governing electromagnetic field propagation E_x in the z-direction is introduced, with the field expressed as a function of time t and angular frequency ω (1.7):

$$E_x = E_0 cos(\omega t - kz) \tag{1.7}$$

Here E_0 represents the electromagnetic field at time t= 0. Furthermore, from Maxwell's equations, it is possible to determine the propagation speed of the wave in a medium (1.8):

$$\nu = \frac{c}{\sqrt{\varepsilon\mu}} \tag{1.8}$$

where μ is the magnetic permeability and ε represents the permittivity of the material in consideration, and consists of a real and an imaginary component $\varepsilon = \varepsilon_{real} + i\varepsilon_{im}$. In nonpolar media, these two parameters remain constant. In contrast, in polar media, such as water and ice, they vary as a function of frequency ω and consequently wavelength λ. The refractive index is known to be $n = \sqrt{\varepsilon\mu}$. Therefore, it can be deduced that the refractive index will also have a real part and an imaginary part $n = n_{real} + n_{im}$ [54], where the real part describes the propagation speed of the wave in the material, and an imaginary part is associated to the absorption coefficient k_a of the wave in the medium, through the (1.9) [55]

$$k_a = \frac{4\pi n_{im}}{\lambda} \tag{1.9}$$

In consideration of Lambert-Beer's law (1.10), which links the absorbed radiation intensity I to the optical path z with respect to the incident intensity I_0 and an extinction coefficient K, the latter is given by the sum of the scattering (k_{scat}) and absorption phenomena. Assuming that the scattering phenomena are negligible, equation (1.10) can be expressed as a function of the absorption coefficient k_a.

$$I(z, \lambda) = I(0, \lambda)e^{-Kz} \tag{1.10}$$

A number of studies have investigated how the refractive index in ice varies from the UV to the IR [55, 56]. As demonstrated in figure 1.3, particularly with regard to the imaginary part, a pronounced discrepancy is evident between the ultraviolet and infrared regions. While fluctuations in the real part are evident, they are

less pronounced in comparison to the imaginary part. Of particular interest is the region between 200 and 700 nm, where the refractive index (and consequently the absorption coefficient) is remarkably low, reaching the order of 10^{-8}. However, as the wavelength increases towards the infrared region, the absorption phenomena related to the (roto)vibrational motions of water molecules become more pronounced. This phenomenon is the reason why, in pure ice (free from chemical impurities and air bubbles), radiation can penetrate several metres into the interior, absorbing the red radiation and giving the ice a blue colour.

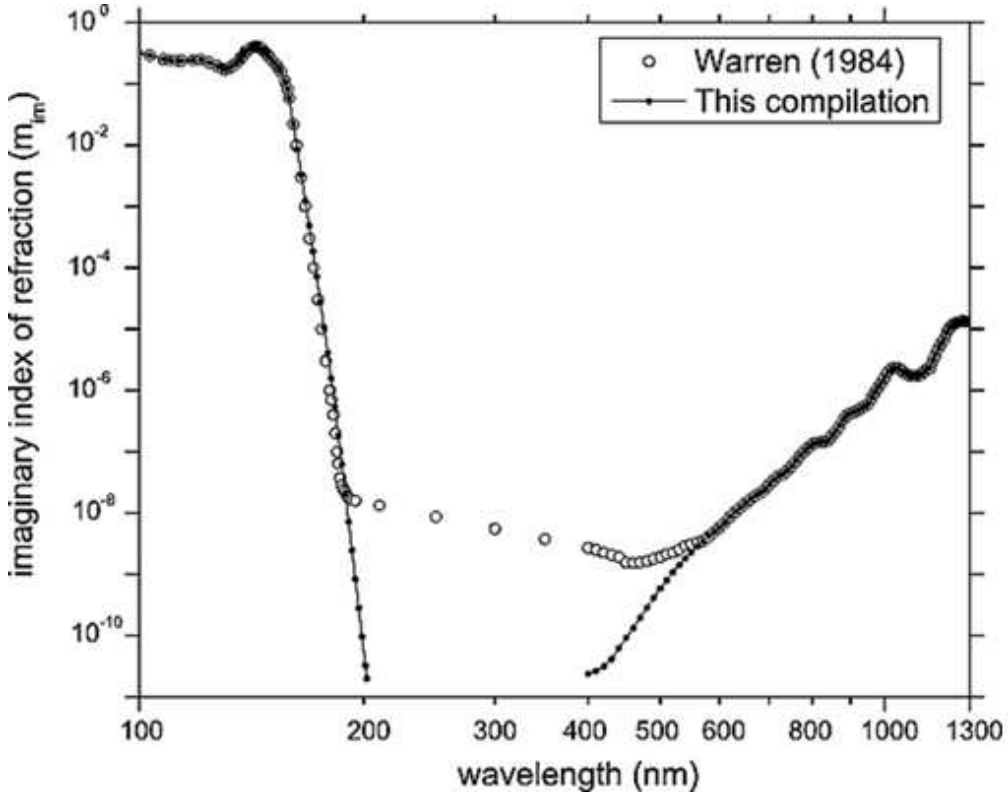

Figure 1.3: Imaginary part of the refractive index in the 100-1300 nm region [55, 56]

Although the k_a term in the UV/Vis region is generally neglected in models of albedo due to its contribution to infinitesimal errors, this approach is not generally adopted in models used to study photochemistry, particularly that of snow (see section 1.2.1) [57–61].

1.2 Types of ice in nature

Ice is present in nature in various forms. Indeed, the polycrystalline structures possessed by ice that forms on rivers or lakes will differ from those of sea ice and even from those formed in the atmosphere.

1.2.1 Snow and ice

In order to provide an accurate description of the physicochemical characteristics of the snowpack, it is necesary provide a brief overview of its formation and the thermodynamic processes that influence its development. The formation of the snowpack is initiated by the development of clouds, which subsequently produces ice crystals. These crystals undergo a process of growth and eventually precipitate to the ground.

The formation of clouds is contingent on the uplift of moist air and the occurrence of adiabatic cooling, which gives rise to the supersaturation of water vapour within the air mass. Under these conditions, the formation of droplets of supercooled water, typically measuring approximately 20 μm in diameter, becomes possible [62]. These droplets are characterised by their exceptional stability, which prevents their immediate transformation into precipitation. Indeed, they can persist in a liquid state down to temperatures as low as -40°C before freezing occurs. This phenomenon underscores the importance of heterogeneous ice nuclei (IN) in facilitating the formation of the hexagonal ice crystal phase (Ice Ih) [63]. The heterogeneous nucleation process can occur via three main mechanisms:

- Immersion freezing: the supercooled droplet forms around a particle, which then initiates ice crystallization from within.
- Contact freezing: freezing is triggered when a supercooled droplet comes into direct contact with a particle, resulting in immediate ice formation.
- Deposition nucleation: it occurs when specific conditions allow water vapour to undergo deposition (inverse sublimation) onto a particle surface without passing through the liquid phase.

These particles have been observed to increase the freezing temperature, potentially up to -9°C, and may originate from various sources. Examples include clay dust with suitable crystalline structures, such as kaolinite, biological structures like bacterial proteins, and sulfuric acid aerosols, which, due to their high hygroscopicity, are also efficient cloud condensation nuclei (CCN) [63].

Subsequent to the deposition of snow on the ground, the process of snow metamorphism is initiated. These processes result in the snowpack settling, leading to a reduction in volume and an increase in density. The distinction of different types of snow is based on their respective densities, each exhibiting distinct morphological characteristics that, in turn, influence its macroscopic properties. As metamorphism progresses, the snowpack transforms into a solid frozen state, known as ice. This transformation is of particular significance as the thickness of the snowpack exerts a substantial influence on the temperature at the ground surface. Two primary heat fluxes interact with the snow: the atmosphere-snow flux and the geothermal flux. At the surface of the snow cover, heat exchanges occur with the atmosphere. During periods of cold weather, this results in heat being transferred from the snow to the overlying air, leading to further cooling of the snowpack [64].

Snow chemical composition

The snowpack contains a wide range of inorganic and organic compounds from a variety of sources, and these substances can come into contact with the snow in a number of ways. As discussed previously, the formation of ice crystals in the atmosphere requires the presence of substances such as plant debris, dust, and aerosols that act as Cloud Condensation Nuclei (CCN). Consequently, these substances are inevitably found within the snow itself [63]. Furthermore, during the crystal growth process in the atmosphere, gases, aerosols, and atmospheric particulates are incorporated into the ice structure. Following the exit of the crystal from the cloud during precipitation, the falling snow has the capacity to capture additional gases, dust, and aerosols[18]. These may adsorb onto the surface of the crystal or, in some cases, penetrate into the pores of the crystal lattice [65].

Consequently, the composition of snow deposited on the ground is representative of the processes involved in crystal formation, as well as the composition of the cloud and the air mass through which the snow has

fallen. However, it is important to note that significant alterations in snow chemistry occur after deposition. In particular, dry deposition of particulates and aerosols leads to the formation of surface hoar layers that are enriched with exogenous substances. Observations indicate that the rate of dry deposition increases with wind speed, as the snowpack functions as a filter, trapping airborne particles [66, 67]. Finally, metamorphic processes – especially those involving wet snow – contribute to the redistribution and removal of more soluble species from the snowpack through percolation [65].

In the context of analyzing the contributions of the Earth crust to the composition of the snow, particular attention is paid to the presence of ions Ca^{2+} and Mg^{2+}, whose abundance can be mainly attributed to geological factors and the wind transport, as of the Saharan sands across the northern hemisphere [68]. Further elements associated with crustal impurities, taking into account specific local geological conditions, include Mn, Ti and Fe, as documented in the specific context of the Dolomites [69]. In addition to inorganic compounds, the presence of organic species of natural origin is observed, including low molecular weight alkanes and phenols, humic acids, fulvic acids, and compounds of high molecular weight of biological origin [41]. The presence of ions Na^+, Cl^-, and K^+ is indicative of a marine origin. The Cl^-/Na^+ ratio is a frequently used parameter to distinguish between marine and anthropogenic sources. A value above 1.8, which is the typical ratio for seawater, suggests the presence of an additional anthropogenic component, which may result from waste combustion [69]. Among organic compounds of marine origin, methanesulfonic acid (MSA) is frequently used as a tracer of algal bloom, as a by-product of the oxidation of dimethylsulfide (DMS) emitted by marine phytoplankton [70]. With regard to substances of anthropogenic origin, POPs play a particularly important role. These compounds are distinguished by their high persistence in the environment, which facilitates their dispersion over extensive geographical distances and their capacity to bioaccumulate within trophic networks. This phenomenon has the potential to have serious consequences for human health and ecosystems. Several classes of contaminants have been determined to fall into this category. Such classes include the already mentioned PAHs, polychlorinated biphenyls (PCBs), organochlorine pesticides (e.g., dichlorodiphenyltrichloroethane -DDT-) and other halogenated organic compounds (e.g., hexachlorocyclohexanes -HCHs-). The most widely known and prevalent isomer of HCH is lindane (γ-HCH). The environmental and health significance of POPs has stimulated extensive scientific research aimed at their identification and quantification in remote environments. The most significant studies include investigations on the presence of PCBs in the Arctic, analyses conducted on firn and fresh snow at Col del Lys (Monte Rosa), as well as research carried out on the glaciers of Mount Everest, in particular on the East Rongbuk Glacier. Of particular relevance is the study of temporal trends in species, such as PAHs and synthetic fragrances, whose presence is closely correlated with changing socio-economic conditions on a global scale. These trends show significant increases in recent decades, particularly in geographic areas close to sampling sites, reflecting dynamics such as population growth, urbanization, and improved living conditions. This phenomenon can be situated within the paradigm of the so-called Great Acceleration, which is defined as the concurrent intensification of numerous environmental, economic, and social indicators since the mid-20th century, with evident repercussions on the contamination of remote environments [71].

Snow optical proprieties

As previously discussed, snow is a porous matrix consisting of of ice crystals and air interstices. This configuration enables photons from the solar spectrum to be reflected directly from the surface of the snowpack, as well as to penetrate into it. Once inside, photons can undergo multiple scattering phenomena, which can lead to their re-emission outwards or their temporary entrapment within the snow mass [55]. A schematic

representation of these processes is illustrated in Figure 1.5, in which the interaction of incident solar radiation with the snowpack is visible. A significant proportion of the radiation is reflected directly from the snow surface, while a smaller proportion penetrates the snow. Of the latter, a fraction is entrapped within the ice-air matrix. A portion of the entrapped energy can be absorbed, thereby triggering photo-induced reactions. As illustrated in the figure, reference is made to the photolysis of NO_3^- with the consequent release of NO_2. The residual radiation, after undergoing multiple scattering events within the snow, can be re-emitted to the external environment [40].

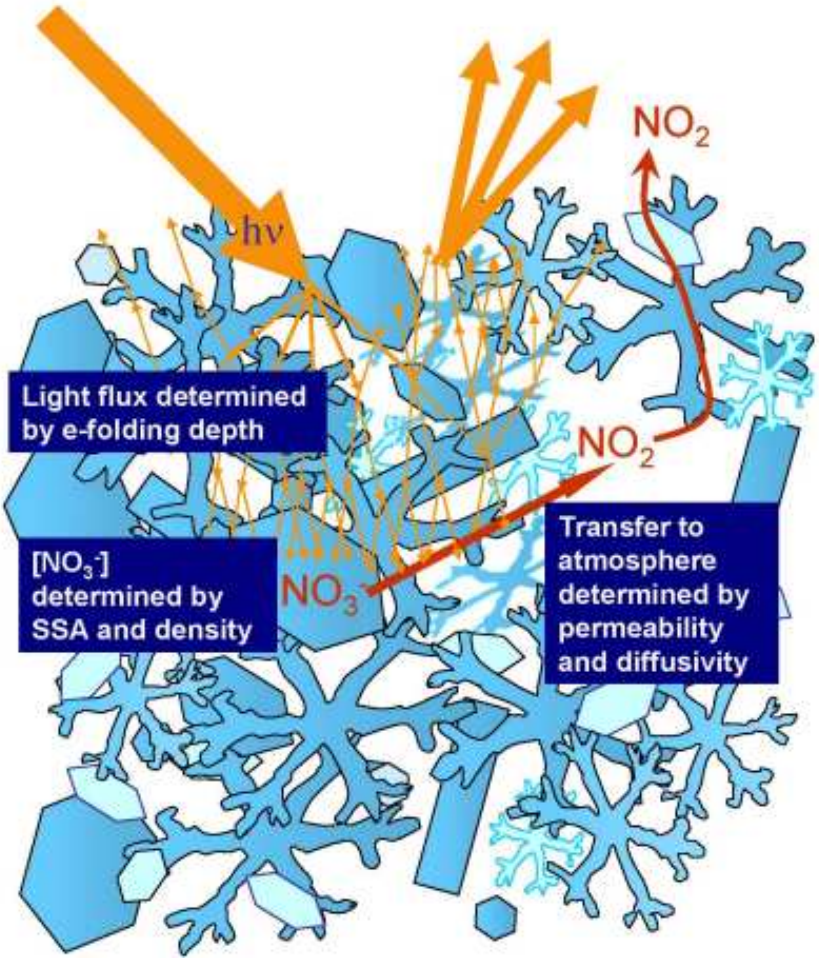

Figure 1.4: Qualitative description of solar radiation activity within the snowpack, both from a physical point of view and with regard to possible photochemical reactions (in this case with nitrate)[40].

It is important to note that snow is not an optically homogeneous medium; rather, it is composed of a disordered collection of ice crystals and pores. As a result, individual crystals are commonly approximated to spheres in order to simplify radiative calculation models. In this context, the Specific Surface Area (SSA) is a pivotal parameter, defined as the total area of ice per mass unit. The SSA is closely related to the size of snow grains, in particular their average radius (r), and is a key indicator for understanding the absorption, scattering and light penetration into the snowpack (1.11)

$$SSA = \frac{3}{r\rho_i} \tag{1.11}$$

The albedo is inversely proportional to the SSA. A high SSA, which is indicative of snow formed from small crystals, corresponds to a greater reflective surface area per mass unit. This phenomenon is known to enhance albedo, as finer grains exhibit superior reflectance of solar radiation, particularly within the visible spectrum. However, over time, the snowpack undergoes processes of aging and metamorphosis that result in the aggregation and swelling of crystals. Consequently, the SSA diminishes, resulting in a reduction of albedo. Larger grains have been observed to reflect light less efficiently and to absorb more photons [72, 73].

As has been previously established, the discussion has centered on the processes occurring at the surface. However, to fully understand the photochemical reactions within the snowpack, it is essential to also examine how solar radiation penetrates into it. As outlined in the preceding paragraphs, particularly in equation (1.9), in the case of pure ice, radiation within the 300-1200 nm spectral range experiences negligible absorption, thereby facilitating its deep penetration. However, when considering the scattering phenomena due to the presence of snow grains, an extinction coefficient can be introduced, which is inversely proportional to the size of the grains themselves. This suggests that the probability of absorption of photons ($\beta = k_{abs}/k_{ext}$), when considered in isolation, tends to zero; in other words, light can effectively penetrate the mantle. Adjusting Equation (1.10) to account for these factors, it becomes possible to calculate the fold depth e z_e, defined as the depth at which incident radiation is reduced by a factor e: $z_e = 1/K$, where K is the parameter introduced in Equation (1.10). This coefficient is proportional to both the absorption coefficient and the snow scattering coefficient. By reformulating the model, it is possible to estimate the value of $z_e(\lambda_0)$ through Equation (1.12), which relates the wavelength of the radiation considered ($\xi \propto \sqrt{\lambda_0}$) to the square root of the grain size, normalised with respect to the snowpack density (ρ_s).

$$z_e(\lambda_0) = \xi \frac{\sqrt{d}}{\rho_s} \tag{1.12}$$

In addition, ξ also takes into account parameters related to scattering asymmetry and snow grain morphology, allowing for a more accurate estimate of radiation penetration within the snowpack [60, 73]. As the equation (1.12) shows, the z_e value varies depending on both the shape and size of the snow grains. Experimental studies have shown that, in the UVA region (around 300 nm), for typical fresh snow grains, the penetration depth of radiation can reach around 20 cm. This finding confirms the remarkable transparency of the fresh snowpack at these wavelengths, with important implications for the photochemical processes occurring in the deeper layers of the snow [60, 61, 73].

1.2.2 Sea ice

A significant part of the cryosphere is made up of sea ice, which covers about 12 % of the ocean surface, corresponding to about 7% of the Earth's surface. Sea ice performs several key functions: it is an essential habitat for polar species and indigenous peoples; it contributes to the regulation of global climate by reflecting solar radiation; it limits heat exchange between the ocean and the atmosphere; and it also modulates gaseous exchanges, such as CO_2. It also participates in the control of ocean circulation through the formation of denser, saline waters. After formation, sea ice is prone to multiple physical, chemical and biological processes that progressively alter its structure and composition [8].

Seawater has an average salinity of about 34 Practical Salinity Units (PSU) and, in the absence of impurities, solidifies at a temperature of about -1.86 C. When cold air cools the ocean surface, the surface water, which has become denser, tends to sink, allowing warmer water masses to rise from the deep layers. Consequently, in order for ice to actually form, several layers of the ocean must be close to the freezing point.

The rate of growth (as well as the rate of melting) of ice is highly dependent on heat exchange between the ocean, ice and atmosphere. Once formed, the ice sheet acts as a thermal insulator, reducing heat exchange between ocean and atmosphere. This insulating effect further slows the growth of the ice, as it takes longer for the underlying water to cool and increase in density. This slowdown is even more pronounced in the presence of an overlying snow cover, which further increases thermal insulation and reduces the efficiency of heat exchange with the atmosphere [54]. The first crystals formed during the freezing of seawater typically take on a needle-like shape and tend to aggregate in suspension, giving rise to a phase known as frazil ice. As freezing progresses, these crystals consolidate into an initially granular structure, which is later followed by the growth of columnar ice. The latter may grow vertically for several centimetres, forming a layered structure typical of older sea ice (Figure 1.5).

Sea ice can be classified according to its age in two main categories: first-year ice and multi-year ice.

- First-year ice consists of floating structures that form during the cold season and generally do not survive the summer period. During winter, these ices reach thicknesses between 30 cm and 2 m, and can be further subdivided according to thickness: thin ice (30-70 cm), medium ice (70-120 cm) and thick first-year ice (120-200 cm). The distribution of these types varies with latitude: thin ice typically forms in regions close to the Polar Circle, while thicker ice is common within polar areas [74].

- Multi-year ice, on the other hand, is characterised by greater thickness, generally between 2 and 5 metres, and survives at least one melting season. Compared to annual ice, it has lower salinity and more air pockets, characteristics that make it more rigid and resistant to fracture [74].

Observationally, young ice and multi-year ice show significant differences in terms of colour and electromagnetic properties, making it possible to distinguish and monitor them using satellite remote-sensing techniques.

Sea ice optical proprieties

Sea ice is a complexly structured translucent material, consisting mainly of ice, brine inclusions, air bubbles, biota and particulate matter. The absorption of radiation in sea ice (k_{si}) represents the sum of the absorption contributions of its main components: ice (i), brine (b,) gas and particulate matter ($part$), as expressed in equation 1.13. Assuming that absorption by air bubbles is negligible, the expression of total absorption can be simplified accordingly.

$$k_{si} = V_i k_i + V_b k_b + V_s k_s + V_{bio} k_{bio} + V_{part} k_{part} \tag{1.13}$$

where k represents the absorption coefficient, V is the volume fractions of different components.

Ice represents the predominant component of sea ice. Under ideal conditions, in the absence of air bubbles and scattering, the absorption coefficients of pure ice can be determined by applying equation 1.10. These coefficients were measured in the laboratory using pure, bubble-free soft ice. Knowledge about absorption by solid salts in ice, which may play a significant role at very low temperatures, is still limited [cite]. Particles embedded in ice may include sediment, dissolved organic substances, black carbon and biota. If these materials are present in significant quantities, their contribution to radiative absorption must be appropriately considered [75].

However, deviating from the ideal situation, even a small sea ice sample contains with high probability numerous scattering elements, makes direct measurements of scattering coefficients and phase functions particularly complex. Consequently, scattering properties are usually estimated by theoretical models based on the microstructure of the sea ice or inferred from integrative measurements of the Apparent Optical

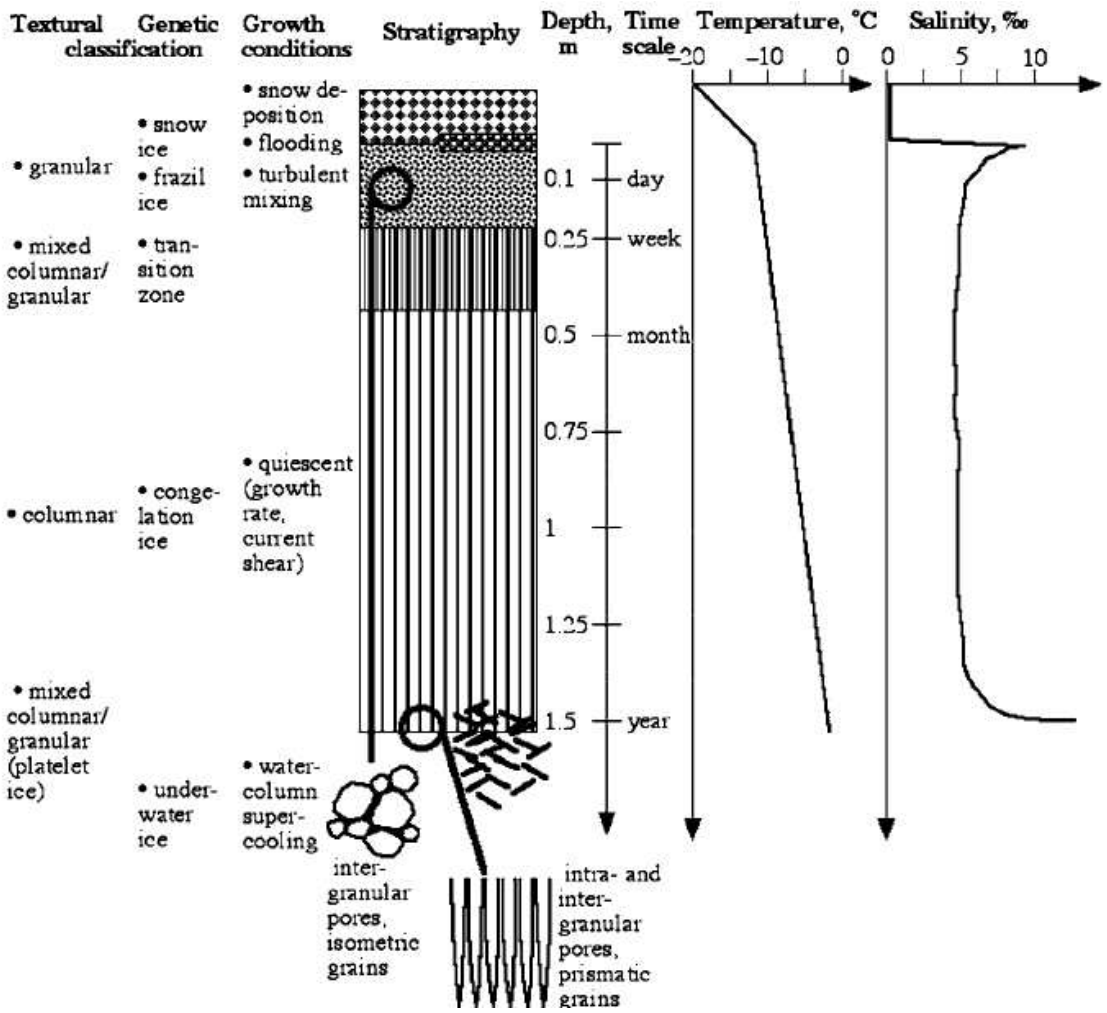

Figure 1.5: Representative scheme of the stratigraphy of first-year sea ice growth. The temperature and salinity profile is also depicted. [54]

Properties (AOPs) of the ice. However, both approaches have limitations. Theoretical estimates require not only knowledge of the volumes of brine, air and solid salts, but also a detailed description of their spatial distribution, including the numerosity, size and distribution of inclusions. Similarly, the inference of scattering properties from albedo and transmittance measurements requires accurate information on the vertical profiles of the structure and physical characteristics of the ice. The particles, sediments and biota present in sea ice contribute mainly to the absorption of radiation, while their effect on scattering is generally negligible. Similar to absorption, scattering in sea ice can be described as a weighted sum of the contributions of its main constituents: ice, brine, gases and solid salts [75].

Among the AOPs of sea ice, albedo is undoubtedly the most widely used and, in all likelihood, the most important. Its determination is based on measuring the incident irradiance from the sky and the reflected irradiance from the surface; the ratio of these two quantities gives the albedo value. A large amount of albedo data is available for different ice types and surface conditions. The albedo is strongly influenced by the surface characteristics, and the scattering and absorption processes occurring within the ice. In the early stages of sea ice formation, albedo is particularly sensitive to thickness. A slight increase in total albedo is observed as thickness increases. In the presence of snow cover, albedo values can reach as high as 0.87. The

asymptotic thickness of the ice, i.e. the thickness beyond which the albedo stabilises, is inversely related to the absorption coefficient: lower absorption values correspond to higher albedo and asymptotic thicknesses. Surface conditions play a crucial role in modulating albedo, particularly during the melting season. The main surface types observed in multi-year ice include: cold dry snow, melting snow, melting bare ice, light melt ponds (light blue and blue), dark melt ponds and leads. These categories represent the dominant conditions in multi-year ice. As the snow melts, the albedo decreases significantly at all wavelengths; complete removal of the snowpack results in a further reduction. The spectral albedos of melting multi-year ice are slightly higher than those of melting annual ice [75].

Chapter 2

An overview of photochemistry

List of acronyms and variables

PPRIs	Photochemically produced reactive intermediate
CDOM	Chromophoric dissolved organic matter
ROS	Reactive oxygen species
$\mathbf{p}_a^0(\boldsymbol{\lambda})$	Incident spectral photon flux
$\mathbf{P}_a$	Total absorbed photon flux density
$\mathbf{R}_x$	Rate of formation
$\boldsymbol{\Phi_x}$	Quantum yield
HOMO	Highest occupied molecular orbital
LUMO	Lowest unoccupied molecular orbital
SOMO	Singly occupied molecular orbital

Photochemical processes play a central role in the transformation of xenobiotic compounds within a variety of environmental settings [76, 77]. In addition to physical and biological [78, 79] processes, these reactions can facilitate the breakdown of pollutants, yielding their degradation products. Photochemical reactions are typically classified into two main categories: direct and indirect. Direct photolysis refers to a chemical transformation driven by the direct absorption of light by the compound itself. This pathway is followed by certain micro-contaminants. To illustrate, the direct photolysis of bentazone [80] (a herbicide), nitrophenols [81], and pharmaceutical compounds [82] represents a principal degradation pathway under UVA and UVB radiation in freshwater systems. In contrast, indirect photolysis occurs when sunlight is absorbed by a third compound, known as a photosensitiser, which then produces transient reactive species responsible for the degradation of the target compound. These transient species are often called Photochemically Produced Reactive Intermediates (PPRIs) and have been found to be photoproduced in surface waters, atmospheric waters and in ice/snow. The most common photosensitizers found in surface waters are nitrate and nitrite [83], as well as Chromophoric Dissolved Organic Matter (CDOM), which is the fraction of Dissolved Organic Matter (DOM) that is capable of absorbing radiation [84], and reactive oxygen species (ROS) [85]. Finally, halogens, if activated, can also become oxidizing species in their turn. Although a considerable body of research has been devoted to the study of photochemical reactions in water and atmospheric systems, investigations into analogous processes occurring in snow are a relatively recent phenomenon, having emerged as a topic of scientific interest only within the past two decades [4, 11, 14, 41]. It is also possible that photosensitizers present in water or the atmosphere may be found within the snowpack.

This chapter examines the different reactive species that play a key role in icy matrices. However, it is also necessary to know the rate at which these reactive species are formed. To do so, it is essential to calculate the flux density of the absorbed photon ($p_a(\lambda)$), which represents the amount of radiation absorbed by a photosensitizing species. This value depends on two main factors (2.1): the incident spectral photon flux ($p_a^0(\lambda)$) and the fraction of absorbed photons $f_a(\lambda) = 1 - 10^{-A(\lambda)}$.

$$p_a(\lambda) = p_a^0(\lambda)\ [1 - 10^{-A(\lambda)}] \tag{2.1}$$

The validity of this equation is restricted to the monochromatic radiation. In the case of polychromatic radiation, the total absorbed photon flux density (P_a) is given by (2.2):

$$P_a = \int_\lambda p_a(\lambda) d(\lambda) \tag{2.2}$$

This value is crucial for calculating the rate of formation of reactive species (R_X), according to the equation (2.3):

$$R_X = \Phi_X P_a \tag{2.3}$$

Φ is the quantum yield of the transient species X. In the presence of wavelength-dependent quantum yield, the weighted integral is used [77] (2.4):

$$R_X(\lambda) = \int_\lambda \Phi_X(\lambda) P_a d\lambda \tag{2.4}$$

2.1 Direct photolysis

A chemical species, when exposed to solar radiation, can absorb photons and thus acquire energy. The absorbed energy can be dissipated by non-radiative or radiative processes, such as the release of heat or fluorescence, or it can be used to induce a chemical transformation. As anticipated above, when the absorption of electromagnetic radiation by the molecule directly induces a chemical reaction, it is called direct photolysis. In this mechanism, the photon energy is sufficient to place the molecule in an excited state, from which chemical bond breaking, isomerization [86] or other structural changes can occur. Direct photolysis is thus a fundamental photochemical process that is particularly relevant to the degradation of organic pollutants in the natural environment.

However, not all species are capable of absorbing the solar radiation available at ground level. For direct sunlight-induced photolysis to occur, the species must absorb in the spectral region above 280 nm, which is the lower limit of solar radiation reaching the earth's surface due to atmospheric absorption. In practice, for a compound to be photoactive in sunlight, it must exhibit significant absorption above 300 nm, corresponding to the UVA-visible portion of the solar spectrum. Consequently, the capability of a pollutant to undergo direct photolysis is strictly dependent on its spectral properties, in particular the position and intensity of the absorption bands [80]. However, it is important to note that there are some compounds that, although absorbing weakly in the >300 nm region, nevertheless undergo direct photolysis. A relevant example is ibuprofen, which exhibits a relatively low absorption coefficient at wavelengths of incident solar radiation but still degrades significantly under UV irradiation. This behavior can be attributed to the high quantum yield of the photochemical reaction, which compensates for the low absorption efficiency, and demonstrates that the effectiveness of photolysis depends not only on the molecule's capability to absorb light, but also on the probability that the absorbed energy results in a chemical transformation [87]. In the case of direct photolysis, the reaction speed can be expressed as given in equation (2.4).

2.2 Reactive oxigen species

ROS are a group of molecules and radicals derived from molecular oxygen, characterised by high chemical reactivity. In aqueous environments, ROS can be generated through different mechanisms, including photocatalytic processes, redox reactions, activation of oxidants and the photochemical activity of CDOM. The main ROS relevant to aquatic systems include the hydroxyl radical ($^{\bullet}OH$), which is extremely reactive and capable of oxidising a wide range of organic compounds, and singlet oxygen ($^1O_2$), an excited non-radical state of molecular oxygen that exhibits selective but significant reactivity towards certain substrates. In addition to these there are superoxide ($O_2^{-\bullet}$), a radical less reactive than $^{\bullet}OH$ but involved in important redox reactions and in the secondary formation of other ROS, and hydrogen peroxide (H_2O_2), a non-radical oxidant that can act directly or serve as a precursor for the generation of $^{\bullet}OH$ through Fenton reactions. Under certain conditions, the peroxyl-radical ($ROO^{\bullet}$) may also be present, involved in secondary oxidative pathways.

The reactivity and behavior of $^{\bullet}OH$ and singlet oxygen, the species most studied for their role in the photochemical transformation of organic pollutants, are described in more detail below.

2.2.1 Hydroxyl radicals

Hydroxyl radicals are among the most reactive transient species that can be generated, especially as a result of photochemical processes. Their high reactivity, close to the diffusion limit ($k_{diff} \approx 10^9$-10^{10} M^{-1} s^{-1}), translates into very high second-order kinetic constants with respect to numerous organic compounds.

However, due to their extremely reactive nature, $^{\bullet}OH$ radicals are rapidly eliminated from the aquatic environment through reactions with various natural components of water, in particular with DOM. This means that their steady-state concentration in surface water is extremely low, generally between 10^{-18} and 10^{-16} M [88, 89].

Hydroxyl radicals can be produced in surface waters by the photolysis of nitrates (NO_3^-) and nitrites (NO_2^-). However, the photolysis of NO_3^- competes with photoisomerisation, an alternative process that limits efficiency. The generation of $^{\bullet}OH$ from NO_3^- depends on pH. The $^{\bullet}OH$ radical has a pK_a of 11.5, meaning it is stable as a neutral species at environmental pH levels. Conversely, NO_2^- photolysis is more effective at acidic pH because nitrous acid (HNO_2, $pK_a = 3.39$) absorbs light more efficiently than NO_2^-. However, in waters with a pH greater than 5 (which is the norm), the effect of HNO_2 is limited. Although nitrite is generally less concentrated than nitrate, it exhibits greater absorption (with a maximum at 355 nm compared to 305 nm for nitrate) and has a higher quantum yield of $^{\bullet}OH$ (see the following dedicated paragraph).

Moreover, $^{\bullet}OH$ radicals can be produced through Fenton-type reactions involving ferrous iron (Fe^{2+}) and hydrogen peroxide (H_2O_2). In this process, Fe^{2+} reacts with H_2O_2 to generate $^{\bullet}OH$ and Fe^{3+}. The reaction is particularly efficient in acidic conditions and can be further activated by sunlight (photo-Fenton), which reduces Fe^{3+} to Fe^{2+}, making the cycle continuous [77, 90]. The presence of CDOM influences this mechanism in two ways: on the one hand, it can complex iron, modifying its speciation and availability; on the other hand, it can contribute to the photogenerated production of H_2O_2. In addition, CDOM can also act as a light absorber, promoting photoredox reactions that indirectly generate $^{\bullet}OH$ radicals. However, as it is also an effective radical scavenger, CDOM can limit their actual availability. The interaction between CDOM and iron therefore plays a key role in regulating radical chemistry in natural waters [91, 92].

2.2.2 Singlet oxygen

Singlet oxygen is formed in aerated surface waters through a reaction involving molecular oxygen and the excited triplet state of CDOM ($^3CDOM^*$). The quantum yields of $^1O_2$ formation are similar to those of $^3CDOM^*$, which confirms that this is a major deactivation pathway for $^3CDOM^*$ in the presence of oxygen. The main pathway for deactivation of $^1O_2$ is collision with water molecules, which has a high first-order rate constant. This renders the role of DOM as a scavenger in the aqueous bulk negligible. However, $^1O_2$ can react with specific organic compounds, such as chlorophenols, phenolic pesticides, and some easily oxidisable amino acids [77].

Steady-state concentrations of $^1O_2$ increase with CDOM (and therefore with DOC), but decrease with depth due to reduced radiation. Figure 2.1 shows the trend in the steady-state concentration of $^1O_2$ as a function of DOC and depth, as modelled using APEX software [93], a tool for simulating photochemical processes in natural waters. There is a clear direct relationship between $[^1O_2]$ and DOM content: as DOC increases, $^1O_2$ production increases, as CDOM acts as a photosensitiser under solar radiation. This effect is particularly marked in more superficial waters, which are well lit and more exposed to gas exchange with the atmosphere. However, $[^1O_2]$ decreases rapidly with depth, due to reduced light penetration and the

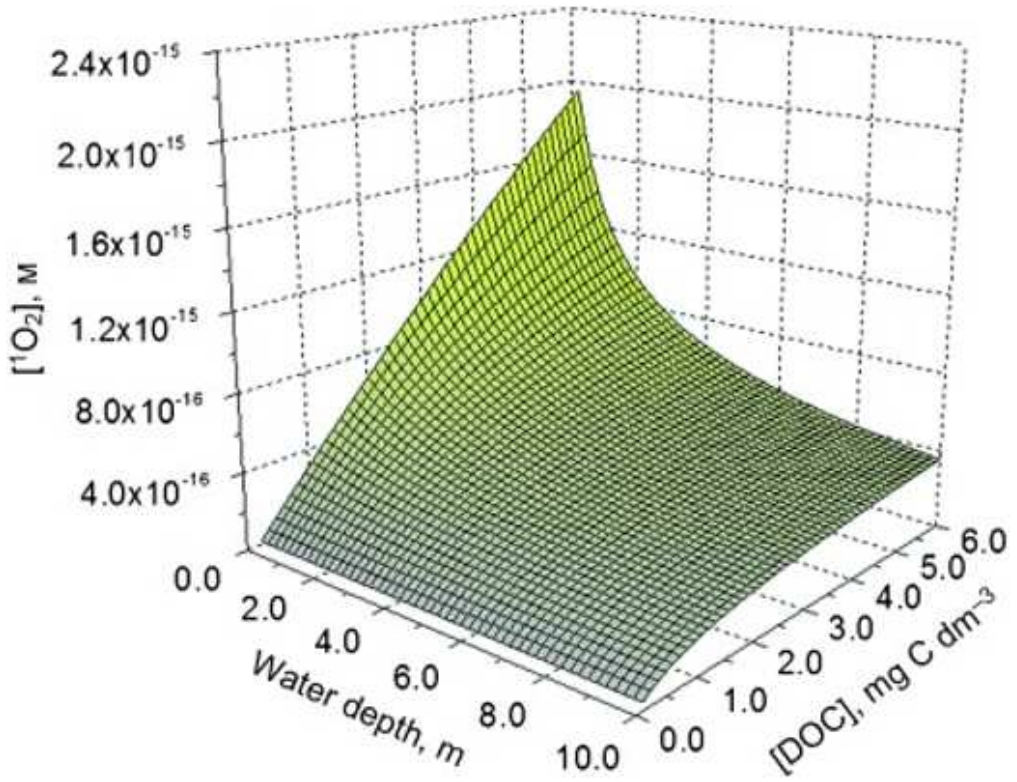

Figure 2.1: Steady-state [$^1O_2$] as a function of DOC and water depth, in aerated solution [77].

consequent attenuation of photogeneration processes in the deeper zones of the water column. An important aspect is that $^1O_2$ accumulates in the hydrophobic sites of DOM, where it reaches much higher concentrations than in the bulk. In these microenvironments, $^1O_2$ can effectively degrade hydrophobic pollutants, but not hydrophilic ones, which remain in the bulk [94]. The poor effectiveness of $^1O_2$ in the bulk is confirmed by the lower degradation of hydrophilic probes compared to hydrophobic ones.

2.3 Reactive nitrogen species

Nitrate (NO_3^-) and nitrite (NO_2^-) play an essential role in surface water and snow/ice chemistry. When exposed to light, these compounds can generate highly reactive chemical species. These include reactive oxygen species, such as $^\bullet$OH, and Reactive Nitrogen Species (RNS), such as nitrogen dioxide (NO_2), nitrogen monoxide (NO) and peroxynitrite ($ONOO^-$) [95]. The study of the photochemistry of nitrates in frozen matrices is of increasing interest, as these reactions may have significant implications in various fields, particularly in the modeling of ozone chemistry in the boundary layer of polar regions. Photolysis of nitrates entrapped in snow and ice releases nitrogen oxides (NO_x, including NO and NO_2), gaseous species that, once released into the atmosphere, can promote ozone formation through a series of photochemical reactions. These processes contribute to modulating the chemical composition and air quality in polar areas, with possible repercussions both locally and globally [4, 39, 96]. The production of RNS is described through the photoinduced R1-R4 reactions. In particular, the R1 reaction represents the photoisomerisation of NO_3^-, a process that requires wavelengths below 280 nm. However, given the atmospheric absorbance at these wavelengths, this pathway is of little environmental relevance. The formation of NO_2 can also occur indirectly through the oxidation

of NO_2^- by $^\bullet OH$, as described by the reaction R5. The latter can be secondarily generated from transient oxygenated species ($O^{\bullet -}$) produced in reactions R2, R3 and R4, if they are dissolved in the aqueous phase.

$$NO_3^- \xrightarrow{h\nu} ONOO^- \quad \text{(R1)}$$

$$NO_3^- \xrightarrow{h\nu} NO_2 + O^{\bullet -} \quad \text{(R2)}$$

$$NO_3^- \xrightarrow{h\nu} NO_2^- + O(^3P) \quad \text{(R3)}$$

$$NO_2^- \xrightarrow{h\nu} NO + O^{\bullet -} \quad \text{(R4)}$$

$$NO_2^- + OH^\bullet \longrightarrow NO_2 + OH^- \quad \text{(R5)}$$

$$NO_2 + NO \longrightarrow N_2O_3 \quad \text{(R6)}$$

In surface waters, the concentration of NO_3^- is typically around 4 mg L^{-1}, although this value may vary significantly depending on the characteristics of the water body. In contrast, the concentration of NO_2^- is generally 2-3 orders of magnitude lower, being in the μg L^{-1} range. This quantitative imbalance would suggest, at first sight, that photochemical processes predominantly involve NO_3^- [97]. Similar considerations can be extended to cryospheric environments. In fresh snow and ice (e.g. glacial cores), NO_3^- concentrations are generally lower than in surface water systems, with typical values in the order of 10-1000 μg L^{-1}, depending on location (e.g. Alps, Greenland, Antarctica) and the influence of atmospheric deposition. Nitrite, on the other hand, is present in ultratrace concentrations, often ¡ 1 μg L^{-1}, and is chemically unstable, as it is subject to rapid oxidation and/or photodegradation [96]. However, this interpretation does not take into account the distinct optical properties of the two species. The molar absorption coefficient of NO_3^- exhibits a maximum around 300 nm, a spectral region where solar radiation penetrating into aquatic ecosystems is strongly attenuated, either by atmospheric absorption or by dissolved and suspended matter. In contrast, NO_2^- absorbs more effectively in the 360 nm region, where the intensity of available solar radiation is much higher (Figure 2.2 [95]).

It follows that, despite its lower concentration, NO_2^- can contribute comparably, or in some cases even more, to the production of photoinduced reactive species. In other words, the actual photochemical reactivity of NO_3^- and NO_2^- in the aquatic environment does not depend solely on their relative abundance, but is strongly modulated by the interaction between absorption spectrum and photon availability in the water column.

In the previous section, the reactivity of the hydroxyl radical was discussed in detail, but the reactivity of the $NO_2^{\bullet -}$ also deserves particular attention. This radical, in addition to participating in further photochemical reactions in the atmosphere, with relevant implications for stratospheric ozone chemistry, as well shows marked reactivity towards dissolved aromatic compounds in aqueous or cryospheric compartments. In particular, $NO_2^{\bullet -}$ is known to react efficiently with phenolic compounds, generating a variety of aromatic nitro compounds as end products. Such transformations are of considerable environmental interest, as the nitriding products are often more persistent and more toxic than the original phenolic precursors. This implies that secondary photochemical processes induced by $NO_2^{\bullet -}$ not only influence the degradation or transformation of contaminants, but may also lead to an increase in the overall toxicity of the system [98].

However, it is possible that during freezing processes in the presence of NO_2^-, nitration reactions can occur even in the complete absence of solar radiation. This behaviour suggests that, in frozen environments, dark chemistry reactions involving NO_3^- and NO_2^- may contribute significantly to the transformation of organic matter, thus being not negligible in the overall reactive balance of the system [99, 100]

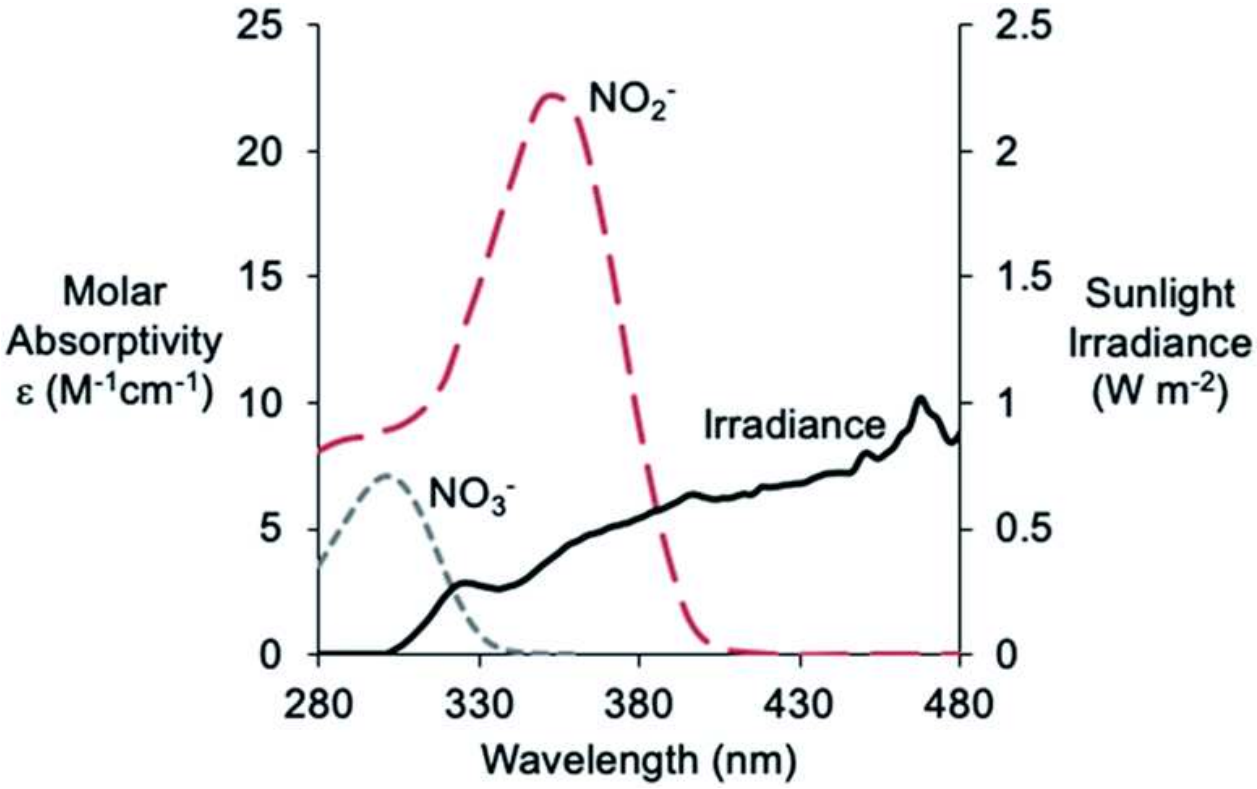

Figure 2.2: NO_3^- and NO_2^- molar absorptivity and sunlight irradiance spectrum from 280–480 nm [95]

2.4 Chromophoric dissolved organic matter

Chromophoric dissolved organic matter is defined as the fraction of dissolved organic matter that absorbs light. The origins of these compounds are diverse, with potential sources including aquatic microbial sources or terrestrial sources such as lignin that has undergone degradation and dissolution. The CDOM is predominantly derived from humic substances, which include Humic Acids (HA, soluble above pH 2) and Fulvic Acids (FA, soluble at all pH values) [101, 102].

Once CDOM has absorbed radiation with $\lambda < 500$ nm, thus including visible light, it can be promoted from the fundamental state to an excited singlet state, referred to as ^{1}CDOM*. This excited singlet state possesses an energy higher than that of the excited triplet state, ^{3}CDOM*, and is therefore potentially more chemically reactive. However, the decay of the singlet state is extremely rapid, with very short lifetimes that limit its stationary concentration under typical environmental conditions. This process, known as intersystem crossing (ISC), facilitates the transition of CDOM from the excited singlet state to the excited triplet state. The triplet state exhibits a lower energy level in comparison to the singlet state; however, its half-life is significantly longer. This property enables the species to accumulate at higher concentrations within the system. Consequently, although the singlet state is more energetic and potentially more reactive, in practice the triplet state is the more significant in terms of photochemical effects and the formation of reactive species in natural waters [91].

Once promoted to the excited triplet state (^{3}CDOM*), CDOM can return to the fundamental state via several de-excitation pathways. The aforementioned processes encompass direct radiative decay, which is characterised by the kinetic constant k, energy transfer to other species in solution, and oxidation-reduction

reactions. The ^{3}CDOM* is therefore considered to act as a photoactive species, capable of triggering a variety of secondary chemical processes.

The energy of the triplet state of CDOM has been estimated to range from approximately 180 to 320 kJ mol^{-1}. One of the most environmentally significant reactions is the transfer of energy to dioxygen O_2 in the fundamental triplet state ($^3O_2$), which can be excited to the singlet state $^1O_2$. The energy jump required for this transition is approximately 90 kJ mol^{-1}, which is significantly lower than the energy of ^{3}CDOM*, thus rendering this process highly thermodynamically favourable. The singlet oxygen ($^1O_2$) that is produced is a ROS with strong oxidising potential and significant impact on water and ice chemistry [103].

This energy transfer reaction also offers a useful means of estimating the steady-state concentration of ^{3}CDOM*. Under steady-state conditions, the rate of formation of the excited state is assumed to be equal to the sum of its dissipation paths. Under such conditions, the concentration of ^{3}CDOM* can be described by the following expression (2.5):

$$[\mathrm{CDOM}^*] = \frac{R_{\mathrm{abs}}\,\Phi_{\mathrm{isc}}}{k_{\mathrm{O_2}}[\mathrm{O_2}] + k_{\mathrm{td}}} \tag{2.5}$$

where R_{abs} represents the rate of absorption of radiation by the CDOM, $\Phi_{\mathrm{isc}}$is the quantum yield of the intersystem crossing process, $k_{\mathrm{O_2}}$ is the rate constant of energy transfer to oxygen, $[\mathrm{O_2}]$ is the concentration of dissolved molecular oxygen [91]. This formulation makes it possible to assess the relative importance of ^{3}CDOM* dissipation pathways and to understand their role in the formation of transient oxidant species in natural aquatic systems.

When CDOM absorbs radiation, the promotion of an electron from the highest energy occupied orbital (HOMO) to the lowest energy unoccupied orbital (LUMO) occurs, as illustrated in Figure 2.3. This process generates two half-occupied orbitals (SOMOs), which give the excited molecule new chemical properties [91]. In particular, the electron promoted to the higher energy orbital takes on a reducing character, as it is

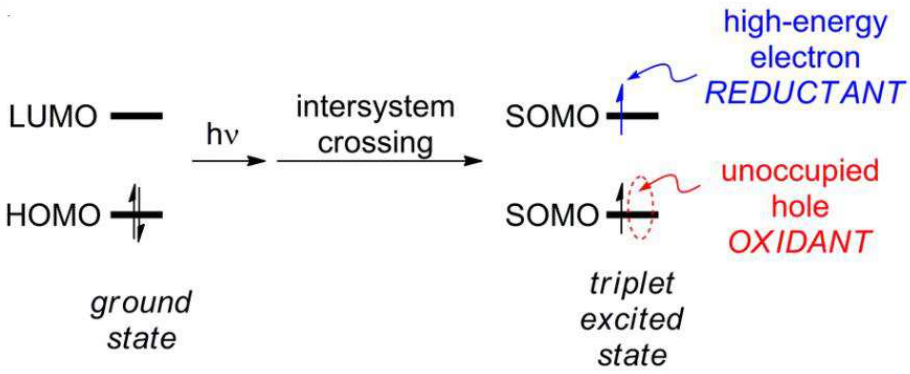

Figure 2.3: Schematic representation singlet ground state, absorption of a photon, promotion of an electron and attainment of the first excited singlet state; inter-system crossing and representation of the triplet state.[91]

more easily donated. Conversely, the electronic vacancy created in the HOMO orbital gives the molecule an oxidising potential, as it tends to accept electrons. This electronic arrangement elucidates the capacity of excited CDOM to engage in both oxidation and reduction reactions, although oxidative reactions are

prevalent in CDOM-associated photochemical processes.

The excited state of CDOM, particularly in the triplet form (^{3}CDOM*), is known to react with electron-rich substrates such as aromatic compounds, including phenols and aromatic amines, through oxidation mechanisms. In addition, inorganic substrates can also be involved in such reactions, leading to the formation of other reactive species. Relevant examples include carbonates and halogenated species, which, by interacting with ^{3}CDOM*, can generate ROS or halogenated radicals [104, 105].

Due to the considerable heterogeneity and structural complexity of natural CDOM, it is difficult to replicate its photoreactive behaviour in a representative manner in the laboratory. For this reason, model compounds capable of mimicking its photochemical properties are used. In the past, one of the most widely used compounds was anthraquinone-2-sulphonate, known for its ability to generate stable and reactive triplet states [106]. However, subsequent studies have shown that this compound tends to overestimate the steady-state concentration of ^{3}CDOM*, leading to assessments that are not always realistic. Currently, a preferable alternative is benzophenone-4-carboxylate, which provides a more reliable estimate of the photochemical reactivity of natural CDOM [107].

Under controlled experimental conditions, DOM of different origins (terrestrial, microbial and Arctic) efficiently promoted the photochemical degradation of Aldrin, a hydrophobic contaminant, showing significantly higher reactivity in ice than in liquid water. This behaviour is attributed to the concentration of solutes in thin liquid regions (liquid-like layers) in the ice, where chemical reactions are accelerated. The experiment revealed that both $^{\bullet}$OH and $^1O_2$ are ROS generated during DOM irradiation in ice, and that their relative importance depends on the type of DOM. These results show that DOM is also an important chromophore in icy environments, contributing significantly to chemical transformation processes in polar systems [12].

2.5 Halogens

Halogens can play a key role in environmental photochemical processes. In aqueous media, such as seawater or saline water, the presence of Cl^-, Br^- or I^- species can lead to the formation of photoinduced halogenated radicals, including $X^{\bullet}$, $X_2^{-\bullet}$ and mixed species $XY^{\bullet}$ (where X and Y represent Cl, Br or I). In specific marine and coastal environments, the photochemical contribution of halogenated radicals may exceed that of the hydroxyl radical in the transformation of organic compounds. Their relative importance depends both on their actual concentration in the aqueous system and their reactivity towards the substrates present, which change depending on the chemical structure of the substrate and the type of halogenated radical involved [108].

The production of these radical species can take place through several mechanisms. The first process consists of the oxidation of the halide ((X^-) by highly reactive radical species, such as $OH^{\bullet}$ or the sulfate radical ($SO_4^{-\bullet}$) (R7–R10). Alternatively, excitation of CDOM by solar radiation can lead to the formation of photoexcited species capable of transferring energy or electrons to other molecules (R11), thus promoting the formation of $X^{\bullet}$ radicals or $X_2^{-\bullet}$ anions. Finally, under strongly acidic pH conditions (pH < 2), direct photolysis of iron-halogenate complexes can be observed, which represents a further route of radical generation (R12) [108].

$$OH^{\bullet} + X^{-} \rightleftharpoons HOX^{\bullet -} \longrightarrow OH^{-} + X^{\bullet} \quad \text{(R7)}$$

$$HOX^{\bullet -} + H^{+} \longrightarrow H_2O + X^{\bullet} \quad \text{(R8)}$$

$$HOX^{\bullet -} + X^{\bullet} \longrightarrow OH^{-} + X_2{}^{\bullet -} \quad \text{(R9)}$$

$$SO_4{}^{\bullet -} + X^{-} \longrightarrow SO_4{}^{2-} + X^{\bullet} \quad \text{(R10)}$$

$$^3CDOM^{*} + X^{-} \longrightarrow CDOM^{\bullet -} + X^{\bullet} \quad \text{(R11)}$$

$$FeX^{2+} + h\nu \longrightarrow Fe^{2+} + X^{\bullet} \quad \text{(R12)}$$

The reactivity of these species is strongly influenced by both the nature of the substrate with which they react and the intrinsic characteristics of the species itself. In particular, the reduction potential of halogen radical species decreases as their atomic number increases. Furthermore, the $X^{\bullet}$ species has a higher reduction potential than the corresponding di anionic species X_2^{-} [109].

Reactions with saturated aliphatic compounds occur mainly *via* hydrogen abstraction: $Cl^{\bullet}$ reacts very rapidly (k = 10^7-10^9 $M^{-1}s^{-1}$), while $Cl_2^{\bullet}$ and $Br^{\bullet}$ show lower and more variable rates (k = 10^3-10^7 and 10^4-10^8 $M^{-1}s^{-1}$, respectively), partly dependent on the energy of the C-H bond. With olefinic compounds, halogen radicals , except $I^{\bullet}$, react rapidly (k = 10^6-10^9 $M^{-1}s^{-1}$), often forming halogenated products. Reactions with aromatic compounds take place *via* different mechanisms, including addition to electron-poor systems (k < 10^5-10^7 $M^{-1}s^{-1}$) and electronic abstraction from electron-rich substrates (k = 10^7-10^9 $M^{-1}s^{-1}$), with an overall variability that can cover several orders of magnitude (k = 10^5-10^{10} $M^{-1}s^{-1}$). By comparing these values with the bimolecular rate constants of the hydroxyl radical (k $\approx 10^{10}$ $M^{-1}s^{-1}$)), it is observed that halogen radicals show comparable reactivity, particularly towards aliphatic and aromatic compounds. This suggests that such reactions may play a significant role in aquatic systems. However, the actual concentration of halogen radical species is highly dependent on the availability of dissolved halogens in solution. As a result, in environments with a low content of halides (X^{-}), the concentration of the corresponding radical species will be significantly lower than, for example, seawater, where halogens are present in much higher concentrations [108].

2.6 Photochemistry in ice matrices

The discussion so far applies to both aquatic and ice and snow systems. However, one crucial aspect is the speed at which reactions occur. It is well known that temperature plays a fundamental role in chemical kinetics, according to Arrhenius' law:

$$k = Ae^{-E_a/(RT)} \quad (2.6)$$

where k is the rate constant, A is the pre-exponential factor, E_a is the activation energy, R is the gas constant, and T is the absolute temperature. This relationship shows that k depends exponentially on T: as the temperature decreases, a decrease in the reaction rate is expected. However, numerous studies have shown that many photochemical reactions occur more rapidly in ice and snow systems than in liquid water, even when the initial conditions are the same [13, 14, 41, 110, 111].

For example, Kahan et al. (2010) [110] examined the degradation of anthracene in three different matrices: liquid water, ice, and crushed ice. The results revealed significant variations in the observed first-order rate constants (k). In water, the observed rate constant was approximately 2.5x10^{-4} s^{-1}, whereas in ice it

increased to 4x10^{-4} s^{-1} and reached values of up to 10x10^{-4} s^{-1} in the case of crushed ice. In the case of compact ice, the observed increase in reaction speed is attributed exclusively to the concentration effect of reactive species in the QLL. As described above, during freezing, many impurities are expelled from the crystal lattice and accumulate in thin interstitial liquid layers, causing a local increase in the concentration of reactants. In the case of crushed ice, in addition to the concentration effect in QLLs, the increase in the specific surface area of the system must also be considered (eq 1.11). The latter leads to greater diffusion and scattering of incident light, thus increasing the probability of photochemical reactions being activated.

The literature currently highlights an increase in photochemical reactivity as the matrix varies (i.e. liquid water, compact ice and crushed ice). However, to the best of our knowledge, there are still no systematic and in-depth studies on how the nature of degradation products changes as the reactive matrix varies. Interest has emerged in assessing how the physical environment of the reaction influences not only the rate of degradation, but also the qualitative and quantitative profile of photoproducts, based on the results reported in the study by Kahan et al. (2010). Understanding these differences is crucial for predicting the environmental fate of organic pollutants in various cryospheric compartments, and for evaluating the potential impact of secondary products on the chemical and biological processes in polar ecosystems.

The following chapters will report the results of photochemical studies on BPA, followed by work on the identification of bromate and its production caused by sunlight.

The following chapters will present the results obtained in photodegradation studies applied to different frozen matrices. In particular, Chapter 4 will be devoted to the analysis of the photochemical processes that determine the degradation of BPA under cryogenic conditions, highlighting the kinetic dependencies, the reactive intermediates involved and the influence of the physicochemical characteristics of ice. Chapter 5, on the other hand, will explore the mechanisms of photoinduced transformation of bromine in the same matrices, with particular attention to speciation, emerging radical pathways, and the environmental implications of the processes observed. These chapters will provide an integrated picture of photochemical dynamics in icy environments, helping to clarify the role of natural ice as active reactors in the biogeochemical cycles of organic and inorganic substances.

Chapter 3

Bisphenol A

Bisphenols constitute a class of organic compounds characterised by the presence of two hydroxyphenyl functional groups. Among these, bisphenol A (BPA), also known as 2,2-bis(4-hydroxyphenyl)propane, is the most widely used monomer in numerous consumer products. Bisphenol A finds application in the production of polycarbonates, epoxy resins, food packaging materials, thermal receipts, medical devices and dental sealants [112–114]. The first synthesis of BPA was described in 1891 by Russian chemist Aleksandr Pavlovič Dianin. The process involves a condensation reaction between acetone and two moles of phenol, catalysed by a strong acid, typically hydrochloric acid, in the presence of methanthiol as co-catalyst. The result of the reaction is the formation of BPA and water as a by-product [115]. The extensive use of BPA has led to a steady increase in its production, estimated at more than 7.7 million tonnes in 2015 and with an annual growth rate of 4.8% observed from 2016 to 2022; in fact, it has been defined as a pseudo-persistent substance, as although it has a short half-life, its continuous release into the environment makes it ubiquitous [116].

Bisphenol A is known to act as an endocrine disruptor and a teratogen in various vertebrate species [117]. Teratogenic effects typically occur only at high concentrations of BPA that are rarely encountered under environmentally realistic conditions. For instance, in *Xenopus laevis*, concentrations above 4.6 mg L^{-1} can induce microcephaly, reduced body length, abnormal intestinal coiling and edema [118], while levels exceeding 5.7 mg L^{-1} may result in malformations and suppression of organogenesis [119]. In contrast, endocrine-disrupting effects have been observed at concentrations commonly detected in aquatic environments, leading to significant impacts on wildlife, such as altered sex determination and impaired gonadal function [117]. The toxicological activity of BPA is attributed to its ability to bind to nuclear and membrane estrogen receptors, thyroid hormone receptors, and interfere with steroidogenic enzymes [120, 121].

The presence of BPA is of concern not only for human exposure, but also for its impact on various environmental compartments. High concentrations of BPA have been detected in freshwater in various areas of the world. Yamazaki et al. analyzed BPA contamination in four Asian countries (Japan, China, Korea, and India), focusing exclusively on river waters, where BPA concentrations are particularly high. In Japan and China, detected concentrations ranged between 3.1 and 120 ng L^{-1} and between nondetectable (n.d.) and 98 ng L^{-1}, respectively; in Indian rivers, concentrations ranged between n.d. and 1950 ng L^{-1} [122]. As far as China is concerned, a follow-up study conducted in the Pearl River showed that BPA concentrations had remained stable five years later and identified numerous sources of contamination, mainly related to domestic discharges and industrial effluents [123]. Freshwater contamination by BPA is not limited to countries in the East, but extends globally. In Canada, for example, concentrations comparable to those found in urban

rivers in India have been found [124].

Currently, scientific literature on bisphenols in snow matrices is limited. The lack of specific data on snow prompted a more extensive investigation, which in this thesis was addressed through a seasonal snow sampling campaign conducted in 2023 across the Alps, with a particular focus on its eastern portion (see Figure 3.1 and Table 3.1). Thirteen compounds were quantified in all samples, selected from the class of bisphenols and their derivatives, including: BPA, Bisphenol Z (BPZ), Bisphenol AF (BPAF), Bisphenol F (BPF), Bisphenol AP (BPAP), Bisphenol FL (BPFL), Bisphenol S (BPS), Bisphenol M (BPM), Bisphenol C (BPC), Tetrabromobisphenol A (TBBPA), Tetramethyl Bisphenol A (TMBPA), 4,4'-Dihydroxybiphenyl (2OH-BP) and Tribromophenol (3Br-Ph). These compounds were analysed using high-performance liquid chromatography coupled with mass spectrometry (HPLC-MS) on samples previously filtered through a 0.45 μm Teflon filter (methodological details are described in the Appendix A).

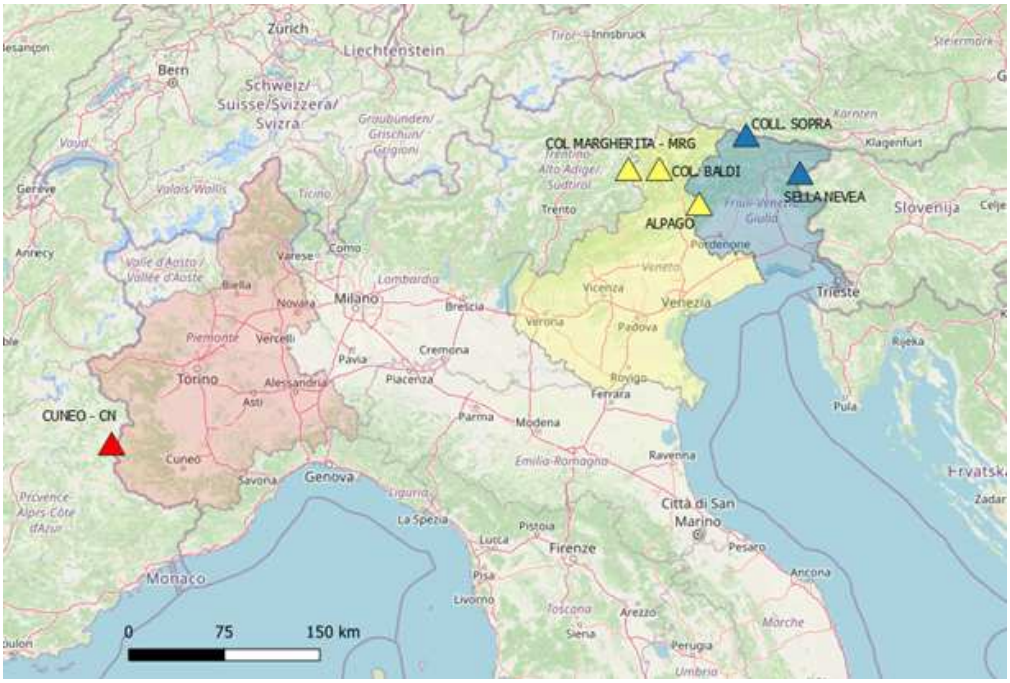

Figure 3.1: Map of the sampling sites

Table 3.1: Sampling sites, dates, geographical coordinates and altitude

Acronym	Site	Coordinates	Sampling data	Altitude (m a.sl)
Cuneo A	Ventasuso peak (CN)	44°23'53" N 06°54'01" E	2023-04-05	2444
Cuneo B	Ventasuso peak (CN)	44°24'37" N 06°54'30" E	2023-04-05	2120
MRG A	Col Margherita (BL)	46°21'51" N 11°47'29"E	2023-03-08	2510
MRG B	Col Margherita (BL)	46°22'31"N 11°48'13" E	2023-03-08	2107

Continued on the next page

Table 3.1 continuation

Acronym	Site	Coordinates	Sampling data	Altitude (m a.sl)
MRG C	Col Margherita (BL)	46°21'26"N 1°49'02"E	2023-03-08	1900
NEVEA A	Sella Nevea (UD)	46°22'25"N 13°27'13"E	2023-03-27	2003
NEVEA B	Sella Nevea (UD)	46°22'30"N 13°27'36"E	2023-03-27	1671
BALDI	Col dei Baldi (BL)	46°24'57"N 12°04'25"E	2023-03-22	1902
ALPAGO	Casera Palantina (BL)	46°07'07"N 12°28'36"E	2023-03-09	1500

The concentration profiles of bisphenols, expressed as the sum of the compounds detected at each sampling site, are illustrated in Figure 3.2. Data on the concentrations measured at the various sites under study are presented below. Among the compounds analysed, four bisphenols showed concentrations above their respective detection limits: BPA, BPS, BPAF and BPAP. At all sites, with the exception of sites Cuneo A and Nevea A, BPA appears to be the predominant bisphenol, with concentrations ranging from below the limit of detection (<LOD) to around 600 pM. BPS was detected systematically, although less frequently than BPA. The compounds BPAF and BPAP were detected only sporadically in some samples.

The presence of bisphenols in the surface layers of the snowpack observed in this study could be attributed to recent snow events, during which air masses from distant areas could have transported these compounds to the sampling sites. The low volatility of BPA, in particular, may have favoured its accumulation, making it the most stable and persistent compound in the snowpack among those analysed.

Comparison with data in the literature confirmed the trend observed in previous studies. The BPA concentrations reported by D'Amico et al. (2024) in Arctic areas range from 10 to 1051 pM [125], while those found by Ferrey et al. (2018) lie between 10 and 20 μM [126]. In the latter case, there is a slight discrepancy with the values obtained in the present work, probably attributable to the geographical location of the sampling sites in Minnesota, which are located close to the St. Paul sewage treatment plant.

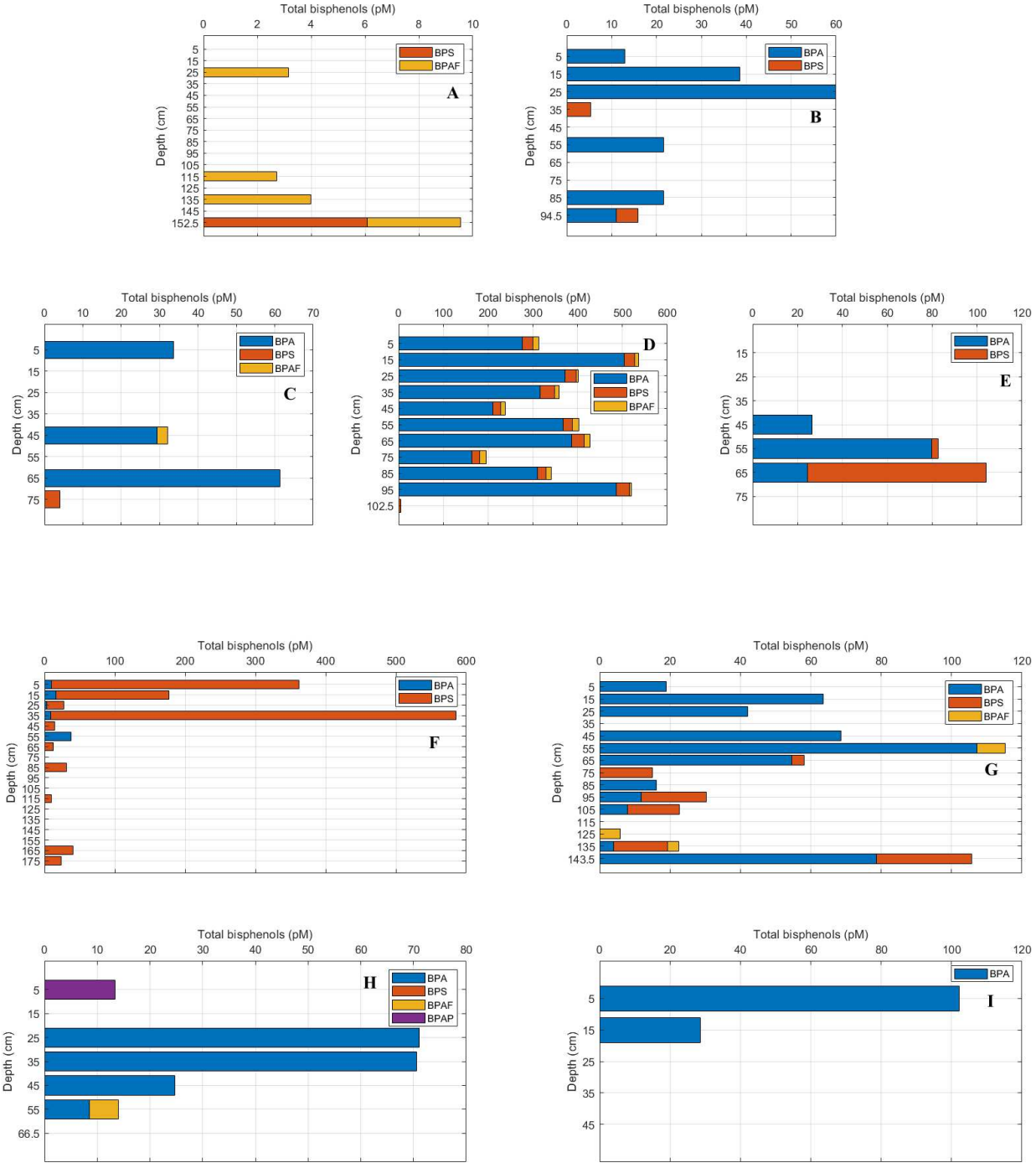

Figure 3.2: Trends in BPA (blue), BPS (red), BPAF (yellow) and BPAP (purple) concentrations are shown for the following sampling sites: A, B (Cuneo A and B) C, D, E (corresponding to MRG sites A, B and C respectively), F and G (Nevea A and B), H (Col dei Baldi) and I (Alpago).

3.1 Photodegradation of bisphenol A in ice

In this study, carried out in collaboration with Korean Polar Research Institute (KOPRI) and the Research Group headed by Dr. Kiate Kim group, photodegradation experiments of BPA were conducted in aqueous solution and ice under consistent chemical conditions. The primary goals of the work were to determine of the kinetics of BPA degradation; secondly, and to identify the degradation products formed in both matrices. Subsequently, the products from the two conditions were compared to determine common compounds and significant differences. The experiment was conducted using direct photolysis or with photosensitisers including NO_2^- anthraquinone-2-sulphonate (AQ2S) and rose Bengal (RB), which served as proxies for CDOM. Samples were prepared in aqueous solution either at 25 °C or frozen at -20 °C. For each condition, experiments were performed under both light and dark settings to assess the effects of photodegradation *versus* non-photoinduced processes. Regarding degradation kinetics, the results showed that processes conducted in ice, in the presence of organic photosensitisers, proceed significantly faster than those in aqueous solution. This findings appear to contradict Arrhenius' law, which predicts an increase in the kinetic constant with increasing temperature, can be explained by the exponential increase in the concentration of the reactants within the QLL. Concerning the degradation products, it was observed that some compounds are common to both aqueous solution and ice. However, the work, published in *Environmental Science and Pollution Research* in 2024, emphasises the importance of further study of the ice matrix, as the formation of different degradation products can affect the impact of pollutants on ecosystems differently, depending on where their degradation takes place.

Photodegradation of bisphenol A in water and ice: identification of products using three photosensitizers

Stefano Frassati[a,b], Elena Barbaro[b,a], Marco Vecchiato[a], Marco Roman[a,b], Kitae Kim[c], Yong-Yoon Ahn[c], Andrea Spolaor[b,a], Carlo Barbante[a,b], Andrea Gambaro[a,b].

[a] Ca' Foscari University of Venice, Department of Environmental Sciences, Informatics and Statistics, Venice Mestre, Italy.

[b] Institute of Polar Sciences – National Research Council (CNR-ISP), Venice Mestre, Italy.

[c] Korea Polar Research Institute (KOPRI), Incheon 21990, Republic of Korea.

Corresponding author: Stefano Frassati Corresponding author's email: Stefano.frassati@unive.it

Keyword: BPA, direct photochemistry, indirect photochemistry, ice, Rose Bengal, antraquinon-2-solfunate, nitrite

Abstract

Bisphenol A (BPA) is a widespread organic micro-pollutant, found in most environments, including alpine and Arctic regions, and several matrices such as waters and aerosols. Polar regions are characterized by periods of intense irradiation with no sunset due to the continuous sunlight, while alpine areas, despite following the day-night cycle of mid-latitudes, also undergo strong irradiation. For such conditions, it is possible that a fraction of the BPA present in snow may degrade through direct photolysis, producing other unknown species with different environmental mobility and possible ecotoxic effects. Furthermore, the snowpack is rich in species (known as photosensitizers) that facilitate indirect photodegradation processes through reactions involving hydroxyl radicals ($^{\bullet}OH$), singlet oxygen ($^1O_2$), excited triplet states of the organic fraction ($^3CDOM^*$), and nitrite/nitrate. In this study, we investigated both direct and indirect photodegradation of BPA in the presence of specific photosensitizers producing $^{\bullet}OH$, $^1O_2$, $^3CDOM^*$ and NO_2^- to specifically explore the products of the reaction. The study was conducted in both liquid water and ice, under light and dark conditions. Results, obtained by HPLC-HRMS, revealed that the matrix in which the reaction takes place, in addition to the photosensitiser used, may influence the degradation by-products. This allows for the possibility of distinguishing the reaction environment based on the identified product.

Introduction

Bisphenols (BPs) are organic synthetic compounds formed by two phenolic hydroxyl groups [127], the most used being 2,2-Bis(4-hydroxyphenyl)propane, commonly named bisphenol A (BPA) [128]. The economic value of BPA is considerable, as marked by a worldwide production of over 7,7 million tons in 2015 and an annual growth rate of 4.8 % observed from 2016 to 2022 [116]. It was synthetized in 1890 even if a massive use began in 1950s, when BPA started to be used as raw material for the production of polycarbonate plastics and epoxy resin, for the sectors of food contact materials, thermal paper, and several synthetic materials [128]. Public opinion started talking about BPA when many studies suggested a strong correlation between BPA's exposure and cancer, obesity, and neurobehavioral disorders [114, 129, 130]. Moreover, human studies suggest that BPA could be an endocrine disruptor, reduces sperm quality and ovarian response, and causes premature delivery [131]. For that reasons, BPA was inserted into the EPA's list (Environmental Protection Agency) of emerging contaminants [132]. Traces of this compound were found in many types of human tissues and fluids, including serum, plasma, whole blood and urine [114].

The presence of BPA concerns not only the human exposure, but also different environmental compartments. High concentrations of BPA have been found in fresh waters around the world. Yamazaki et al. in 2015 studied BPs contamination in four Asian states (Japan, China, Korea and India), focusing only on river waters, where the presence of BPA is extremely high [122]. Similar contamination was found in Japan and China, respectively 3.1-120 ng L^{-1} in Japan and nd-98 ng L^{-1} in China; contamination of Indian river waters, on the other hand, ranged from nd-1950 ng L^{-1}. As for China, a follow-up study conducted in the Pearl River showed that BPA concentrations were stable after five years and identified many sources, originating from domestic sewage and wastewater [123] . The contamination of fresh water with BPA does not only affect Eastern countries but can extend globally. In Canada, for example, concentrations very similar to those in Indian urban rivers have been recorded [124]. As far as Europe is concerned, many studies have been conducted [133–135] and all are in agreement with the above data, e.g. in the rivers of the Czech Republic, values between 14-800 ng L^{-1} [136]. Moreover, similar behaviour is also found in the atmosphere, ranging from higher concentrations in urban areas [137] to trace amounts in remote areas with very similar average values, 6 pg m^{-3} in Antarctica and Canadian arctic [130] and BPA has been found in Arctic snow, with concentrations reaching up to 250 ng L^{-1} [125].

The scientific community focuses extensively on the polar areas because, due to long-range atmospheric transport, are considered important sink of persistent organic pollutants (POPs). Moreover, polar areas are characterized by intense solar UV irradiation and, link with a lower biological activity, there are the best condition for photochemical reactions [138] Solar-induced reactions may occur by direct photolysis, by the absorption of a photon, or occur through formation of h intermediate species namely as indirect photolysis [139]. Indirect photochemical reactions consist of the degradation of the compound of interest by reactive species (e.g. $^{\bullet}OH$ [140], O_3, NO_2^- [96] and triplet states of organic matter) products by their activation through another compounds, known photosensitizer (like chromophoric dissolved organic matter, CDOM [12], or NO_x). Snow photochemistry has been studied for a few years and a lot of works have been conducts in laboratory testing many kinds of snow and atmospheric conditions and making comparisons between responsiveness in water and in snow [11, 14, 141–143].

In the present study, the photodegradation processes of BPA through direct photolysis and indirect photolysis in water and ice (-20 °C) conditions were conducted, with the focus on the investigation of by-products. Anthraquinone-2-sulphonate (AQ2S), rose Bengal (RB) and NO_2^- were chosen in order to stimulate

specific reactions like the excited state produce, excited states of organic matter (^{3}CDOM*), singlet oxygen ($^1O_2$), $^\bullet OH$ and $^\bullet NO_2$. In particular, ^{3}CDOM* is well simulated by AQ2S [144, 145] , while $^1O_2$ is generated by RB [146, 147]. Since CDOM can have different compositions, and thus induce different reactions, studying the individual reaction types allows us to overcome the problem of choosing which type of CDOM to use, while NO_2^- is the only photosensitiser actually present in snow and ice, which can also be generated by the photoinduced reaction with nitrate that generates nitrite. The objective of this study was to gain a deeper understanding of potential by-products resulting from specific reaction processes and to characterize them. Presently, the environmental implications of producing these species remain unknown, although they might potentially influence the toxicity of the system where they exist. Moreover, if these various products are detected in the environment, it will enable the identification of the presence or absence of BPA and its fate within ice samples.

Materials and methods

Chemicals

All chemicals were used at standard grade provided by Sigma-Aldrich. In detail, BPA (>99%) was used as a substrate and, RB (>95%), anthraquinone-2-sulphonate (AQ2S, >98%) and sodium nitrite as sensitisers. Sodium sulphate (>99%) was used to keep the ionic strength constant. Ultra-pure water (18.2 MΩ cm, 0.01 TOC) was produced using a Milli-Q Direct 16 system. Formic acid and acetonitrile were used for mobile phases preparation, both as LC-MS grade reagents.

Experimental procedures

All degradation were conducted using a solution of BPA with a constant concentration of 4.5 μM, by direct photolysis while different photosensitisers were added to stimulate the indirect photolysis. Depending on the desired reactivity, photosensitizers was used with different concentrations: RB at 0.5 μM, AQ2S at 0.5 μM, and NO_2^- at 50 μM were added (see absorption spectra in Figure S1). Meanwhile, for RB and AQS, as they simulate the generation of reactive species, they were selected based on previous studies conducted in water for AQS [148] and in ice for RB [149].

The Quasi liquid layer (QLL) thickness is strongly related by the total solutes (C_t^0), according to the following formula [35]:

$$\varphi_{(H_2O)}(T) = \frac{m_{(H_2O)}RT}{1000H_f^0}\frac{T}{T_f - T}C_t^0 \tag{3.1}$$

where φ_{H_2O} is the fraction of the QLL, R is the gas constant, T_f is the freezing temperature in K, m_{H2O} is the water weight and H^0_f is the water enthalpy of melting. The concentration of solute in the QLL is C_t^0 but it is possible to correlate C_t^0 with the concentration in the bulk C_{bulk} using the following formula [150]:

$$C_t^0 = \frac{C_{bulk}}{\varphi_{H_2O}(T)} \tag{3.2}$$

To maintain constant ionic strength conditions, in according to other studies, all samples were prepared

using a solution of Na_2SO_4 (200 μM, C_{bulk}) [151].

All experiments were carried out at room temperature (liquid solution) and in ice (-20 °C) in dark conditions and under illumination for 6 h using a quartz filter > 400 nm for degradation with RB, and filter at > 300 nm for other experiments. The decision to use two different filters is related to the absorption spectra of the photosensitisers shown in Figure S1. Although the absorption maximum for AQ2S and NO_2^- is below 300 nm, the limit of the radiation of environmental interest, there is an absorption tail that reaches a wavelength > 300 nm. For RB, the absorption maximum is at 550 nm and the use of more energetic radiation has a high probability of degrading the photosensitiser itself. Liquid experiments were carried out using 20 mL of solution and located under the lamp, instead, icy degradation was performed putting to solidify 5 mL at -20 °C in a cooling system and then placed under the lamp for degradation. For ice samples, melting process was done at controlled temperature (+4 °C) for 30 min. The illumination system was a 450-W Xe lamp (Newport, 6279 NS) to simulate natural sunlight with photon flux emission at room temperature of 1.2 x 10^{-8} Einstein s^{-1} using 2-nitrobenzaldehyde actinometry, instead, for ice experiment the actinic flux emission was still measured by 2-nitrobenzaldehyde, with value of 6.6 x 10^{-8} Einstein s^{-1}.

BPA products were determined using ultra-high performance liquid chromatography -UHPLC- (Vanquish, Thermo Fisher Scientificp) coupled to a hybrid quadrupole-orbitrap high resolution mass spectrometer (Thermo Fisher Scientific, Q Exactive Focus). The separation was performed on a Hypersil GOLD™ aQ column with a mobile phase composed of 0.1% (v/v) formic acid in ultrapure water (eluent A) and acetonitrile (eluent B). The gradient elution was conducted at a flow rate of 0.3 mL/min and the eluent composition was programmed as follows: 5% eluent B for 0-2 min, 5–100% eluent B for 2-14 min, 100% eluent B for 14-17 min, and eluent B 100-5% for 17-21 min. Mass detection was carried out in positive and negative electrospray ionization (ESI) mode, and the operating parameters were set as follows: a detection range of 65 to 650 m/z, with a resolution of 70,000 (FWHM, at m/z 400; 0.5 s scan cycle time), spray voltage of 3.8 kV (positive mode) and -2.5 kV (negative mode), capillary temperature of 320℃, sheath gas flow rate of 40 a.u., auxiliary gas flow rate of 10 a.u., auxiliary gas heater temperature of 300℃, S lens RF level of 50.0, maximum injection time of 200 ms, and an automatic gain control (AGC) target of 1×10^6. The MS/MS fragmentation was conducted in the HCD collision cell that is filled with pure N_2 gas. The collision energy is 10, 30, and 50 eV. The isolation window was set to ± 1 m/z.

Results and discussion

Kinetics of BPA degradation

Figure 3.3 shows the BPA degradation trends under direct photolysis (A), with NO_2^- (B), AQ2S (C) and RB (D). Considering direct photolysis, only the liquid solution underwent a degradation, almost 50% after 6 h of irradiation, instead, irradiated ice samples did not show changing in concentration. Moreover, to assess possible interferences from Na_2SO_4, the experiment was carried out in its absence, and no significant changes were observed (see Figure S2). Regarding indirect photodegradation, water photo-kinetics were slower than direct photolysis (Table 3.2). The main reason is that photosensitizers, by absorbing incident radiation, can also produce the reactive species that will go on to degrade BPA, but they can also undergo degradation themselves (Figure S3). However, photodegradation by organic photosensitiser is faster than liquid experi-

ments (Table 3.2)). This could be explained by hypothesizing that a fraction of nitrites may dissolve within the ice crystal, thus being removed by the reaction environment. In contrast, organic compounds might be expelled, contributing more significantly to the concentration of the QLL [13]. Finally, it is noteworthy that the degradation of BPA with NO_2^- in a non-irradiated liquid solution occurs much more rapidly compared to its irradiated counterpart. This phenomenon can be attributed to the greater instability of nitrite compared to nitrate, enhancing its affinity with the phenolic rings of compounds, like BPA [152, 153] . Indeed, as detailed in the subsequent section, almost all the identified degradation products are nitro-compounds. Moreover, the reaction is conducted at room temperature, around 25°C, and once the degradation is complete, the samples are refrigerated at 4°C, effectively inhibiting the reactivity of nitrate (Table 3.2).

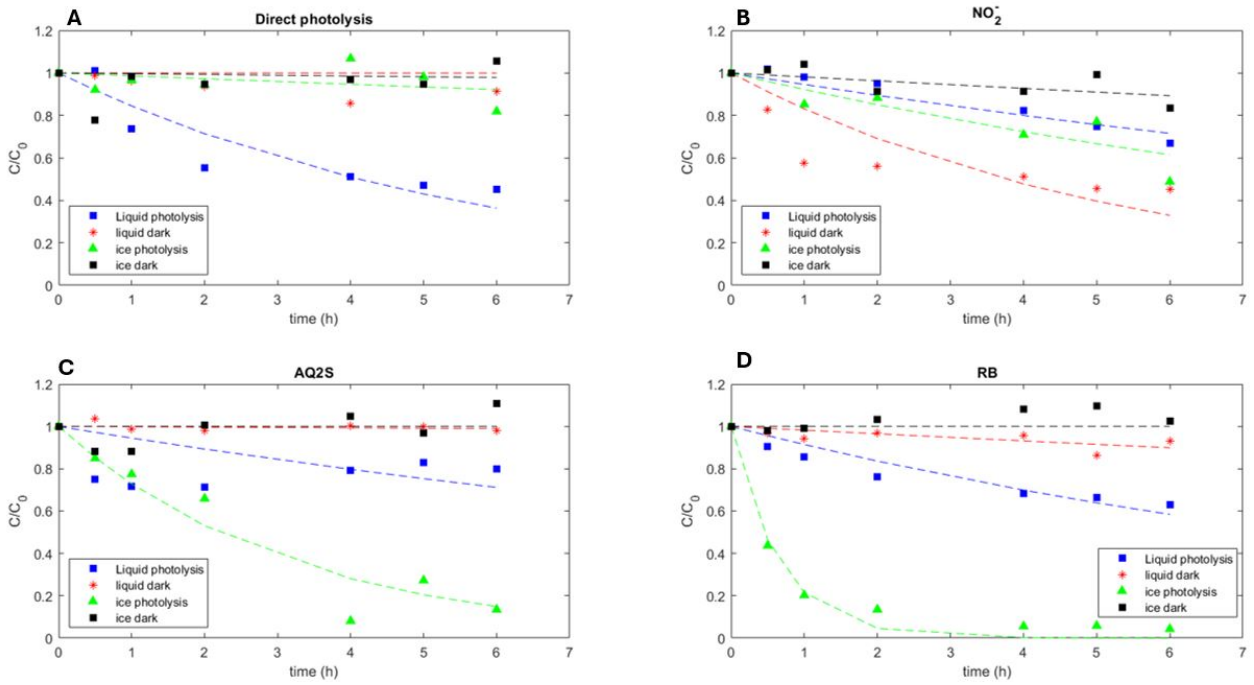

Figure 3.3: Kinetics of BPA (4.5 μ M) degradation in presence of Na_2SO_4 (200 μM) by direct photolysis (A), with NO_2^- (50 μM, B), AQ2S (0.5 μM, C) and RB (0.5 μM, D). The experiments were conducted in liquid solution, dark (red asterisk) and under irradiation (blue circle); and in ice, dark (black square) and irradiated (green triangle) conditions.

To fit the data in Figure 3.3, a (pseudo) first-order kinetic was used to extrapolate the observed degradation constants (k', h^{-1}) $[BPA]_t = [BPA_0]e^{-k't}$ were $[BPA]_0$ is the initial concentration, and $[BPA]_t$ is the concentration at time t. K' are reported in Table 1 in functions of different conditions.

Since the functional groups of BPA consist of two aromatic rings (more precisely, phenols) linked by an ester bond, it is conceivable that it may undergo direct photolysis reactions similar to molecules containing the same functional groups, like vanillin. In fact, some studies suggest that under specific irradiation and pH conditions (which were not controlled in this study), the following reactions could occur for phenolic compounds, and therefore, probably also for BPA [151, 154].

Table 3.2: Kinetic constant (k', h^{-1}) in different experiments. N.d means when the value is equal to 0.

	Liquid dark	**Liquid photolysis**	**Ice dark**	**Ice photolysis**
Direct photolysis	n.d	1.69×10^{-1}	n.d	1.37×10^{-2}
NO_2^-	1.49×10^{-1}	4.45×10^{-2}	n.d	8.11×10^{-2}
AQ2S	n.d	5.67×10^{-2}	n.d	3.17×10^{-1}
RB	n.d	8.96×10^{-2}	n.d	1.54

$$\mathrm{BPA} \xrightarrow{\mathrm{h}\upsilon} {}^1\mathrm{BPA}^* \tag{R13}$$

$${}^1\mathrm{BPA}^* \xrightarrow{\mathrm{ISC}} {}^3\mathrm{BPA}^* \tag{R14}$$

$${}^3\mathrm{BPA}^* \xrightarrow{\Delta} \mathrm{BPA} \tag{R15}$$

$${}^3\mathrm{BPA}^* + \mathrm{BPA} \rightarrow \mathrm{BPA}^{\bullet-} + \mathrm{BPA}^{\bullet+} \tag{R16}$$

$${}^3\mathrm{BPA}^* + \mathrm{O_2} \rightarrow \mathrm{BPA} + {}^1\mathrm{O_2} \tag{R17}$$

$$\mathrm{BPA}^{\bullet-} + \mathrm{O_2} \rightarrow \mathrm{BPA} + {\mathrm{O_2}}^{\bullet-} \tag{R18}$$

$$\mathrm{BPA}^{\bullet+} \rightarrow \text{products} \tag{R19}$$

$$\mathrm{BPA}^{\bullet-} + \mathrm{BPA}^{\bullet+} \rightarrow 2\,\mathrm{BPA} \tag{R20}$$

In these first two reactions, BPA absorbs solar radiation and becomes excited, likely undergoing the process of intersystem crossing (ISC), resulting in the formation of excited BPA in the triplet state. From here, various pathways are possible. The first one is that, constrained by the solvent cage, there is relaxation back to the S_0 state, releasing energy (Δ, R14). Alternatively, several reactions may proceed as follows.

Firstly, ${}^3BPA^*$ reacts with itself in the ground state (R16). This can lead to the formation of two transient species that follow different pathways. For instance, the $BPA^{\bullet-}$ species can reduce oxygen (O_2) and form $O_2^{\bullet-}/HO_2^{\bullet}$ (R18), and this species can react with the aromatic rings of BPA. Alternatively, ${}^3BPA^*$ can react with oxygen (in its ground state as a triplet) and generate singlet oxygen, which exhibits a high affinity for aromatic rings (R17). Finally, the recombination of the two ionic radicals is possible (R20). This reaction is generally favoured in the presence of high substrate concentrations. Shifting the focus to other organic photosensitizers, AQ2S is often used as a sensitizer for triplet state reactions, following reactions R18 and R19, while RB, once it absorbs visible radiation, tends to produce singlet oxygen (hypothetically R17). It is interesting to note that by substituting these two species into the previously mentioned reactions, the same chain of reactions can be obtained. Furthermore, since reactionR20 tends to occur at high concentrations, it can explain why, in ice, despite the expected bathochromic shift in BPA spectra and, therefore, a higher likelihood of reaction, direct photolysis in ice is disfavoured. This is because within the QLL, the concentration can increase up to 10000 times [149].

Photolysis reactions of nitrites and nitrates ($NO_x = NO_3^- + NO_2^-$) are well-known, and they give rise to various reactive oxygen species (ROS), such as $^{\bullet}OH$, $^{\bullet}OOH$, and O_3, and may have reactions with the photosensitisers themselves [39, 96]. Finally, it is also possible that the excited states of BPA can transfer energy to the nitrite producing its radical form, or, the $BPA^{\bullet+}$ species formed in reaction 4 can also reduce $^{\bullet}NO_2^-$.

Products identification

The degradation products obtained in ice in all conditions, and in aqueous solution under photolysis were investigated as described individually in the following subsections. Table 3.3 summarises all products identified with the various photosensitisers under different reaction conditions.

1. *Direct photolysis*

   In the experiments involving direct photolysis in ice, four masses were identified: m/z 133.0658, 151.0761, 243.1099, and 453.2062. Specifically, the first m/z corresponds to a molecular formula of $C_9H_{10}O$ (**1**), while the second one corresponds to $C_9H_{12}O_2$ (**2**). In the case of m/z 243.1099, it corresponds to the structure of hydroxylated BPA (**3**, BPA-OH), and the last mass is associated with the BPA dimer (**4**, see Table 3.3). In the latter case, the chromatogram displayed two peaks at retention times of 12.27 and 12.95 minutes, indicating the presence of both dimers (Figure S4).

   In Figure 3.4, the trends of various degradation products are depicted. It is interesting to note that, for compounds **1**, **2**, and **3**, their formation during photolysis in water is significantly higher compared to that in ice. When comparing the maximum intensity values, the production in water is approximately 5 times higher for compound **1**, and two times higher for compounds **2** and **3**, as compared to their formation in ice. As for the dimer, while its formation in water predominates in the initial phase, in the 6-hour test period, its formation in ice steadily increases, surpassing the degradation in water. In water, both dimers reach their maximum levels after 2 hours of testing.

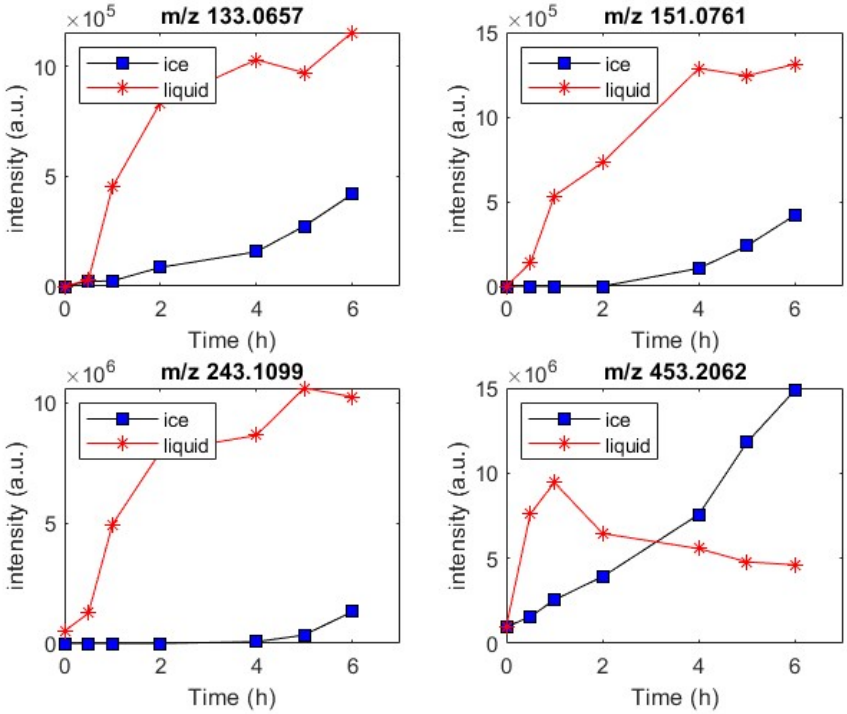

Figure 3.4: Evolution of products of BPA degradation by direct photolysis in water and ice.

2. *Photolysis with Antraquinone-2-solphonate as photosensitizer*

When utilizing AQ2S as a photosensitizer for degradation, a variety of products, including the four compounds mentioned in the previous section, were identified (Table 3.3). In the case of the initial four compounds, a distinct pattern emerged in frozen samples, while they were absent in the aqueous solution. This suggests that, albeit to a minor extent, direct photolysis still contributes to the degradation of BPA. A comparable pattern was also observed for compounds **6** (m/z 195.0652), **7** (m/z 259.0965), and **9** (m/z 377.1759). Compound **5** (m/z 155.0036) exhibited an increasing trend in both scenarios over the 6-hour exposure period, with this trend being notably more pronounced in the liquid solution. Conversely, for compound **8** (m/z 301.1443), the trend pointed to substantially higher degradation in the liquid solution compared to the ice environment. It is worth noting how the BPA dimer in ice is the first compound to get formed, reaching its peak after 4 hours and then degrading almost to disappearance in the following two hours. Its potential product could be compound 1 since it is not detected in the first hour, then its presence increases, reaching a maximum after 5 hours, and subsequently decreases rapidly in the following hour, as if it had consumed a significant portion of the dimer (Figure 3.5A). Furthermore, the di-hydroxylated compound (**7**) also displays a noticeable increase after the initial hour of the reaction. The trend of compound **9** appears to be formed as an additional product of BPA-OH (Figure 3.5B). Finally, it is noteworthy that the lighter compound forms at the end of the experiment. This observation could suggest that if the exposure is continued, there might be an increase in low-molecular-weight molecules and even a potential mineralization, as often observed in many photochemical experiments in aqueous solutions.

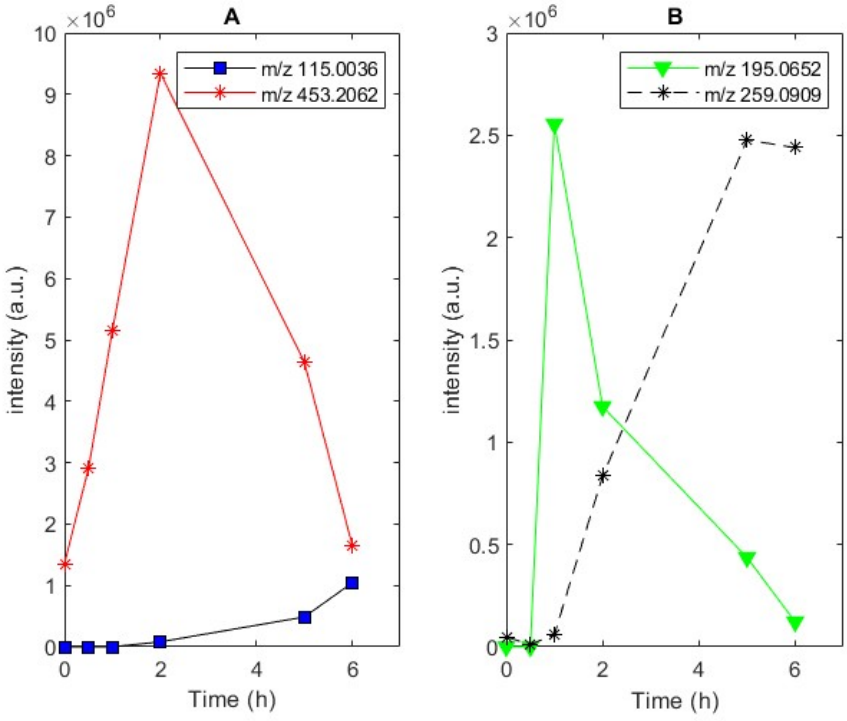

Figure 3.5: Evolution of products **1** and **4** (on the left), and **7** and **9** (on the right) of BPA photodegradation with AQ2S in ice

3. *Photolysis with Rose Bengal as photosensitizer*

Degradation using RB in ice, as observed previously, occurs extremely rapidly. Except for compounds **2** and **3**, which exhibit a clear trend over the 6-hour testing period, the compounds common to direct photolysis are absent. This is possible because the initial substrate degrades very quickly, causing the products to commence their own degradation almost instantaneously. Moreover, the strong reactivity of singlet oxygen with phenolic systems is well-known, which would also explain why the trend of dimers continues to decrease. However, two additional compounds (m/z 137.0317 and 265.07167, denoted as **10** and **11**, respectively) were identified. In the ice degradation process, it is intriguing to note that both compounds **3** and **11** are rapidly formed, reaching their respective peaks after 2 hours. This timeframe coincides with a loss of over 85% of BPA, after which the by-products themselves also begin to degrade. As for compound **5**, it displays an increase from the early stages of degradation. Given that this compound has a lower molecular mass and is more oxidized compared to the starting material, it suggests that the environment created is highly oxidative. Finally, as observed in the graph presented in Figure 3.6 (A) the trend of compound **11** strongly indicates that it might be a degradation product of BPA-OH. Notably, compound **11** commences its formation precisely at the peak of BPA hydroxylated compound formation, subsequently reaching its own maximum after 4 hours of analysis. As for degradation in water, only two compounds were identified, as indicated in Figure 3.6 (B and C): compounds **5** and **10**. Both of them exhibit a clear increasing trend throughout the entire experiment. similar trend, but with faster kinetics for their production in ice for compound **5**.

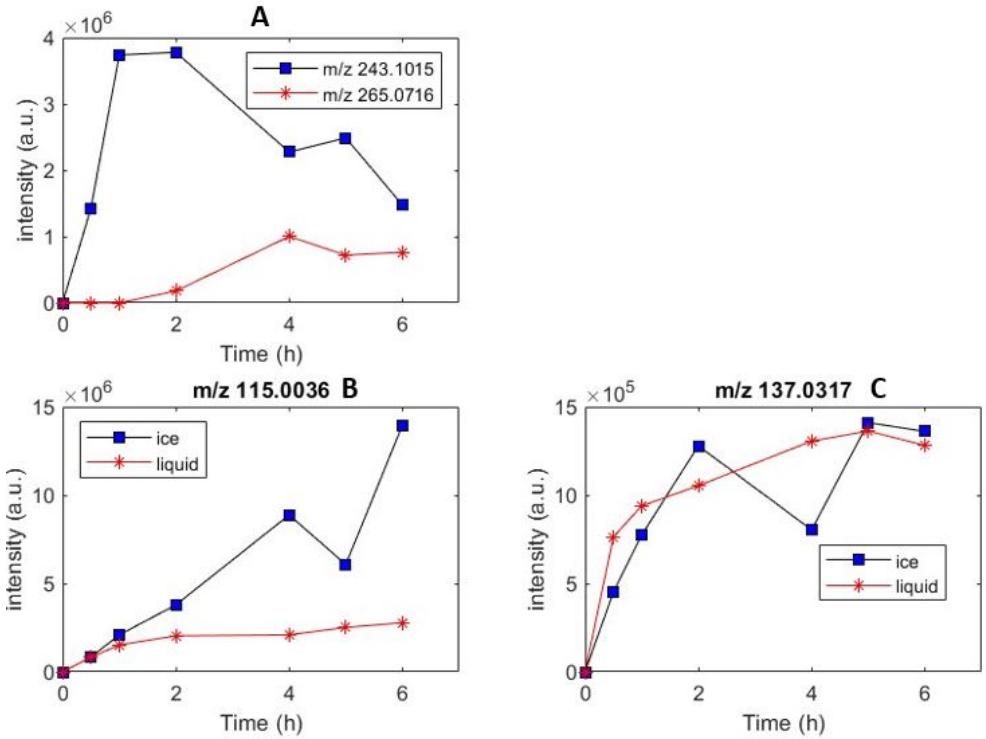

Figure 3.6: Top (A) formation of products **3** and **11** in ice. Bottom left (B) formation of product **5** and bottom right (C) formation of product **10** in water and ice

4. *Photolysis with addition of nitrite*

In the case of degradation with nitrite, in addition to photoreactions in liquid solution and ice, the degradation of BPA in a darkened liquid solution must be considered. It is important to emphasize that such a reaction does not occur in ice, suggesting a significant influence of temperature. Furthermore, in water photodegradation, products arise from both the reaction with nitrite and the hydroxylation reaction, or a combination of both. Conversely, in dark degradation, only nitration products are observed. However, not all nitro-products identified in dark degradation are found in the light-expose system. In all systems, except for the dark ice condition (where no degradation occurred), the presence of compound **1**, identified in previous degradations, is observed.

During dark degradation, three series of compounds appear to be closely interconnected. As seen in Figure 3.7, compounds **12**, **32**, and **37** exhibit very similar trends, with correlation coefficients between their respective patterns exceeding 89%. These three compounds differ in molecular weight due to the addition of NO_2 groups to the BPA molecule. Specifically, compound **32**, with the lowest molecular weight among the three, corresponds to BPA-NO_2, compound **12** to BPA-2NO_2, and compound **37** to BPA-3NO_2. Simultaneously, compounds **15** and **16** were identified, which could correspond to degradation products resulting from the fragmentation of BPA with the addition, in this case, of one and two NO_2 groups (see Figure 3.7B). In this instance as well, a correlation exceeding 90% was achieved.

Lastly, compounds **30** and **31** can be attributed to the formation of nitrophenol and dinitrophenol (Figure 3.7C) Here, a high correlation between these two compounds is observed, but the value is even higher when compared to compounds **30** and **12**. In this case, nitrophenol and BPA-OH exhibit a correlation of 94%, while compounds with two NO_2 groups show a correlation exceeding 98%. This suggests that since compounds **15** and **16** begin to grow significantly after 2 hours (Figure 3.7B), they may result from the degradation of compounds **32** and **12**, respectively.

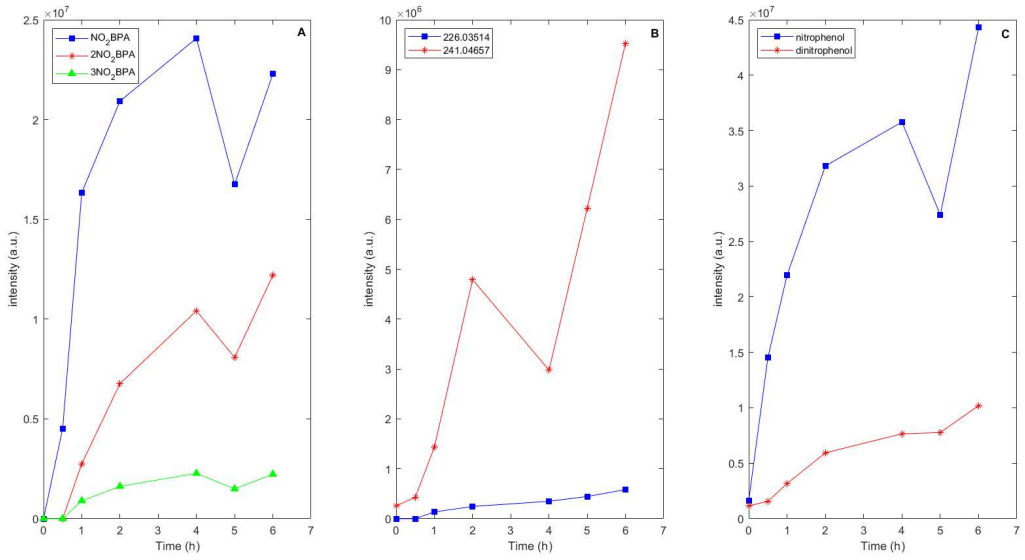

Figure 3.7: Evolution of BPA degradation products with nitrite in the dark and liquid solution: A) products obtained from the nitration of BPA; B) compounds **31** and **32**; C) nitrophenol and dinitrophenol.

As for the photodegradation experiments in the liquid solution, it is intriguing to note the presence of four groups of compounds exhibiting significant trends throughout the experiment duration. Similar to the dark degradation case, compounds **12** and **32**, resulting from the nitration of BPA (see Figure 3.9A), are present and, once again, show a correlation coefficient exceeding 90%. Additionally, the group composed of nitrophenol and dinitrophenol (**30** and **31**) is strongly correlated (coefficient ¿ 97%). As observed in the previous case, these two groups of compounds are interconnected. Specifically, when comparing the trend of nitrophenol with BPA-NO_2 (**32**), a correlation exceeding 99% emerge. Moreover, the correlation between compound **32** and **30** is approximately 90%, once again suggesting that lower molecular weight products may originate from the degradation of nitro-BPA (Figure 3.9B) Other products of interest include compound **4** and **20**. The first has the mass of the BPA dimer, while

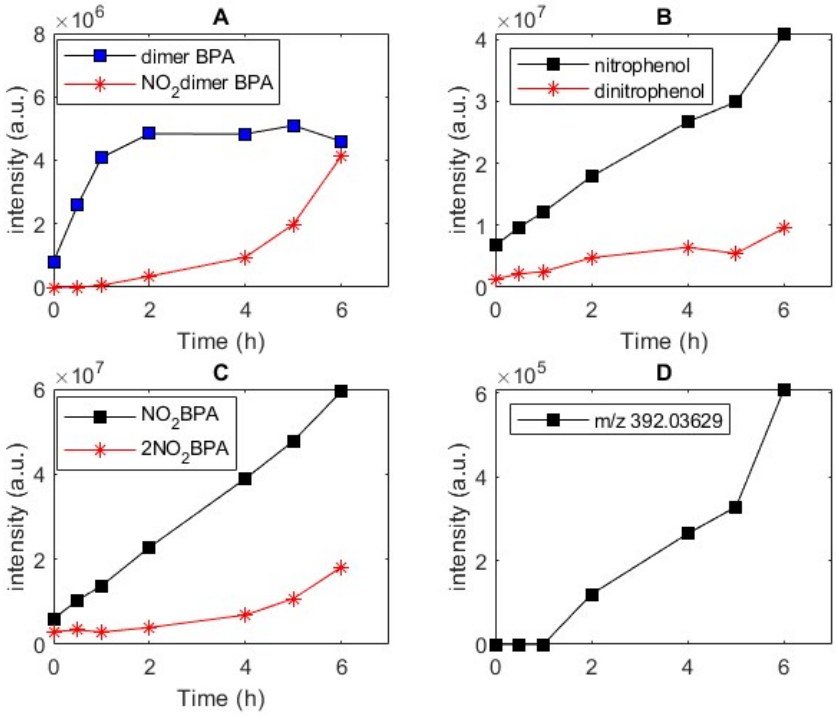

Figure 3.8: Evolution of BPA photodegradation products obtained with nitrite in liquid solution: A) dimerization and formation of nitro-dimer; B) nitrophenol and dinitrophenol; C) nitro-BPA and dinitro-BPA; D) compound **23**.

the second has a mass equivalent to the dimer plus one NO_2 group. In this case, we observe a rapid initial increase in the formation of the dimer, stabilizing after 2 hours and then decreasing after 6 hours (Figure 3.9A). Regarding the dimer formation with the addition of NO_2, there is no presence in the system initially, followed by a gradual increase after 2 hours of irradiation, precisely in the sample where compound **4** reaches its maximum. Subsequently, it grows almost exponentially until the end of the experiment (Figure 3.9C). Finally, the mass of compound **23** corresponds to BPA that has undergone double hydroxylation and the addition of three NO_2 groups. It is noteworthy that this compound exhibits a clear increasing trend after 3 hours of degradation (Figure 3.9D). This compound is strongly correlated (correlation coefficient exceeding 97%) with compound **12**. It appears that during the attack of an NO_2 radical, there could also be an attack by an OH group. A similar trend is observed for these

compounds in the case of ice degradation. However, in this case, after reaching a peak at 4 hours, there is a relatively rapid decrease. This suggests that whereas in the case of liquid solution degradation there is subsequent diffusion of the compounds within the solvent, in ice the diffusion of compounds within the QLL is slower. Therefore, various degradation products continue to degrade until fully mineralized species or compounds with higher volatility are formed, being removed from the degradation system. However, it is interesting to note that in ice, neither nitro-BPA nor BPA-OH were found. This could mean that the nitration and oxidation reaction occur extremely rapidly, and in ice, there is not enough time for these two compounds to diffuse within the system.

Focusing on the compounds **4**, **20** and **38** (present only in ice degradation), it can be observed that initially, there is the formation of the dimer, followed by the attack of NO_2. The di-nitrated product reaches a maximum earlier than the mononitrate, which could be crucial information in terms of reactivity. Indeed, this result indicates that the dimerization process occurs first, followed by nitration. (Figure 3.9)

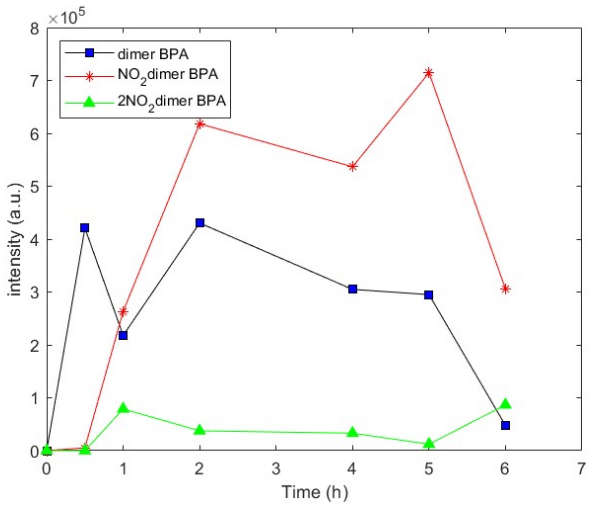

Figure 3.9: Figure 7 Formation of the dimer, nitro-dimer and dinitro-dimer in the photodegradation of BPA with nitrite in ice.

Lastly, as seen in Table 3.3, some compounds are exclusively present in ice photodegradation. Specifically, the mass of compound **19** is compatible with the formation of the ether between BPA and nitrophenol. This reaction is plausible, given that nitrophenol was not found in the system, indicating that, as mentioned earlier, there is confinement of species in the QLL that inhibits the diffusion of compounds. As seen in Figure S 5A compound **19** shows an increase during the initial degradation phase, followed by a decrease after 5 hours. However, focusing on compounds **21**, **24**, and **25** (Figure S 5B), it is observed that starting from the 4 and 5-hour samples, they begin to show an increase in the system. This could indicate that these three compounds derive from the degradation of compound **19**. Finally, compound **26** exhibits an almost exponential growth trend during the ice photodegradation experiment (Figure S 5C). These results thus indicate a significant production of nitro compounds, especially in ice, intensifying the toxicity of the system. This is particularly concerning as nitro compounds have the potential to interfere with metabolic processes, exacerbating the overall impact, acting as ATP uncouplers [155].

Table 3.3: list of the products identified during degradation in water and ice through direct photolysis, addition of AQ2S, and RB and nitrite. In the case of direct photolysis, with RB and AQ2S, degradations occurred only through light-activated processes. In brackets are the formulae of the species for which a structure could not be assigned, for the other molecules please refer to the supplementary materials for the structure formula..

				Direct photolysis		AQ2S		RB		Nitrate		
N°	Molecular mass	Suggested formula	Suggested structure	Liquid	Ice	Liquid	Ice	Liquid	Ice	Ice	Liquid photo	Liquid dark
1	133.0658	$C_9H_{10}O_2$		✓	✓		✓		✓	✓		
2	151.0761	$C_9H_{12}O_2$	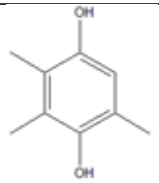	✓	✓	✓	✓		✓		✓	✓
3	243.1015	$C_{15}H_{16}O_3$	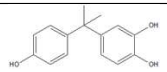	✓	✓		✓		✓	✓	✓	✓
4	453.2062	$C_{30}H_{30}O_4$	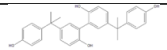	✓	✓	✓	✓	✓		✓		
5	115.0036	$C_4H_4O_4$	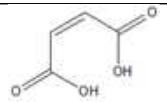			✓	✓	✓	✓			
6	195.0652	$C_{10}H_{12}O_4$					✓					
7	259.0965	$C_{15}H_{16}O_4$	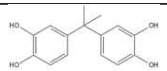				✓					
8	301.1443	$C_{18}H_{22}O_4$				✓	✓					
9	377.1759	$C_{24}H_{26}O_4$					✓					
10	137.0317							✓	✓			
11	265.0716	$C_{13}H_{14}O_6$							✓			
12	317.0769	$C_{15}H_{14}O_6N_2$	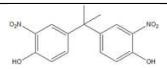							✓	✓	✓

Continued on the next page

Table 3.3 continuation

N°	Molecular mass	Suggested formula	Suggested structure	Liquid	Ice	Liquid	Ice	Liquid	Ice	Ice	Liquid photo	Liquid dark
13	362.0630	$C_{15}H_{13}O_8N_3$	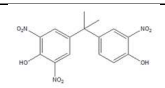							✓		✓
14	133.9914									✓		✓
15	226.0351	$C_{15}H_{12}O_8N_2$								✓	✓	✓
16	241.0466	$C_9H_{10}O_6N_2$	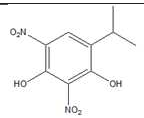							✓		✓
17	333.0728	$C_{15}H_{14}O_7N_2$	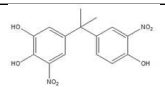							✓		✓
18	347.0510	$(C_{15}H_{12}O_8N_2)$								✓	✓	✓
19	364.1193	$C_{21}H_{19}O_5N$	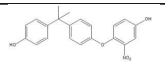							✓		
20	498.1923	$C_{30}H_{29}O_6N$	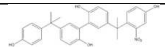							✓	✓	
21	207.0115									✓		
22	318.0809									✓	✓	
23	392.0363	$(C_{15}H_{11}O_{10}N_3)$								✓	✓	✓
24	240.2057									✓		
25	137.0353									✓		
26	225.0148	$(C_8H_5O_6N_2)$								✓		
27	364.0415									✓		
28	230.0453									✓	✓	
29	180.0298	$(C_8H_7O_4N)$								✓	✓	

Continued on the next page

Table 3.3 continuation

N°	Molecular mass	Suggested formula	Suggested structure	Liquid	Ice	Liquid	Ice	Liquid	Ice	Ice	Liquid photo	Liquid dark
30	138.197	$C_6H_5O_3N$	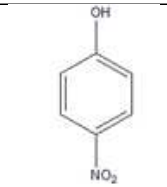								✓	✓
31	183.0046	$C_6H_4O_5N_2$	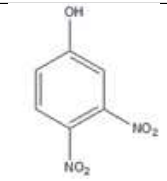								✓	✓
32	272.0928	$C_{15}H_{15}O_4N$	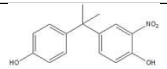								✓	✓
33	196.0610	$(C_9H_{11}O_4N)$									✓	✓
34	215.0076	$(C_7H_7O_7N)$									✓	
35	302.0662	$(C_{13}H_{10}O_5N_4)$									✓	
36	454.0893	$C_{21}H_{17}O_9N_3$	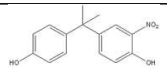									✓
37	362.0630	$C_{15}H_{13}O_8N_3$	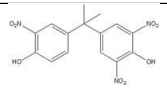							✓		✓
38	543.1774	$C_{30}H_{28}O_8N_2$	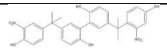							✓		

Conclusions

In this study, the focus was on investigating the photodegradation products of BPA in water and, for the first time, in ice through direct photolysis and with the use of three different photosensitizers, aiming to understand three distinct types of reactions. Specifically, RB is a photosensitizer used for singlet oxygen production, AQ2S is employed for understanding reactions induced by excited triplet states of the organic fraction, and nitrate, which can lead to reactions with OH radicals or aromatic ring nitration.

As observed from the kinetics study, there is a significant difference in reaction rates when working with organic photosensitizers in water compared to ice. Indeed, in the latter matrix, the reaction rate is notably higher than in the liquid solution. This is attributed to the fact that in the quasi-liquid layer, organic impurities are more readily expelled. However, it should be noted that this consideration does not apply to degradation with nitrate, as it may dissolve in the crystalline structure of the ice.

The use of different photosensitizers has allowed the identification of products resulting from various processes. Specifically, the application of AQ2S has facilitated the generation of compounds **6**, **7**, **8**, and **9**, whereas the use of RB results in the formation of compounds **10** and **11**. As for the degradation products obtained with NO_2, the predominant compounds are nitro-derivatives. These compounds, if indeed produced in the environment, should deserve more attention. Indeed, nitro compounds tend to be disruptive to the metabolic system, thus leading to possible negative repercussions on ecosystems.

Ethics declarations

Ethics approval and consent to participate.

Ethics approval and consent to participate.

Not applicable

Consent for publication

Not applicable.

Funding

The authors declare that no funds, grants, or other support were received during the preparation of this manuscript.

Competing Interests

The authors have no financial interests to disclose.

Author contributions

Conceptualization: Stefano Frassati, Elena Barbaro, Kitae Kim, Yong-Yoon Ahn; *Methodology*: Stefano Frassati, Elena Barbaro, Kitae Kim, Yong-Yoon Ahn, Marco Vecchiato; *Formal analysis and investigation*: Stefano Frassati, Elena Barbaro, Yong-Yoon Ahn, Marco Vecchiato; *Writing - original draft preparatio*n: Stefano Frassati, Elena Barbaro; *Writing - review and editing*: Stefano Frassati, Elena Barbaro, Marco Vecchiato, Marco Roman, Kitae Kim, Yong-Yoon Ahn, Andrea Spolaor, Carlo Barbante, Andrea Gambaro; *Supervision*: Andrea Gambaro, Carlo Barbante, Kitae Kim.

Supplementary material

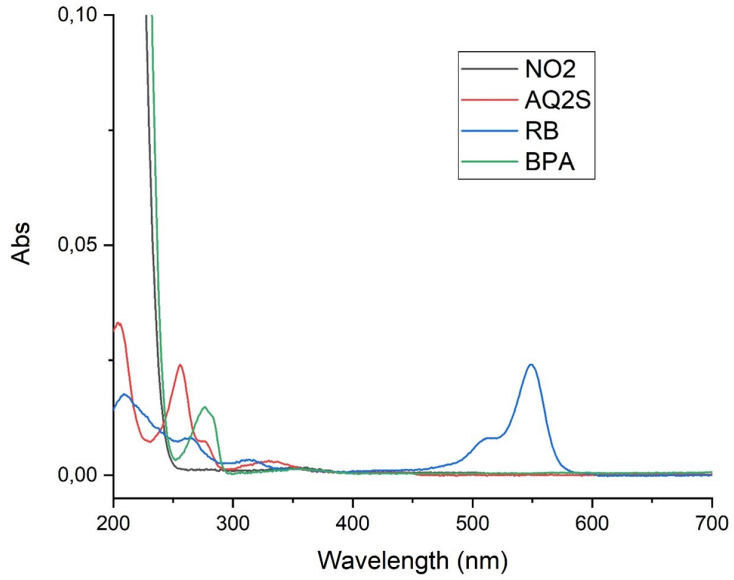

Figure S1 Absorption spectra of nitrate (black), AQ2S (red), RB(blue) and BPA (green).

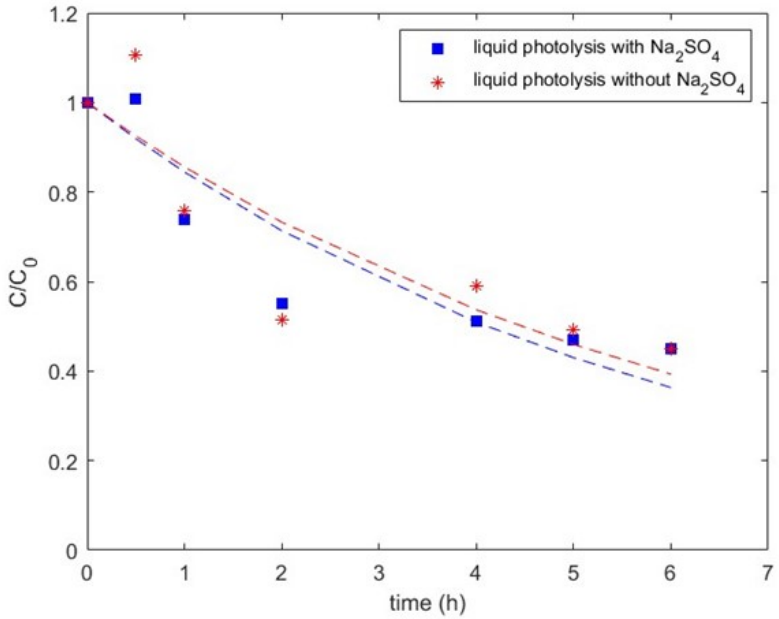

Figure S2 Degradation of BPA in liquid solution with (blue) and without (red) the addition of 200 μM Na_2SO_4. The kinetic constant, calculated as a first order kinetic, is $1.56x10^{-1}h-1$, very close to that calculated with the addition of Na_2SO_4.

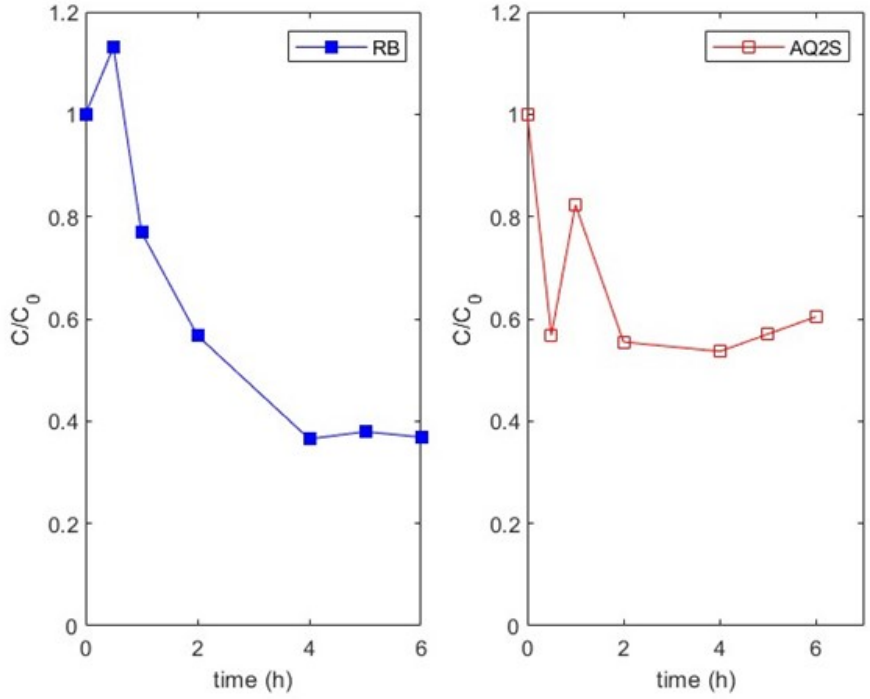

Figure S3 Degradation of rose bengal (RB, left) and anthraquinone-2-sulfonate (AQ2S, right) during irradiation in ice.

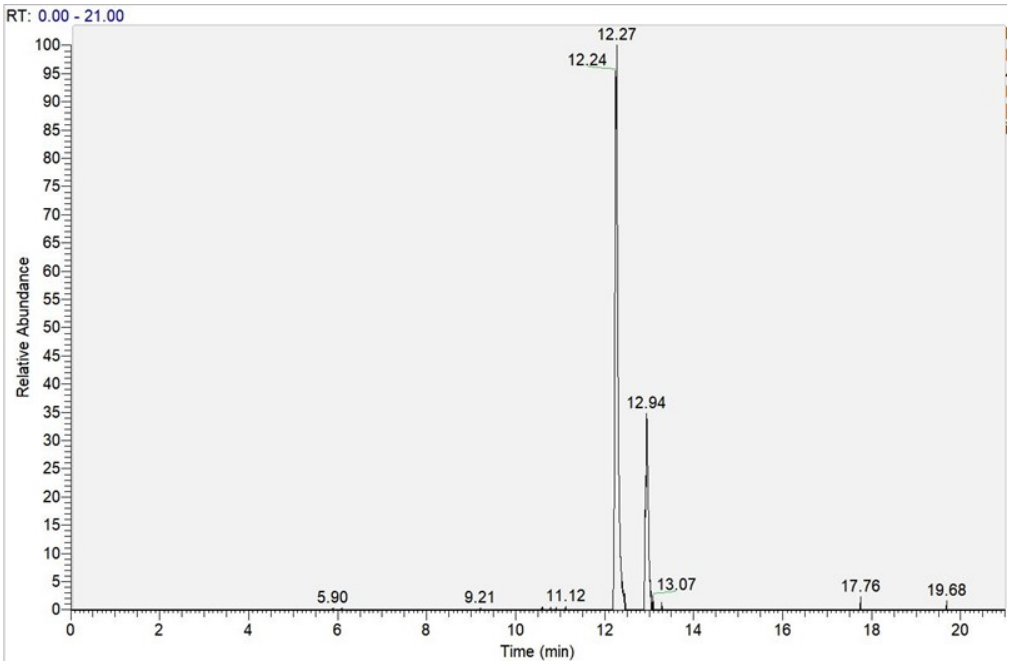

Figure S4 Chromatogram of the sample at 6 hours of direct ice photolysis of BPA. Mass 453.2062 corresponding to the BPA dimer (compound **4**) was extracted.

3.2 Photodegradation of bisphenol A in snow

This work, published in *Environmental Pollution* (2025), was a collaboration with the Chemistry Department of the University of Turin, specifically with the Research Group headed by Prof. Claudio Minero. The experiment replicated the chemical conditions (sensitiser type and concentrations) as the previous study on ice, but degradations was conducted in a snow matrix. The goal was to assess whether two establish whether similar matrices - ice and snow - would yield different degradation products. The results showed that snow acts as a transitional medium between the aqueous and ice matrices, but it also generates some snow-specific products. Consequently, the reactivity, while similar to that observed in ice, differed not only in terms of kinetics, an aspect already well studied in previous works, but also in the resulting degradation products. In addition, two real snow samples from different areas of the Alps were selected: one from above the treeline and one from below, which had significantly different organic fraction content. After melting and filtering the snow, the samples were treated identically to those in the ultrapure water experiments, i.e. BPA was added and the solution was sprayed to recreate the snow. From a kinetic standpoint, it was observed that samples with lower CDOM content degraded BPA faster, even tough the types of CDOM were similar in both samples. This suggests that a higher CDOM abundance may favour self-degradation processes of the CDOM itself, thus influencing overall reactivity. Finally, the toxicity of the system was assessed using *in silico* techniques. In samples prepared in ultrapure water a decrease in toxicity was observed over time. In contrast, the toxicity of the real samples remained almost constant even after 30 hours of irradiation under a UV lamp.

Photodegradation of bisphenol A and identification of photoproducts in artificial snow under UVA radiation

Stefano Frassati[a,b], Luca Carena[c] , Elena Barbaro[b,a], Marco Roman[a,b], Matteo Feltracco[a], Marco Minella[c], Fabrizio Sordello[c], Claudio Minero[c], Andrea Spolaor[b,a],Elisa Scalabrin[b,a], Carlo Barbante[a,b], Andrea Gambaro[a,b].

[a] Ca' Foscari University of Venice, Department of Environmental Sciences, Informatics and Statistics, Venice Mestre, Italy.

[b] Institute of Polar Sciences – National Research Council (CNR-ISP), Venice Mestre, Italy.

[c] Dipartimento di Chimica, Università di Torino, Via Pietro Giuria 5, 10125, Torino, Italy

Corresponding authors: Stefano Frassati, Luca Carena
Corresponding author's email: Stefano.frassati@unive.it, luca.carena@unito.it

Keyword: contaminants; direct photolysis; indirect photochemistry; snow

Graphical abstract

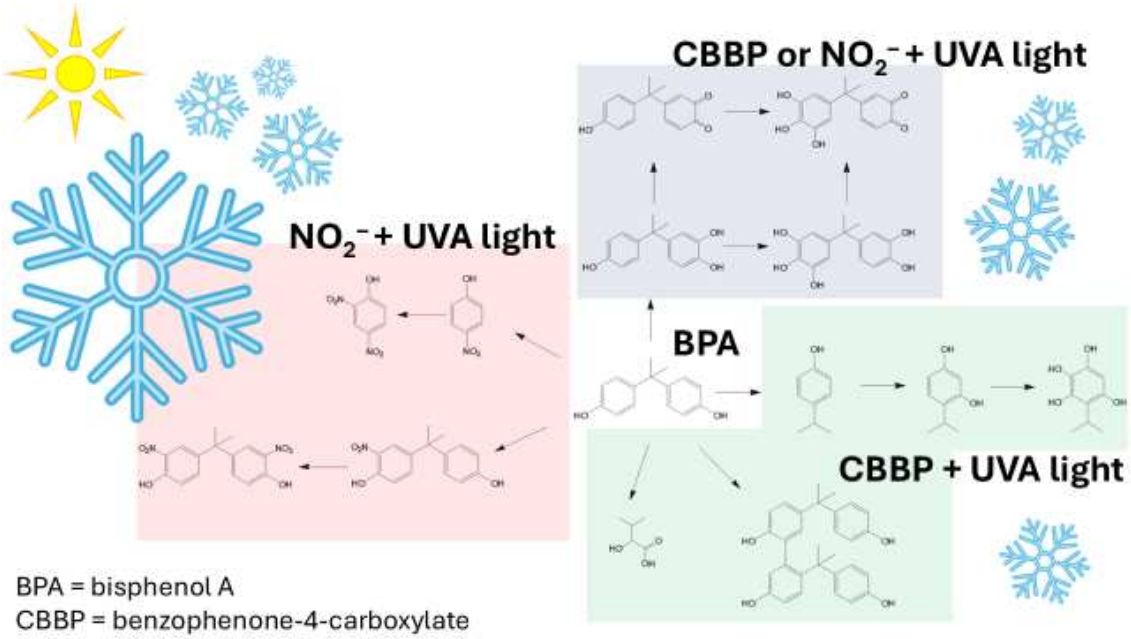

BPA = bisphenol A
CBBP = benzophenone-4-carboxylate

Abstract

Bisphenol A (BPA) is an organic micropollutant detected in various environments, from urban to remote areas, including Arctic snow. As a known endocrine disruptor, it is essential to investigate its environmental fate and potential impact on ecosystems. Previous studies have explored BPA photodegradation and its transformation products in different aqueous environments (freshwater, seawater, and ice), by using photosensitizers to trigger specific reactions. However, there is still a significant gap in understanding the photodegradation processes in snow, which, although similar to ice, has distinct chemical and physical characteristics.

Herein, we investigated the direct and indirect photodegradation of BPA in artificial snow and identified its degradation products through HPLC-HRMS. Nitrite and benzophenone-4-carboxylate, the latter used as a surrogate of chromophoric dissolved organic matter, induced significant BPA photodegradation under UVA irradiation. The photoproducts found in snow were partly similar to those previously observed in liquid water and ice. Their toxicity towards aquatic organisms was predicted with ECOSAR software as well. Finally, BPA photolysis and formation of photoproducts were investigated in two Alpine snow samples collected above and below the tree line, with a different organic matter content. Oxidation and nitration products of BPA were detected in these samples, suggesting that BPA photodegradation may indeed occur in natural snow. It was also noted that the aquatic toxicity of several identified photoproducts would be similar to that of BPA, but others may be even more toxic than the parent contaminant.

Introduction

The presence of contaminants in environmental waters is undoubtedly concerning, due to the adverse effects that these compounds can have on ecosystems and human health [156]. Contaminants, such as pharmaceuticals, personal care products, flame retardants, and pesticides, have been widely detected in surface waters, oceans, groundwaters, atmospheric water as well as in alpine and polar snowpacks [156]. The latter case highlights how the long-range transport of xenobiotics released at mid latitudes can contaminate remote areas [157, 158]. However, different chemical phenomena can induce the degradation of contaminants in the environment, thereby potentially lowering the concerning effects of the latter. Among these, photochemical reactions play a key role in the transformation of contaminants, especially in environmental waters [159, 160].

Photochemical reactions are classified into direct and indirect photolysis. Direct photolysis refers to the direct absorption of sunlight by a contaminant, which undergoes chemical transformation as a consequence. This pathway is important for those compounds that effectively absorb sunlight and have photolysis-quantum-yield values high enough [161]. In contrast, indirect photolysis occurs when sunlight is absorbed by a naturally occurring photosensitiser, generating transient reactive species that trigger contaminant degradation. These transient species are often called *Photochemically Produced Reactive Intermediates* (PPRIs) and have been found to be photoproduced in surface waters, atmospheric waters and in ice/snow. The most common photosensitisers found in environmental waters are nitrate and nitrite ions, as well as the chromophoric fraction of dissolved organic matter (CDOM) [84, 162]. Hydroxyl radicals ($HO^{\bullet}$), the excited triplet states of CDOM ($^3CDOM^*$) and singlet oxygen ($^1O_2$) are the main PPRIs which play an important role in the indirect photodegradation of contaminants [77, 160]. In particular, photolysis of nitrate and nitrite under UV radiation yields $HO^{\bullet}$, while CDOM absorbs a broader region of the solar spectrum, from UV to visible light, forming $HO^{\bullet}$, $^3CDOM^*$ and $^1O_2$ [84, 163–165]. Hydroxyl radicals can be formed upon UV photolysis of H_2O_2 in the atmospheric liquid phase and in ice [140, 166]. Furthermore, photolysis of both nitrate and nitrite yields nitrogen oxides (NO_x), which can be reactive towards some contaminants [167]. Although both the direct photolysis and the reactions with PPRIs can decrease the environmental harmfulness of some contaminants by inducing their degradation into less toxic products, in other cases these reactions can produce intermediate compounds as or even more harmful than the original contaminant [168, 169].

Although a considerable amount of research has been devoted to the study of photochemical reactions in surface and atmospheric waters, investigations into analogous processes occurring in ice/snow have emerged as a topic of scientific interest only during the last two decades [141, 170–173].

Photoreactions in ice/snow exhibit distinctive properties because they take place in liquid-like microenvironments of ice. These microenvironments are the liquid-like regions (LLRs), *i.e.* micropockets of liquid-like water within the ice bulk and at the ice-grain boundaries, and the quasi-liquid layer (QLL) or brine, which is a very thin layer of quasi-liquid water at the ice-crystal surface. Indeed, during water freezing, solutes are excluded from the ice bulk and accumulate in these liquid-like microenvironments [14, 35, 174]. This concentration effect can significantly enhance the photoreactivity of compounds in ice compared to bulk liquid water under similar irradiation conditions [100, 175, 176]. For instance, singlet oxygen production in ice has been found to be up to 10,000 times faster than in liquid water [149].

Bisphenol A (hereafter, BPA) is a widely used additive in the polymer industry, primarily for plastics, with an estimated production of approximately eight million tonnes in 2015 [116]). Extended exposure to BPA has been linked to detrimental effects on human health and ecosystems [114, 129, 130]. Nevertheless, BPA is often detected in diverse environmental matrices from both urban and rural areas. A notable example

is the presence of BPA in the snowpack of the Svalbard Islands, where its concentration has been found to be as high as 250 ng L^{-1} [125].

Several previous works have investigated the photodegradation of BPA in surface and atmospheric waters, as well as in ice [76, 111, 177, 178]. However, to the best of our knowledge, no information is available on BPA photolysis in snow. The present work investigated the photodegradation of BPA in artificial snow, particularly focusing on the identification of its transformation products. Indeed, snow is a complex medium comprising ice, liquid water, and air, that must be treated as a distinct matrix from bulk ice. Consequently, studying the photochemical degradation of contaminants in snow and the related potential formation of concerning by-products is imperative.

Materials and methods

Chemicals

The reagents used in this study, sodium nitrite ($NaNO_2$), BPA, benzophenone-4-carboxylate (CBBP), and sodium bromide (NaBr), were of analytical grade (Sigma-Aldrich). Methanol and acetonitrile (VWR Chemicals) were of gradient grade and used as eluents for HPLC-DAD analysis, while methanol (Sigma-Aldrich, gradient grade) and ultrapure water (UPW, 18.2 MΩ cm, TOC < 10 ppb, Elga LabWater, UK) were used for HPLC-HRMS analysis. All synthetic solutions for irradiation experiments were prepared with UPW.

Sample preparation and irradiation experiments

The artificial snow samples to be irradiated were prepared inside a cold room (3.3 × 1.4 × 2.4 m) set at 243 (± 0.6) K. Artificial snow was put in glass cells (volume of 20.4 mL) open on the top and slightly compacted until the glass cells were full filled. Samples were then irradiated in the same chamber under UVA LED lamp (see Carena et al. (2023) for a schematic of the irradiation set-up [151]). Snow samples were 1.8 cm thick and the photon flux density passing through the samples was 2.310^{18} photons $L^{-1}s^{-1}$, as determined by chemical actinometry with 2-nitrobenzaldehyde [151, 179] (see Figure S5 for the spectral photon flux density). Since the light extinction coefficient of snow is ≈ 0.1-0.2 cm^{-1}at 400 nm [59] , the light flux passing through snow samples can be considered almost homogeneous with depth. All experiments were conducted in duplicate and dark controls were carried out for each experiment to assess any pathway of BPA degradation in the absence of light. Artificial snow samples preparation followed an established procedure described elsewhere [151] , based on nebulisation of aqueous solutions at 243 K. The obtained snow had a density of 0.33 ± 0.02 g cm^{-3}. In particular, the synthetic aqueous solutions contained BPA (initial concentration of 4.5 μM), a photosensitizer if relevant, and Na_2SO_4 to maintain constant the total solute concentration at 200 μM, because both temperature and total solute concentration significantly affect the extent of the liquid-like microenvironments in ice/snow [35]. No loss of BPA (*e.g.*, by volatilisation) was observed during artificial snow preparation.

The adopted photosensitizers were the following:

- H_2O_2 (10 μM) to investigate the potential reactivity of BPA with $HO^\bullet$ radicals. The H_2O_2 concentra-

tion was selected based on the environmental range reported in the literature [150, 180, 181].

- $NaNO_2$ (50 μM) to trigger the possible reactivity of BPA with $HO^\bullet$ radicals and with reactive nitrogen species, such as NO_x. Although this nitrite concentration is closer to the value measured in atmospheric water than in snow, similar concentrations have been previously used to study photoreactions induced by NO_2^- in ice and snow [58, 151].

- Benzophenone-4-carboxylate (hereinafter CBBP; 10 μM or $\tilde{1}.7$ mgC L^{-1}) as a surrogate of CDOM. CBBP produces a reactive triplet state ($^3CBBP^*$) upon excitation by UVA light, that is able to react with contaminants [182], such as BPA. Indeed, $^3CBBP^*$ has been used as a proxy of natural $^3CBBP^*$ in photochemical experiments carried out in liquid water [182]. In this work we used CBBP + UVA light to investigate the possible reactivity of BPA with $^3CBBP^*$ in snow. The dissolved organic carbon (DOC) value of CBBP is within the environmental range of surface snow [183, 184] .

- Benzophenone-4-carboxylate (hereinafter CBBP; 10 μM or $\tilde{1}.7$ mgC L^{-1}) in combination with NaBr (6 μM) was employed to examine the potential reactivity of BPA with $^3CBBP^*$ and with reactive bromine species, potentially resulting from the oxidation of bromide by excited triplet states of organic matter. The bromide concentration was selected based on the bromide concentration values observed in surface snow from Arctic coastal regions [15, 185].

After irradiation, the snow samples were melted at room temperature and analysed to assess BPA photodegradation (*vide infra*).

Irradiation experiments were also performed with real snow samples collected near the Simplon Pass (Switzerland; 46.2469 N, 8.0306 E) and Col dei Baldi (Italy; 46.4215 N, 12.0646 E). Real snow was sampled by scraping the top 3 cm of the snowpack by using a plastic spatula and stored in dark plastic bottles at 253 K. Specifically, the Col dei Baldi sample was taken from a clearing outside a pine forest, while the Simplon Pass sample was collected above the tree line. After transport to the lab, the samples were melted and filtered through a 0.45 μm PTFE filter. An aliquot was set aside for major ions analysis, TOC, and optical measurements. For irradiation experiments, BPA was spiked to liquid samples to a final concentration of 4.5 μM, and the obtained solutions were subsequently used to make artificial snow as in the case of the synthetic aqueous solutions.

Analytical methods

BPA and CBBP quantification in irradiated snow samples was performed using high-performance liquid chromatography (HPLC, VWR Hitachi Chromaster) with a LiChroCART RP-18 column (125 mm × 4 mm, 5 μm particle size, Merck) coupled to a diode array detector (DAD). The elution was performed in isocratic mode (60% methanol and 40% water acidified to pH 3 withH_3PO_4) at a flow rate of 1 mL min^{-1} for a total run time of 10 min. The retention time of BPA was 5.3 min and was quantified at 227 nm, whereas CBBP retention time was 6.8 min and quantification was achieved at 259 nm.

BPA photoproducts were identified by ultra- UHPLC (Vanquish, Thermo Fisher Scientific) coupled to a quadrupole-orbitrap high-resolution mass spectrometer (HRMS) Exploris 120 (Thermo Fisher Scientific). The chromatographic separation was conducted using a Synergi Hydro-RP 80 Å column (50 mm × 4.6 mm, 4 µm particle size) at 25 °C, with ultrapure water (A) and methanol (B) as mobile phases. Gradient elution was performed at 0.2 mL min^{-1} with the following program: 10% B (0–5 min), 100% B (5–35 min), and 10% B (35.1–45 min). Mass detection was conducted using an electrospray ionization (ESI) source in both

negative and positive modes. Detection was set in the range 50-600 m/z with a resolution of 120000, RF lens 30%, spray voltage 3.5 kV and 2.5 kV for negative ionizations, respectively. Sheath gas was set at 25 a.u, and auxiliary gas at 5 a.u, while the vaporizer temperature was at 300 C and the ion transfer tube temperature at 320 C. Tandem MS fragmentation was conducted in a High energy Collision Dissociation (HCD) cell pressurized with N_2 gas. Collision energies were set to 10, 30, and 50 eV and the isolation window at $\pm$ 1 m/z.

Ions were quantified using an ion chromatography system (Thermo Scientific Dionex^{TM} ICS-5000, Waltham, MA, USA), coupled to a single quadrupole MS and a conductivity detector (MSQ Plus^{TM}, Thermo Scientific, Bremen, Germany) [186].

The UV-vis absorption spectra were recorded by means of a Varian Cary 100 Scan double-beam UV-vis spectrophotometer with Hellma quartz cuvettes having a 1 cm optical path length. Fluorescence excitation–emission matrices were recorded by a JASCO FP 750 spectrofluorometer to gather information about the organic matter in real snow samples.

In silico toxicity evaluation

Although several biological tests are available to evaluate contaminant ecotoxicity to aquatic ecosystems [187], in silico assessment can be used as screening tool for this purpose. Here, the acute toxicity of BPA photoproducts towards aquatic organisms (fish, green algae, and daphnid) was assessed by means of the ECOSAR 2.2 software, developed by the US EPA as Lethal Concentration 50 % (LC50) and half Maximal Effective Concentration (EC50) [188].

Results and discussion

BPA photodegradation in artificial snow

Irradiation of artificial snow samples containing BPA and without photosensitizers did not show a significant degradation of BPA by direct photolysis, and the concentration of BPA remained constant also in dark conditions, as shown in Figure 3.10A . The absorption spectrum of BPA measured in liquid water does not overlap with the emission spectrum of the UVA lamp (Figure S5). Although the absorption spectrum of BPA in ice/snow is not known, the low to negligible absorption of UVA light by BPA may account for this finding.

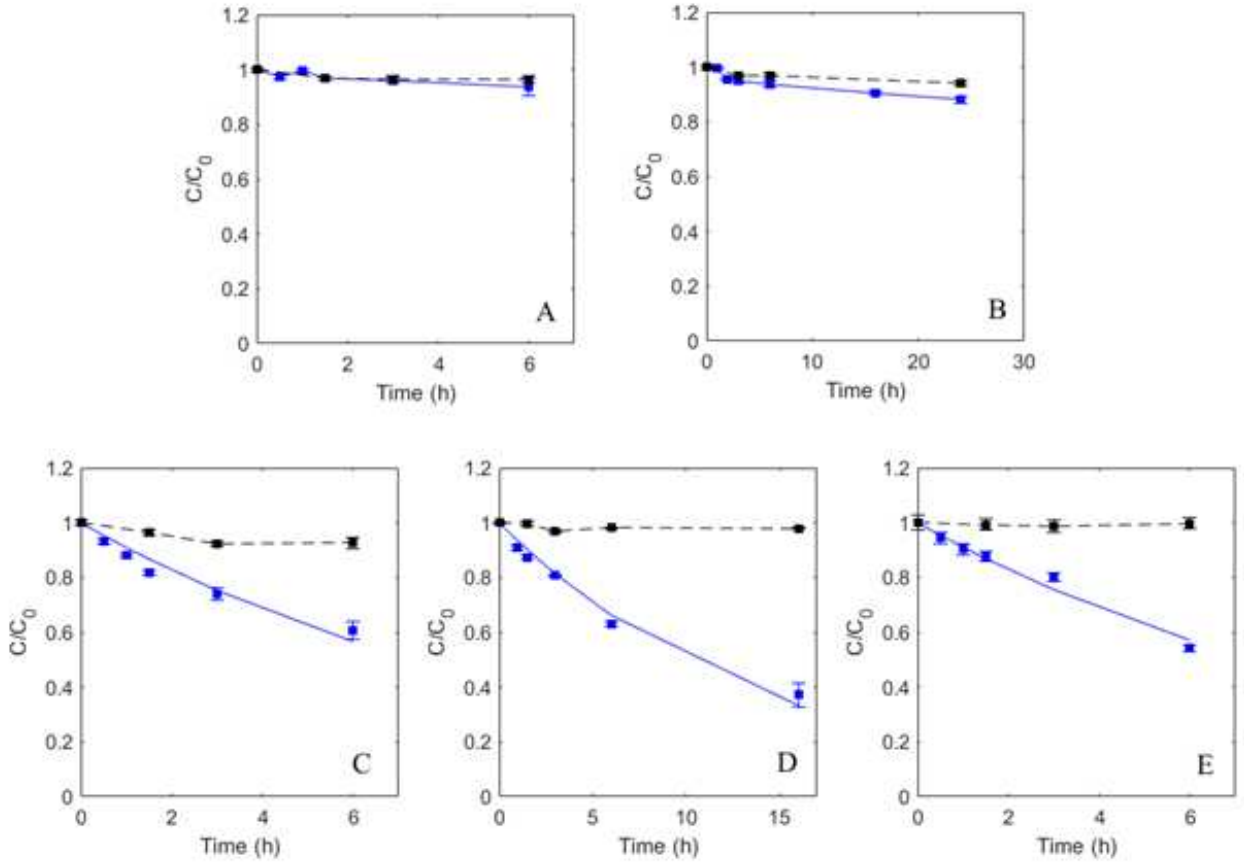

Figure 3.10: Photodegradation profiles of BPA in artificial snow by (**A**) direct photolysis, and in the presence of (**B**) H_2O_2, (**C**) NO_2^-, (**D**) CBBP and (**E**) CBBP + Br^-. Black squares and dashed lines represent dark controls, while blue squares and solid lines show the samples exposed to UV-A light. Error bars refer to duplicate runs.

BPA photodegradation over 24h-long irradiation in the presence of H_2O_2, used as photosensitiser of $HO^\bullet$

radicals, was found to be low (≈12%), while no obvious degradation of BPA was observed in the same samples but in dark conditions (Figure 3.10B). BPA is highly reactive with $HO^{\bullet}$ in liquid water [189, 190]. However, the reaction between BPA and $HO^{\bullet}$ in snow may be dependent on several factors. Indeed, H_2O_2 can be present both in the QLL at the surface of ice grains and/or trapped within the bulk, and the photolysis of H_2O_2 in ice bulk yielding $HO^{\bullet}$ is less efficient than in QLL [191]. We do not know the actual distribution of H_2O_2 in the ice grains of our snow samples. However, H_2O_2 embedding in the ice matrix might limit BPA photodegradation by $HO^{\bullet}$ radicals. Furthermore, H_2O_2 does not efficiently absorb the radiation emitted by the UVA lamp, due to low values of the molar absorption coefficient [83], and the $HO^{\bullet}$ radicals produced upon H_2O_2 photolysis can be scavenged by H_2O_2 itself [192], lowering the amount of $HO^{\bullet}$ available for reaction with BPA. Although it was not possible to study this process in our samples, it is nevertheless conceivable that BPA oxidation in environmental snow may be induced by $HO^{\bullet}$.

Photodegradation of BPA in the presence of NO_2^- was observed after 6 h of UVA irradiation, whereas negligible degradation was observed in dark conditions (Figure 3.10C). BPA photodegradation followed pseudo-first order kinetics, $[BPA]_t = [BPA]_0 e^{-k't}$, where $[BPA]_t$ and $[BPA]_0$ are the BPA concentrations at irradiation time t and before irradiation, respectively, while k' is the pseudo-first order rate constant of BPA photodegradation. The resulting initial photodegradation rate of BPA was $R = k' \cdot [BPA]_0 \approx 1.2 \cdot 10^{-10}$ M s^{-1}. Nitrite undergoes photolysis under UVA light producing $HO^{\bullet}$ and $^{\bullet}NO_2$. Meanwhile, NO_2^- can react with the photoproduced $HO^{\bullet}$ radicals, yielding $^{\bullet}NO_2$ [4, 46, 83, 96]. These reactive species can account for the observed BPA photodegradation in snow. The reactivity of $^{\bullet}NO_2$ with aromatic organic compounds is of particular environmental importance, because it could give rise to nitroaromatic compounds with a higher toxicity than the starting substances [81].

In the presence of CBBP, ≈60% of BPA photodegradation was observed after 16 h of UVA irradiation, showing a rate ≈$8.7 \cdot 10^{-11}$ M s^{-1} (pseudo-first order kinetics), while no degradation of BPA was observed in dark conditions over the same period of time (Figure 3.10D). Furthermore, CBBP underwent ≈8% photodegradation under UVA light, while its concentration remained constant in the dark. In liquid water, CBBP can absorb UVA light and produce ^{3}CBBP* as a consequence of excitation to the single state and subsequent intersystem crossing (ISC; **R21**) [182]. ^{3}CBBP* is then deactivated by internal conversion (**R22**) and collisions with dissolved (ground-state) oxygen molecules (**R23**). The latter process forms singlet oxygen as a result of energy transfer [193] and is favoured under aerated conditions. The high specific surface area of snow facilitates the O_2 exchange at the air-snow interface [15, 194], thus potentially promoting the production of $^1O_2$. These reactions may take place also in liquid-like microenvironments of snow, since photoproduction of singlet oxygen and excited triplet states of organic molecules has been observed in ice [149], and both ^{3}CBBP* (**R24**) and $^1O_2$ (**R25**) can react with BPA. In liquid water, the rate constant of reaction **R25** is significantly higher than that of reaction **R25**: $4.6 \cdot 10^9$ M^{-1} s^{-1} and $3 \cdot 10^5$ M^{-1} s^{-1}, respectively [178, 195]. These reactions can account for the observed BPA photodegradation in artificial snow in the presence of CBBP, suggesting a key role of $^3CBBP^*$ in BPA photodegradation (**Text S1**).

$$\text{CBBP} + h\nu \rightarrow {}^1\text{CBBP}^* \xrightarrow{\text{ISC}} {}^3\text{CBBP}^* \quad \text{(R21)}$$

$${}^3\text{CBBP}^* \rightarrow \text{CBBP} \quad \text{(R22)}$$

$${}^3\text{CBBP}^* + \text{O}_2 \rightarrow \text{CBBP} + {}^1\text{O}_2 \quad \text{(R23)}$$

$${}^3\text{CBBP}^* + \text{BPA} \rightarrow \text{products} \quad \text{(R24)}$$

$${}^1\text{O}_2 + \text{BPA} \rightarrow \text{products} \quad \text{(R25)}$$

In liquid water, the excited triplet states of organic matter can produce halogens radicals in the presence of halogen anions, which can in turn react with contaminants [196, 197] (Jin et al., 2022; Lei et al., 2021). In this work, BPA was irradiated in snow samples containing both CBBP and Br^- to investigate the possible reactivity of BPA with bromine radicals in artificial snow. However, the observed BPA photodegradation kinetics was not significantly different from that measured in the presence of CBBP, but without Br^- (Figure**3.10E**).

By-products of BPA photodegradation in artificial snow

The formation of by-products of BPA photodegradation was investigated in all the adopted irradiation conditions and are summarized in **Table 3.2**. The identification of the compounds was based on fragmentation patterns obtained via HR-MS and comparison with existing literature. This level of confidence is classified as "Tentative candidate(s)" or Level 3 and, Level 4 was used for some compounds [198]. Formation of hydroxylated BPA compounds, specifically BPA-OH (**1**) and BPA-$(OH)_3$ (**2**), was observed in the presence of NO_2^- and CBBP (**3.12**), while BPA-$(OH)_2$ was not detected. An additional step of oxidation of BPA-OH and BPA-$(OH)_3$ would occur with the formation of compounds **3** and **4**, respectively.

1. *Nitrite as photosenitizer*

   In addition to compounds **1-4**, most of the BPA photoproducts identified in the presence of NO_2^- were found to be formed by nitration or combined nitration and oxidation reactions. Of particular interest are compounds **10** and **11,** namely the mono-and di-nitrated forms of BPA (red pathways in **Scheme 1**; **Figure 3.11A**).

   Finally, compounds **12** and **13** represent the nitro- and dinitro-phenol, respectively. As illustrated in **Figure 3.11B**, 4–nitrophenol, once formed, can undergo further nitration processes to become 2,4–dinitrophenol.

   It is interesting to note that a BPA dimer undergoing nitration reactions has been previously detected in synthetic ice, but was not observed here in artificial snow [111], suggesting that specific reactivity may occur in snow differently from that observed in ice.

2. *CBBP as photosenitizer*

   BPA photodegradation in the presence of CBBP produced compounds **5** to **9**, additionally to **1**–**4**. Interestingly, these have been previously identified in studies about BPA photodegradation in liquid water under various conditions [177, 199, 200], while the formation of compound **5** has been also observed in ice. However, the hydroxylated derivatives of the latter, that can be formed in ice [111], were not detected in the present case. Compounds **7** and **8** detected in snow (Figure S3) may be

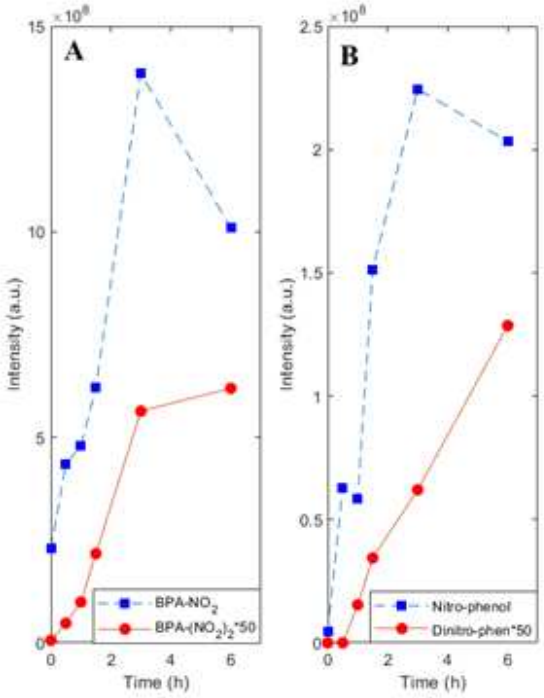

Figure 3.11: Photoproduction of nitrocompounds from BPA photolysis in the presence of NO_2^- in snow: **(A)** BPA-NO_2 (blue) and BPA-$(NO_2)_2$ (red); **(B)** 4–nitrophenol (blue) and 2,4–dinitrophenol (red). Signal intensities of the dinitro compounds were multiplied by 50 for better readability.

produced upon successive oxidation steps of **6**. The possible photodegradation pathways of BPA in the presence of CBBP in snow are illustrated in Figure 3.12 (green pathway). No specific photodegradation by-products of BPA were detected in the presence of CBBP + Br^-, and also the kinetics of BPA photolysis was consistent with that observed with CBBP, but without Br^-, as described above. For these reasons, the two experimental scenarios will be considered equivalent. These findings suggest that BPA photodegradation by bromine radicals might be unlikely in artificial snow in the presence of CBBP + Br^- under UVA light.

Finally, $^3CBBP^*$ undergoes deactivation in liquid water by collision with ground-state molecular oxygen yielding $^1O_2$ (R23), and this process may be operational also in snow. Furthermore, Bower and Anastasio have reported that BPA is degraded by $^1O_2$ in ice at 263 K [149]. Therefore, in irradiated snow samples containing CBBP, BPA can be potentially degraded by both $^3CBBP^*$ and$^1O_2$ (R4 and R5). In order to qualitatively assess the contribution of $^1O_2$ in BPA photodegradation in the presence of CBBP, artificial snow samples containing BPA (4.5 μM), Na_2SO_4 (65 μM) and Rose Bengal (10 nM) were irradiated under visible LED lamp. Rose Bengal is a widely adopted photosensitizer in both liquid water and ice that produces $^1O_2$ upon absorption of visible light. BPA photodegradation was 20% after 6 h and the formation of BPA-OH was observed. Since BPA-OH was also found in the experiments with CBBP, this finding would not exclude a contribution of singlet oxygen in BPA photodegradation due to CBBP-photosensitized reactions.

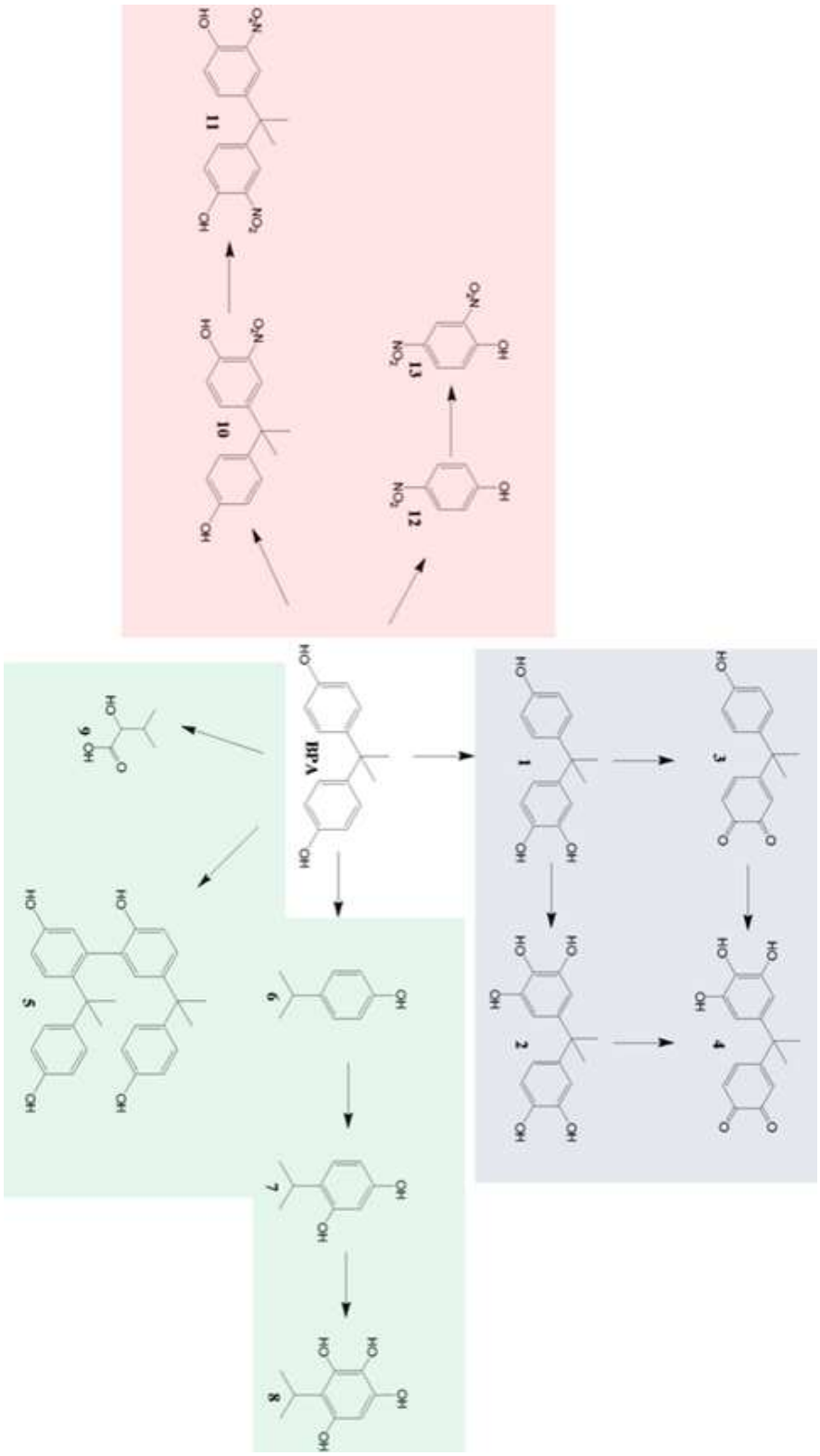

Figure 3.12: Possible photodegradation pathways of BPA in artificial snow in the presence of CBBP (green) and NO_2^- (red). The compounds highlighted in blue are those common to both experiments.

Table 3.4: List of BPA photodegradation products identified in artificial snow samples in this work. 'W', 'I', and 'S' mean liquid water, ice and snow, respectively, and refer to the matrices in which the photoproducts were identified as reported in the literature or as found in this work. Compounds identification was possible through analysis in negative mode $[M\text{-}H]^{2-}$.

Compound	Molecular formula	Molecular mass	[M-H]− exp.	[M-H]− theor.	Error (ppm)	Level of confidence	t_r (min)	Experiment	Matrix
BPA	$C_{15}H_{16}O_2$	228.1144	227.1079	227.1066	0.77	1	26.25		
1	$C_{15}H_{16}O_3$	244.1093	243.1028	243.1015	0.70	3	23.56	NO_2^-, CBBP, real snow	W, I, S
2	$C_{15}H_{14}O_5$	276.0992	275.0927	275.0914	0.78	4	14.06	NO_2^-, CBBP, real snow	W, I, S
3	$C_{15}H_{14}O_3$	242.0837	241.0723	241.0759	-8.5	3	21.37	NO_2^-, CBBP, real snow	W, I, S
4	$C_{15}H_{14}O_5$	274.0835	273.0770	273.0757	0.56	4	13.80	NO_2^-, CBBP, real snow	S
5	$C_{30}H_{30}O_4$	454.2138	453.2893	453.2060	-1.24	4	29.22, 30.24	CBBP	W, I, S
6	$C_9H_{12}O$	136.0882	135.0446	135.0455	0.9	3	19.40	CBBP, real snow	W, I, S
7	$C_9H_{12}O_2$	152.0831	151.0765	151.0753	0.31	3	18.30	CBBP, real snow	W, I, S
8	$C_9H_{12}O_4$	184.0664	183.0651	183.0651	0.64	3	3.34	CBBP	W, I, S
9	$C_5H_{10}O_3$	118.0635	117.0558	117.0557	0.12	3	2.4	CBBP	W, I, S
10	$C_{15}H_{15}O_4N$	273.1006	272.0930	272.0928	0.17	3	28.90	NO_2^-, real snow	W, I, S
11	$C_{15}H_{14}O_6N_2$	318.0857	317.0779	317.0779	-0.01	3	30.25	NO_2^-, real snow	W, I, S
12	$C_6H_5O_3N$	139.0263	138.0197	138.0185	0.24	3	21.8	NO_2^-, real snow	W, S
13	$C_6H_4O_5N_2$	184.0114	183.0047	183.0036	-0.24	4	6.78	NO_2^-	S

BPA photodegradation in real snow samples

Real snow samples were analysed for TOC, obtaining 88.2 mgC L^{-1} for Col dei Baldi and 0.74 mgC L^{-1} for Simplon Pass. Moreover, the spectrofluorimetric characterisation with excitation-emission matrix (Figure S3) showed a significant fluorescence peak in the protein-like region of organic matter in Col dei Baldi sample, that may be attributed to plant-derived compounds, such as polyphenols and other phenol-containing compounds, rather than being exclusively related to microbial activity [201]. Indeed, the Col dei Baldi sample was collected near a pine forest, whereas that of Simplon Pass, which shows a lower TOC and a significantly less intense fluorescence, above the tree line.

Major ions analyses also showed significant differences between the two samples for marine-origin species such as Na^+ and Cl^-, with values of 2.2 mg L^{-1} and 2.0 mg L^{-1} for Simplon Pass, and 0.2 mg L^{-1} and 0.06 mg L^{-1} for Col dei Baldi, respectively. However, for ions of primarily crustal origin, such as Mg^2+ and Ca^2+, Col dei Baldi exhibited higher values compared to Simplon Pass (434 ng L^{-1} and 321 ng L^{-1} vs. 51.2 ngL^{-1} and 81.7 ng L^{-1}). Nitrate, which can act as a photosensitizer, showed similar concentrations in the two sites, 144 ng L^{-1} for Col dei Baldi and 161 ngL^{-1} for Simplon Pass, respectively. Nitrite was not analysed, as it can be easily oxidized to nitrate upon melting.

The BPA photodegradation in snow from Col dei Baldi was almost negligible after 30 h of irradiation, while in snow from Simplon Pass the photodegradation rate was 2.1·10–11 M s^{-1} (first-order kinetics). This difference might be accounted for by the higher content of organic matter in the Col dei Baldi sample. DOM efficiently consumes $HO^\bullet$ radicals by scavenging, which are also partly responsible of NO_x production through nitrite oxidation. Furthermore, NOx formation by photolysis of nitrate and nitrite can be decreased by CDOM because of light screening. Therefore, $HO^\bullet$ scavenging and lower NO_x photoproduction may have inhibited BPA photodegradation in snow from Col dei Baldi. Moreover, although a high CDOM content would favour the photoproduction of $^3CDOM^*$ and$^1O_2$, the presence of phenolic compounds may inhibit contaminant photodegradation induced by $^3CDOM^*$ due to antioxidant effects [202]. A non-negligible degradation was also observed in dark conditions in snow from Simplon Pass (5.8·10–12 M s^{-1}), suggesting that dark chemistry processes can occur even in frozen samples (Figure 3.13).

Concerning the photodegradation products of BPA, compounds **1**, **2** and **4** were formed in both samples, indicating that oxidation process also occurs in the Col del Baldi sample (Figure 3.14), although at a much slower rate. The remaining common compounds were **6**, **7**, **10, 11** and **12**. It is noteworthy that compounds 6 and 7 were already present before irradiation and exhibited a considerable increase during irradiation. This indicates that they may also originate from the degradation of other organic substances in snow, making them unsuitable as specific tracers for BPA photodegradation. A comparable phenomenon was observed for nitrophenol and 2,4–dinitrophenol, although only at the Simplon Pass site. Conversely, compounds **10** and **11** may potentially serve as specific markers of BPA photodegradation, together with compounds **1**, **2** and **4** (see the Supplementary Material for the mass spectra of all compounds).

Finally, dark degradation of BPA in the Simplon Pass sample resulted in the formation of BPA-NO_2 and BPA-OH, with minor formation of nitrophenol, suggesting the possible occurrence of NO_2^- mediated dark reactions. Nitrite can induce hydroxylation and nitration of organic compounds during freezing [99, 100]. Since the dark degradation of BPA in artificial snow with NO_2^- was negligible, in this case the complex matrix of real snow favoured this process.

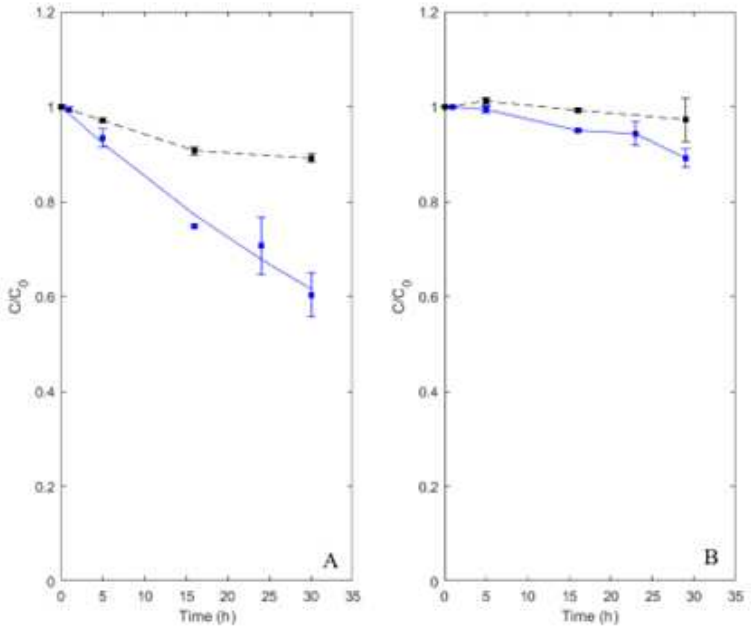

Figure 3.13: Photodegradation profiles of BPA in snow from Simpon Pass (**A**) and Col dei Baldi (**B**). Black squares and dashed lines refer to dark controls, while blue squares and solid lines refer to irradiated samples.

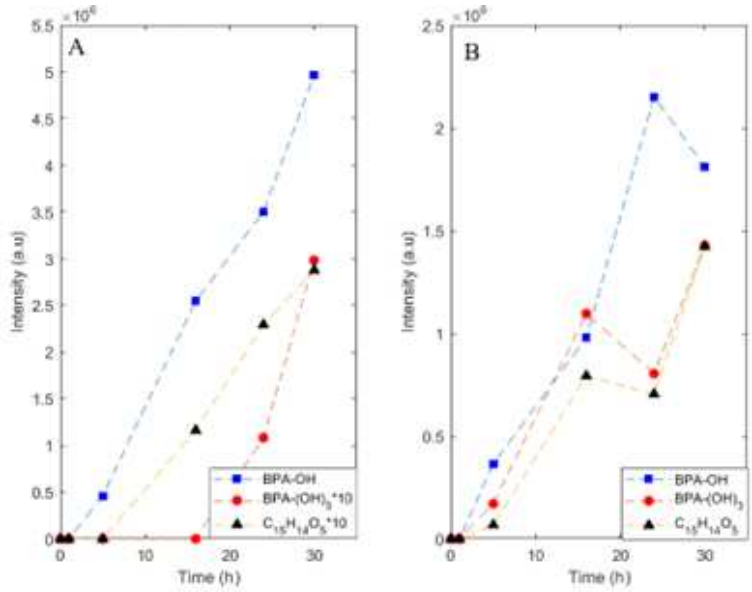

Figure 3.14: Photoproduction of compounds **1** (blue squares), **2** (red circles) and **4** (black triangles) in snow samples from Simplon Pass (**A**) and Col dei Baldi (**B**).

Modelling the toxicity of BPA photoproducts

The previous findings show that BPA photodegradation in snow may produce several compounds, some of them nitrated. Since contaminants and their photoproducts formed in snow can be released into water bodies after snow melting [171], it is interesting to assess their toxicity towards aquatic organisms. In order to evaluate the toxicity of the BPA photodegradation by-products, a QSAR approach was employed by using

the ECOSAR software [188]. Table S1 shows the acute toxicity of BPA and its photodegradation by-products as predicted by ECOSAR, namely the LC50 data for fish and daphnids, as well as the EC50 data for green algae. Contaminants can be classified through levels of aquatic toxicity as very toxic (LC/EC50 $\leq$ 1 mg L^{-1}), toxic (1 $<$ LC/EC50 $\leq$ 10mgL^{-1}), harmful (10 $<$ LC/EC50 $\leq$ 100mgL^{-1}), and not harmful (LC/EC50 $>$ 100 mg L^{-1}) [203]. According to this classification, the toxicity of several identified photoproducts is similar to BPA for different trophic levels, and some of them are even less toxic (Table S1). However, compounds **8**, **10**, and **11** are predicted to be more toxic than BPA, especially for fish and green algae. It is noteworthy that compounds **10** and **11** were found to be photoproduced in the irradiated real snow samples with added BPA, thereby suggesting potential environmental concerns about BPA photodegradation in snow.

Conclusions

In this study, the photodegradation of BPA in artificial snow was investigated under UVA light, both in the absence and in the presence of photosensitizers, as well as in real snow samples containing natural DOM and ions. Photodegradation of BPA was faster in the presence of NO_2^- or CBBP, the latter used as a surrogate of CDOM. The identified photoproducts showed different degree of oxidation, carrying further hydroxyl groups that can in turn be oxidized, and nitrated phenols were also detected when BPA is photodegraded in the presence of NO_2^-. Some of these photoproducts have been found also in ice and liquid water, while others may be characteristic of snow. In contrast, the direct photolysis and the photoreactions triggered by H_2O_2 + UVA did not induce a significant BPA photodegradation.

In real snow samples, BPA underwent faster photodegradation in the presence of a low content of (C)DOM, while it was inhibited in a sample with a high TOC value. Some photoproducts identified in real snow samples were the same as those detected in artificial snow with the adopted photosensitisers, suggesting similar photodegradation pathways of the contaminant.

Finally, BPA photoproducts showed toxicity towards aquatic organisms similar to the parent contaminant, but some of them are more toxic, highlighting the importance of further studies focusing on the resulting by-products.

Since snowpacks can serve as reservoirs of contaminants collected from, for instance, atmospheric deposition, and these compounds can be eventually released into water bodies after snow melting (a process that is enhanced by global warming), the study of post-depositional processes taking place in snow, such as photochemical reactions, is of great environmental significance. The present work highlights the importance of investigating both contaminant photodegradation in snow/ice and the resulting formation of photoproducts, which sometimes can be environmentally concerning. Future studies should thus focus on photodegradation processes of further contaminants in sow/ice, and on the identification, characterization and, if possible, quantification of photoproducts.

Ethics declarations

Funding

LC, FS, MM and CM acknowledge financial support from the Project CH4.0 under the MUR program "Dipartimenti di Eccellenza 2023-2027" (CUP: D13C22003520001). This work has benefited from the infrastructural support of the Centre for Trace Analysis (CeTrA) of Ca' Foscari University through the project IR0000032, Italian Integrated Environmental Research Infrastructures System (ITINERIS), funded by the EU: NextGenerationEU, PNRR, Mission 4 ("Education and Research"), Component 2 ("From research to business"), Investment 3.1 ("Fund for the realization of an integrated system of research and innovation infrastructures").

Acknowledgements

Elga Lab water, High Wycombe UK, supplied the pure water system used in this study.

Competing Interests

The authors have no financial interests to disclose.

Author contributions

Conceptualization: Stefano Frassati, Luca Carena, Elena Barbaro, Marco Minella, Fabrizio Sordello, Claudio Minero; Formal analysis and investigation: Stefano Frassati, Luca Carena, Elisa Scalabrin; Writing - original draft preparation: Stefano Frassati, Elena Barbaro, Luca Carena. Writing - review and editing: Stefano Frassati, Luca Carena, Elena Barbaro, Marco Roman, Matteo Feltracco, Marco Minella, Fabrizio Sordello, Claudio Minero, Andrea Spolaor, Elisa Scalabrin, Carlo Barbante, Andrea Gambaro.

Supplementary materials

Text S1: Assessment of the relative contribution of CBBP triplet state and $^1O_2$ in BPA photodegradation in artificial snow.

In the presence of CBBP, BPA photodegradation in snow can be potentially accounted for by reactions with the excited triplet state of CBBP ($^3CBBP^*$; R S5) and singlet oxygen (R 6S). The quenching of $^3CBBP^*$ by molecular oxygen produces $^1O_2$ (R S3).

$$\mathrm{CBBP} \xrightarrow{\mathrm{h}\nu,\ \mathrm{ISC}} {}^3\mathrm{CBBP}^* \quad \text{(R S1)}$$

$${}^3\mathrm{CBBP}^* \rightarrow \mathrm{CBBP} \quad \text{(R S2)}$$

$${}^3\mathrm{CBBP}^* + \mathrm{O_2} \rightarrow \mathrm{CBBP} + {}^1\mathrm{O_2} \quad \text{(R S3)}$$

$${}^1\mathrm{O_2} \xrightarrow{\mathrm{H_2O}} \mathrm{O_2} \quad \text{(R S4)}$$

$${}^3\mathrm{CBBP}^* + \mathrm{BPA} \rightarrow \mathrm{products} \quad \text{(R S5)}$$

$${}^1\mathrm{O_2} + \mathrm{BPA} \rightarrow \mathrm{products} \quad \text{(R 6S)}$$

The relative contribution of reactions R S5 and R 6S can be assessed through the ratio of the pseudo-first order rate coefficients of the relevant reactions ($k'_{snow,^3CBBP^*}$ $k'_{snow,^1O_2}$ and , respectively) as follows:

$$\frac{k'_{snow,^3CBBP^*}}{k'_{snow,^1O_2}} = \frac{k'^{snow}_{BPA+^3CBBP^*}[^3CBBP^*]_{snow}}{k'^{snow}_{BPA+^1O_2}[^1O_2]_{snow}} \quad \text{(Eq. S1)}$$

In Eq. S1, and are the bimolecular rate constants of, respectively, reactions R S5 and R 6S. $[^3\mathrm{CBBP}^*]_{\mathrm{snow}}$ and $[^1\mathrm{O_2}]_{\mathrm{snow}}$ are the steady-state concentrations of $^3\mathrm{CBBP}^*$ and $^1\mathrm{O_2}$ in the liquid-like microenvironments of snow ice crystals. The values of these rate constants and concentrations are not known, preventing the direct determination of the ratio $k'_{snow,^3CBBP^*}{}^*(k'_{snow,^1O_2})^{-1}$. However, some modelling considerations can be made based on experimental results reported in the literature. Previous works have shown that photodegradation of organic substrates (S) induced by $^1\mathrm{O_2}$ and excited triplet states of organic photosensitizers ($^3\mathrm{Sens}^*$) are significantly enhanced in liquid-like regions of ice compared to liquid water. This reactivity increase has been described by means of an enhancement factor F, which is defined as the ratio between the pseudo-first order rate coefficient of S photodegradation by $^1\mathrm{O_2}/^3\mathrm{Sens}^*$ as measured in ice ($k'_{ice,^1O_2}$ or $k'_{ice,^3CDOM^*}$) and the same rate coefficient as observed in liquid water ($k'_{lw,^1O_2}$ or $k'_{lw,^3CDOM^*}$) [149, 204]. That is $F_{^1O_2} = k'_{ice,^1O_2}(k'_{lw,^1O_2})^{-1}$ and $F_{^3Sens^*} = k'_{ice,^3Sens^*}(k'_{lw,^3Sens^*})^{-1}$.

Furthermore, one has that $k'_{lw.^1O_2} = k^{lw}_{S+^1O_2}[^1O_2]_{lw}$ and $k'_{lw.^3Sens^*} = k^{lw}_{S+^3Sens^*}[^3Sens^*]_{lw}$, where $k^{lw}_{S+^1O_2}$ $k^{lw}_{S+^3Sens^*}$ and are, respectively, the second-order rate constants of the reactions S + $^1\mathrm{O_2}$ and S + $^3\mathrm{Sens}^*$, while and are the steady-state concentrations of singlet oxygen and $^3\mathrm{Sens}^*$. These parameters refer to liquid water (lw). Consequently, the photodegradation rate coefficients in ice can be expressed as follows:

$$k'_{ice,^1O_2} = F_{^1O_2}k^{lw}_{S+^1O_2}[^1O_2]_{lw} \quad \text{(Eq. S2)}$$

$$k'_{ice,^3Sens^*} = F_{^3Sens^*}k^{lw}_{S+^3Sens^*}[^3Sens^*]_{lw} \quad \text{(Eq. S3)}$$

Eq. S2 and Eq. S3 can be applied for the CBBP+BPA case (Sens = CBBP and S=BPA), to roughly assess the relative contributions of ^{3}CBBP* and $^1O_2$ in BPA photodegradation in snow (Eq. S4).

$$\frac{k'_{snow,^3CBBP^*}}{k'_{snow,^1O_2}} = \frac{F_{^3CBBP^*} k^{lw}_{BPA+^3CBBP^*} [^3CBBP^*]_{lw}}{F_{^1O_2} k^{lw}_{BPA+^1O_2} [^1O_2]_{lw}} \qquad \text{(Eq. S4)}$$

Note that = 4.6·10^9 M^{-1} s^{-1} and = 3·10^5 M^{-1} s^{-1} [178, 195]. The concentrations [^{3}CBBP*]$_{lw}$ and [$^1O_2$]$_{lw}$ can be modelled by considering the kinetics of reactions Eq. S1-Eq. S4 and by assuming the steady-state approximation.

$$[^3CBBP^*]_{lw} = \frac{R^{lw}_{f,^3CBBP^*}}{k'_{d,^3CBBP^*} + k^{lw}_{BPA+^3CBBP^*}[BPA]_{lw}} \cong \frac{R^{lw}_{f,^3CBBP^*}}{k'_{d,^3CBBP^*}} \qquad \text{(Eq. S5)}$$

$$[^1O_2]_{lw} = \frac{R^{lw}_{f,^1O_2}}{k'_{d,^1O_2} + k^{lw}_{BPA+^1O_2}[BPA]_{lw}} \cong \frac{0.3 R^{lw}_{f,^3CBBP^*}}{k'_{d,^1O_2}} \qquad \text{(Eq. S6)}$$

In Eq. S5, is the photoproduction rate of ^{3}CBBP* upon reaction R S1, = 6·10^5 s^{-1} is the first-order deactivation rate constant of ^{3}CBBP* in aerated solution (R S2 + R S3) [182]. Note that when [BPA]$_{lw}$ is of some μM, as in our case. In Eq. S6, is the formation rate of singlet oxygen, that can be calculated as = 0.3 under the steady-state approximation. The factor 0.3 is the yield of $^1O_2$ formation upon deactivation of ^{3}CBBP* through reactions R S2 + R S3 in liquid water [107]. $k'_{d,^1O_2}$= 2.5·10^5 s^{-1} is the rate constant of deactivation of singlet oxygen by collisions with water molecules (R S4) and it is $k'_{d,^1O_2} >> k^{lw}_{BPA+^1O_2}[BPA]_{lw}$ when [BPA]$_{lw}$ is of some μM, as in our case.

By introducing Eq. S5 and Eq. S6 into Eq. S4, one gets:

$$\frac{k'_{snow,^3CBBP^*}}{k'_{snow,^1O_2}} = \frac{k^{lw}_{BPA+^3CBBP^*}}{0.3 k^{lw}_{BPA+^1O_2}} \frac{k'_{d,^1O_2}}{k'_{d,^3CBBP^*}} \frac{F_{^1O_2}}{F_{^3CBBP^*}} \cong 2 \cdot 10^4 \frac{F_{^3CBBP^*}}{F_{^1O_2}} \qquad \text{(Eq. S7)}$$

The values of and F_{1O2} in snow are not known. However, F_{1O2} has been found to span over three order of magnitude in ice (between 60 and 10^4; [141, 149]), while $F_{3Sens^*} = 10^2$ has been observed for the triplet state of 3,4-dimethoxybenzaldehyde [204]. These values show that the ratio $()^{-1}$ can range between 10^{-2} and 1.7 in ice. If applied to artificial snow containing CBBP (Eq.S7), this variation range suggests that ^{3}CBBP* may be the key reactive species that causes BPA photodegradation in our experiments. Even in the case of = 1 (no enhancement of ^{3}CBBP* reactivity in snow compared to liquid water) and = 10^4 (huge enhancement of $^1O_2$ reactivity in snow compared to liquid water), the role of ^{3}CBBP* in BPA photodegradation would be still significant (*i.e.*, $k'_{snow,^3CBBP} = 2k'_{snow,^1O_2}$)

Figures

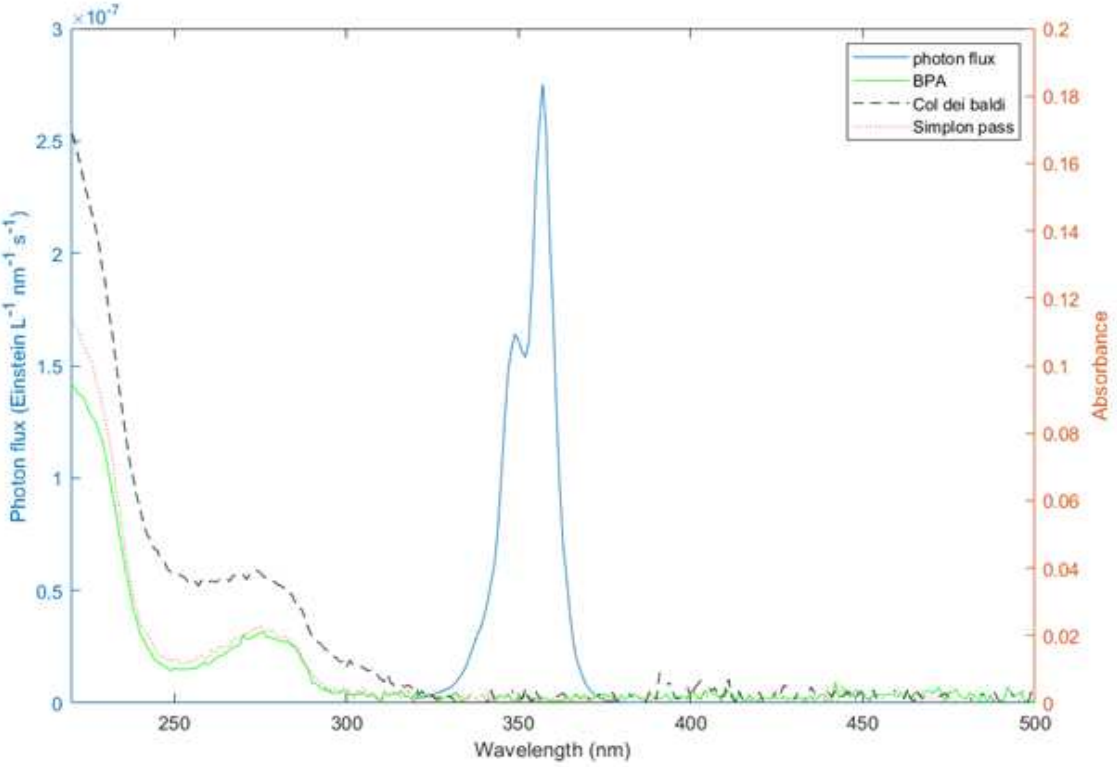

Figure S1 Absorption spectra of real samples fortified with 4.5 /*mu*M BPA (right y-axis) and photon flux of the UVA LED lamp (blue solid line; left y-axis).

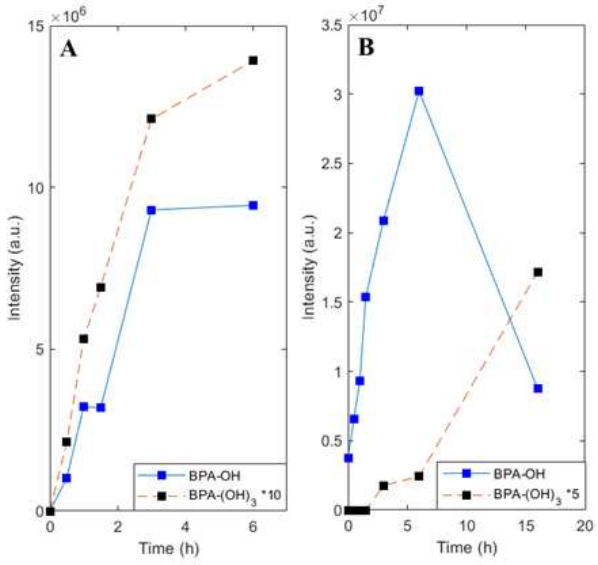

Figure S2 Production of BPA-OH (solid blue line) and BPA-$(OH)_3$ (dashed black line) in the presence of NO_2– (**A**) and CBBP (**B**). BPA-$(OH)_3$ intensities have been multiplied by **5** and **10** for better readability.

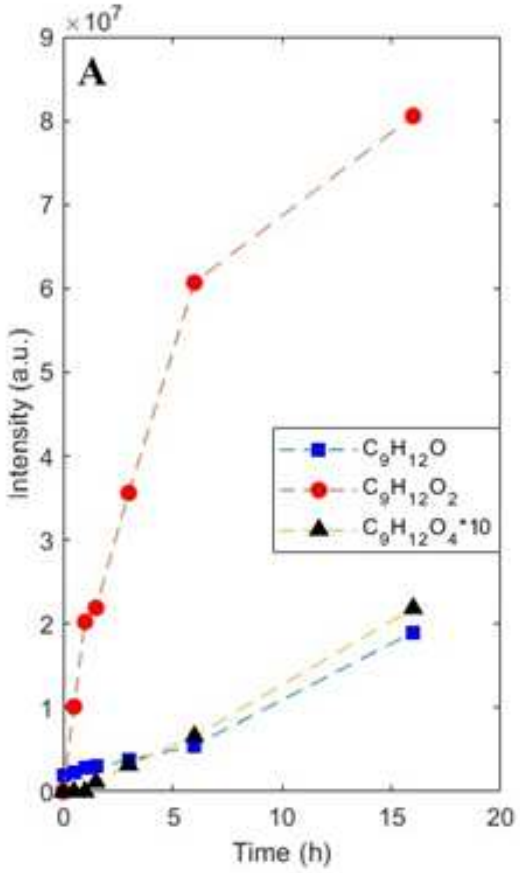

Figure S3 Production of compounds **6** (blue), **7** (red) and **8** (black) during BPA photodegradation in the presence of CBBP.

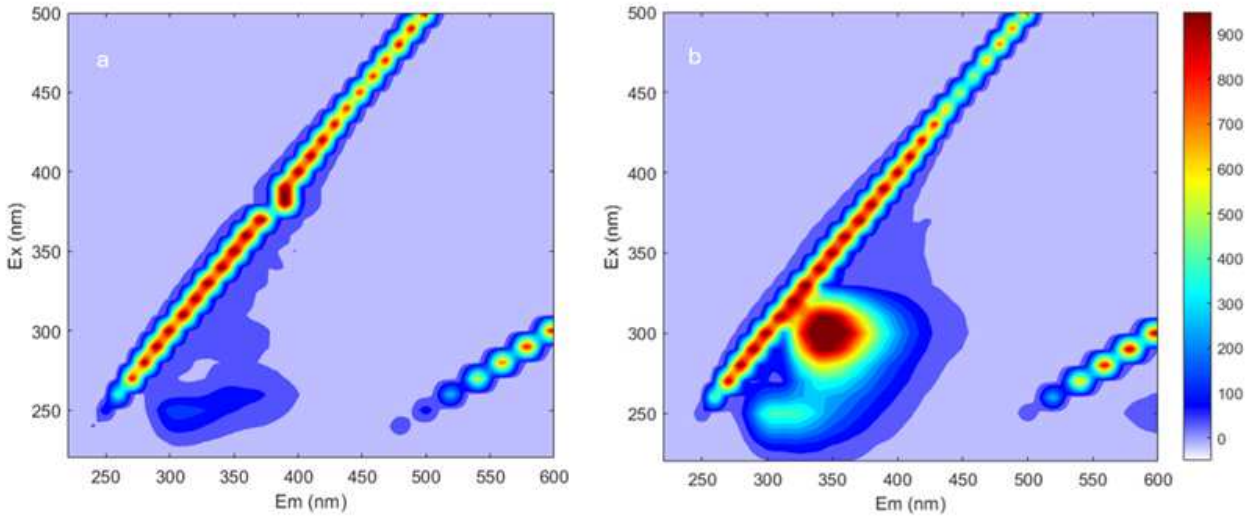

Figure S4 Three-dimensional fluorescence excitation–emission matrices (as contour plots) of Simplon Pass (**a**) and Col dei Baldi (**b**).

Table

Table 3.5: Acute toxicity parameters (mg/L) of BPA and its photodegradation products towards aquatic organisms predicted by using ECOSAR. [a] values above water solubility.

Compound	Molecular formula	Fish (LC 50, 96h)	Daphnid (LC 50, 48h)	Green algae (EC 50, 96h)
BPA	$C_{15}H_{16}O_2$	6.27	4.15	5.78
1	$C_{15}H_{16}O_3$	18.1	11.5	13.3
2	$C_{15}H_{14}O_5$	62.4	37.6	35.5
3	$C_{15}H_{14}O_3$	13.3	8.5	10.4
4	$C_{15}H_{14}O_5$	45.8	27.9	27.9
5	$C_{30}H_{30}O_4$	0.02 [a]	0.02[a]	0.19[a]
6	$C_9H_{12}O$	15.1	9.37	10.1
7	$C_9H_{12}O_2$	45.5	27.0	24.3
8	$C_9H_{12}O_4$	56.8	33.5	29.4
9	$C_5H_{10}O_3$	35476	17153	6575
10	$C_{15}H_{15}O_4N$	3.32	2.27	3.69
11	$C_{15}H_{14}O_6N_2$	1.7	1.21	2.29 [a]
12	$C_6H_5O_3N$	138	77	56
13	$C_6H_4O_5N_2$	267	148	99

Mass spectra of BPA photodegradation products

The following images show the chromatograms obtained by extracting the m/z of the compounds identified with a mass tolerance of 10 ppm.

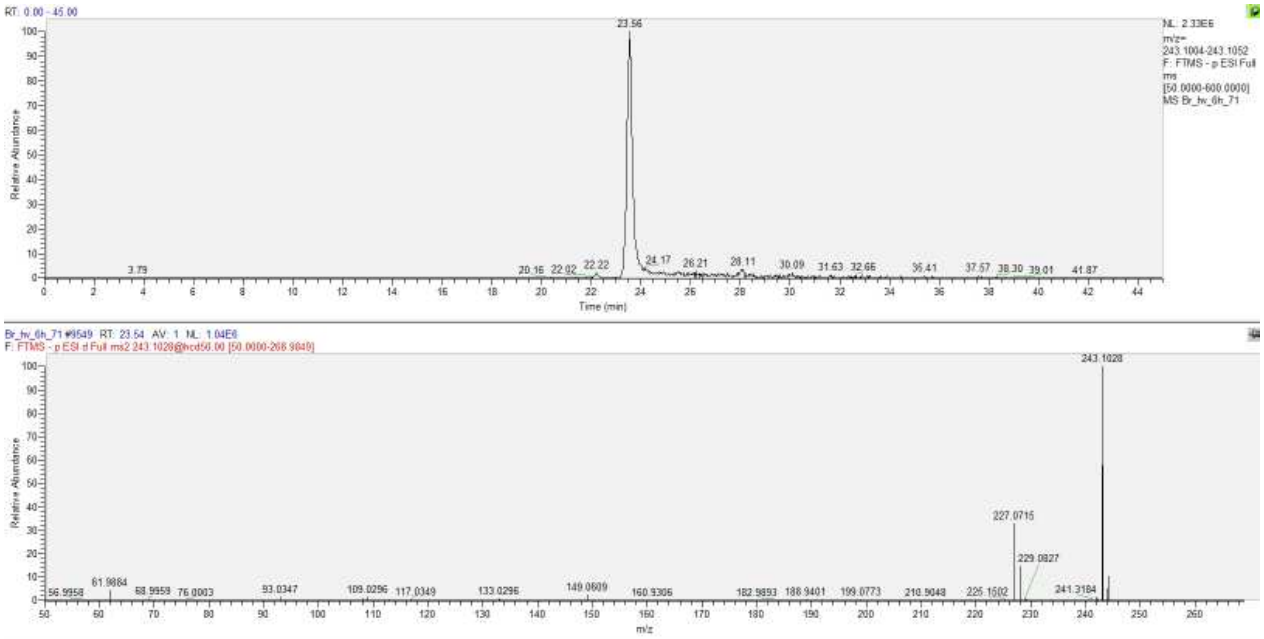

Chromatogram 1 and MS/MS of compound BPA-OH

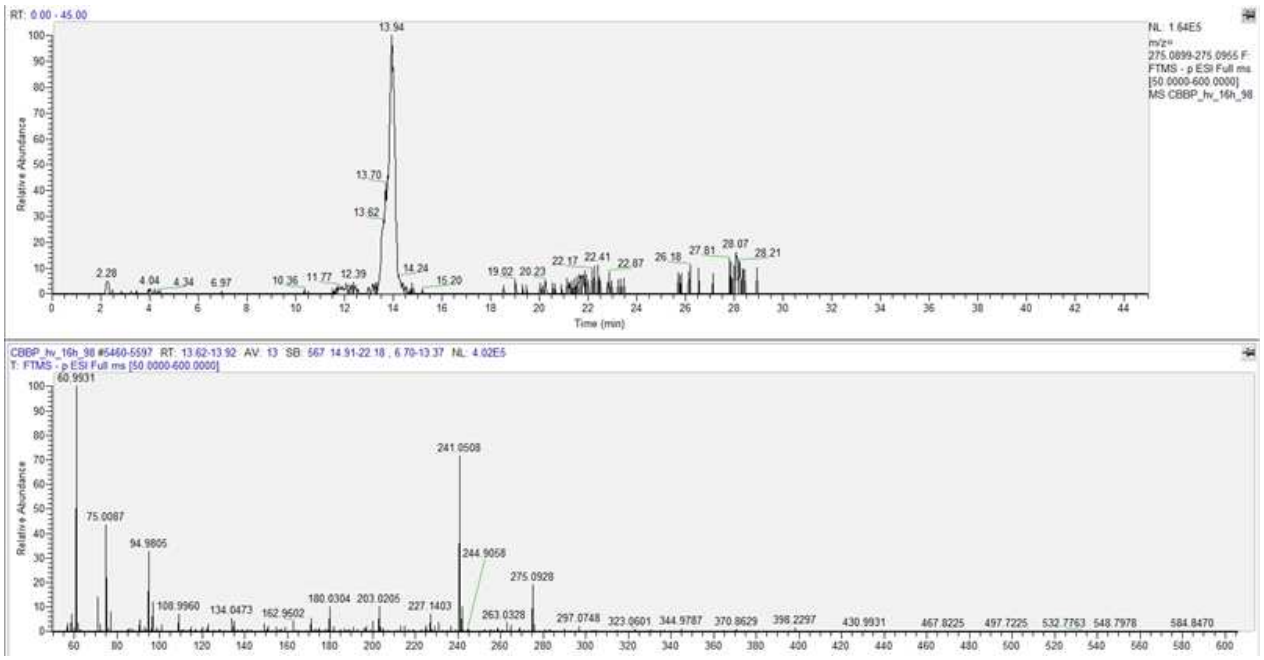

Chromatogram 2 and MS/MS of compound BPA-$(OH)_3$

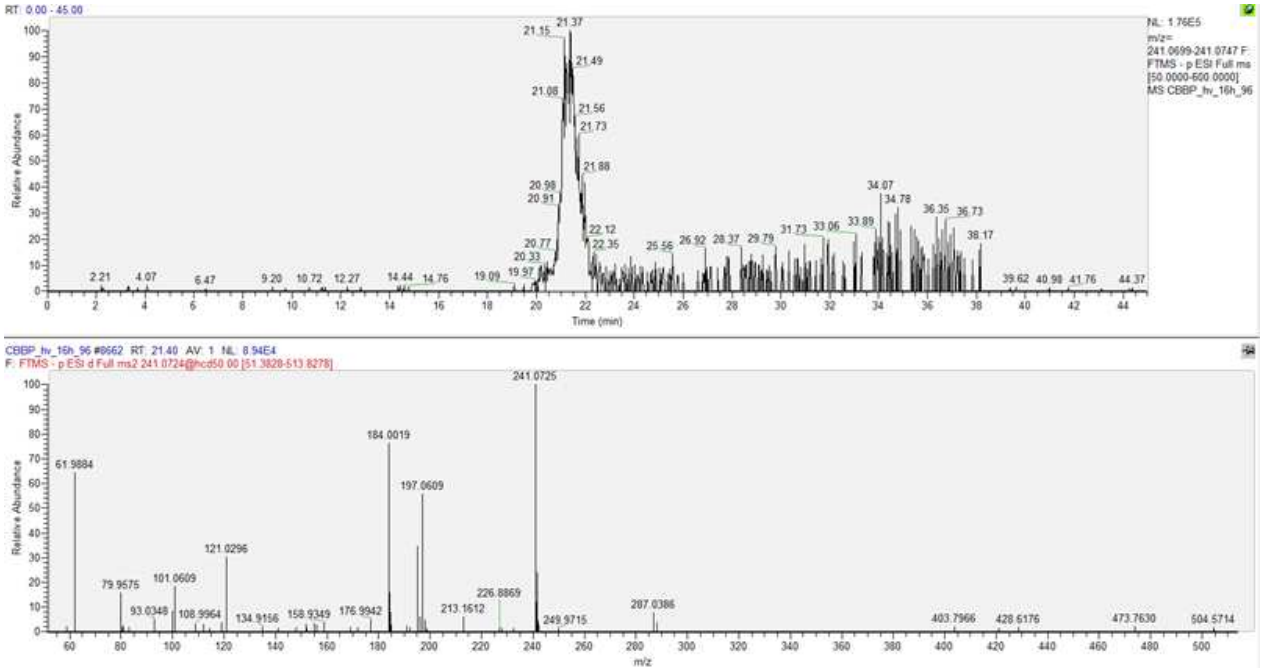

Chromatogram 3 and MS/MS of compound 3

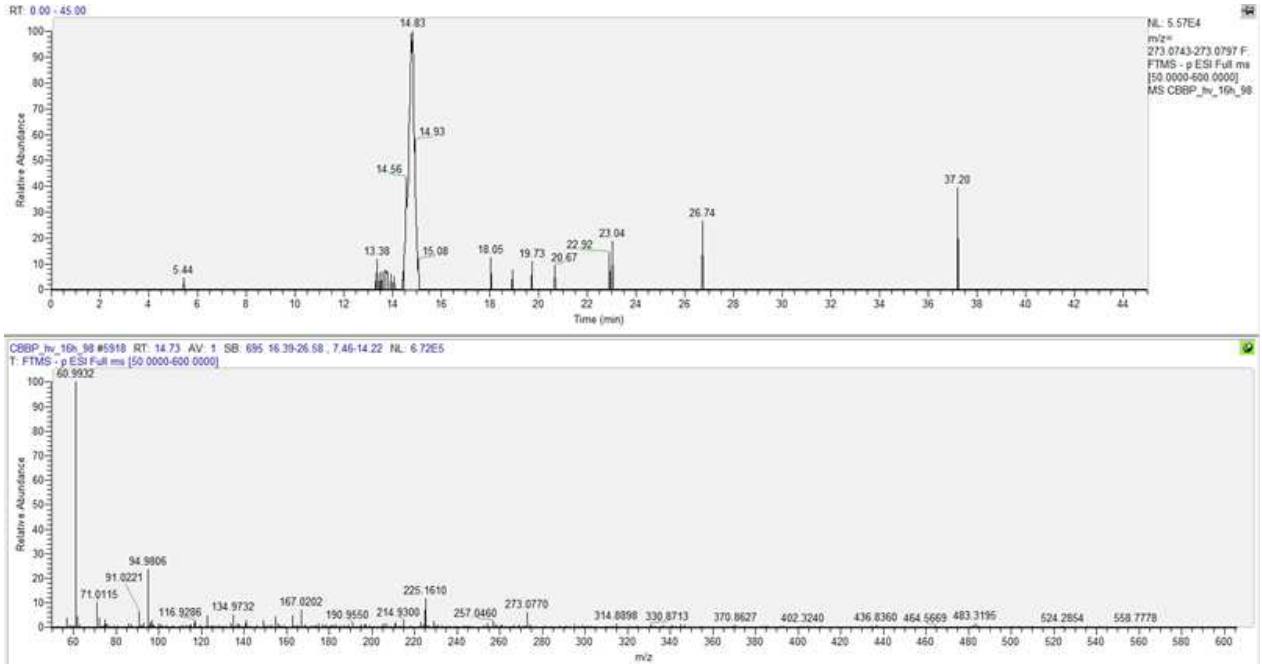

Chromatogram 4 and MS/MS of compound 4

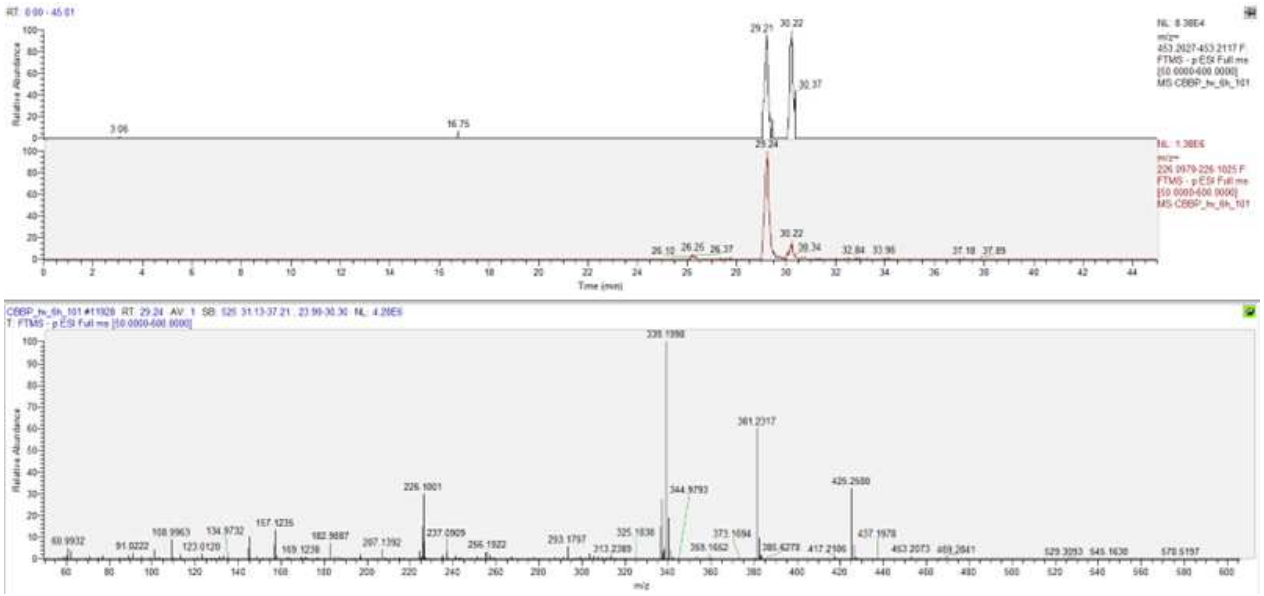

Chromatogram 5 and MS/MS of compound 5

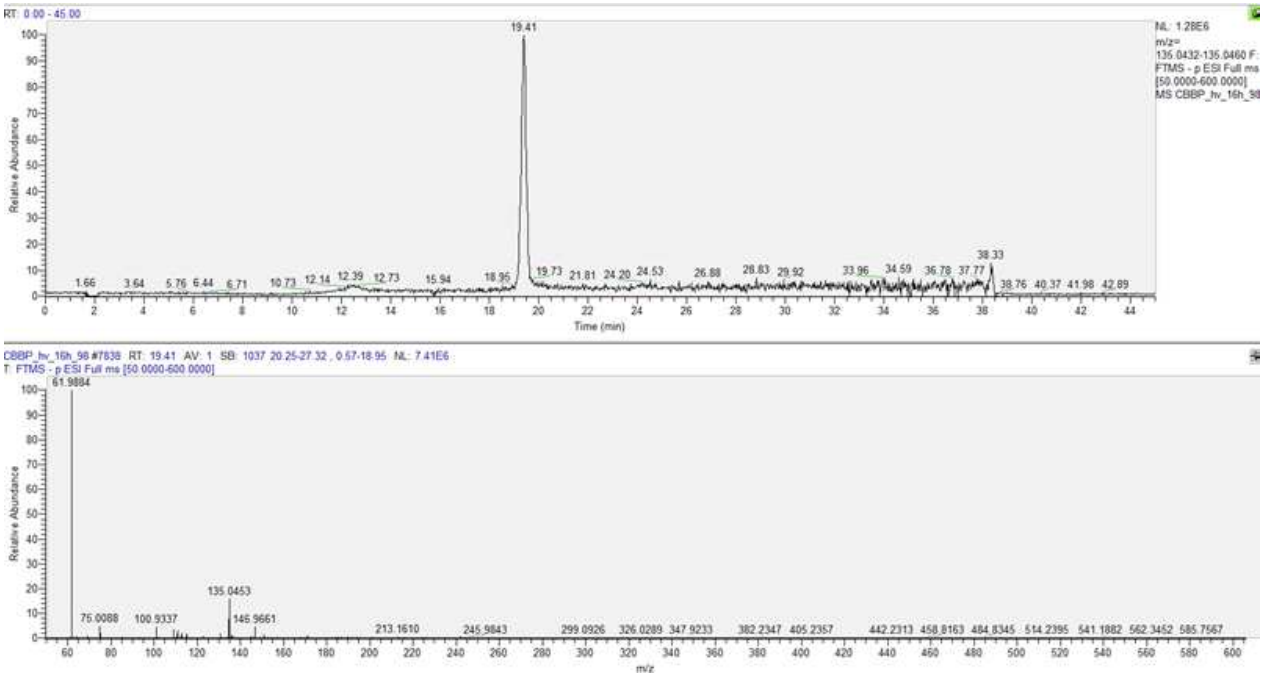

Chromatogram 6 and MS/MS of compound 6

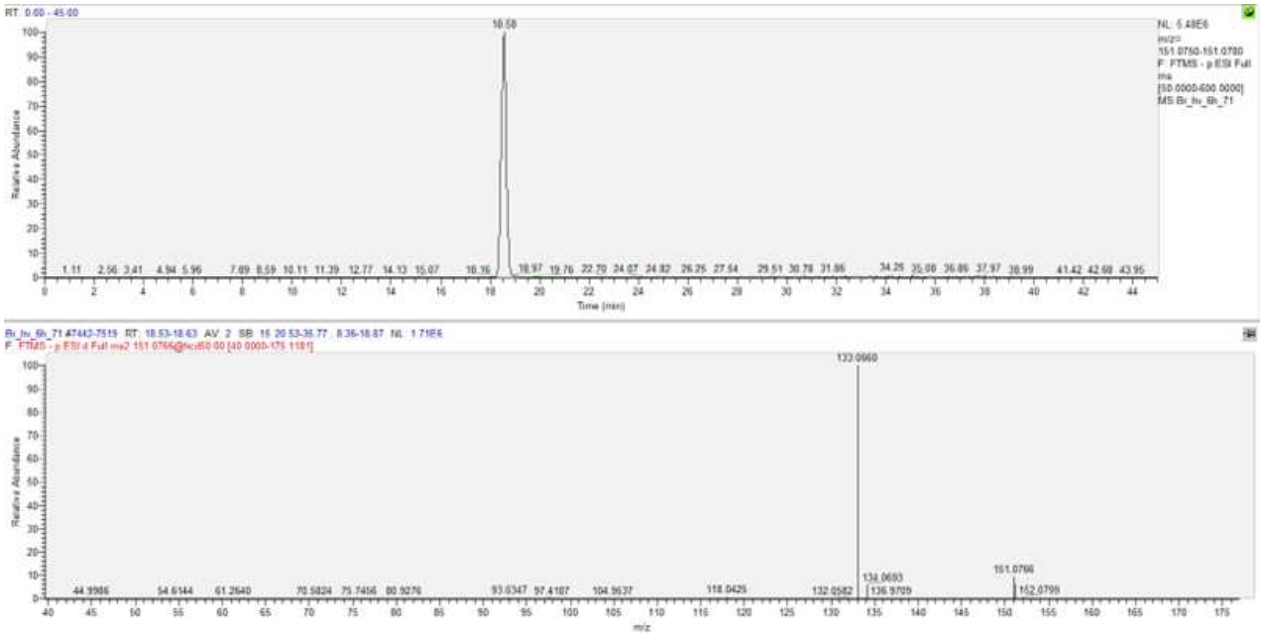

Chromatogram 7 and MS/MS of compound 7

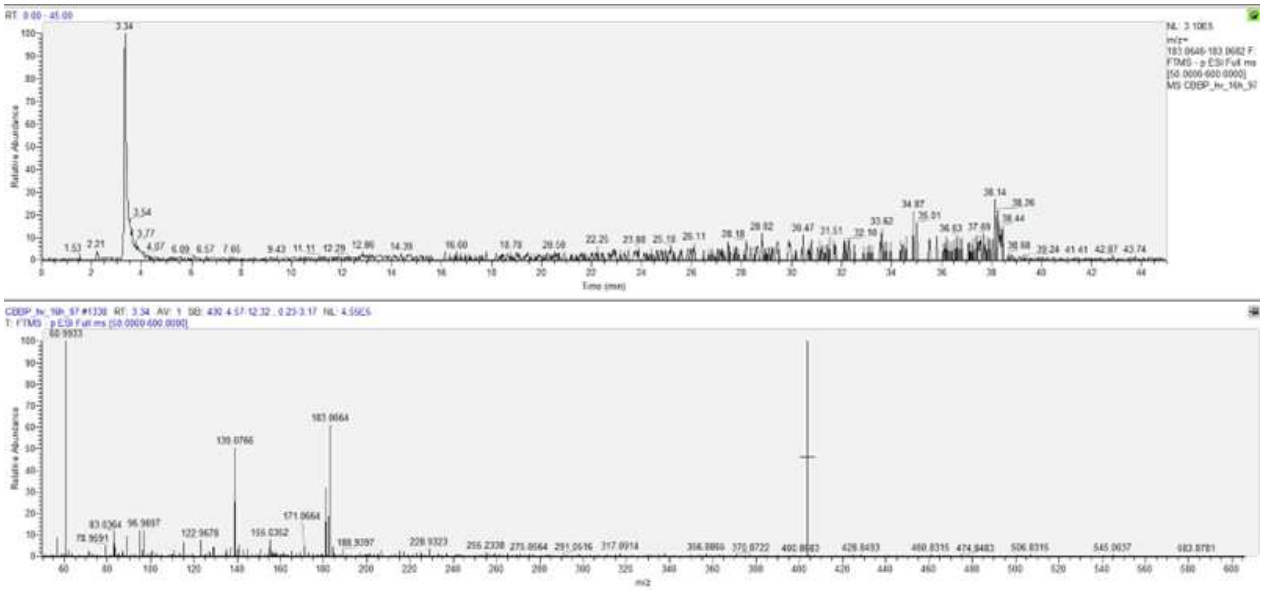

Chromatogram 8 and MS/MS of compound 8

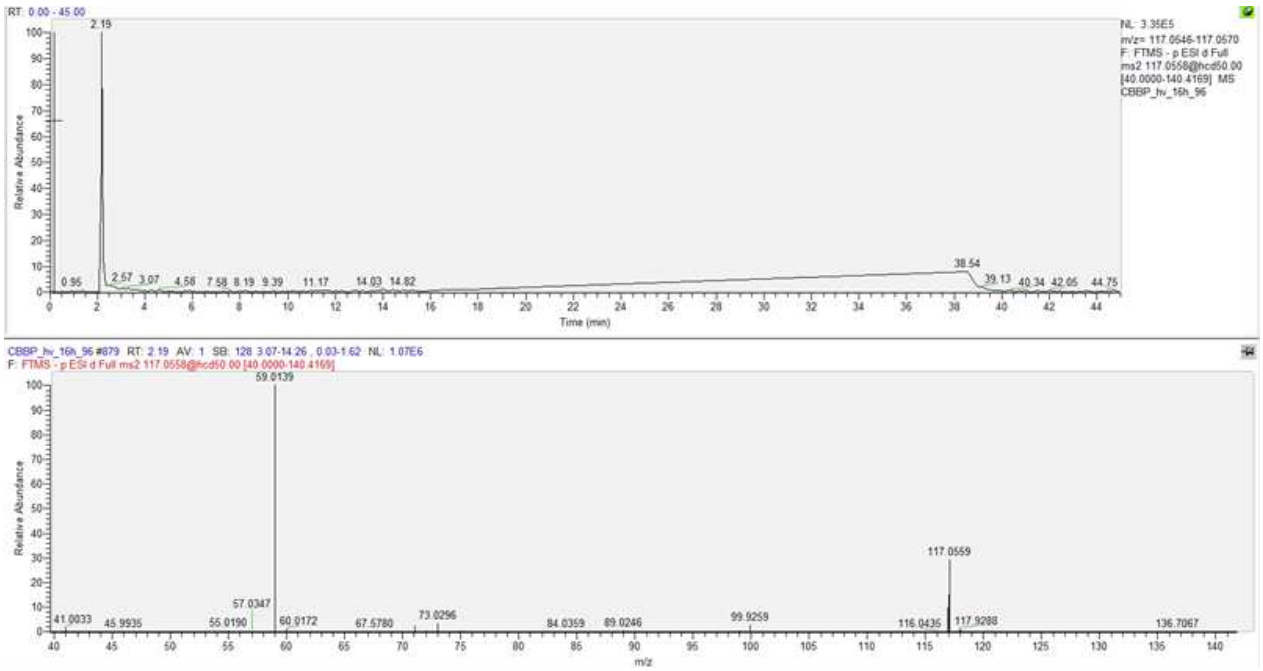

Chromatogram 9 and MS/MS of compound 9

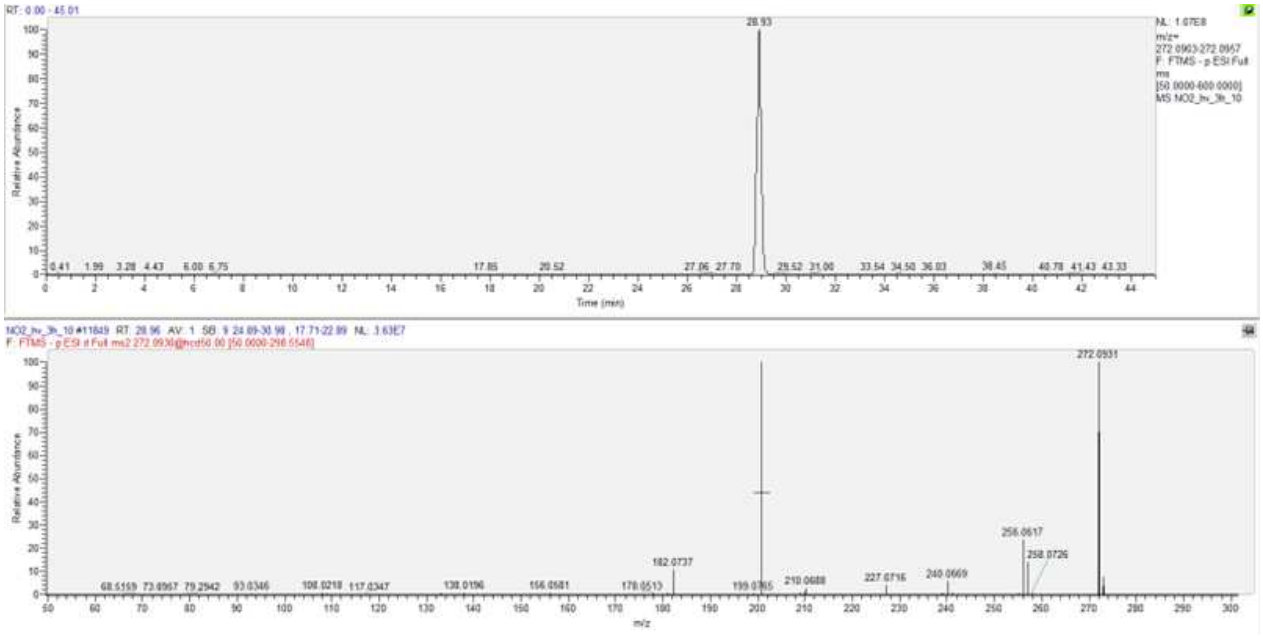

Chromatogram 10 and MS/MS of BPA-NO_2

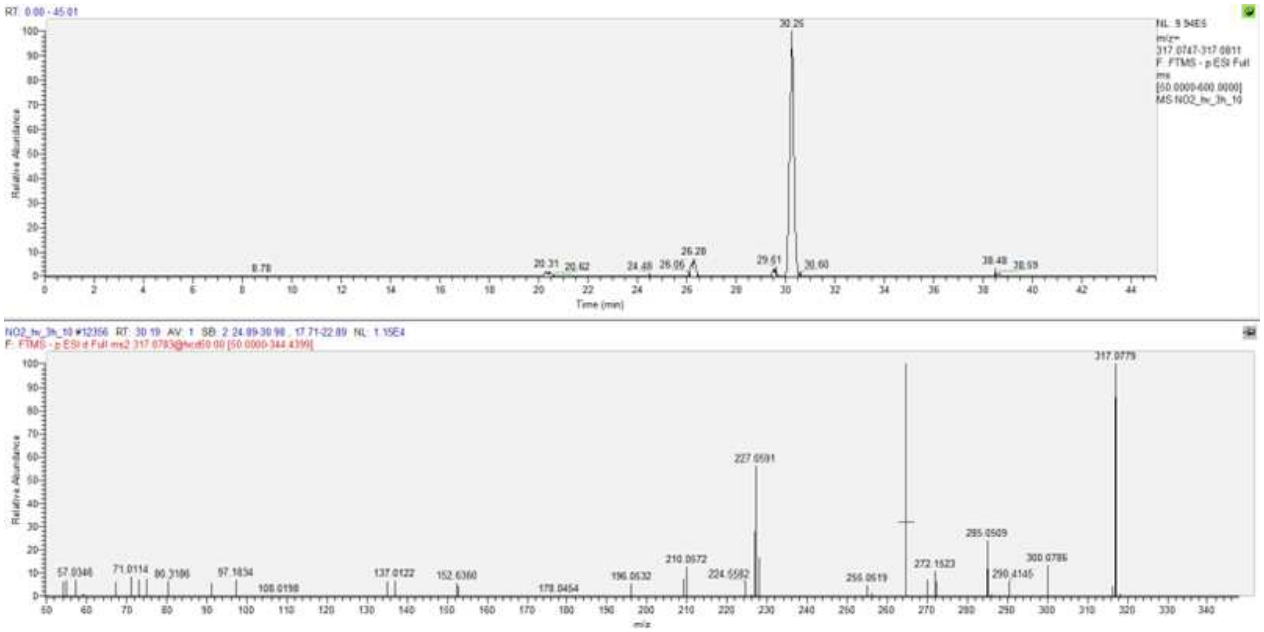

Chromatogram 11 and MS/MS of BPA-$(NO_2)_2$

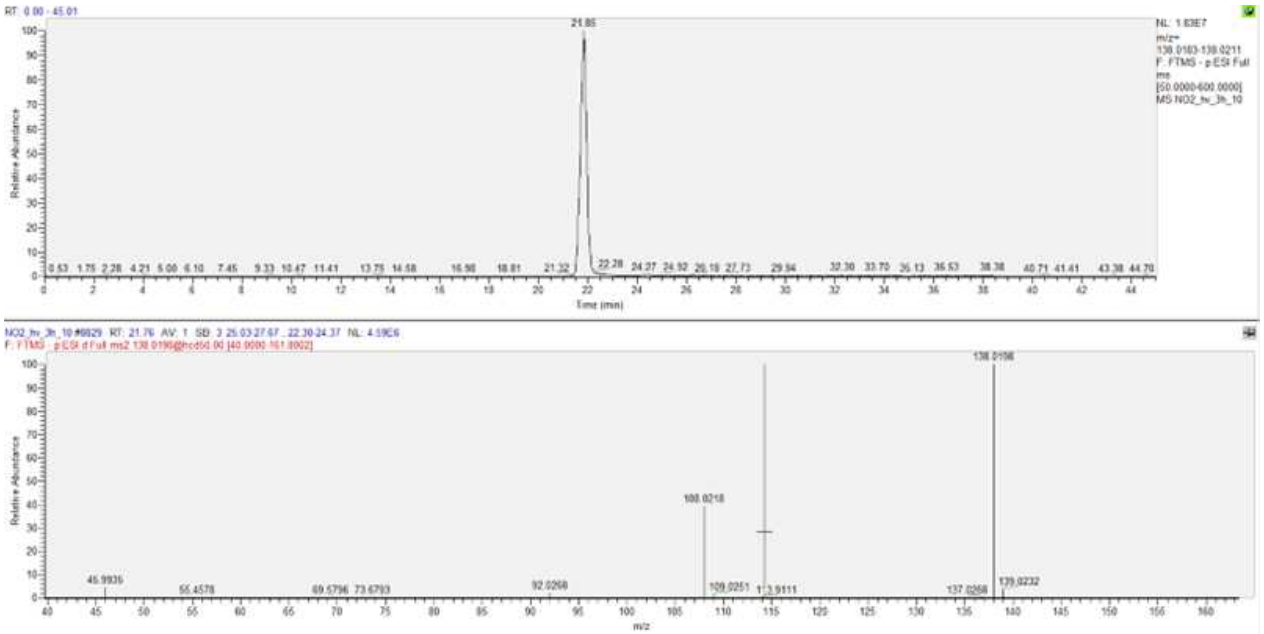

Chromatogram 12 and MS/MS of nitrophenol

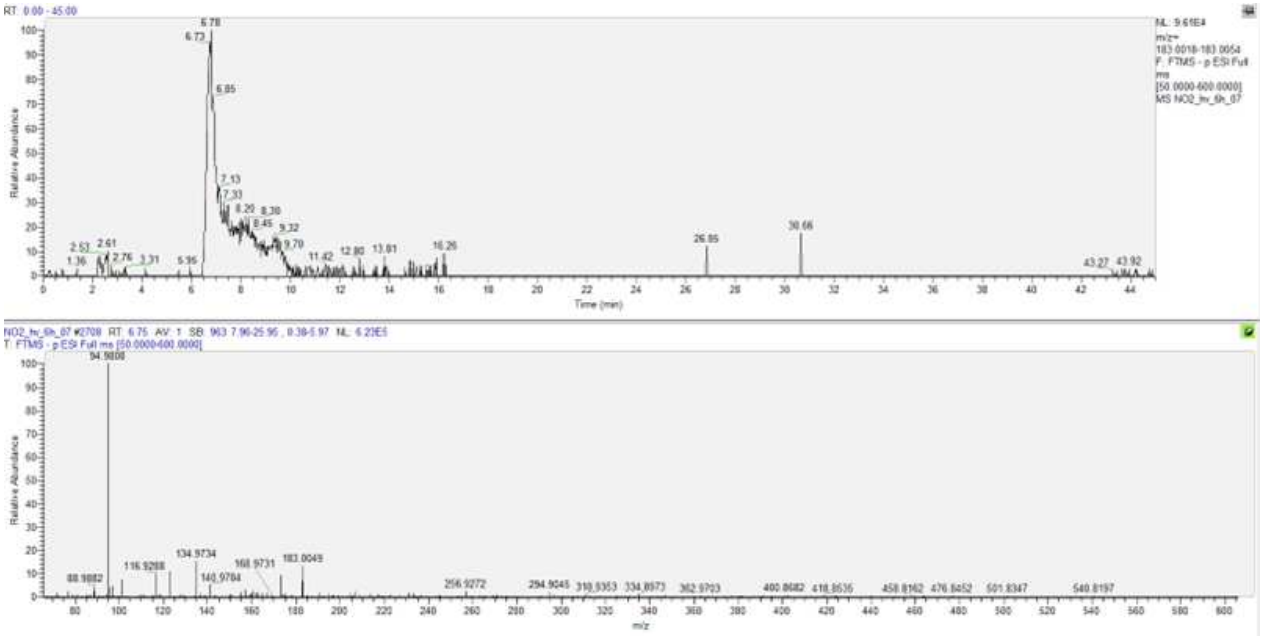

Chromatogram 13 and MS/MS ofdinitrophenol

3.3 Photodegradation of bisphenol A in sea ice

This work was carried out in collaboration with the Research Group headed by Prof. Jan Kaiser at the University of East Anglia (UK) and with the support of the Roland von Glasow Air-Sea-Ice Chamber (RvG-ASIC) experimental infrastructure. For the first time, RvG-ASIC was used to conduct photochemical studies using UV light. A significant part of the work involved optically characterisation of the experimental chamber. Specifically, the two-dimensional spatial distribution of UV radiation on the surface of the tank was measured using optical fibers, as well as its penetration depth into the simulated sea ice. The intensity of the radiation at a given depth was also monitored over time during the experiment, suggesting a possible effect of ice aging. From a chemical perspective, the chamber was divided into two sections: two-thirds were directly exposed to UV light, while the remaining third was shielded to prevent direct irradiation and simulate dark chemistry reactions. The results indicate that, in this specific experimental setting, reactions in the dark can be predominant over photo-induced reactions. This behaviour is in stark contrast to what is observed in liquid seawater conditions, where photochemical reactions tend to dominate. The observed differences can be attributed to significant variations in pH and ionic strength within the frozen system, which may favour acid-base reactions that are not observable in a liquid aqueous environment.

Chemistry of Bisphenol A in artificial sea ice

Stefano Frassati[a,b], Victoria Dutch[c], Jan Kaiser[c], Andrei Munteanu[a,b], Elena Barbaro[b,a], Marco Roman[a,b], Elisa Scalabrin[b,a], Carlo Barbante[a,b], Andrea Gambaro[a,b], Andrea Spolaor[b,a].

[a] Ca' Foscari University of Venice, Department of Environmental Sciences, Informatics and Statistics, Venice Mestre, Italy.

[b] Institute of Polar Sciences – National Research Council (CNR-ISP), Venice Mestre, Italy.

[c] Centre for Ocean and Atmospheric Sciences, School of Environmental Sciences, University of East Anglia, Norwich NR4 7TJ, United Kingdom

Corresponding author: Stefano Frassati
Corresponding author's email: Stefano.frassati@unive.it,

Keyword: contaminants; photochemistry, dark chemistry, BPA, Sea ice

Abstract

Bisphenol A (BPA) is a toxic organic micropollutant widely used as a monomer in the production of plastics. Its presence has been widely documented in various environmental matrices, including seawater. However, to the best of our knowledge, no studies have been conducted to identify the presence and behaviour of BPA in sea ice. Considering that sea ice forms from saline water but has profoundly different chemical and physical properties compared to the liquid phase, in particular due to the exclusion of salts and organic compounds from the crystal lattice and the consequent formation of briny veins with high ionic strength and altered pH, it is plausible to hypothesise a different chemical reactivity for this matrix.

Herein, we investigat the distribution of BPA within simulated sea ice and studied its possible (photo)chemical transformations during a 9-day experiment. The results show that there are no significant differences in BPA degradation between samples irradiated with UV light and those kept in the dark. This suggests that, in the specific case of sea ice, parameters such as pH and ionic strength may play a predominant role in BPA degradation processes compared to light irradiation alone.

Introduction

Bisphenols (BPs) are synthetic organic compounds that possess two phenolic hydroxyl groups [127]. Of these, the most common is 2,2-bis(4-hydroxyphenyl)propane, which is known commercially as bisphenol A (BPA) [128]. BPA has considerable economic value, with global production exceeding 7.7 million tonnes in 2015, accompanied by an annual growth rate of 4.8 % between 2016 and 20223. Production increased exponentially from 2.8 million tonnes in 2002 to over 8 million tonnes in 2024 [205]. Although bisphenol A (BPA) was first synthesised in 1890, its extensive use only commenced in the 1950s, when it was adopted as a raw material for the production of polycarbonate plastics and epoxy resins. These materials were widely used in food contact materials, thermal paper and numerous other synthetic products[116, 128, 206]. BPA has been identified as an emerging contaminant due to its chronic toxicity, which has been linked to an increased risk of obesity, cancer, and severe hormonal disorders. The extensive documentation of adverse effects demonstrates the detrimental impact of BPA on human health and ecosystems. Its capacity to act as an endocrine disruptor renders it particularly hazardous, affecting vital biological processes [114, 206–208]. Nevertheless, its utilisation remains only partially regulated, with a considerable release into the environment. The increasing production has resulted in a considerable environmental impact, with more than 2000 tonnes of BPA being released into the environment annually [209]. This figure does not account for the contribution from the chemical and physical degradation of nano-, micro- and macro-plastics [210].

BPA has been identified in a multitude of environmental matrices, spanning urban and remote areas. In urban settings, BPA has been detected in rivers and lakes at concentrations of $5.8\text{x}10^{-2}$ μg L^{-1} and 50 ng L^{-1} (Aja River in Japan [211], and Laguna lake in the Philippines [212]), as well as in the atmosphere in a range between 1–17.400 pg m^{-3} [130]. Nevertheless, traces of BPA have also been identified in remote environments, including Antarctic aerosols [130] and Arctic snow [125]. Furthermore, BPA has been detected in marine environments, with concentrations reaching tens of μg L^{-1} in seawater [205, 213, 214]. As evidenced by numerous studies, the concentration of BPA in seawater can be affected by both dilution effects [205] and degradation processes [215–221]. Among the latter, a significant role is played by photo-oxidative processes, which have already been extensively investigated in the literatur [172, 177, 222]. These processes contribute to the transformation and reduction of BPA in the marine environment, thereby underscoring the intricate dynamics that govern its persistence.

The considerable quantities of BPA identified in sea water provide compelling evidence that it is also present in sea ice. This hypothesis is corroborated by a study that identified traces of BPA in Antarctic sea ice in the vicinity of McMurdo Station. The results demonstrated comparable concentrations of BPA in both sea ice and seawater obtained via borehole sampling, thereby substantiating the contaminant's capacity to integrate into polar ice systems [223] As might be expected, the concentrations of BPA in sea and sea ice are comparable. The distribution of organic compounds, including PFAS [224] and other persistent organic pollutants [225] (POPs), has been observed to follow a 'C' profile in studies conducted at the Roland von Glasow Air-Sea-Ice Chamber [54] (RvG-ASIC) at the University of East Anglia, UK. In this model, concentrations at the surface and at the ice-sea interface are comparable to those observed in seawater. However, in the central region of the ice, there is a notable decline in the concentration of pollutants and other natural species, which is contingent upon the specific characteristics of the compound in question.

In this study, the behaviour of BPA in artificial sea ice was analysed through the simulation of first-year sea ice (FYSI). The distribution of BPA within the ice and the (photo)chemical processes that could occur over the course of nine days were examined.

Materials and methods

Chemicals

In this study, a concentration of 10 ppb of bisphenol A (BPA) dissolved in artificial seawater was used. During the HPLC-Orbitrap analysis, bisphenol A-$^{13}C_{12}$ was added as an internal standard. Both reagents were purchased from Sigma-Aldrich and had a purity greater than 99%. The study was carried out in the Roland von Glasow Air-Sea-Ice Chamber (RvG-ASIC) at the University of East Anglia, UK [54]. Once the tank was filled with ultrapure water, sea salt (produced by Tropical Marin) was added until a salinity of approximately 35 g L^{-1} was reached, corresponding to typical seawater conditions at 20°C. Ultrapure water (UPW, eluent A, 18.2 MΩ cm, TOC <10 ppb, Elga LabWater, UK) and methanol (eluent B, Sigma-Aldrich, gradient grade) were used for HPLC-HRMS analysis.

Sample preparation, irradiation experiments, analysis and sea ice optical characterization

Once a salinity of approximately 35 g L^{-1} was reached, the temperature of the room was lowered to -30 °C for one week, allowing the formation of sea ice with an initial thickness of 10 cm. This phase was conducted in total darkness. Once the desired thickness was reached, the temperature of the room was increased to -5 °C, allowing the UV lamps to provide more irradiance while maintaining suitable conditions for the stability of the ice. The tank was partially covered 1/3 of its surface in order to obtain control samples not directly exposed to UV light. Ice samples were taken once a day using a titanium corer (Kovacs, 75 mm I.D.) [54], with the exception of the first day, when two samples were collected three hours apart. At each sampling interval, three irradiated ice cores were taken and three kept in the dark, thus ensuring a representative sampling of the pool. Finally, samples were cut at 3 cm intervals, melted in the dark at room temperature and analysed. During the experiment, sea water was sampled at different stages: before sea ice formation, during irradiation and at the end of this phase, as well as during melting until the ice had completely melted. Sampling was carried out using pre-washed and decontaminated glass bottles.

BPA and its photoproducts were identified by ultra- UHPLC (Vanquish, Thermo Fisher Scientific) coupled to a quadrupole-orbitrap high-resolution mass spectrometer (HRMS) Exploris 120 (Thermo Fisher Scientific) using a Synergi Hydro-RP 80 A column (50 mm×4.6 mm, 4 μm particle size). The chromatographic procedure adopted follows that described in the work of Frassati et al 2025 [226], with the difference that the first 5 minutes of analysis were excluded due to the high salinity of the matrix, which interfered with the quality of the data obtained.

In order to assess photoinduced reactions along the density profile of the sea ice, it was necessary to quantify the radiation penetrating the ice. For this purpose, four optical fibres (ocean optics spectrometer (USB 2000+), integration time 3 sec, average scan 3) were placed in the illuminated part of the tank, distributed in the first 15 cm depth, as well as an additional fibre at the surface (see figure Sx).

Results and discussion

Sea ice physical characterization

Sea ice thickness

The first physical parameter monitored was the thickness of the sea ice and its variation over time. As shown in the Figure 3.15, one third of the tank was covered with a metal foil placed approximately 20 cm from the ice surface (shaded area in the Figure 3.15) in order to obtain a control sample not directly exposed to solar radiation. In this way, it was possible to minimise light-induced photochemical reactions. It can be seen from the figure that the uncovered samples tended to grow more than the covered ones over the nine-day experiment. In particular, the initial ice thickness was similar in both areas of the tank, with values of around 12 cm at time zero. However, at the end of the experiment, the thickness in the covered area remained almost unchanged (12.7 $\pm$ 1.5 cm), while in the uncovered area it increased to 14.5 $\pm$ 1.4 cm, showing an average increase of about 2 cm. This difference can be explained by considering that partially covering the tank, even with a non-insulating material, reduced the heat transfer between the surface of the already formed ice and the environment of the cold chamber. This reduction in heat transfer results in less efficient cooling in the covered area, thus slowing down the ice growth process compared to the uncovered part, where heat exchange with the environment is more direct and efficient.

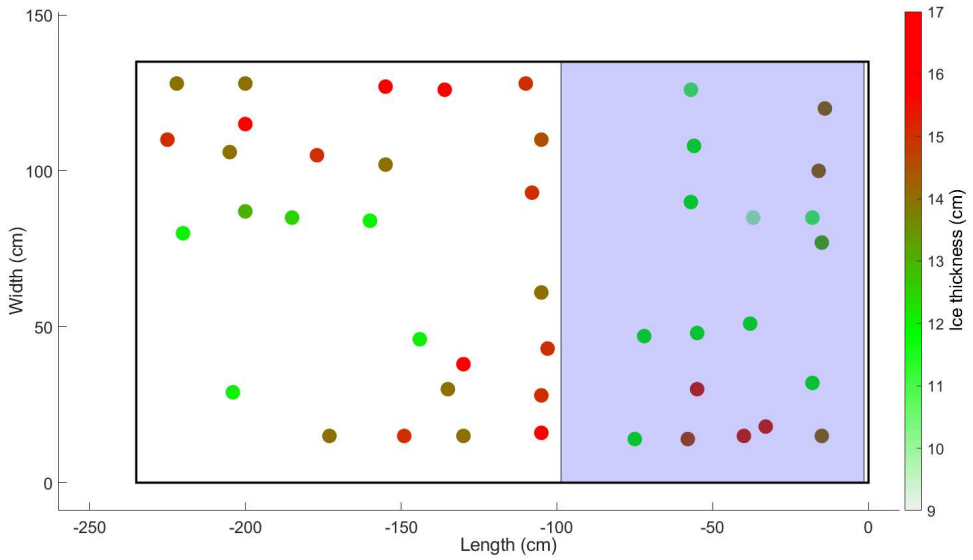

Figure 3.15: Distribution of sea ice thickness during the 9-day experiment. The shaded part represents the part of the tank covered to reduce the effect of the radiation

Sea ice optical properties

Optical fibres were placed inside the tank with the aim of monitoring the variation of radiation as a function of depth during the entire experimental period. Specifically, the fibres were inserted into the sea

ice at depths of 5, 10 and 15 cm, while a control fibre was placed 5 cm above the ice surface. The latter made it possible to monitor any changes in the spectrum and intensity of incident radiation unaffected by ice absorption and scattering.

Each day, prior to ice sampling, a measurement of the radiation penetrating the sea ice was carried out, focusing on the maximum absorption in the UVA region at 360 nm. For this purpose, the ratio between the intensity of the radiation measured at the surface and that measured inside the ice was calculated. This approach made it possible to assess whether, during the irradiation period, the radiation penetrated the ice constantly or whether there were variations over time.

At t0, the measured radiation was almost constant on all three fibres positioned at different depths in the ice. However, as shown in Figure 3.16 (where, by way of example, the trend at a depth of 10 cm is shown), it can be observed that on the first three days there is no significant difference between the radiation measured inside the ice and that measured at the surface. From the fourth day onwards, however, there is a gradual reduction in the intensity of the radiation in the ice, a phenomenon that also manifests itself in a similar manner at the other depths monitored.

This attenuation was accompanied by a progressive whitening of the surface of the sea ice, which can be attributed to an ageing phenomenon specific to the experimental conditions in the chamber used. This effect is particularly relevant, as the decrease in photon influx in deeper areas can significantly influence the study of photochemical processes, slowing down the reaction kinetics of the compounds of interest.

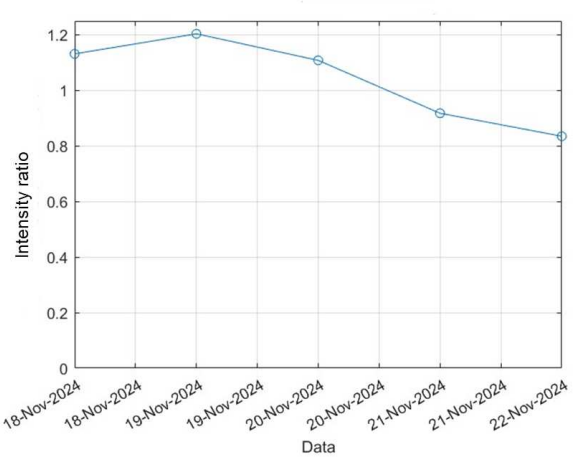

Figure 3.16: Variation in intensity ratio at 350 nm above sea ice and at 10 cm depth

Finally, the homogeneity of the radiation within the tank was assessed. As shown in Figure 3.17, although the covered part of the tank has areas with a higher UV radiation intensity, the area in which the study was conducted corresponds to the area to the left of the tank. This choice was made in order to ensure an almost uniform irradiation of the samples exposed to light.

Compared with what was observed for visible light, the results show significant differences [54]. In fact, while for visible light there is a maximum intensity in the centre of the pool with a gradual decrease towards the edges, in the case of UV light there are marked differences between the various points of the pool, except for the area selected for irradiation, where the intensity is more uniform.

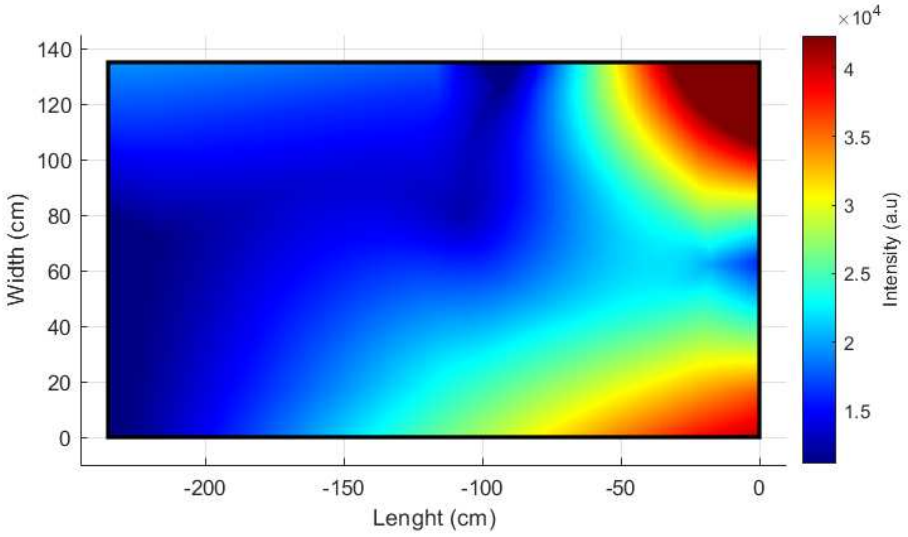

Figure 3.17: UV light dispersion on the surface of the tank

Sea ice chemical characterization

Vertical distribution

The first aspect considered was the distribution of BPA within the sea ice. Previous studies have analysed the distribution of other pollutants, such as PFAS [225], PAHs [227] and the like, in sea ice. In all these cases, a typical C-shaped distribution was observed, characterised by higher concentrations both at the surface and at the ice-water interface, while concentrations were lower in the central part of the ice. A similar behaviour was also observed for BPA, where the concentrations at the surface and at the ice-sea interface are comparable to those of seawater, while in the bulk the concentration is about half (Figure 3.18). Moreover, this behaviour is also typical of the major ions commonly found in sea ice, whose distribution follows similar C-shaped profiles. As far as the non-irradiated samples are concerned, no diffusion from higher to lower concentration areas was observed. Therefore, as will be discussed in the following section, the hypothesis of species diffusion towards the centre of the ice is rejected, as the C-shaped distribution remains constant throughout the experiment.

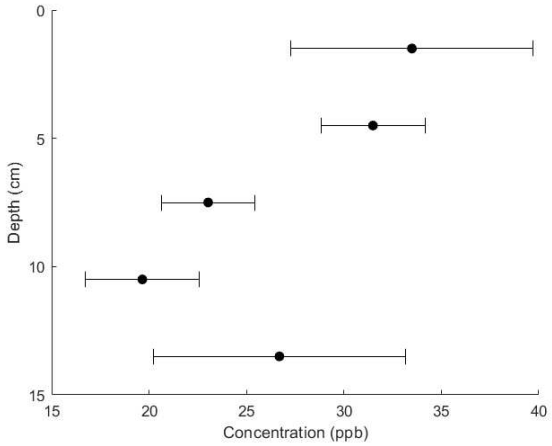

Figure 3.18: Measured chemical concentrations of BPA at different depths of sea ice

Degradation kinetic

Figure 3.19a shows the trend of BPA degradation as a function of time, at different depths within the sea ice under UV radiation, while Figure 3.19b shows the trend of C/C_0 in non-irradiated samples over time.

The data, particularly those relating to surface samples, show considerable scatter. This can be attributed to the importance of spatial variability, which plays a crucial role when working on a mesoscale scale. For this reason, three ice cores were taken at each irradiation time in order to ensure better representativeness and reliability of the results. The analysed samples from the various layers suggest a decrease in BPA concentration over time. This decrease is particularly marked in the superficial (0-3 cm) and deeper samples, while in the middle band (6-9 cm) the degradation appears almost absent. It is interesting to note that this behaviour is closely related to the BPA concentrations present at the respective depths. Similarly, similar behaviour is observed in samples kept in the dark. This suggests that the degradation processes observed are not exclusively attributable to photochemical phenomena, but that there are alternative mechanisms, such as spontaneous chemical reactions or physio-chemical micro-processes within the ice, that contribute to the reduction in BPA concentration over time. Consequently, it can be assumed that, at least in this specific system, photodegradation is not the main factor responsible for the disappearance of the contaminant.

It is well known that during the solidification process, impurities in the water are expelled from the ice's crystal lattice and concentrate in thin quasi-liquid interstitial layers. In these micro-phases, the concentrations of chemical species can be significantly higher than in pure liquid water; for example, increases of up to 10,000 times have been reported for singlet oxygen [149]. This phenomenon depends on several factors, including freezing temperature and initial solute concentration. Such conditions can promote chemical reactivity even in the absence of light, thus contributing to the transformation of contaminants trapped in the ice [35]. Besides concentrating organic species within the interstitial veins of the sea ice, the freezing process also leads to a significant increase in ionic concentration, resulting in marked changes in both ionic strength and pH. In particular, the ionic strength can increase up to 6-7 times that of seawater [228], while the pH tends to decrease, resulting in a more acidic environment, reaching pH below 6.5. This phenomenon can be attributed to the fact that some chemical species, which act as buffering agents in solution, may precipitate during solidification, breaking their buffering effect within the sea ice lattice [229].

Considering that the pKa_1 of BPA is 9.59, at pH values below 6.5 the compound is predominantly

found in a protonated (associated) form, a condition that tends to disfavour complexation processes with metals. However, the chemical environment that develops in brackish veins of sea ice, rich in ions and often characterised by acidic conditions, may on the contrary favour oxidation reactions by metal oxides such as MnO_2 or Fe^{3+}.

In the specific case of MnO_2, the redox reaction directly involves the proton:

$$\frac{1}{2}MnO_2 + 2\,H^+ + e^- \rightarrow \frac{1}{2}Mn^{2+} + H_2O \tag{R26}$$

This mechanism implies that the oxidative potential of the system increases as the pH decreases, from around 0.76 V at pH 8 to 0.99 V at pH 4. This increase in potential makes the acidic conditions of the interstitial veins of the ice particularly favourable for oxidative reactions, even against organic compounds such as BPA [230].

However, it is also possible for reactions known as Fenton reactions to occur in seawater, leading to the formation of reactive oxygen species, including the hydroxyl radical ($^{\bullet}OH$) and superoxide ($^{\bullet}O_2^-$). The main reactions involved are:

$$Fe^{2+} + H_2O_2 + H^+ \rightarrow Fe^{3+} + {}^{\bullet}OH + H_2O \tag{R27}$$

$$Fe^{3+} + H_2O_2 \rightarrow Fe^{2+} + {}^{\bullet}OOH + H_2O \tag{R28}$$

These reactions require the presence of hydrogen peroxide (H_2O_2) as a fundamental reactant [231–233]. While the presence of H_2O_2 is well documented in natural sea water [234], where it can be produced both photochemically and through biotic and abiotic processes, it cannot be stated with certainty that hydrogen peroxide is also formed in the controlled experimental system used in this study. In the absence of a defined source of H_2O_2, it is therefore difficult to assume a significant role for Fenton reactions in the system adopted in this study.

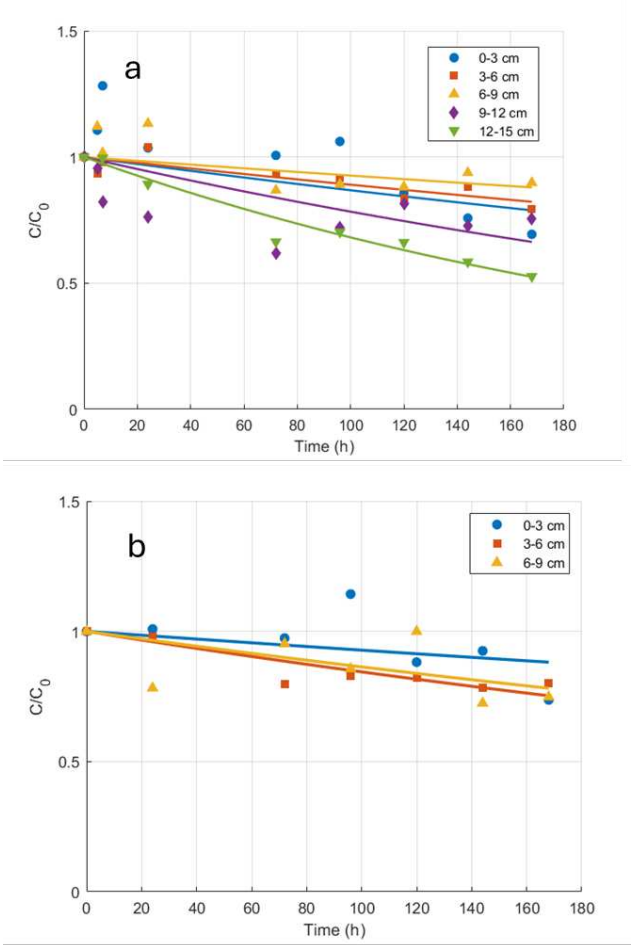

Figure 3.19: BPA degradation profiles in sea ice under UV light (a) and in the dark (b) at different depths

Environmental implications

The results of this study show that, within laboratory-scale sea ice subjected exclusively to UV radiation, the degradation of BPA can also occur to a significant extent through non-light-dependent mechanisms. This has major implications when transferred to the real environment: degradation of pollutants in the ice could occur, at least in the initial stages, even during periods of no sunlight. This behaviour is in contrast to what is observed in the aqueous environment, where degradation processes are generally much more dependent on the presence of light radiation.

The saline veins of the sea ice represent an extremely peculiar chemical microenvironment, characterised by a marked increase in the concentration of organic species, a significant increase in ionic strength and significant pH variations. Added to these factors is the limited mobility of molecules within these channels, which contributes to reactive conditions very different from those typical of conventional aqueous environments. To fully understand the chemical processes taking place in sea ice, future studies will therefore be needed to investigate in detail the chemical and physical characteristics of this environment, not only in terms of pH and ionic strength, but also in relation to how these parameters influence the oxidative potential and overall reactivity of the system.

Author contributions

Conceptualization: Stefano Frassati, Victoria Dutch, Jan Kaiser, Elena Barbaro, Andrea Spolaor

Formal analysis and investigation: Stefano Frassati, Victoria Dutch, Elisa Scalabrin, Andrei Munteanu

Writing - original draft preparation: Stefano Frassati, Elena Barbaro, Andrea Spolaor.

Writing - review and editing: Stefano Frassati, Victoria Dutch, Jan Kaiser, Andrei Munteanu, Elena Barbaro, Marco Roman, Elisa Scalabrin, Andrei Munteanu, Carlo Barbante, Andrea Gambaro and Andrea Spolaor.

3.4 Conclusions on bisphenol A

This chapter outlines the studies conducted on the degradation processes of BPA in different icy matrices, and its precese (along with other compounds of the same class) in samples of alpine snow. The mechanistic and kinetic experiments were designed to maintain constant chemical and physical conditions (such as pH and ionic strength), with only the solid matrix in which the reaction takes place being varied. According to Arrhenius' law, which states that the reaction rate k is exponentially dependent on temperature T $k = Ae^{-E_a/(RT)}$, one should reasonably expect chemical reactions to be significantly slower at temperatures below 0 °C than those in aqueous solution. However, this research and numerous studies in the literature have confirmed, BPA degradation can occur even more efficiently in frozen matrices. This apparent paradox is explained by considering the local concentration effect that occurs during the liquid-to-solid phase transition. During freezing, impurities such as salts and organic compounds are not incorporated into the crystal lattice of the ice; instead, they are segregated into briny veins and at the junctions between crystals. These micro-niches have conditions that are extremely different from those in the bulk liquid phase, with much higher concentrations of reactants, which can promote chemical reactions despite the low temperature. Furthermore, as already reported in the literature, photochemical reactions tend to occur more rapidly in snow than in ice. This behaviour is attributable to greater exposure to solar radiation, expressed in terms of SSA, which is significantly higher in snow than in compact ice. To date, no systematic studies have verified whether the degradation products generated in these two solid matrices are identical. The results of this work showed that, although most BPA secondary products are common to water, ice and snow, two degradation products were identified exclusively in the snow. This observation suggests that the solid matrix not only influences the speed of reactions but can also determine the selective formation of different transformation products, likely due to local variations in reactive micro-environments. With respect to sea ice, it has been observed that dark chemistry reactions play a predominant role compared to photo-induced reactions. This behaviour can be attributed to marked variations in pH and ionic strength within the briny veins of the ice. Such conditions can promote acid-base reactions, hydrolysis processes or even precipitation phenomena, which are more efficient in an icy environment than in an aqueous solution.

Chapter 4

Bromide

Bromine concentrations in ice and snow vary significantly among geographical regions due to different proximity to marine sources, deposition processes and post-depositional removal. In alpine areas, data obtained from ice cores show historical average values of around 0.7 ng g^{-1} in the 1940s, with an increase to around 1.6 ng g^{-1} in the 1970s, probably linked to changes in atmospheric emissions and dry and wet depositions [235]. In the Arctic region, the average concentration of Br is typically higher, with average values in the pre-industrial era (1750) ranging from approximately 2.02 $\pm$ 0.88 ng g^{-1} to 3-7 ng g^{-1} in recent decades. [236]. This increase has been observed in several ice cores from six Arctic sites, although signal preservation is not uniform. [237]. In Antarctica, Br values are typically lower than in other regions. In the ice of the eastern plateau (Dome C), concentrations range from values below the detection limit (<0.05 ng g^{-1}) to a maximum of 0.41 ng g^{-1}. The average for the period 1800-2012 was 0.10 $\pm$ 0.05 ng g^{-1}, while since 2004 there has been an increase to approximately 0.23 $\pm$ 0.09 ng g^{-1} [238].

However, it has been demonstrated that a considerable proportion of deposited bromine can be released back into the atmosphere due to photochemical processes, particularly at sites with minimal snow accumulation [238]. Research conducted on Arctic snow has confirmed that Br is susceptible to photochemical processes that regulate its concentration and atmospheric availability. This supports the significance of snow as a reservoir and a source of reactive Br within the Arctic environment [239].

Bromine explosions are atmospheric photochemical events characterised by the rapid conversion of Br deposited on snowy or icy surfaces into highly reactive species, such as Br_2 and BrO, which are then released into the atmosphere. This process is central to the chemistry of the Arctic and the Antarctica, impacting the Br cycle and the composition of tropospheric ozone [15, 239]. During bromine explosions, deposited inorganic bromine can be photoactivated and recycled several times, significantly increasing the concentrations of reactive Br in the air, up to orders of magnitude higher than baseline levels. This phenomenon typically occurs in early polar spring, when solar radiation increases and the snow cover is still extensive. Bromine explosions have a significant impact on the preservation of the element in ice cores. Due to active photochemical recycling in the snow cover, a significant proportion of deposited Br can be released back into the atmosphere before being definitively incorporated into the ice, causing a post-depositional loss that can alter the paleoclimatic record of this species [238, 240].

The discrepancies found in the experimental data have a significant impact on the accuracy of models that predict ozone depletion events in polar regions. For instance, the WRF-Chem model, which does not incorporate a module for halogens chemistry, tends to overestimate ozone concentrations compared to

observed values, particularly in Arctic coastal areas during the spring, when ozone depletion events are most prevalent [241]. Conversely, more complex models incorporating Br and other halogen reactions frequently underestimate the total amount of ozone in the Arctic in early spring, while simultaneously overestimating the emission of reactive Br species from the snow cover [242, 243]. This finding suggests that, while halogens chemistry is essential for accurate simulation of ozone depletion, the parameterisation of Br release and recycling processes remains uncertain and requires further studies. In order to mitigate these discrepancies, models introduce the hypothesis of a non-reactive Br reservoir present in the snow, which acts as a temporary reserve and limits the immediate release of highly reactive brominated species into the atmosphere [237, 242]. This component is essential for improving consistency between simulations and observations, as it reflects the complex processes of interaction between surface chemistry and the atmosphere, that are not yet fully understood. Incorporating halogens chemistry into global models is essential for accurately simulating surface ozone concentrations during the spring season in polar regions. Furthermore, results indicate that halogen-induced ozone depletion is not a phenomenon confined to the Arctic regions, but propagates to mid-latitudes, thus affecting air quality on a larger scale. [244].

4.1 Speciation of inorganic halogens in snow

In this study, published in *Journal of Analytical Science and Technology* (2024), a significant improvement in the technique for the speciation of inorganic iodine (I) and Br in Arctic snow samples is presented. This was achieved by developing a dedicated instrumental method based on ion chromatography (IC) coupled to inductively coupled plasma high-resolution mass spectrometry (ICP-HRMS). This integrated methodology fully exploits the strenghts of both analytical systems: ion chromatography efficient separates the main inorganic species, namely iodide (I^-), iodate (IO_3^-), bromide (Br^-) and bromate (BrO_3^-), while ICP-HRMS allows for the selective detection of specific isotopes, particularly ^{129}I and ^{79}Br. This approach significantly minimises isobaric and molecular interference, which greatly improves detection limits and increasing the reliability of the analysis. As a result, for the first time, it was possible to reduce the detection limits for the four analysed species by approximately 30-fold. The developed method was then applied to the analysis of real snow samples from Gruvebadet (Ny-Ålesund, Svalbard archipelago). The results showed IO_3^- concentrations on the order of ∼100 pg g^{-1} and I^- levels around ∼50 pg g^{-1}. Similar values were also observed for Br^-, while BrO_3^- was only detected in traces in the analysed samples. The analyses also revealed the presence of additional halogenated species potentially present in Arctic snow. These include intermediate oxides (e.g., XO^-, XO_2^-) and organohalogen compounds, suggesting a complexity of the chemical system in the solid phase greater than previously recognised.

Inorganic iodine and bromine speciation in Arctic snow at picogram-per-grams levels by IC-ICP-MS

Stefano Frassati[a,b], Elena Barbaro[b,a], Claudia Rossetti[a], Giulio Cozzi[b,a], Clara Turetta[b,a], Federico Scoto[b,a], Marco Roman[a,b], Matteo Feltracco[a], Kitae Kim[c],Carlo Barbante[a,b], Andrea Gambaro[a,b], Andrea Spolaor[b,a],

[a] Ca' Foscari University of Venice, Department of Environmental Sciences, Informatics and Statistics, Venice Mestre, Italy.

[b] Institute of Polar Sciences – National Research Council (CNR-ISP), Venice Mestre, Italy.

[c] Korea Polar Research Institute (KOPRI), Incheon 21990, Republic of Korea.

Corresponding authors: Elena Barbaro

Corresponding author's email: elena.barbaro@cnr.it

Keyword: Halogen speciation, Arctic snow, ion chromatography, ICP-MS

Abstract

Iodine and bromine play central roles in polar atmospheric chemistry: iodine influences the atmospheric oxidative capacity and can generate cloud condensation nuclei, while bromine participates in ozone depletion reactions, known as bromine explosions. Here we present a very sensitive analytical method for Br and I speciation by coupling the ion chromatography system (IC) with an inductively coupled plasma sector field mass spectrometer (ICP-SFMS).

We achieved sub-picogram per gram (pg g-1) as limits of detection (LODs) ranging from 0.4 pg g^{-1} for I^-, 0.8 pg g^{-1} for IO_3^-, 4 pg g^{-1} for Br^-, and 1 pg g^{-1} for BrO_3^-, respectively. These values represent a decrease of up to 30 times compared to the LODs reported in other studies. The method was validated using deep snow samples from the Svalbard Islands, collected at the end of the polar night to quantify various oxidized compounds during their seasonal minimum.

In the future, this method could prove useful in the paleoclimatic study of ice cores and snow, as well as in ice chemistry research.

Introduction

The Arctic and Antarctica significantly impact the global atmosphere [245], particularly regarding stratospheric ozone depletion [246]. Iodine primarily enters the atmosphere from oceanic species through photolysis, linked to biological activity [247, 248]. In Antarctica, iodine emission is correlated with phytoplankton production, nevertheless, a photochemical remobilization of iodine from the snowpack was found during the summer at Neumayer station [247] and in Halley Bay [249] of IO [17, 239]. Indeed, these species composed of iodine deposit on the snowpack and subsequently may undergo photo-oxidation leading to the formation of IO_3^- [247, 249], or photo-reduction with a remobilization of iodine as I_2 [250]. These reactions have been studied at high concentrations (100 μmol L^{-1}), but they can probably occur even at environmental concentrations [251]. Additionally, iodine oxides form ultrafine particles acting as cloud condensation nuclei in polar and mid-latitude regions [252–254]. Iodine can also be absorbed by soil and vegetation, adding complexity to the iodine cycle in polar areas [255].

Bromine mainly sourced from the ocean plays a crucial role in polar regions due its autocatalytic reactions that produce gas species, like $BrO^\bullet$ and other radical species responsible for ozone depletion. These reactions are favoured in acidic conditions and cold temperature [17, 256]. Since the snowpack is rich in reactive oxygen species (ROS), such as $^\bullet OH$, $^\bullet OOH$, $^1O_2$ and O_3 [13, 41, 149], it can be assumed that there may be production of bromate (BrO_3^-), through reactions similar to those in water treatment plants, where bromide is oxidized to BrO_3^- by O_3.

Although the concentration of total iodine (I^- + IO_3^-) in the ocean is 400-500 nmol L^{-1} [257–259], during atmospheric transport and deposition (dry or wet) a significant reduction in concentration can occur depending on the distance of the sampling site from the sea. In a previous work by Spolaor et. al the concentration of I^- and IO_3^- were measured in an ice core from Talos Dome [260]. The results have shown that for I^- the mean concentration was 11 pg g^{-1}, but IO_3^- was for each analysis under the detection limits (5 pg g^{-1}). A similar behaviour was observed for bromine, in which higher concentrations of Br^- were measured, nevertheless bromate under the detection limits.

The case of iodine and bromine speciation in the Antarctic ice core mentioned above is not the only case where some IO_3^- and BrO_3^- were not determined [261–263]. This might be related to analytical performance. In fact, as reported in previous works [264–268], there are limits above 1 pg g^{-1} for iodine species, and in the few cases where bromine speciation was performed by analysing iodine at the same time, but LODs above a dozen pg g^{-1} were obtained.

In this paper, we propose a very sensitive analytical method for the speciation of iodine and bromine using only 1 mL of samples by a high-pressure anion exchange chromatography (HPAEC) coupled with inductively coupled plasma sector field mass spectrometer (ICP-SFMS). This new validated method is applied to four snow samples collected at Ny-Ålesund (Svalbard Archipelago).

Materials and methods

Chemicals

All standards and samples were prepared in polyethylene vials, pre-cleaned with ultrapure water in a sonic bath for 30 minutes (UPW, 18.2 MΩ cm,0.01 TOC, Elga LabWater, HighWycombe, UK). For speciation analysis for Br^- and I^- and their total quantification, standard solutions 1000 mg L^{-1} (IC standard) were

purchased by VWR chemicals (Leuven, Belgium). BrO_3^- and IO_3^- standard solutions were prepared using potassium bromate (Sigma-Aldrich, St. Lous, MO, USA) and iodic acid (99,5%, Acros Organics, Geen, Belgium), respectively.

Instrumentation

Speciation analyses were carried out by ion chromatography system (IC, Dionex-2100, Thermo Scientific) hyphenate to an inductively coupled plasma sector field mass spectrometer (ICP-SFMS, Element XR, Thermo Scientific). Chromatographic separation was carried out using an anion exchange column Dionex Ion AS19 2 x 250 mm equipped with Dionex Ion Pac AG19 guard column (2 x 50mm). The column was thermostated on the oven at 30°C. The gradient of sodium hydroxide (NaOH), produced by an eluent generator with a 0.25 mL min^{-1} flow rate was: isocratic elution 0-6 min at 0.5 mM; 6–15 min gradient from 15 to 45 mM; 15-18 min, column cleaning with 45 mM; 18.1–25 min; equilibration at 15 mM. A suppressor (ASRS 600, 2 mm, Thermo Scientific) removed NaOH before entering the ICP-SFMS. 1 mL of sample was manually injected using a peek rheodyne valve, using 5 mL plastic syringes. The ICP-SFMS instrument was tuned using a solution of 1 ppb of In and the gas flow rate was optimized daily to maximize sensitivity and signal stability. The operating conditions and measurement parameters of the ICP-SFMS are shown in Table 4.1.

Table 4.1: ICP-MS instrumental parameters. * An indicative value of indium sensitivity is reported since this parameter was being optimized daily.

Plasma power	1250 W
Cool gas	16.03 L min^{-1}
Auxiliary gas	0.66 L min^{-1}
Sample gas	0.954 L min^{-1}
Additional gas	0.251 L min^{-1}
Accurate mass (I)	126.904
Accurate mass (Br)	78.918
Sample time (mass 129 a.u.)	0.05 s
Spray chamber	Cyclonic Peltier (2 °C)
Nebulizer	Polypro micro-concentric nebulizer, 400 μL min^1
Scan type	EScan
Sensitivity (direct measurement) *	300 000 cps (1 ng g^1 of In)

Results and discussion

Instrumental performance

The analytical method was validated considering the linearity, the reproducibility (relative standard deviation), limits of detection and quantification and matrix effect for each species. LOD and LOQ (Table 4.2) were calculated using the following formulas:

$$LOD = 3\frac{\sigma_b}{m} \qquad LOQ = 10\frac{\sigma_b}{m} \tag{4.1}$$

where σ_b is the standard deviation of the UPW and m is the slope. Subsequently, nine standard solutions

in UPW were prepared ranging from 0.1 to 75 pg g^{-1} for I^-, Br^- and IO_3^-, regarding BrO_3^- a calibration curve from 0.1 to 50 pg g^{-1} was used. For each calibration curve, linearity was evaluated by R^2 value, and values greater than 0.9 were obtained for all analytes. However, for Br- and BrO_3^- the less concentrated standards were discarded because there were lower than the LOD, while for I^- and IO_3^- only the first standard was discarded. The method precision was assessed injecting three times standard at 10 pg g^{-1}. The relative standard deviations (RSD%) were 2% for Br^-, 4% for I^-, 8% for BrO_3^- and 6% for IO_3^- and the LOD calculated for I^-, IO_3^-, Br^-, BrO_3^-, were 0.4 pg g^{-1}, 0.8 pg g^{-1}, 4 pg g^{-1}, and 1.2 pg g^{-1}, respectively.

Table 4.2: Parameters of calibration curve for I^-, IO_3^-, Br^- and BrO_3^-.

	$\mathbf{I^-}$	$\mathbf{IO_3^-}$	$\mathbf{Br^-}$	$\mathbf{BrO_3^-}$
Slope	17090	14726	1294	556
Intercept	55548	-19404	5330	2557
$\mathbf{R^2}$	0.97	0.96	0.94	0.98
RSD%	4	6	2	8
LOD (pg g−1)	0.4	0.8	4	1.2
LOQ (pg g−1)	1.3	2.7	13.3	4

Since within the plasma the ionization of an element is mainly given by the operating temperature, it can be assumed that the signal is not affected by significant interference when analysing compounds containing the same element. However, it will be necessary to correct the signal for the molar fraction of the compound under analysis. In other words, analysis of a standard at a known concentration of I^- should give a similar signal of a standard at the same concentration of IO_3^- corrected for the mass fraction of iodine contained in IO_3^- (73 %). Similarly for bromine, where the mass fraction of bromine in BrO_3^- is 63 %. If one corrects the slopes of IO_3^- and BrO_3^- (Table 4.2) for the relative molar fractions, one obtains values similar to those of $I^-$and Br^- with an error of 6% and 1%, respectively. Thus, this assumption allows for a semi-quantitative analysis of unknown compounds in the following section.

Figure 4.1 shows the triplicate chromatogram of the 10 pg g^{-1} standard. The peaks are chromatographically separated at 9.86 and 12.27 min for BrO_3^- and Br^-, respectively, while 8.83 and 16.81 min for IO_3^- and I^-. The chromatographic performance was also evaluated taking into account possible peak asymmetry effects using the following formula proposed by United States Pharmacopeia (USP)[269]:

$$TF = A + B2A \tag{4.2}$$

Where TF is USP tailing factor, A and B refer to bandwidth at 5% height, when the value TF > 1, tailing occurs, while if TF <1, fronting is defined. In this case TF was evaluated during the triplicate analysis of the standard at 10 pg g^{-1} values of 1.3 ± 0.1, 1.6 ± 0.2, 1.4 ± 0.3 and 1.1 ± 0.2 were obtained for IO_3^-, I^-, BrO_3^- and Br^-, respectively. These effects may be due to the use of a 1 mL loop leading to possible column overload.

Table 4.3 shows, to the best of our knowledge, the works that use the speciation technique using IC-ICPMS with the lowest possible LODs and the relative aqueous investigation matrices. For all the species analysed, the LOD was lowered by about 10 times, for I^- and IO_3^-, for the first time, it fell below 1 pg g^{-1}. As far as $BrO_3^-$is concerned, in previous works the value was about 30 pg g^{-1}, but in our case the value of 1.2 pg g^{-1} was reached, almost 30 times lower. Spolaor et al. showed the best LODs but they used 0.3 mL of sample, while we improved the method to obtain low LODs but using only 1 mL of sample [260].

In order to assess potential matrix effects arising from the possible presence of dust and dissolved carbon

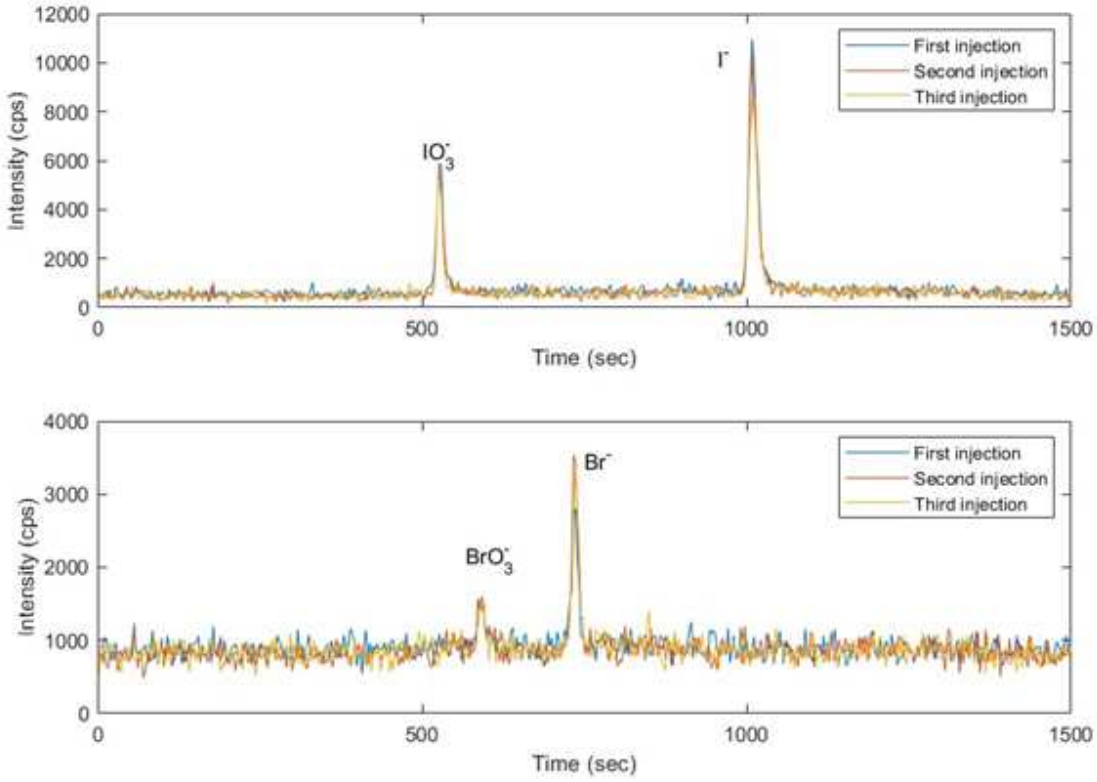

Figure 4.1: Triplicate analysis of the standard 10 pg g^{-1} for I^-, Br^- and IO_3^- and 6 pg g^{-1} for BrO_3^-.The chromatogram for iodine is shown in the upper part, while the chromatogram for bromine is shown in the one below.

that can influence ionization within the plasma, the robustness of the method was tested on a sample of Arctic snow. The latter was evaluated by analysing the same sample unfiltered, filtered through a 0.45 μm filter, and through a 0.2 μm filter. The analyses showed that the relative standard deviation (RSD%) among the different analytes were, respectively: 4% for Br^-, 3% for I^-, 6% for BrO_3^- and 2% for IO_3^-, quantified through an external calibration curve. A qualitative evaluation method to determine the effect of particles that could reduce the ionization efficiency was carried out comparing two calibration curves obtained by spiking the analytes into filtered and unfiltered melted snow, and a calibration curve in ultrapure water. The variation in concentration between methods, calculated as the signal response of a standard present in the sample extract compared with the response of a standard prepared in a UPW and expressed as a percentage [270, 271], was 5.2% for Br^-, 2.8% for BrO_3^-, 0.87% for I^- and 5.1% for IO_3^-.Consequently, this indicates that the matrix effect (ME) is negligible.

To test the proposed method on environmental matrices, four snow samples from Ny-Ålesund (Svalbard) were analysed. The samples were collected during a snow pit dug on 23 February 2022 (corresponding to the beginning of the day-night cycle at the Svalbard islands) in a delimited sampling area near the Gruvebadet Aerosol Observatory (78° 55.018' N, 11° 53.698' E, 43 m a.s.l. [272]). Although the total height of the seasonal snowpack was 82 cm, we decided to consider only the deepest snow layers (i.e., the first 40 cm starting from the ground) to exclude any influence of possible photo-induced reactions that would lead to an increase in

Table 4.3: Summary of some recent work related to the speciation of iodine and bromine

	LOD (pg g^{-1})									
Detection	I^-	IO_3^-	Br^-	BrO_3^-	Column	IC flow (mL min^{-1})	Plasma power (W)	mL of sample	Matrices	Ref.
IC-ICP-MS	12	8	63	32	ICS-A23	0.8	1370	1	Tap water	[267]
IC-ICP-MS	38	52			AS-16	0.9		1	Snow and rain	[261]
IC-ICP-MS	5	7	8	38	AS-16	0.28	1500	0.3	ice core	[260]
IC-ICP-MS	0.4	0.8	3.7	1.2	AS-19	0.25	1250	1	Snow	This work

the concentrations of iodine-containing species. In fact, the onset of the light period in Arctic areas could bring an increase in marine biological productivity, thus an increase in I_2 in the atmosphere, and trigger photochemical reactions that would lead to the oxidation of I^- to IO_3^-. This assumption then allows these compounds to be identified and quantified in their period of lowest production. A four-point calibration curve was made before each series of analysis, to calculate the concentration in the real samples analysed.

The iodine results, as seen in the chromatogram in the Figure 4.2, show that the separation of the two analytes of interest was effectively obtained, with concentrations ranging from 146 to 175 pg g^{-1} for IO_3^- and from 67 to 80 pg g^{-1} for I^-.

In addition to I^- and IO_3^- other peaks were found systematically in the real samples, as shown in Figure 4.2 snow samples showed other peaks. Since the quantification was done by ICP-MS, it is implicit in the technique that the sample is ionized and then analysed by mass spectrometry, and in the case of iodine we focused on 127 m/z. However, given the assumptions made in the previous paragraph, it was still possible to perform a semiquantitative analysis of the results obtained (Table 4.4). All unknown compounds were quantified using the parameters of the calibration curve for I^-. Although it is implicit in ionization techniques, it is not possible to assign a structure to unknown species that contain iodine. Some works focused on the speciation of iodine by IC-ICPMS in snow and rain suggest that the unknown compounds could be iodine-bound organic species [135, 261, 262], but it is possible that they are other iodine oxides (e.g., IO^- or IO_2^-) that can be found within the snowpack. Only future studies can confirm the actual structure of these compounds.

Table 4.4: Iodine-related concentration results expressed as pg g^{-1}. n.d = not detected

ID	**I^-**	**IO_3^-**	**t_r 640 s**	**t_r 859 s**	**t_r 965 s**	**t_r 1113 s**
Sample 1	146	67	7	nd	15	4
Sample 2	175	75	6	nd	7	7
Sample 3	156	80	7	nd	24	6
Sample 4	167	67	6	13	21	5

Focusing on bromine, concentrations above the detection limit have been obtained for Br- in the range

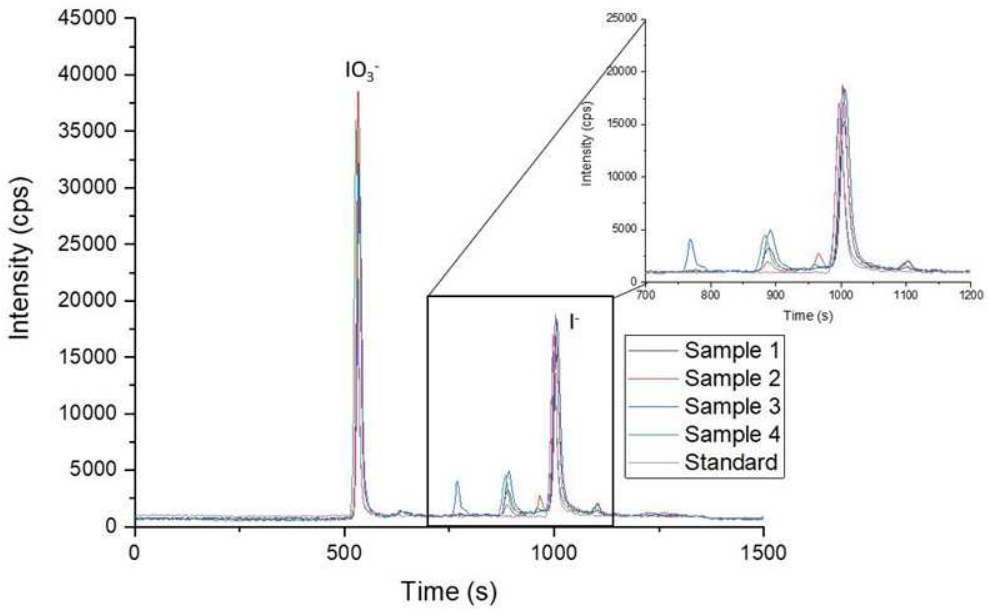

Figure 4.2: Overlay of the chromatograms of the iodine-related samples. Moreover, standard (140 pg g^{-1} for IO_3^- and 75 pg g^{-1} for I^-) chromatogram was overlapped to clearly identify the retention times of IO_3^- and I^-.

between 8-11 ng g^{-1}, according to other studies on bromine in Svalbard snow [273], while bromate was under the LOD in any samples. Again, another unknown peak was identified at 637 s retention time. In this case, there are no works, to the best of our knowledge, confirming the structure of this species, so the existence of bromine-related organic species, as well as other bromine oxides, is plausible. (Figure 4.3). As in the case of iodine, a semi quantitative analysis was performed on this peak using the bromate calibration curve. In these samples the average is 56 $\pm$ 4 pg g^{-1}.

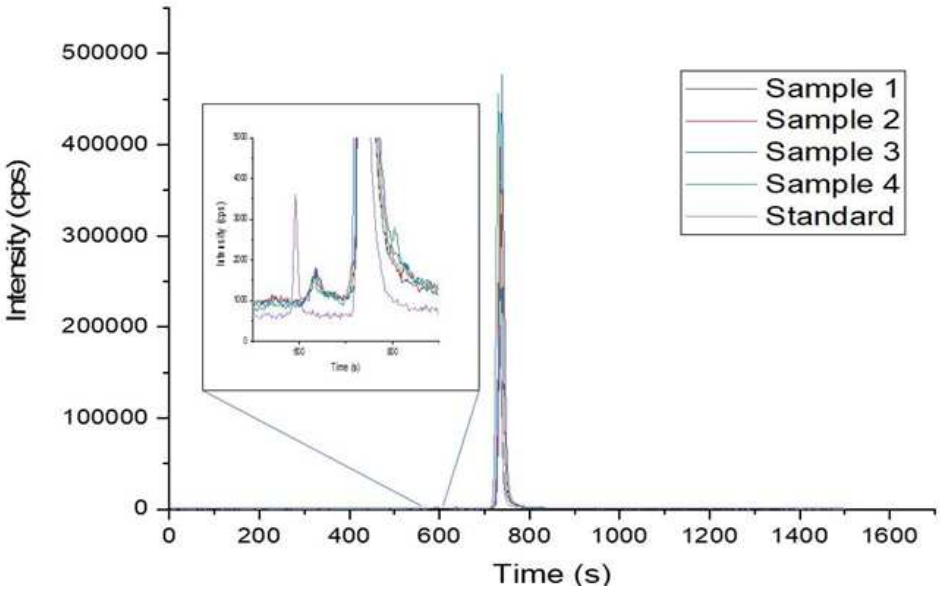

Figure 4.3: Overlay of the chromatograms of the samples related to bromine and standard (500 pg g^{-1} for Br^- and 10 pg g^{-1} for BrO_3^-). The inset clearly shows the separation of BrO_3^- of the standard (in purple) from the unknown species present in the samples.

Conclusions

This work reported the development of a speciation method using IC-ICPMS that enabled chromatographic separation of iodine and bromine with 10-fold lower limits of detection, for I^-, IO_3^- and Br^-, and 30-fold lower for BrO_3^- compared with preexisting work carried out with an analytical method using IC-ICPMS. In particular, LODs were obtain of 0.4 pg g^-1 for I^-, 0.8 pg g^-1 for IO_3^-, 4 pg g^-1 for Br^-, and 1 pg g^-1 for BrO_3^-, respectively. An additional strength of this work is that we were also able to separate unknown compounds that will need further study to be identified.

This method was developed with the intention of improving the analytical capabilities currently available for halogen speciation. The primary objective of enhancing the detection limits for iodine and bromine species is threefold: i) to provide the scientific community with a powerful analytical tool for two main purposes: ii) the determination of iodine and bromine inorganic species in natural environments that were previously undetectable due to the higher detection limits of existing methods. iii) to investigate the formation of iodine and bromine species and potential changes in speciation under laboratory conditions, even at ultra-trace levels. By achieving lower detection limits for these halogen species, this method opens up new possibilities for studying these elements in both natural and controlled environments, expanding our understanding of their behavior and impact. Since these species provide valuable information on various atmospheric chemistry process and have the potential to be used in paleo and climatic study (e.g., sea ice extent and atmospheric chemistry), it is necessary to improve knowledge of iodine and bromine speciation in polar areas.

4.2 Bromate in Arctic snowpack

This study reports for the first identification and quantification of BrO_3^- in Arctic snow sampled collected from the Svalbard archipelago. At the time of this thesis's submission, the study is under review by the journal *Science Advances*. The samples were collected from various areas near Ny-Ålesund, with a focus on two types of snow. The first set of samples consisted of surface snow collected daily over a seven-day period during late spring, immediately after a snow event. This time interval corresponds to the continuous insolation phase (no sunset) typical of high Arctic latitudes at that time of year. The data show a progressive increase in BrO_3^- concentrations over time, which appears to correlate with an increase in total solar radiation, suggesting a possible photochemical role in its post-depositional formation. In order to investigate the origin of the BrO_3^- and its link to photochemical activity, several snowpit from Gruvebadet were analysed at different times of the Arctic season: during the polar night, in the day-night alternation phase and at the end of spring, under continuous sunlight conditions. In parallel, a systematic analysis of aerosol filters collected during the entire campaign was conducted. The results show that BrO_3^- was not present in snow samples collected during the period of total darkness, while it appears and increases progressively with the onset of the day-night cycle, again suggesting a photochemical origin. Furthermore, the aerosol filter analyses excluded a significant direct atmospheric input of BrO_3^-, reinforcing the hypothesis that its formation occurs *in situ*, presumably through oxidative processes triggered by solar radiation. Finally, two snowpits from different glaciers and different years were also analysed. In both cases, BrO_3^- concentrations were significantly higher in the surface layers of the snow, i.e. those directly exposed to solar radiation. This result provides further confirmation of the crucial role of light in the formation of BrO_3^- in the snow environment. The formation of BrO_3^- from Br_- by oxidation from O_3 or $^{\bullet}OH$ is a well-documented process in aqueous solution, especially in the context of water treatment and purification applications. However, to date, these mechanisms have never been investigated in a snow environment. Therefore, using a theoretical approach based on quantum-mechanical calculations, it was possible to explore and predict the most favourable oxidative pathway for BrO_3^- formation under representative Arctic snow conditions. This study identifies, for the first time, the presence of a stable reservoir of BrO_3^- in Arctic snow. Due to its greater stability than Br^-, bromate may represent a form of reactive Br accumulation and help to improve the representation of Br cycles in atmospheric models, particularly those describing Br explosion phenomena in snow.

Seasonal bromate formation in the Arctic snowpack: implications for the bromine biogeochemical cycle

Stefano Frassati[1,2*], Elena Barbaro[2,1*], Giulio Cozzi[2,1], Clara Turetta[2,1], Federico Scoto[2,1], Claudia Rossetti[2,1], Marco Roman[1], Matteo Feltracco[1], Kitae Kim[3], François Burgay[4], Alfonso Saiz-Lopez[6], Joseph S. Francisco[6], Ward Van Pelt[7], Feiyue Wang[8], David Cappelletti[9], Sofia Lerda[9], Giovanni Bistoni[9], Filippo De Angelis[9], Carlo Barbante[1,2], Andrea Gambaro[1] and Andrea Spolaor[2,1*]

[1]Ca' Foscari University of Venice, Department of Environmental Sciences, Informatics and Statistics, Venice Mestre, Italy.

[2]Institute of Polar Sciences – National Research Council of Italy (CNR-ISP), Venice Mestre, Italy.

[3] Korea Polar Research Institute (KOPRI), Incheon 21990, Republic of Korea.

[4]Department of Environmental Sciences, University of Basel, 4001 Basel, Switzerland

[5]Department of Atmospheric Chemistry and Climate, Institute of Physical Chemistry Blas Cabrera, CSIC, 28006 Madrid, Spain

[6]Department of Earth and Environmental Science and Department of Chemistry, University of Pennsylvania, Philadelphia, PA 19104, USA

[7]Department of Earth Sciences, Uppsala University, Sweden

[8]Centre for Earth Observation Science, and Department of Environment and Geography, University of Manitoba, Winnipeg, Manitoba, Canada

[9]Department of Chemistry, Biology and Biotechnology, University of Perugia, Perugia, 06123, Italy

*Corresponding author email: andrea.spolaor@cnr.it, elena.barbaro@cnr.it, stefano.frassati@unive.it

Graphical abstract

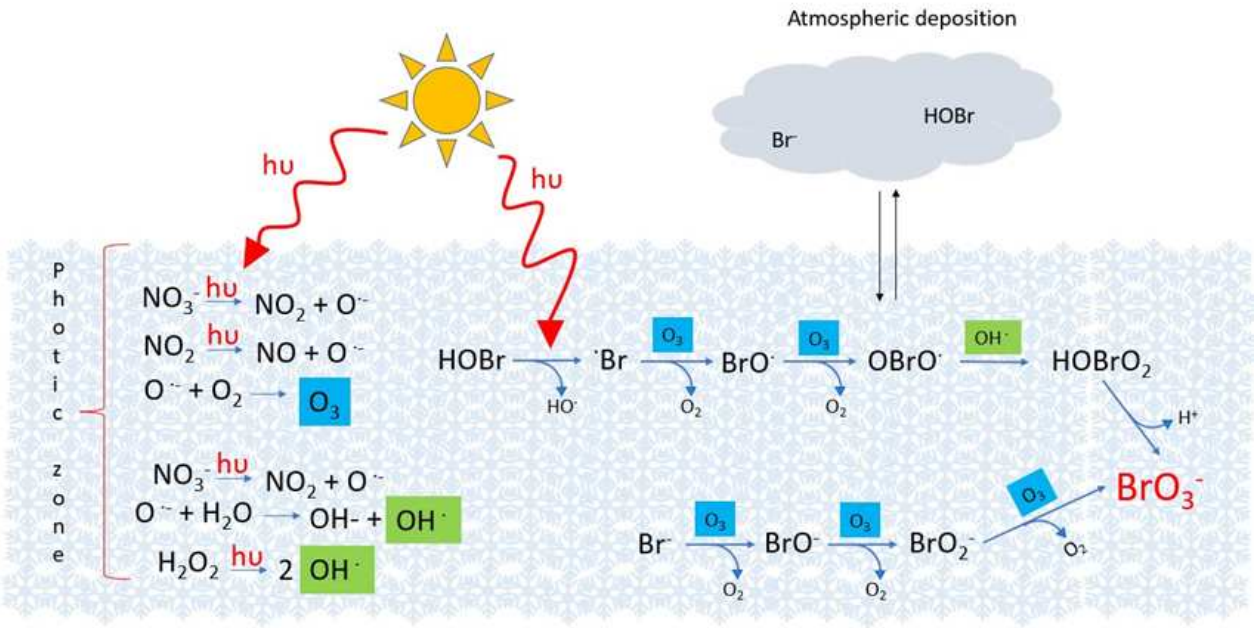

Abstract

Bromine exists in multiple chemical forms in the atmosphere, with. bromide being the predominant species in snow. Here, we experimentally detect the formation of bromate (BrO_3^-) in Arctic snow and propose a mechanism for its production. Our observations reveal, for the first time, significant $_3^-$- concentrations, reaching up to 5% of total bromine, during springtime across the study sites. The persistence of $_3^-$ in the snowpack and its production as a function of solar radiation suggest a photochemically driven process. Experimental evidence confirms in situ $_3^-$ formation within the snowpack, with negligible contributions from direct aerosol deposition. The absence of $_3^-$ in aerosol samples further underscores the snowpack's role as a reactive matrix for photooxidation, providing new insights into the Arctic bromine cycle. We supported experimental findings with state-of-the-art quantum chemical calculations, exploring both radical and ionic reaction mechanisms and the matrix effect. The formation of $_3^-$ in snowpack represents a stable reservoir of non-reactive bromine, with potential implications for understanding halogen chemistry in polar environments.

Main text

Bromine in polar regions plays an important role in atmospheric processes affecting tropospheric and stratospheric ozone depletion reactions, as well as atmospheric mercury depletion events (AMDEs), with far-reaching implications for our understanding of the Earth's radiative budget and energy dynamics [245, 246]. The presence of bromine in the snowpack of polar regions is caused by direct emissions and deposition of bromide-containing sea spray aerosols, along with the re-emission of gas-phase bromine during springtime from photochemical processes over the sea ice, especially over first-year sea ice [274–276]. In the atmosphere, bromine can be present in several forms, both inorganic [277, 278] (such as Br_2, BrO, HOBr, BrCl, $BrNO_2$) and organic (such as CH_3Br), its main form in the snowpack is bromide (Br^-) [15].

Although bromine activation over the first-year sea ice snow is well documented [274–276], the activation and release of bromine from terrestrial snowpack into the atmosphere remain uncertain. Discordant observations and hypotheses [279, 280] have led to debate regarding the potential storage of bromine in the snowpack [238]. The photo-stimulated emission of gaseous bromine (Br_2) from the snow surface into the atmosphere has been observed in Greenland and Alaska [280, 281]. However, a specific study of the diurnal remobilization of halogens from the snowpack indicated that there was no significant variation in bromine levels between day and night, suggesting that there is no emission of brominated species into the atmosphere [239].

These discrepancies in experimental data therefore affect the accuracy of models that predict, for example, ozone depletion events. The WRF-Chem model, which lacks a halogen chemistry component, overestimates the amount of ozone compared to observation, especially at Arctic coastal sites in the spring [241]. In contrast, other models that include halogen reactions tend to underestimate total ozone in the Arctic in the early spring and overestimate the emission of reactive bromine species from snow [242, 243]. To minimize these effects, it is assumed in the models that there is a pool of non-reactive bromine in the snow [237, 242, 282]. The implementation of halogens in a global model highlights the necessity of accounting for halogen chemistry to accurately reproduce springtime surface ozone in polar regions, and shows that halogen-induced ozone depletion is exported from the Arctic to mid-latitudes [244, 283].

One of such non-reactive bromine species is bromate (BrO_3^-), the ultimate oxidation product of Br^- through reactions with oxidants such as O_3 or $^\bullet$OH [284]. Numerous studies have documented the presence of oxidant species in snow, including reactive oxygen species (ROS; e.g., O_3, $^\bullet$OH, $^\bullet$OOH, and H_2O_2), some of which are active participants in bromine explosion reactions [39, 41, 58, 149]. ROS in the snowpack could be produced through photochemical reactions involving NO_3^- and NO_2^- (at λ=320 nm). These reactions, under acidic conditions (pH < 6), can produce O^-, which rapidly reacts with water to form the $^\bullet$OH [58]. Alternatively, nitrate photolysis can release atomic oxygen, which may react with dissolved molecular oxygen to form O_3 [4, 39, 285]. At these same wavelengths, H_2O_2 can undergo homolytic photolysis, producing hydroxyl radicals ($^\bullet$OH) [140, 286]. Most of these oxidants require UV light to be formed in situ in the snowpack. Conversely, ozone can diffuse into the snow from the atmosphere, there being the most effective oxidant in dark conditions. BrO_3^- formation has been well studied in aqueous media, especially in water treatment systems due to its carcinogenic properties [287]. The initial reaction step for its formation involves the oxidation of bromide to either a bromine atom or hypobromous acid, HOBr. Both pathways could then lead to further oxidation steps to BrO_3^-. However, to the best of our knowledge, no studies have investigated the presence of BrO_3^- in snow.

This study presents the first evidence of BrO_3^- in Arctic snowpacks. We experimentally demonstrate for

the first time that the surface layers of the polar snowpack can create an ideal environment for fostering the oxidation of bromide to BrO_3^- when exposed to sunlight, thereby acting as a non-reactive bromine reservoir that has not yet been considered in current models. We also provide a theoretical framework to understand the oxidation pathways in BrO_3^- formation.

Bromate occurrence in the surface snow and seasonal snowpack

To examine the presence of BrO_3^- in Arctic snowpacks and the mechanism that controls its formation, we designed and conduct specific experiments in the Svalbard archipelago at different sites and with different temporal resolutions.

Firstly, to quantify the presence of BrO_3^- in surface snow and evaluate potential in situ production processes, daily snow samples were collected at the Gruvebadet Snow Research Site (GSRS) in Svalbard following a snowfall event, from April 28 to May 3, 2023 (see Supplementary Information, Section 1). The results revealed a tenfold increase in BrO_3^- concentration over the five days, rising from 0.4 nM on the first day to 4.3 nM on the last day (see Figure S5). Concurrently, bromide (Br^-) concentration increased from 20 to 63 nM, showing a similar trend to BrO_3^- (Fig. S5). To determine if the increase in BrO_3^- was solely related to a parallel rise in bromide, BrO_3^- concentrations were normalized to Br^- concentrations. During the study period, $BrO_{3\,nor}^-$ increased from 2.05x10$^-$2 (April 27) to 7.00x10$^-$2 (May 3), as shown in Figure 4.4.

The second experiment was aimed at investigating the effect of varying solar radiation on the potential bromate production within the seasonal snowpack. We analyzed a series of snow pit samples collected at the GSRS through weekly sampling during the 2021-22 snow season. Three sets of snowpit samples were collected during the polar night, three during the day/night cycle period and three during the polar day, thus with a full exposure of the upper part of the snowpack to sunlight. BrO_3^- concentrations in the snowpack collected during the polar night and in the day-night cycle period were similar, ranging between 2.0 x 10^{-2} to 3.6x10^{-1} μM, with mean value of $BrO_{3\,nor}^-$ of 1.4x10^{-3} $\pm$ 6.6x10^{-4}. Nevertheless, the most superficial samples collected in April 2022 showed higher values of $BrO_{3\,nor}^-$, up to 2.2 x 10^{-2} (4.3 nM BrO_3^-) while the deepest samples present BrO_3^- concentrations below the instrumental limit of detection (7.8 x 10-3 nM, figure S6), due to rain on snow event on March 13 2022 (Figure 4.5). Regarding Br^-, as illustrated in Figure S6, no trend is evident within the snowpack, with an average concentration of 160 $\pm$ 104 nM. Figure 4.5 (and figure S2) illustrates that in the deeper layers, which refers to the dark period the concentrations of BrO_3^- are below the limit of detection (LOD).

Finally, snow samples from two snow pits, dug in April and in the accumulation area of two glaciers nearby Ny-Ålesund, Holtedahlfonna (HDF) and Kongsvegen (KNG), were analysed to evaluate the seasonality in bromate production and concentration in absence of winter melting and percolation events. The results obtained from the HDF, sampled in 2022, snow pit indicate that the $BrO_{3\,nor}^-$ values in the lower snow strata are approximately ten times lower than those observed in the upper layers (ranging from 3.3 $\times$ 10^{-3} to 7.4 $\times$ 10^{-3}), with a maximum value of 4.9 $\times$ 10^{-2} observed at the top of the snowpack (Figure 4.6). The snow pit samples in 2015 from KNG, similarly to the HDF ones, indicate the highest $BrO_{3\,nor}^-$ values near the surface, with a maximum value of 3.21x10^{-3} at a depth of 40 cm. In the middle section of the annual snow pack (90-140 cm) the ratio tends to decrease to an average value that is four times lower than at the surface layers, and rising again in the deepest part (140-200 cm), with a ratio similar to the uppermost one (Figure 4.6 and supplementary information Section 1 for site description). At both sites Br^- has an average concentration

of 106 ± 60 µg g^{-1} for HDF and 48 ± 41 nM for KNG. As illustrated in Figure S7, in both snow pits, the bromate appears to increase at the surface, rising from values of approximately $5.1x10^{-1}$ ± $0.2x10^{-1}$ nM in the deeper samples to a maximum of 2.3 ± 0.5 nM near the surface for HDF. In contrast, for KNG, the lowest layers show values of $9.5x10^{-2}$ ± $4.3x10^{-2}$ nM, while the maximum value of $3.8x10^{-1}$ is found in the layer at a depth of 30 cm.

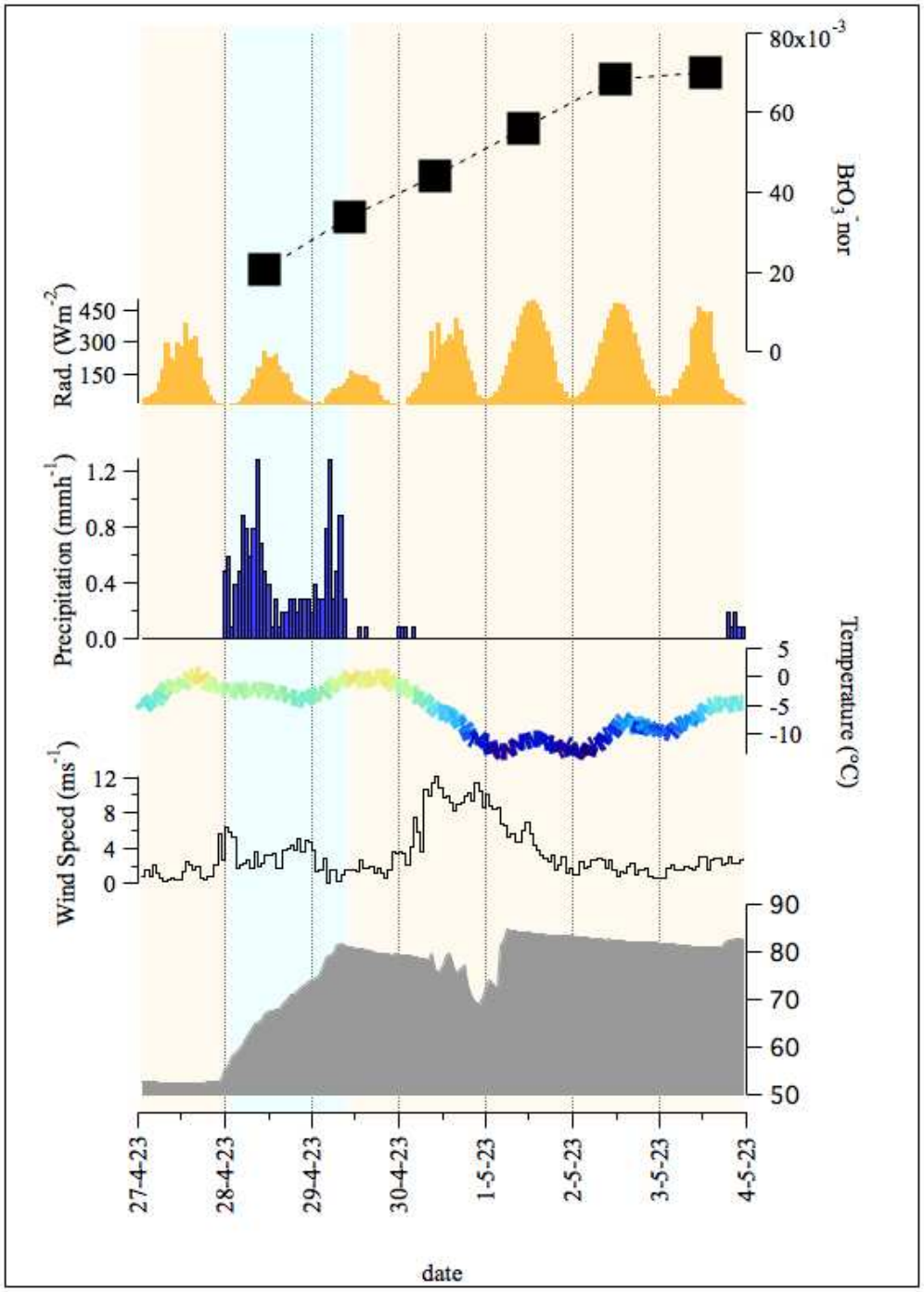

Figure 4.4: **Daily evolution of $BrO_3^-{}_{nor}$ levels in surface snow.** Trends in BrO_3^- values in relation to meteorological parameters (such as shortwave radiation, precipitation, temperature and wind speed) and snow hight during the period from 28 April to 3 May 2023 at GSRS. Blue band represents the period of precipitation. The meteorological precipitation and snow depth data are shown at hourly frequency (*https://seklima.met.no/observations*), while the irradiance data are shown at 30 min resolution and come from CCT[288].

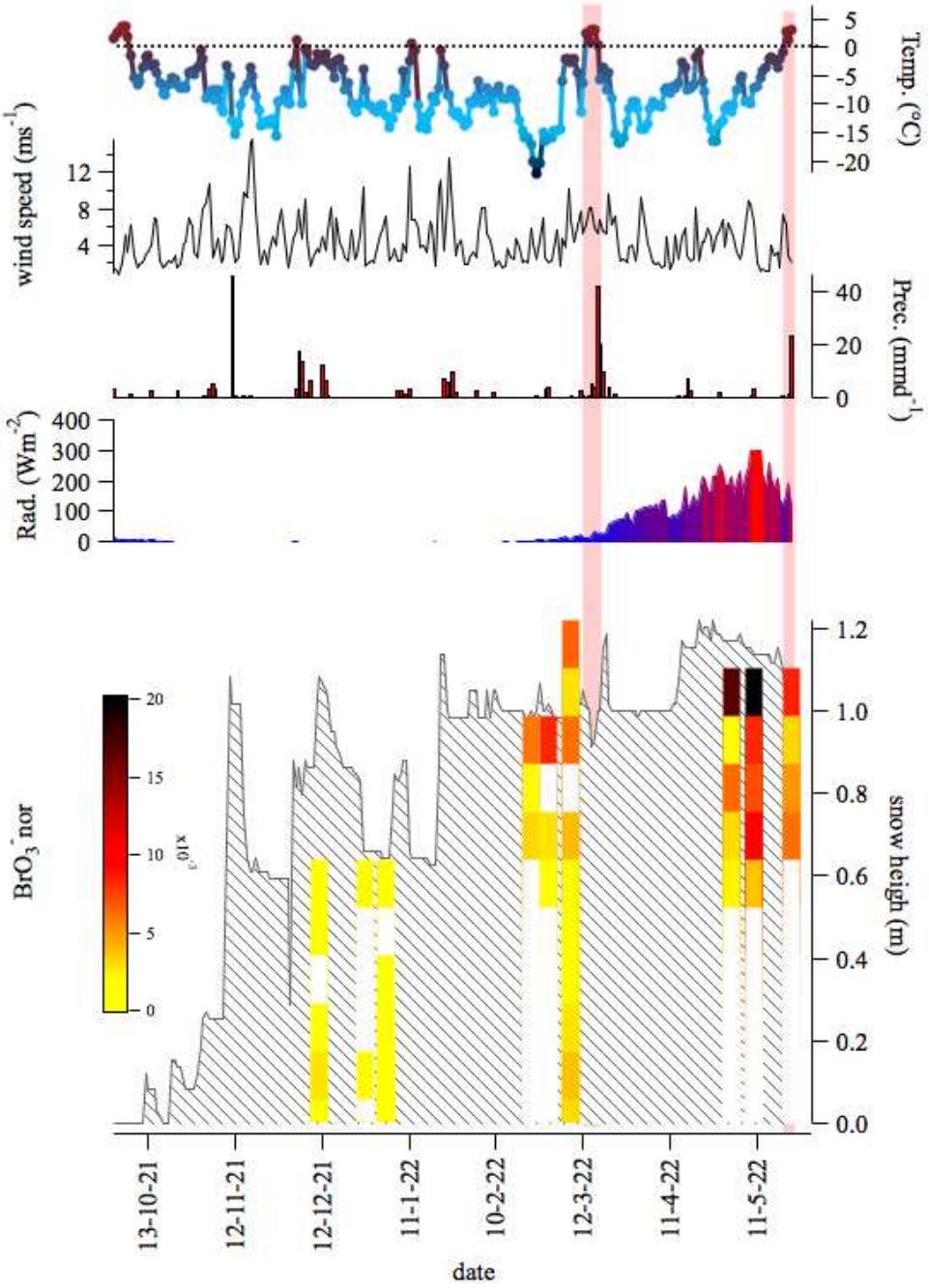

Figure 4.5: **Seasonal evolution of $BrO_{3\ nor}^-$ levels in snow.** Time series of bromate in the seasonal snowpack at GSRS in relation to temperature, wind speed, precipitation and radiation. Samples were collected during the polar night, dawn and full day. The discrepancy between the height measured during the sampling and the height measured by the automatic measuring device is due to the punctual instrumental measurement while the sampling area covers an area of 6m x 10m with possible surface irregularities and different accumulations of snow. The red band represents the rainfall period.

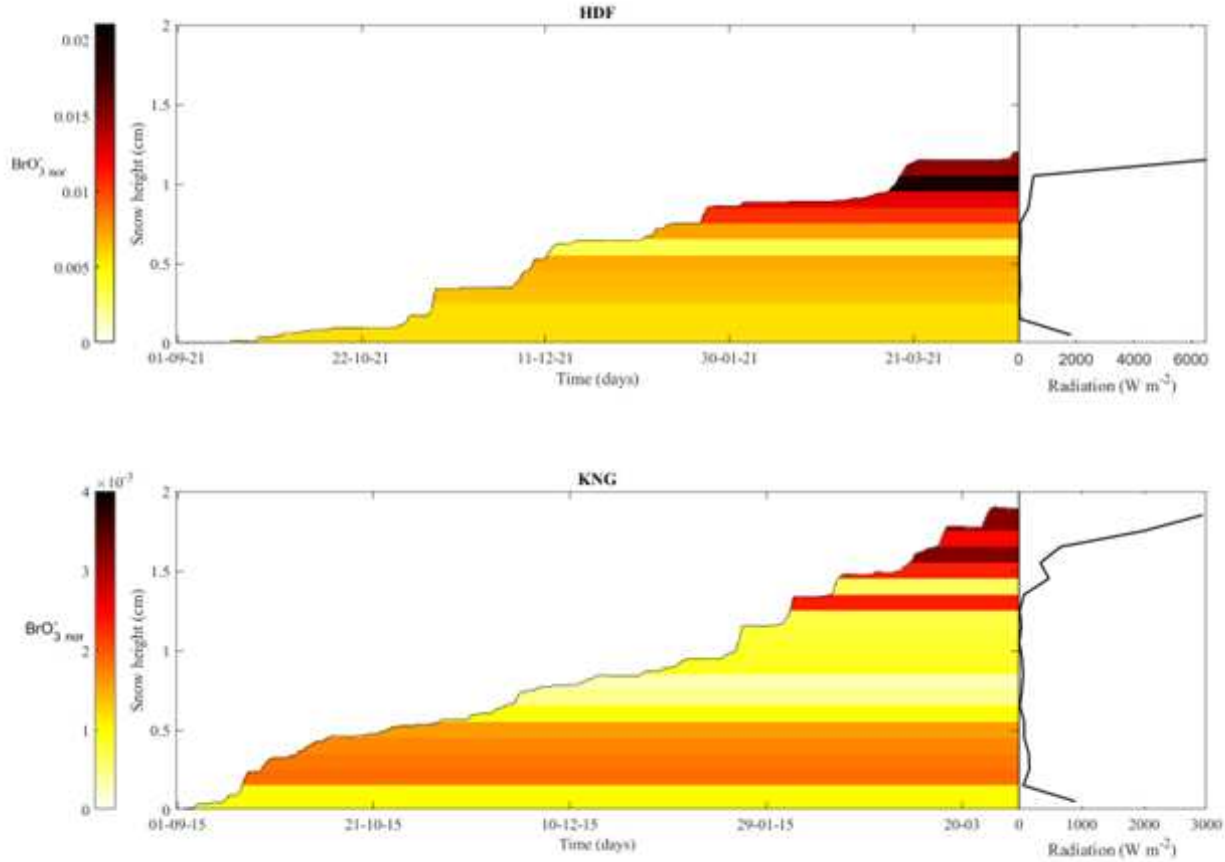

Figure 4.6: **Cumulative $BrO_{3\ nor}^{-}$ production in glacier snow.** Trend of BrO3-nor measurements in seasonal snow samples in the HDF (top, sampled in 2022) and KNG (bottom, sampled in 2015) glaciers. The graphs on the right show the radiation penetrated across 10 cm depth (refer to Methods), using the incoming radiation data from the CCT.

The relationship between bromate production and sunlight.

The ultimate source of bromine in the snowpack is sea salt aerosols originating from the oceans. Possible mechanisms for BrO_3^- formation in the snowpack include (i) gas-phase reactions during the atmospheric transport of sea salt bromide followed by deposition and (ii) *in situ* production through oxidation reactions of bromine species in the snowpack.

First hypothesis is contradicted by analyses of aerosol samples collected in Ny Alesund from February 2022 to June 2022 (see Table S1), which found no traces of BrO3- despite showing an methanesulphonic acid (MSA) trend consistent with prior work in the same area and a Br- concentration ranging from 1.39 to 20.8 ng m^{-3}. In our preliminary data analysis, we observed a correlation between BrO_3^- and MSA concentrations (Pearson's r = 0.71, p-value <0.001; see Table S2) in the snowpack, indicating a relationship between the two species. It is well known that the formation of MSA occurs through atmospheric photo-oxidative reactions of dimethylsulfide (DMS), a compound released during algal blooms in the atmosphere. Therefore, our first hypothesis is that BrO_3^- may originate from photochemical processes in the atmosphere after being released as bromide from the same marine source as MSA. A second possibility is that the production processes for MSA and BrO_3^- are both linked to solar radiation but in different contexts (i.e. atmosphere vs snowpack), leading to only an apparent correlation between their final concentrations. The connection with photochemistry has been documented for MSA in the atmosphere, but not for bromate in snow.

Considering the daily sampling of surface snow in Ny Ålesund (Figure 4.4), the observed increase in $BrO_{3\,nor}^-$ began after a two-day snowfall followed by a regular sunlight illumination cycle, with bromate concentrations continuously increasing and peaking after approximately five days. The radiation data (Fig. 4.4b) were collected at the Amundsen-Nobile Climate Change Tower (CCT), located 500 m from the snow sampling site. Radiation reaching the surface is typically extinguished within the first 10 cm of snow [41]. Indeed, for samples that were never exposed to sunlight, the $BrO_{3\,nor}^-$ values remained low and relatively constant. However, during sunrise, $BrO_{3\,nor}^-$ values in the sunlight-exposed layers gradually increased, suggesting an effective mechanism for BrO_3^- production triggered by sunlight (Figure 4.5). The formation of the snowpack in the HDF experiment was characterized by a few intense snowfalls, allowing prolonged exposure of the surface layer to solar radiation (Figure 4.6a). In contrast, the KNG snowpack experienced several less intense snowfalls that reduced the exposure time of the surface snow layer to sunlight (Figure 4.6b). Consistently, we observed the lowest BrO_3^- values in the deepest dark snow layers, whereas the illuminated surface layers showed an increase in concentration.

The findings above indicate at least two possible formation mechanisms for bromate. The first appears to correlate with sunlight intensity and the subsequent photochemical production of radicals in the snowpack. The ozone pathway for the formation of BrO_3^- has been extensively studied for its application in water cleaning systems. The Br_2 production process involves the condensed-phase reaction of BrO and $BrONO_2$, producing HOBr in an aqueous solution [284]. This species may undergo photolysis under UV light radiation, generating Br radicals, which can then oxidize further by reacting with the OH radical. A second mechanism, possibly occurring also in the dark, may consist of an ionic pathway driven by O_3, analogous to that of Cl^-, as observed in Arctic and Antarctic snow samples [289]. Both computational and experimental studies support that the oxidation reaction of Br^- can occur at the gas-liquid interface. It is a reasonable hypothesis that the production of bromate may take place within the quasi-liquid layer (QLL), which is a thin film of water molecules situated between the solid and liquid phases. It has been demonstrated that within the QLL, dissolved species can undergo a substantial increase in concentration, with some studies reporting a

10,000-fold enhancement [149, 290].

To shed light on these hypotheses, we conducted a quantum mechanical calculation (see SM for details) to ensure a consistent understanding of the proposed reaction mechanisms. The photodissociation of HOBr triggers the first mechanism (Figure 4.7, left) and proceeds through radical intermediates. The second mechanism (Figure 4.7, right) involves only ionic species and begins with the oxidation of Br^- by ozone. Both mechanisms involve multiple spin transitions, necessitating the calculation of sections of potential energy surfaces with different spin multiplicities. Additionally, calculations were performed both in the gas phase and in the presence of water using the implicit solvent model C-PCM (Water).

The potential energy surface of the proposed radical mechanism initiated by photo-absorption is shown in Fig. 4.7 (left-hand side), which reports the relative free energies of all intermediates computed in the gas phase (red) and in water (black). The photodissociation of HOBr requires an initial energy of 43.7 kcal/mol. Notably, while all the successive steps involving the oxidation of Br are significantly exergonic and irreversible in water, the situation changes dramatically in the gas phase. In particular, when simulated in the gas phase rather than in water, one step (the third) even switches from exergonic to endergonic.

The right-hand panel of Fig. 4.7 displays the computed section of the potential energy surface for the alternative ionic mechanism. The steps of this mechanism were found to be exergonic in both the presence and absence of the solvent. The first step of the ionic mechanism presents an energy barrier which was further examined by (i) calculating the transition states for both the singlet and triplet states, and (ii) identifying the minimum energy crossing point (MECP) between their potential energy surfaces. Two possible pathways were found. In the "early" crossing scenario (Fig. S12), the singlet–triplet crossing occurs before the transition state, while in the "late" crossing case (Fig. S13), it occurs afterward. The latter corresponds to the minimum energy path, with an associated energy barrier of 20.7 kcal/mol.

The existence of significant reaction barriers at the entrance of both radical and ionic channels is a possible explanation for the generally low efficiency of bromate formation in the snowpack. However, the initial reaction barrier associated with the photodissociation of HOBr in the radical mechanism can be overcome by the action of sunlight. On the other hand, the ionic mechanism may operate even in the dark, but with low efficiency due to the energy barrier associated with crossing singlet-triplet potential energy surfaces.

The calculations suggest that the radical mechanism should occur in the QLL, while the ionic mechanism could also be effective in the interstitial air of the snowpack. Reactive species such as OH radicals can be formed from the photolysis of NO_3^-. Nevertheless, the correlations shown in Table S2 do not demonstrate a direct link between BrO_3^- production and NO_3^-. This may be due to the consumption of reactive species by other compounds, leading to an absence of a direct correlation with NO_3^-, which could produce, in large excess, the reactive species useful for the oxidation of Br^-. Furthermore, the observed correlation value between BrO_3^- and Br^- indicates that bromide is present in significant excess of the reactive species. This suggests that it should not be considered a limiting reagent and that UV radiation is the primary driver for BrO_3^- formation.

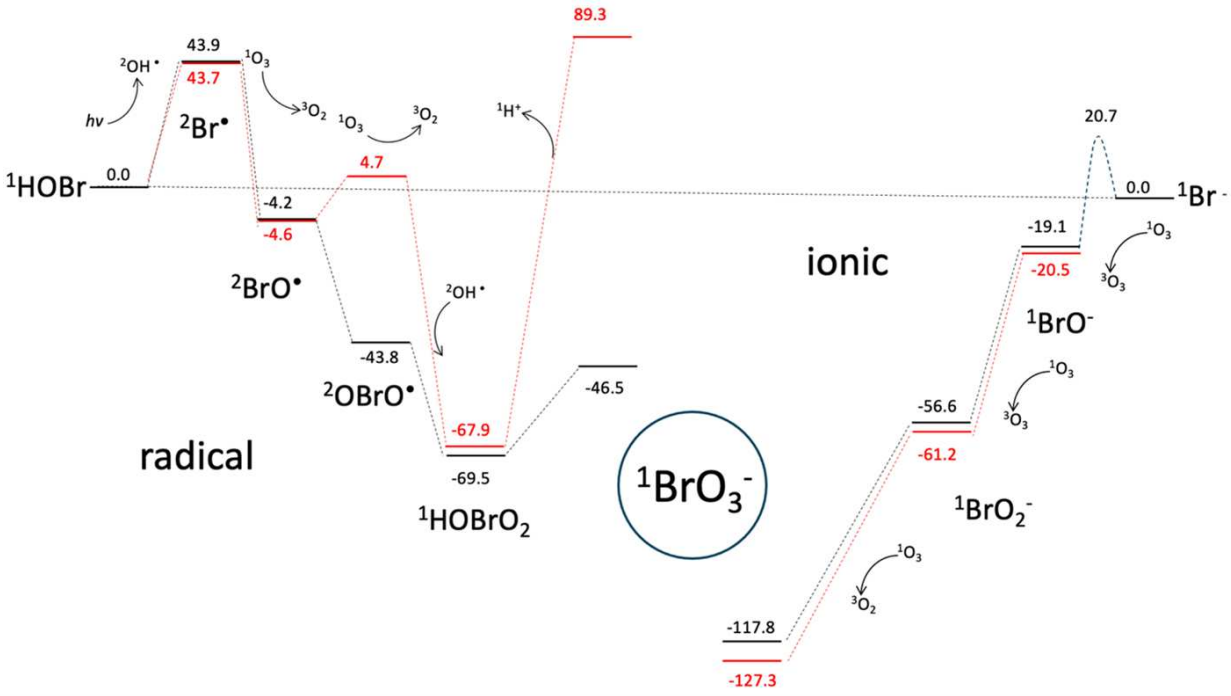

Figure 4.7: **Potential energy surface of the radical (left) and ionic (right) mechanisms computed at WB97X-D3BJ level of theory.** Gas-phase results are reported in red, while calculations performed with the implicit solvent model C-PCM(Water) are reported in black.

Implication of bromate formation in snowpack.

Our study demonstrates that bromate formation occurs within the Arctic snowpack due to sunlight-driven oxidation of bromine, effectively immobilizing a significant fraction of bromine (up to 5%) and decreasing the pool of potentially reactive bromine. This previously unaccounted transformation challenges existing atmospheric and geochemical models of bromine cycling.

The snowpack, particularly under solar irradiation, emerges as a highly oxidizing environment, emphasizing the need for further studies on its role in polar region chemistry. Future experimental and theoretical investigations are necessary to refine the kinetic parameters governing bromate formation and stability in snow. The inclusion of a non-reactive bromine pool is a key element in improving the implementation of predictive models of the ozone depletion process, helping to reduce prediction errors, particularly during periods characterized by a marked day-night cycle.

Furthermore, the accumulation of bromate in Arctic snow during winter implies its potential release into the environment during the melting season, which has implications for biogeochemical cycling. Beyond the Arctic, this mechanism may also apply to other snow-covered regions, including Antarctica and mid-latitude mountain ranges like the Alps. Understanding bromate formation in these environments could offer broader insights into the role of snowpack photochemistry in atmospheric halogen cycles and its effects on climate-related processes

Supplementary material

Materials and Methods

Snow pit sampling

Nearby Gruvebadet Snow Research Site (GSRS, 78.55°N, 11.53°E; 50 m a.s.l, Figure S1) a weekly snow pit sampling was done to collect snow samples and physical parameters such as temperature and density. Daily surface snow samples were collected between 2023 April 28th and May 3rd at 12 PM. For the seasonal study, three series of samples taken during the polar night and another three series during the all-day period were used.

Snow samples from glaciers were collected from a snow pit near stake 3 (78.95° N, 13.40° E, 600 m a.s.l.) on the Holtedahlfonna ice cap (HDF) on 24 April 2022. HDF is the largest ice cap (ca. 300 km^2) on north-western Spitsbergen, about 40 km from the Ny-Ålesund station. It is distributed over an elevation range of 0–1241 m a.s.l. The front of Kongsvegen (KNG) is located approximately 20 km to the east of Ny-Alesund extending about 20 km inland. Samples were collected at stake 8 (78.45° N, 13.20° E, 750 m a.s.l.) on 10 April 2015 (see supplementary material).

A clean surface was made in all snow pits by removing about 10 cm of the snow pit wall using a cleaned polyethylene scraper to avoid potential contamination during digging. The snow wall was sampled using polyethylene pre-cleaned tubes with a depth interval of 10 cm so that twelve samples were taken for each snow pit. Snow pit samples were transported frozen (-20 °C) and in dark conditions directly to the ISP-CNR laboratories in Venice, melted at room temperature under a laminar flow bench (class 100) inside a clean room.

Aerosol sampling

Aerosol samples were collected using a PM_{10} high-volume air sampler (TE-6070) operating at a flow rate of 68 $m^3\,h^{-1}$. The sampler was fitted with an 8×10 inch Quartz Fiber Filter (QFF) that had been pre-combusted for 4 hours at 400 °C in a muffle furnace. Field blanks were obtained by placing the same filters on the sampler with the air pump turned off. Both samples and blanks were stored and transported at −20 °C in dark conditions. Bromate was extracted by sonication (30 min) in ultrapure water (10 mL) [291].

Analytical measurements

Snow speciation analyses were carried out by ion chromatography system (IC, Dionex-2100, Thermo Scientific) coupled with inductively coupled plasma sector field mass spectrometer (ICP-SFMS, Element XR, Thermo Scientific). The chromatographic separation was performed on a Dionex Ion AS19 anion exchange column (2 × 250 mm) with a Dionex IonPac AG19 guard column (2 × 50 mm). The instrumental detection (LOD) calculated were: $5x10^{-2}$ nM for Br^- $8x10^{-3}$ nM for BrO_3^-, respectively [292].

Quantification of BrO_3^- in the aerosol samples was performed with an HPAEC (Dionex, Thermo Scientific, ICS-5000, Waltham, USA) coupled to a TSQ Altis Plus triple quadrupole mass spectrometer (Thermo Scientific™, ICS-5000, Waltham, USA) using a heated electrospray source (H-ESI) operating in negative mode. Chromatographic separation, carried out with a KOH gradient was performed using a Dionex IonPac AS24

RFIC 2 × 250 mm anion-exchange column (Thermo Scientific™) equipped with a Dionex IonPac AG24 RFIC 2 × 50 mm guard column (Thermo Scientific) [291].

Major anions were determined using an ion chromatography sistem (Thermo Scientific Dionex ICS-5000, Waltham, MA, USA), coupled to a single quadrupole mass spectrometer (MSQ Plus, Thermo Scientific, Bremen, Germany), while cations using the same ion chromatograph coupled to a conductivity detector, following a previously published method [186]. A multi-anion standard for ion chromatography (Cl^- 10 mg L^{-1}; NO_3^- 20 mg L^{-1}; Br^- 20 mg L^{-1}; SO_4^{2-} 20 mg L^{-1}) and single standard solution of MSA (1000 mg L^{-1}) were purchased from Sigma Aldrich and prepared from the solid standard dissolved in ultrapure water. The multi-cation standard solution for ion chromatography (Ca^{2+}, Na^+, NH_4^+) at the concentration of 100 mg L^{-1} was provided by Sigma Aldrich [293]. Correlation matrices are available in supplementary materials

In the case of BrO_3^-, values that fell below the LOD, these were not included in the calculation of $BrO_{3\ nor}^-$. Furthermore, in the color bar of the graphs, these values were represented in grey.

Snowpack modelling and snow pit dating

In order to reconstruct the evolution of the snowpack during the season, a coupled energy balance – snow modelling system was used [294, 295]. It simulates multi-layer snow density, temperature and water content with <5 cm vertical resolution, in response to water transport, storage and refreezing, as well as gravitational compaction and heat diffusion. The model is based on Van Pelt et al. [294], but uses a new description of fresh snow density and snow compaction following Van Kampenhout et al. [295]. Here the model is forced with meteorological data from the NORA3 reanalysis dataset [296], providing fields at 3-km spatial resolution, which are then downscaled to a 1-km resolution grid as described in Van Pelt et al. [294]. From the model output, we extract seasonal snow height as a function of time for the period from September 1 (2014 for KNG and 2021 for HDF) to the day of sampling. Model values were then rescaled to the snow depth measured on the day of sampling to remove biases while maintaining temporal variability. It is noteworthy that the NORA3 reanalysis dataset assimilated weather station data, e.g. from the Ny-Ålesund weather station, thereby assuring similar meteorological conditions close to weather station locations. The radiation for each 10-cm layer was calculated by integration of the following formula below, considering the 10-cm photic zone:

$$R_d = R_0 e^{\frac{d-d_0}{z_e}} \tag{4.3}$$

where R_d is the radiation at depth d, R_0 is the incident radiation (data acquired at the CCT [288]), d-d_0 is the depth difference (in this work assumed 1 cm), and z_e is e-folding depth, assuming it to be constant (equal to 2 cm^{-1}) considering the photic zone to be 10 cm and assuming the snowpack to be constant in terms of microstructure and density.

Computational Details

All calculations were carried out using the ORCA quantum chemistry program package [297, 298]. Unless otherwise specified, Density Functional Theory (DFT) calculations were carried out using the WB97-X exchange correlation functional [299]. Dispersion corrections were incorporated using Grimme's-D3 correction combined with the Becke-Johnson damping functions (D3BJ) [300]. The def2-TZVP basis set was used [301]. Implicit solvation effects in water were accounted for using the C-PCM method [302, 303]. Thermal

corrections were computed at 298K.

Supplementary Text

Site description

Gruvebadet Snow Research Site (GSRS), a clean area dedicate to snow research activities ≈1 km southwest from the research village of Ny-Ålesund (78.55°N, 11.53°E, 43 m a.s.l., Figure S 1) [272]. Specifically, samples were collected during the polar night on 21 and 28 December 2021 and 4 January 2022, at sunrise on 23 February 2022 and 1 and 9 March 2022, and during the period of maximum sunlight on 3, 11 and 18 May 2022. Density, temperature profile and water content are shown in Figure S 2. On 16 March 2022, a rain-on-snow event shows that liquid water percolates into the snowpack and is also confirmed by the increase in temperature. Furthermore, since that day, the density of the deep layers has remained unchanged at around 450 kg m^{-3}.

The HDF snow pit was dug on April 24, 2022 on the Holthedalfona glacier (78.95° N, 13.40° E) at an elevation of about 600 m a.s.l. Being located on a flat area of the ice field, the sampling site is not significantly affected by shadows due to the surrounding orography. A coupled energy balance-snow modelling system was used to reconstruct the evolution of the snow cover during the considered season [294, 295]. Based on a model simulation between September 2021, corresponding to the beginning of the snow season, and the sampling date in April 2022, there were 6 distinct snowfall events with at least 15 cm of snow accumulation (see Figure S3 for snowpack evolution).

In addition, to assess the potential effect of different snow accumulations rates, which control the snow layer exposure to sunlight, snow samples from a previous snow pit dug on April 10, 2015 were also analyzed. The snowpit was dug in the accumulation area of the KNG glacier at an altitude of 730 m a.s.l. (78.45° N, 13.20° E). The snow samples collected from the snowpit represented the 2014-15 snow season, i.e. from September 2014 to the sampling date. Compared to the 2021-22 snow season recorded in the HDF snow samples, the modelled 2014-2015 snow season at KNG was comparatively different with more frequent snow precipitation events (11 in the whole season) but of lesser intensity with around 7 cm of snow accumulation on average for each snowfall events (see Figure S4 for snowpack evolution).

Bromine and bromate evolution

In this section we present the concentration of Br^- and BrO_3^- in each site. For all the sites the evolution of BrO_3^- is in continuous evolution from the time of evolution to the time of sampling. As far as Br^- is concerned, only the daily samples (Figure S 5) show a behaviour that tends to increase during the period considered. This is the reason why it was decided to use the Br^-/ BrO_3^- ratio, called $BrO_{3\,nor}^-$. Figures Figure S 6 and Figure S 7 show the concentrations of Br^- and BrO_3^- at 10 cm intervals for HDF and KNG. The concentrations of Br^- are comparable between the two sites, while those of BrO_3^- show significant differences, with values approximately two orders of magnitude lower than those of Br-.

The concentration of Br^- and Br_3^- in aerosols are shown in Table S1

Statistical analysis

We also determined chloride (Cl^-), nitrate (NO_3^-), sulphate (SO_4^{2-}), sodium (Na^+), ammonium (NH_4^+), calcium (Ca^{2+}), and methanesulphonic acid (MSA) in each sample. The results for the major ions show no trend across all snowpits, while MSA demonstrates increasing trends in the samples corresponding to the spring period, consistent with other studies conducted in the same region [273, 304]. In all samples, the concentrations of Cl^- (2.3 ± 1.8 ng g^{-1}) and Na^+ (1.8 ± 1.5 μg g^{-1}) exhibit trends similar to Br^-, with a mean of 10.9 ± 7.7 ng g^{-1}.No trends were observed for SO_4^{2-} and NH_4^+, with average values of 643 ± 553 ng g^{-1} and 53.8 ± 38.5 ng g^{-1}, respectively. Additionally, Ca^{2+} (268 ± 191 ng g^{-1}) and NO_3^- (59.2 ± 47.9 ng g^{-1}) showed no correlations with other ions.

Here we present the Pearson's correlation between the ions presented in this work for all sites and for each sampling area (GSRS, HDF and KNG, Table S 2 Table S3 ,and Table S4 respectively). With the exception of NO_3^-, Ca^{2+} and BrO_3^-, all ions demonstrate correlations with an average value exceeding 0.7. With regard NO_3^- and Ca^{2+}, no correlations were observed with the other ions analysed in this study.

Conversely, both globally and at specific sites (with the exception of KNG), there is a significant correlation (>0.7, p-value <0.001) between $BrO_{3\,nor}^-$ and MSA. This can be attributed to the fact that both can be produced by photo-induced reactions. The former is produced by photo-oxidation in snow, while the latter appears to be a photoproduct of the degradation of DMS in the atmosphere.

Computational validation and results

This computational protocol was validated by means of state-of-the-art DLPNO-CCSD(T) calculations employing the the def2-QZVP basis set and its matching auxiliary correlation counterpart [301, 305–307]. TightPNO setting were used in DLPNO-CCSD(T) calculations.

For the sake of comparison, the results obtained with WB97X-D3BJ/def2-TZVP were also compared with those from M062X/def2-TZVP (M062X) [308] and B3LYP-D3BJ/def2-TZVP (B3LYP) [309–312].

As mentioned in the main text, two possible mechanisms were plausible, denominated the 'radical mechanism' and the 'ionic mechanism'. Both mechanisms involve multiple spin transitions, requiring the calculation of several sections of potential energy surfaces with different spin multiplicities. For calibrating our computational methodology, we initially focused on the first step of the ionic mechanism in the singlet potential energy surface, which sees bromide and ozone as reactants and BrO^- and oxygen as products. This step was investigated at different levels of theory.

Gas-phase results computed with WB97X-D3BJ were initially compared to the data available in literature at the coupled cluster level [313], revealing good agreement in the ΔG values between the reactant and product complexes. The transition state structure for this step was identified using a combined Nudged Elastic Band (NEB)[314] and transition state optimization approach. Frequency calculations confirmed that the TS presented an imaginary frequency associated with the reaction coordinate. The reaction barrier in the gas phase for the first step was found to be 14.87 kcal mol^{-1}, which is more than 20.0 kcal mol^{-1} lower than the one reported in the literature for the same step [313]. To verify the dependence of these results by the nature of the exchange-correlation functional, the transition state was optimized with different functionals, specifically M062X and B3LYP-D3BJ. The resulting geometries were consistent across all methods (Figure S 8).

Furthermore, single point calculations were performed at the DLPNO-CCSD(T) level (Figure S 9) on the NEB "images" along the Minimum Energy Path connecting reactants and products. These results indicate that a transition state with the same energy is also present in the DLPNO-CCSD(T) potential energy surface.

These results indicate that WB97X-D3BJ/def2-TZVP is a robust computational methodology for the chemistry investigated in this work, providing results that are consistent with those from state-of-the-art DPNO-CCSD(T) calculations. The potential energy surface of the proposed radical mechanism initiated by photo-absorption was explored at the WB97X-D3BJ level of theory. Figure S 10 reports the relative free energies of all intermediates computed in the gas-phase (red) and in water (black). Notably, while all the steps involving the oxidation of Br are significantly exergonic and irreversible in water, the situation changes dramatically in the gas phase. In particular, when simulated in the gas phase rather than in water, one step (the third) even switches from exergonic to endergonic. The computed section of potential energy surface for the alternative ionic mechanism is shown in Figure S 11. All steps of this mechanism were found to be exoergonic both in the presence and absence of the solvent.

The first step of the ionic mechanism was further examined by (i) calculating the transition states for both the singlet and triplet states, and (ii) identifying the minimum energy crossing point (MECP) between their potential energy surfaces. Two possible pathways were found. In the "early" crossing scenario (Figure S 12), the singlet–triplet crossing occurs before the transition state, while in the "late" crossing case (Figure S 13), it occurs afterward. The latter corresponds to the minimum energy path, with an associated energy barrier of 20.7 kcal mol^{-1}.

The geometries of the species involved are given in Appendix B

Figures

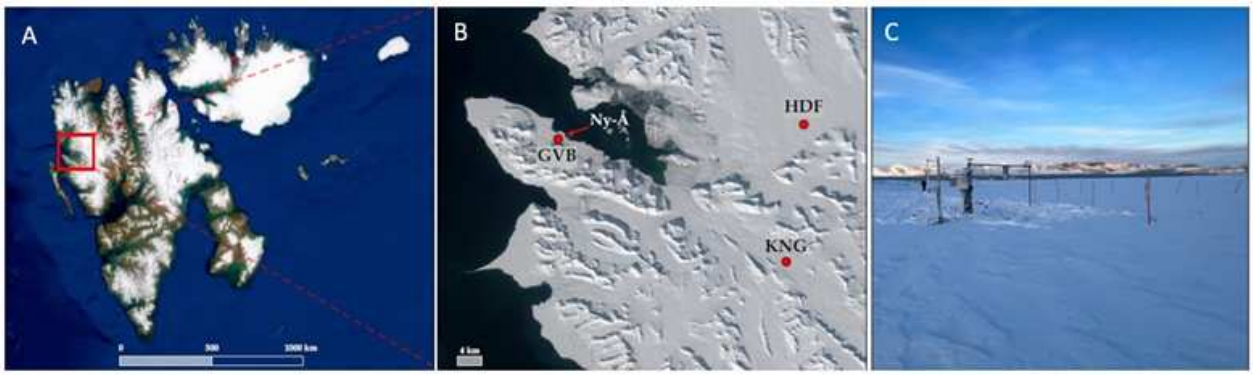

Figure S1 Sampling sites. Sampling was carried out at the Svalbard archipelago. (a)Snowpits were dug in the HDF and KNG glaciers (b); seasonal and daily surface snow samples were collected at the GSRS snowfield (c).

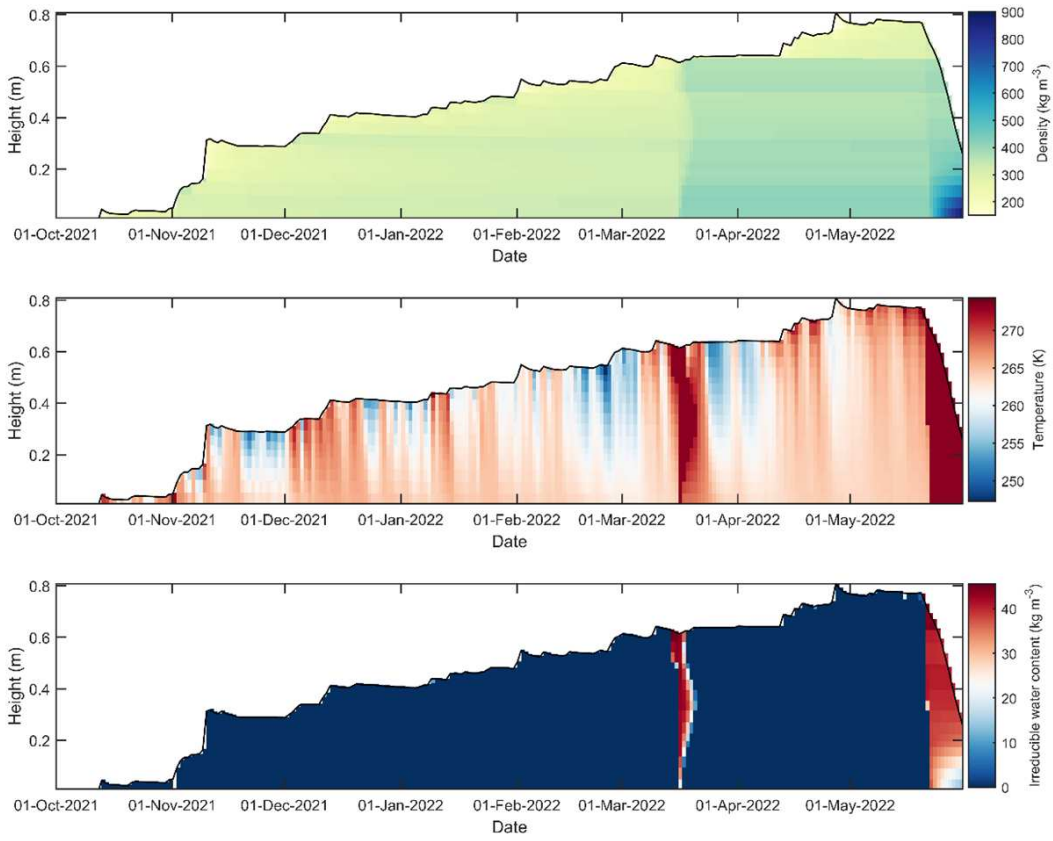

Figure S2 Model of snowpack evolution at GSRS. Density (top), snow temperature (middle) and water content (bottom).

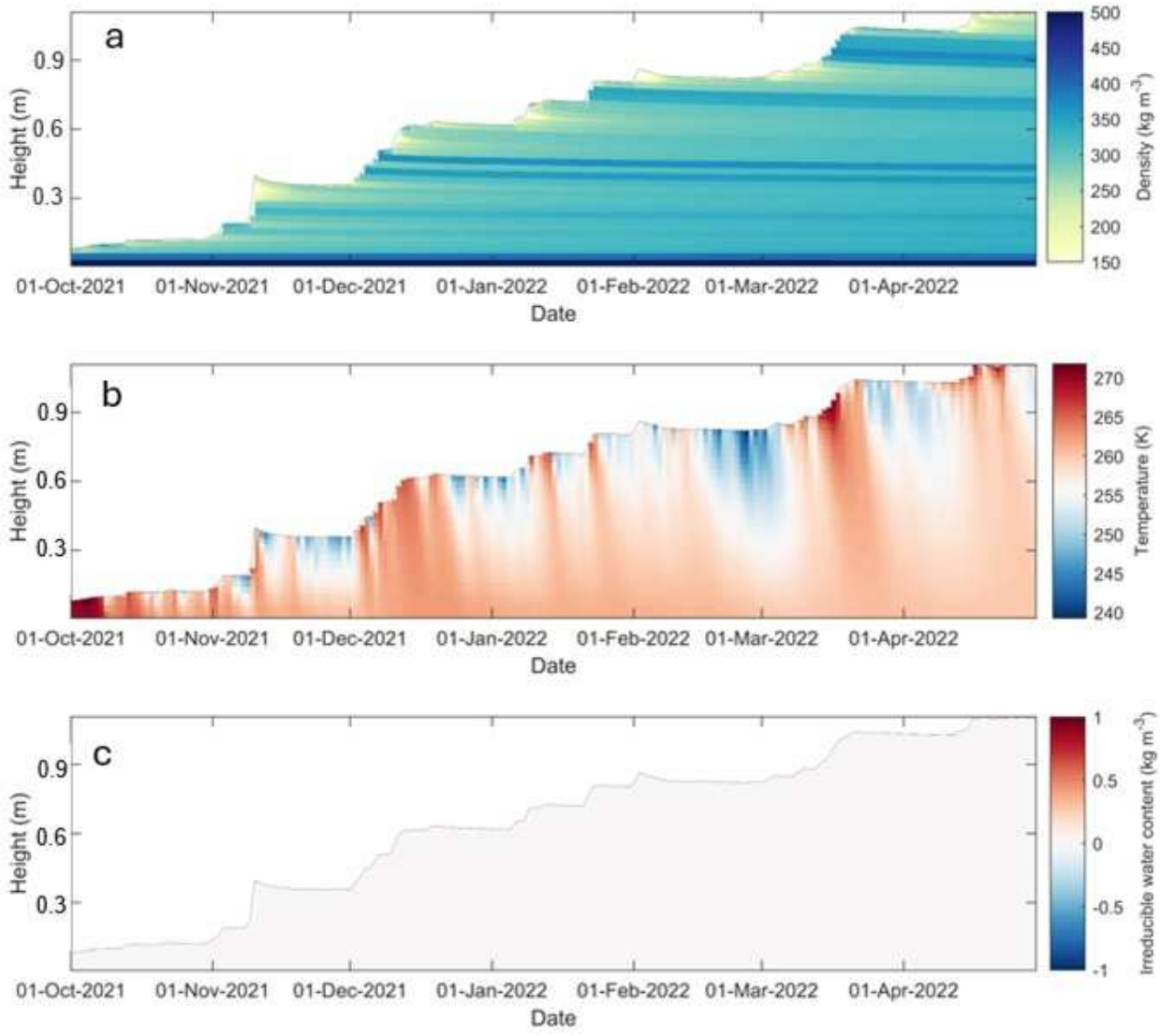

Figure S3 Model of snowpack evolution at HDF Density (top), snow temperature (middle) and water content (bottom).

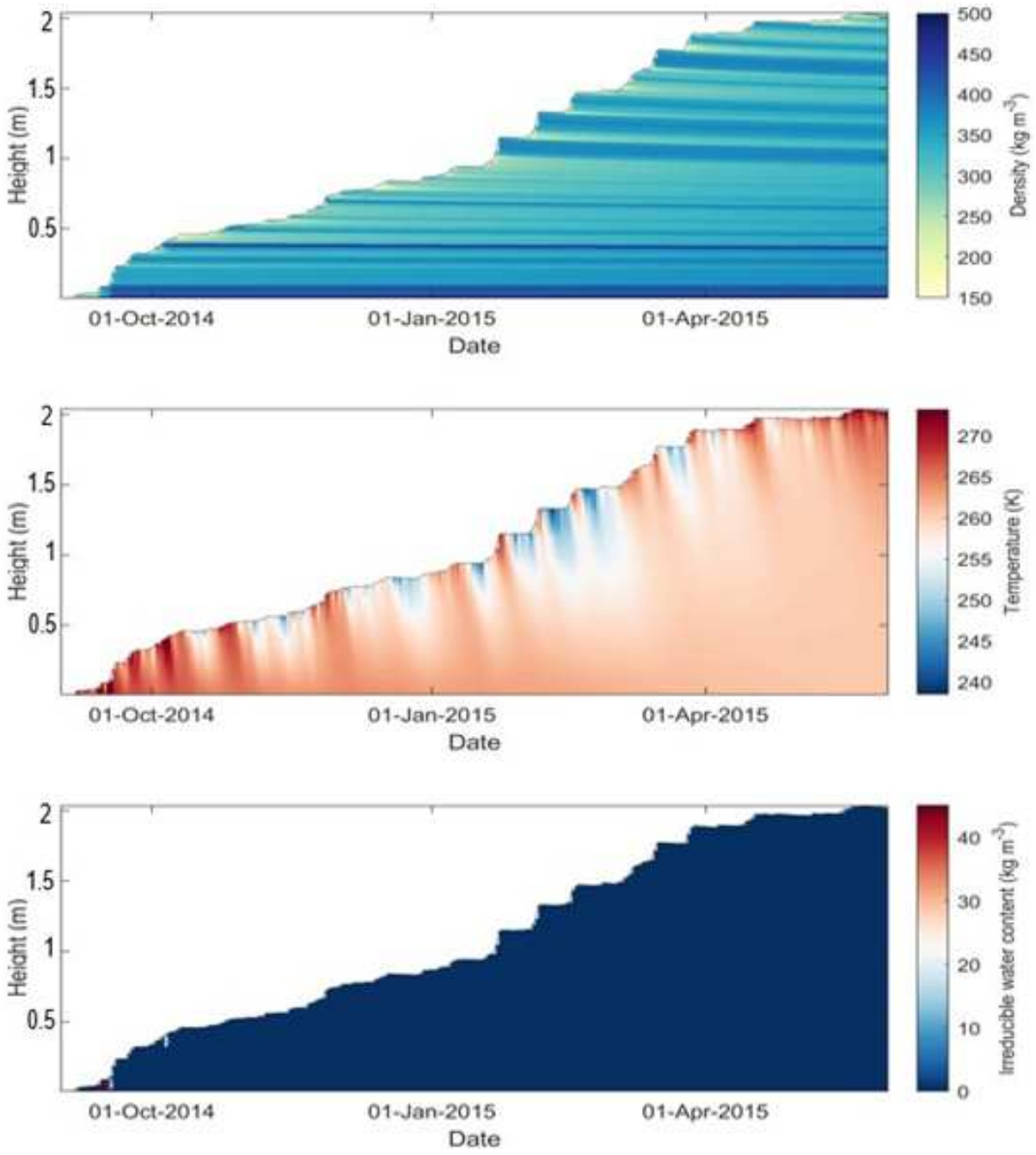

Figure S4 Model of snowpack evolution at KNG. Density (top), snow temperature (middle) and water content (bottom).

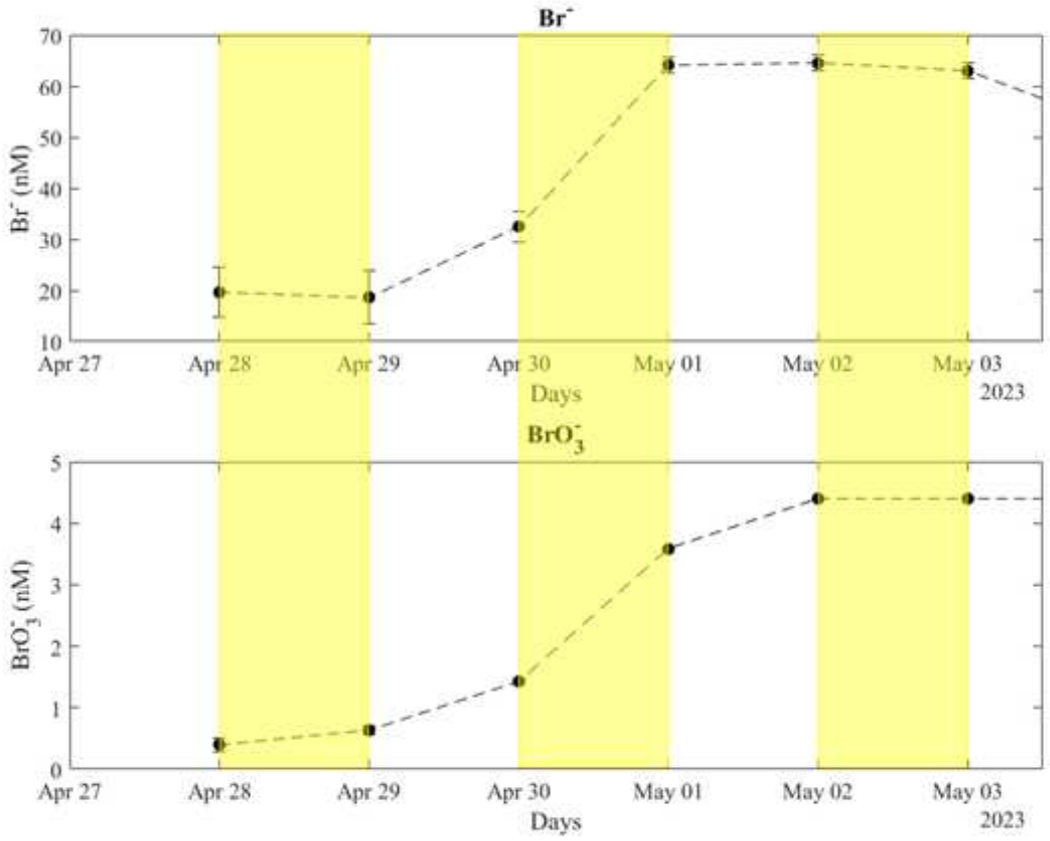

Figure S5 Bromide (Br^-, top) and bromate (BrO_3^-, bottom) trends during daily surface snow sampling.

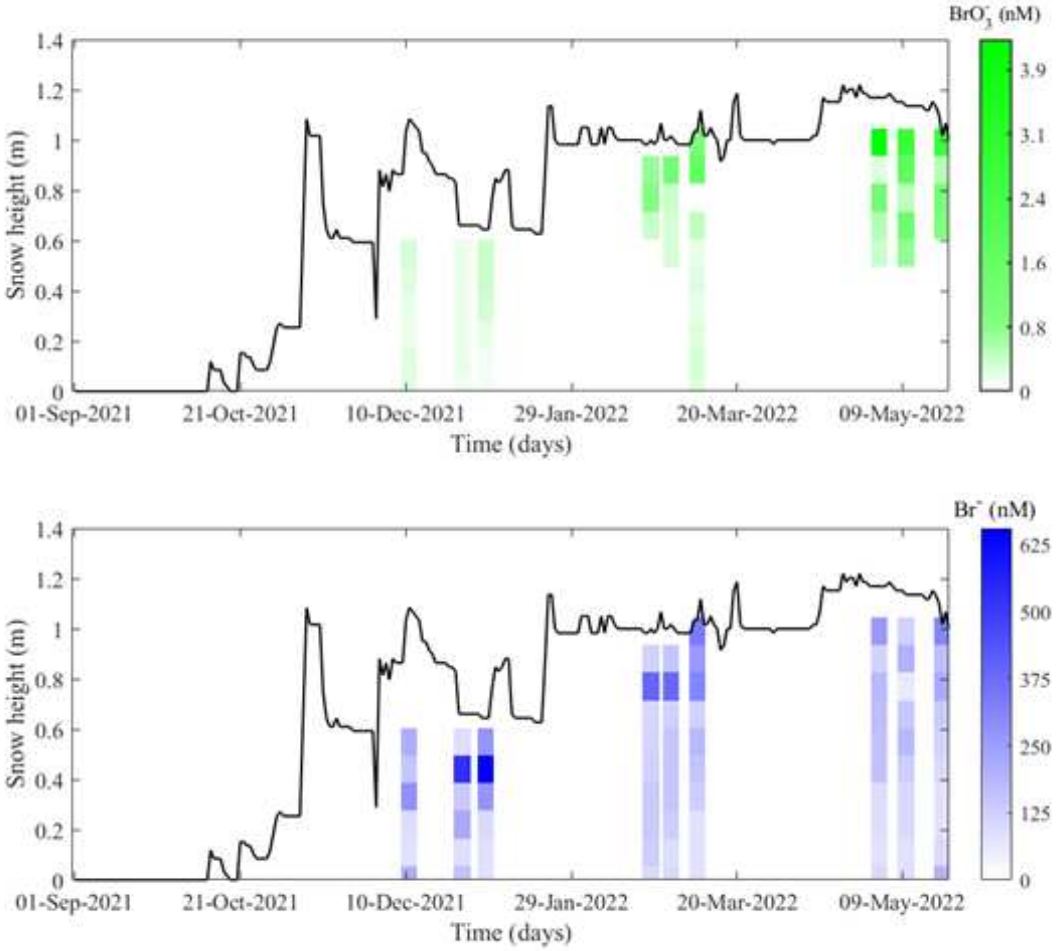

Figure S6 Annual trend of (BrO_3^- top) and Br^-(bottom) in GRSR.

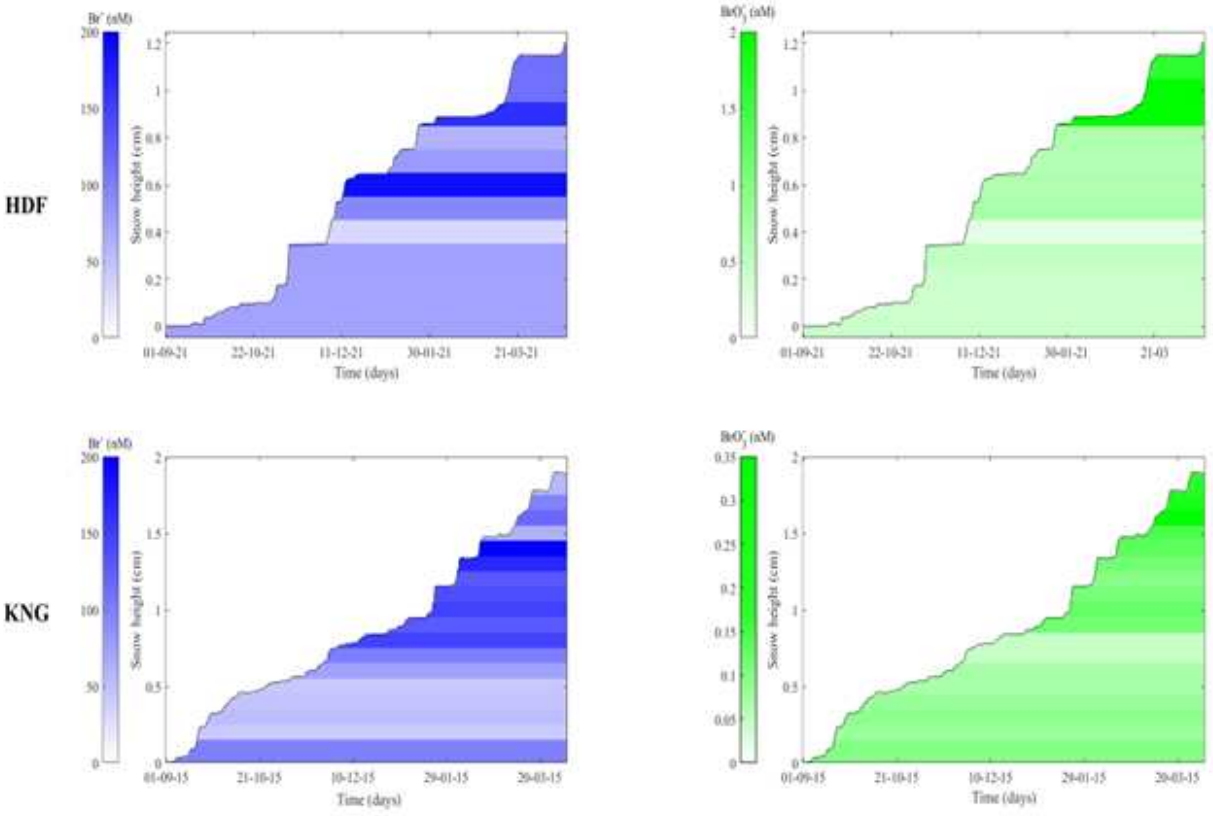

Figure S7 Annual trend of Br^- (left) and BrO_3^- (right) in HDF (top) and KNG (bottom)

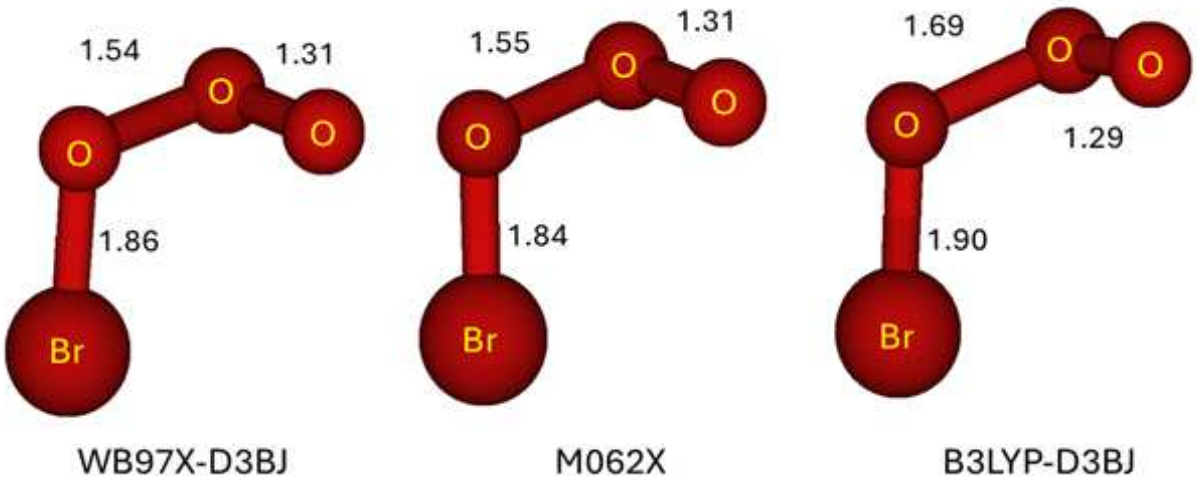

Figure S8 TS structures for the first step of the ionic mechanism. Values were computed at WB97X-D3BJ, M062X and B3LYP-D3BJ levels of theory. Bond lengths are in Angstroms. See text for details.

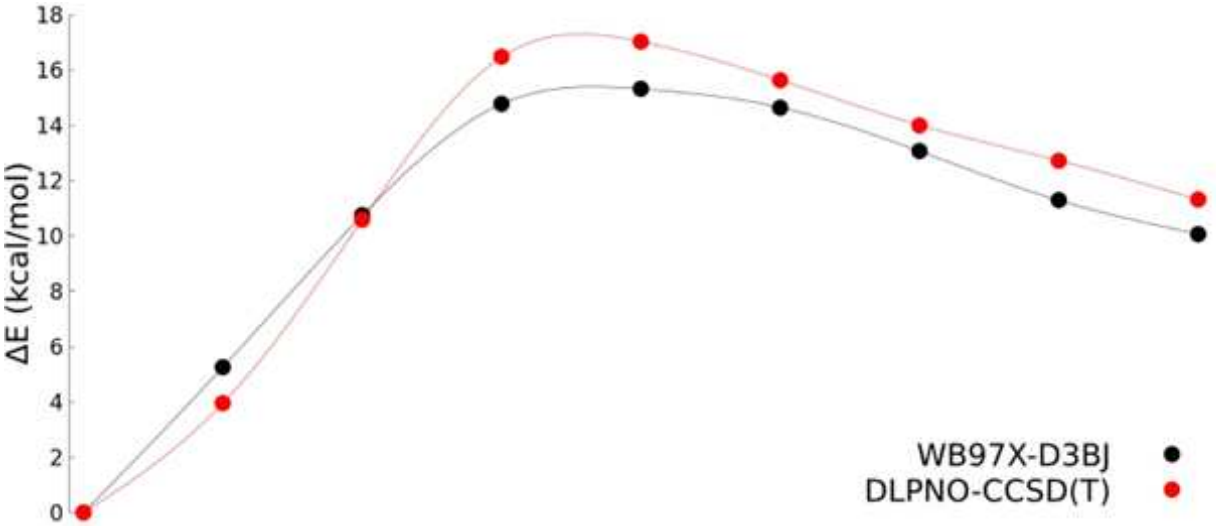

Figure S9 Section of the singlet potential energy surface connecting reactants and products in the first step of the ionic mechanism. DLPNO-CCSD(T) single-point energy calculations were performed on NEB images optimized at the WB97X-D3BJ level. The computed energies of the NEB images are connected by a solid line as a visual aid along the Minimum Energy Path.

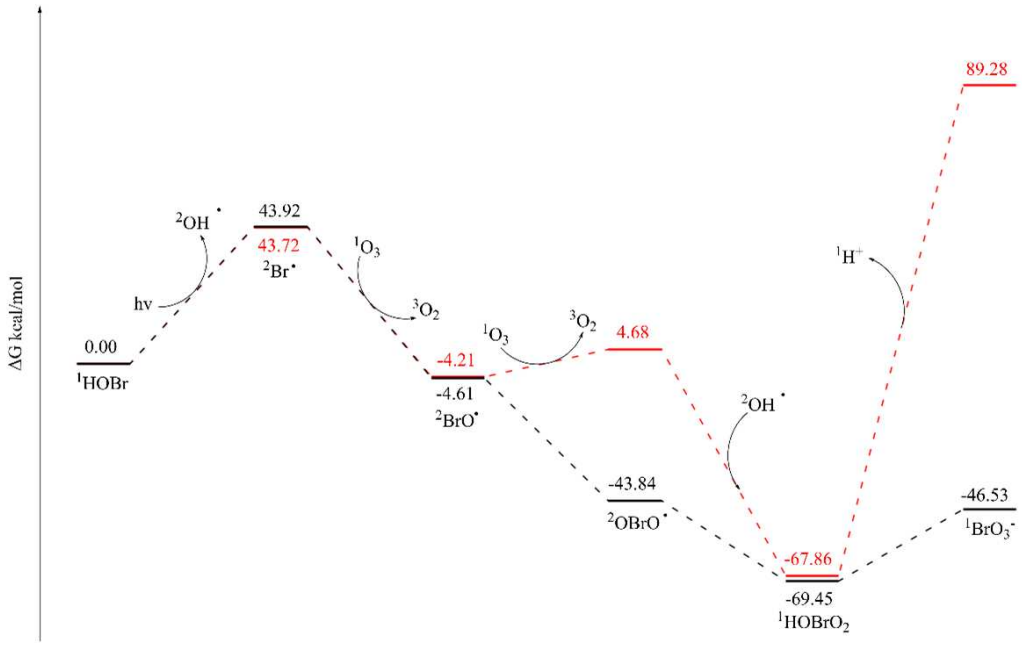

Figure S10 Potential energy surface of the radical mechanism computed at WB97X-D3BJ level of theory. Gas-phase results are reported in red, while calculations performed with the implicit solvent model C-PCM(Water) are reported in black.

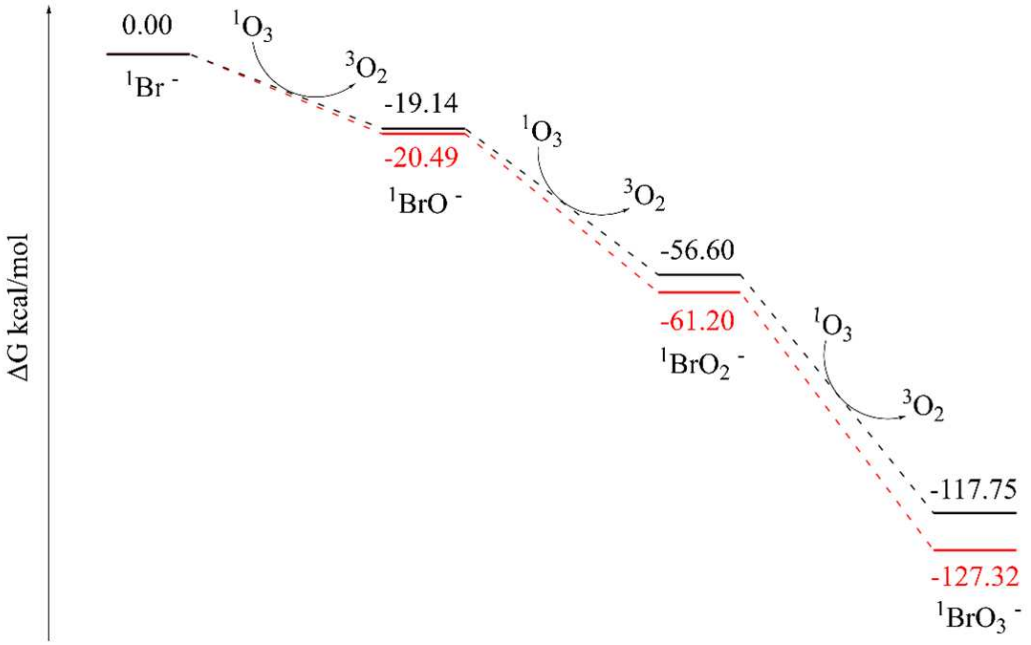

Figure S11 Potential energy surface of the ionic mechanism computed at WB97X-D3BJ level of theory. Gas-phase results are reported in red, while calculations performed with the implicit solvent model C-PCM(Water) are reported in black.

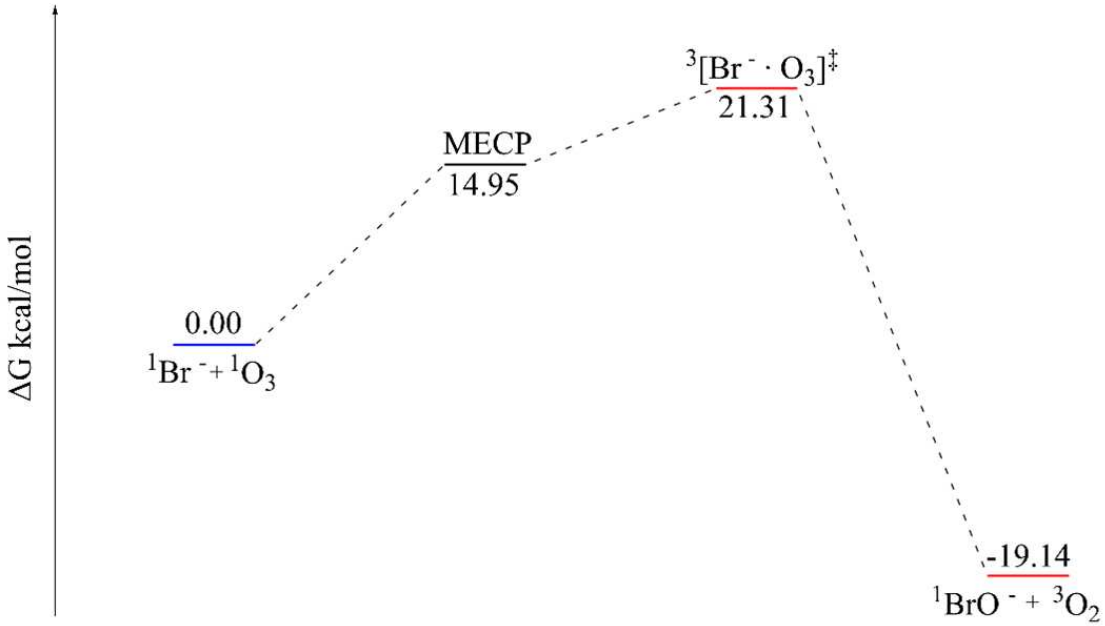

Figure S12 Early MECP of the first step of the ionic mechanism computed at the WB97X-D3BJ level of theory. Calculations were performed with the implicit solvent model C-PCM(Water). Singlet and triplet states are reported in blue and red, respectively; the MECP is reported in black.

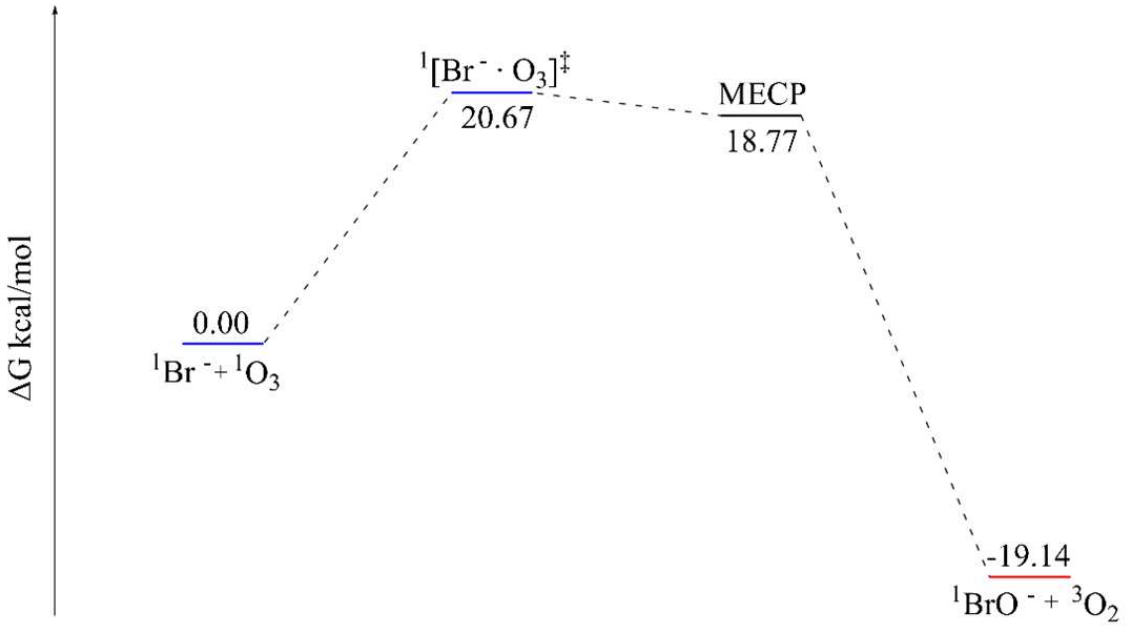

Figure S13 Late MECP of the first step of the ionic mechanism computed at the WB97X-D3BJ level of theory. Calculations were performed with the implicit solvent model C-PCM(Water). Singlet and triplet states are reported in blue and red, respectively; the MECP is reported in black.

Tables

Table S1 Br^- and BrO_3^- concentrations in aerosols at GVB, sampled from February 21 to June 8, 2022. The method detection limit (MDL) for BrO_3^- is 8.34×10^{-4} ng m^{-3}.

Start date	End date	Volume (m^3)	Br^- (ng m^{-3})	BrO_3^- (ng m^{-3})	$BrO_{3\ nor}^-$
21/02/2022	28/02/2022	11011	20.82	<MDL	
28/02/2022	07/03/2022	11127	1.69	<MDL	
14/03/2022	21/03/2022	11091	1.45	$6.63\text{x}10^{-3}$	$4.58\text{x}10^{-3}$
21/03/2022	28/03/2022	10972	4.05	<MDL	
28/03/2022	05/04/2022	12690	4.24	<MDL	
05/03/2022	12/04/2022	11126	4.59	<MDL	
12/03/2022	19/04/2022	11135	2.27	<MDL	
19/03/2022	26/04/2022	11138	2.76	<MDL	
26/03/2022	03/05/2022	11138	3.50	<MDL	
03/05/2022	10/05/2022	11182	7.37	<MDL	
10/05/2022	18/05/2022	12856	3.31	<MDL	
18/05/2022	25/05/2022	11077	2.55	<MDL	
25/05/2022	01/06/2022	11284	3.32	<MDL	
01/06/2022	08/06/2022	11286	1.39	<MDL	

Table S2 Pearson's correlation matrix for ions in all sites. The values in bold indicate a p-value < 0.001.

	Br^-	BrO_3^-	$BrO_{3\ nor}^-$	Cl^-	NO_3^-	SO_4^{2-}	MSA	Na^+	NH_4^+	Ca^{2+}
Br^-	1.00									
BrO_3^-	0.17	1.00								
$BrO_{3\ nor}^-$	-0.08	**0.77**	1.00							
Cl^-	**0.95**	0.15	-0.08	1.00						
NO_3^-	0.17	0.16	0.18	0.18	1.00					
SO_4^{2-}	**0.68**	**0.21**	0.03	**0.76**	**0.34**	1.00				
MSA	0.05	**0.66**	**0.72**	0.01	**0.24**	0.17	1.00			
Na^+	**0.92**	0.14	-0.08	**0.99**	0.17	**0.76**	0.00	1.00		
NH_4^+	**0.73**	**0.43**	**0.23**	**0.73**	0.06	**0.42**	0.08	**0.73**	1.00	
Ca^{2+}	**0.27**	-0.07	**-0.20**	**0.35**	0.16	**0.49**	0.10	**0.38**	0.02	1.00

Table S3 Pearson's correlation matrix for ions in GSRS The values in bold indicate a p-value < 0.001.

	Br^-	BrO_3^-	$BrO_{3\ nor}^-$	Cl^-	NO_3^-	SO_4^{2-}	MSA	Na^+	NH_4^+	Ca^{2+}
Br^-	1.00									
BrO_3^-	0.18	1.00								

Continued on next page

Table S3 continued

	Br^-	BrO_3^-	$BrO_{3\ nor}^-$	Cl^-	NO_3^-	SO_4^{2-}	MSA	Na^+	NH_4^+	Ca^{2+}
$BrO_{3\ nor}^-$	0.03	**0.90**	1.00							
Cl^-	**0.97**	0.11	-0.02	1.00						
NO_3^-	**0.66**	**0.35**	**0.31**	**0.66**	1.00					
SO_4^{2-}	**0.91**	**0.33**	0.23	**0.93**	**0.71**	1.00				
MSA	0.18	**0.90**	**0.81**	0.10	**0.33**	**0.25**	1.00			
Na^+	**0.96**	0.11	-0.02	**0.99**	**0.65**	**0.94**	0.10	1.00		
NH_4^+	**0.84**	**0.36**	**0.25**	**0.84**	**0.60**	**0.85**	**0.25**	**0.84**	1.00	
Ca^{2+}	**0.38**	0.13	0.04	**0.42**	0.16	**0.26**	**0.32**	0.16	**0.42**	1.00

Table S4 Pearson's correlation matrix for ions in HDF The values in bold indicate a p-value < 0.001.

	Br^-	BrO_3^-	$BrO_{3\ nor}^-$	Cl^-	NO_3^-	SO_4^{2-}	MSA	Na^+	NH_4^+	Ca^{2+}
Br^-	1.00									
BrO_3^-	**0.52**	1.00								
$BrO_{3\ nor}^-$	-0.18	**0.67**	1.00							
Cl^-	**0.95**	**0.55**	-0.14	1.00						
NO_3^-	-0.13	-0.02	0.10	-0.33	1.00					
SO_4^{2-}	**0.92**	**0.71**	0.09	**0.97**	-0.31	1.00				
MSA	-0.19	**0.51**	**0.92**	-0.13	0.07	0.09	1.00			
Na^+	**0.95**	**0.56**	-0.14	**0.99**	-0.32	**0.97**	-0.13	1.00		
NH_4^+	0.49	0.42	-0.01	**0.53**	-0.47	**0.55**	-0.04	**0.54**	1.00	
Ca^{2+}	**0.79**	**0.82**	0.25	**0.87**	-0.29	**0.0.93**	0.19	0.87	**0.58**	1.00

Table S5 Pearson's correlation matrix for ions in KNG The values in bold indicate a p-value < 0.001.

	Br^-	BrO_3^-	$BrO_{3\ nor}^-$	Cl^-	NO_3^-	SO_4^{2-}	MSA	Na^+	NH_4^+	Ca^{2+}
Br^-	1.00									
BrO_3^-	-0.03	1.00								
$BrO_{3\ nor}^-$	**-0.55**	**0.76**	1.00							
Cl^-	**0.80**	-0.08	**-0.52**	1.00						
NO_3^-	0.02	0.03	-0.14	0.25	1.00					
SO_4^{2-}	**0.49**	-0.18	**-0.59**	**0.74**	**0.47**	1.00				
MSA	-0.32	0.24	**0.42**	-0.17	-0.07	-0.15	1.00			
Na^+	**0.74**	0.01	-0.37	**0.96**	0.21	**0.67**	-0.18	1.00		
NH_4^+	**0.52**	0.34	-0.04	**0.80**	**0.52**	**0.60**	0.02	**0.82**	1.00	
Ca^{2+}	**0.51**	0.04	-0.30	**0.84**	**0.41**	**0.0.82**	0.09	**0.85**	**0.78**	1.00

4.3 Bromate and bromide reactions in ice

This study, led by researchers at the Korean Polar Research Institute, revealed that freezing solutions containing Br^- can activate a bromide oxidation. This pathway significantly accelerates the reaction with BrO_3^-, that is otherwise negligible in liquid conditions. This acceleration is attributable to the concentration effect of freezing, which increases the likelihood of chemical species encountering each other within the ice.

The work was carried out in close analytical collaboration with Ca' Foscari University and the ISP-CNR, who provided critical support for spectroscopic and instrumental analyses. Several techniques were used to investigate the chemical transformation mechanisms: UV-visible spectroscopy and HRMS to monitor brominated species; ICP-MS to measure total Br content; ion chromatography to analyse dissolved Br species; and Raman microscopy to study the spatial distribution of hypobromous acid generated *in situ* in the ice.

To better understand the conditions influencing bromide activation, the freezing effect was studied by varying experimental parameters such as freezing temperature, initial solution pH, and reactants amount.

Published in *Water Research* in 2025, this study provides concrete experimental evidence for a new mechanism of freezing-induced Br activation, with important implications for atmospheric chemistry in Arctic regions.

Bromide oxidation by bromate in a frozen solution and reactive bromine species production

Yong-Yoon Ahn[a], Quoc Anh Nguyen[a,b], Andrea Spolaor[c,d], Stefano Frassati[c,d], Elena Barbaro[c,d], Giulio Cozzi[d], Clara Turetta[d], Hoon Oh[e], Jaesang Lee[e], Kitae Kim[a, b, ∗]

[a]Korea Polar Research Institute (KOPRI), Incheon, 21990, Republic of Korea

[b]Department of Polar Science, University of Science of Technology (UST), Incheon, 21990, Republic of Korea

[c]Ca' Foscari University of Venice, Department of Environmental Sciences, Informatics and Statistics, Venice Mestre, Italy.

[d]Institute of Polar Sciences-National Research Council (CNR-ISP), Venice Mestre, Italy

[e]Civil, Environmental, and Architectural Engineering, Korea University, Seoul 02841, Republic of Korea

Corresponding authors: Kitae Kim

Corresponding author's email: ktkim@kopri.re.kr

Keyword: ice chemistry, bromine explosion, bromide, hypobromite, freeze concentration

Abstract

A sudden increase in tropospheric reactive bromine species (such as BrO radical) concentration has been observed in the Arctic springtime (bromine explosion). The reactive bromine radicals originate from the Br_2 oxidation; however, the role of ice chemistry in bromine activation, especially freezing-induced Br^- oxidation for Br_2 production, is not significantly considered yet. Notably, the freezing phenomenon is prevalent in polar region. In this study, we demonstrate that the Br^- containing water freezing can provide a potential Br^- oxidation pathway. The oxidation of Br^- by BrO_3^- was negligible under aqueous conditions, while it was highly accelerated by freezing the solution. We proposed that the accelerated chemical reaction was due to the freezing concentration effect. The chemical transformation mechanism was suggested. The chemical transformation of Br^- was considered using the UV-visible absorbance spectrometer and the high-resolution mass spectroscopy (HRMS) measurement. The total Br content was measured using inductive coupled plasma mass spectroscopy (ICP-MS) and the dissolved Br species was monitored using ion chromatography. The spatial distribution of in-situ generated hypobromous acid in ice was analyzed using Raman microscopy. The oxidation characteristics of the system were monitored at various experimental conditions, such as the freezing temperature, the initial pH, and the dose of reactants. This study provides experimental evidence for the freezing-induced bromide activation in the Arctic.

Introduction

The tropospheric halogen species exert on the oxidizing capacitance at the troposphere significantly. Historically, the important role of halogens in the troposphere was firstly identified in the polar regions [315]. Among the four (isotopic) stable halogen elements (^{19}F, ^{35}Cl, ^{79}Br, and ^{127}I), the relative abundances of Br and I on the Earth's surface are smaller than Cl; however, the presence of reactive bromine species in the Arctic atmosphere can be rapidly increased via the bromine explosion event during the sunlit season [316]. It is noted that the local ozone can be completely eliminated in a few days by the BrO at a mixing ratio of tens of parts per trillion [316]. The source of atmosphere Br in the polar region is seawater, and Br in seawater originates from the oceanic lithosphere [317]. The Br in seawater mostly occurs as a form of bromide (Br^-), nevertheless a rare oceanic life (some coral and plankton) can bind Br and make organo-Br species [317, 318]. According to the previous research, Br^- contained brine is separated from the frozen water matrix during seawater freezing [240]. Therefore, high salinity is found on young (first-year) sea ice surface. Possibly, the newly formed sea ice surfaces supply Br^- from seawater to the air by lifting through blowing [319]. In addition, the protonation of Br^- to HBr by the atmospheric acid deposition, such as SO_2 and HNO_3, can contribute Br mass transport between sea and air. Under the oxidative environment, Br^- is oxidized to generate various reactive bromine species [315]. The ice surface catalyzed photochemical process was considered the major oxidation factor [15, 320], but some literature inferred the possibility of dark reaction for bromide activation in the region of high ionic strength in snow and ice [35]. Notably, several studies have detected the freezing-facilitated generation of volatile halogen gases including interhalogen species [250, 251, 321–323]. However, there are no consideration on the BrO_3^- mediated Br^- oxidation at all up to now because two species are chemically stable in general [324]. It is noted that BrO_3^- production from Br^- oxidation by O_3 need to be considered: though the O_3 possibly reduces HOBr, the trace amount of BrO_3^- also can be produced by O_3 induced Br^- oxidation [325]. Here, we first report the ice chemistry between two stable bromine species for Br_2 production.

Previously, it is known that the chemical reaction between Br^- and BrO_3^- can be take place but in the extremely acidic condition and high reactants concentration [326–329].

$$-\frac{d[BrO_3^-]}{dt} = k_1[BrO_3^-][H^+]^2[Br^-] + k_2[BrO_3^-][H^+]^2[Br^-]^2 \tag{4.4}$$

The kinetic reaction constant k_1 and k_2 at 25^{o}C were estimated to be 4.12 ± 0.05 M^{-3} s^{-1} and 0.810 ± 0.02 M^{-4} s^{-1}, respectively [327]. Therefore, at $[BrO_3\text{-}]_0 = 20$ μM, $[Br^-]_0 = 150$ μM, and $[HClO_4]_0 = 1$ mM (ca. pH 3), the half-life for BrO_3- (the period to reach $[BrO_3\text{-}] = 10$ μM) was calculated to be approximately 25 years, which can be considered as a negligible progression at this diluted solution under room temperature and 1 atmosphere (101.3 kPa). We again emphasize that the previous study for the Br^- / BrO_3^- system was investigated at a significantly higher concentration of reactants (in an extremely acidic solution) than the above-calculated condition: the ionic strength was adjusted to 3 M which is approximately 5000 times higher than the above. However, as we demonstrate in the present study, the Br^- / BrO_3^- reaction at diluted conditions, as mentioned above, can be notably accelerated within 30 min via freezing of the solution. This freezing-induced chemical reaction is poorly understood and has been overlooked until the present: although several studies have reported the intriguing BrO_3^- derived chemical reaction in ice, the unique behavior of BrO_3^- for Br^- oxidation in ice has not been reported yet [330–335]. To the best of our knowledge, this is the first study to report on BrO_3^- induced Br^- oxidation in ice.

Freezing process is considered as a chemical reaction freezing procedure because the chemical reaction rate

is normally inhibited by temperature decrease. Therefore, many violent chemical experiments were conducted under low temperatures for safety. The temperature dependence of the chemical reaction can be expressed by the decline in molecular energy in cold conditions. However, several studies have been reported that are associated with the accelerated chemical reaction during the freezing process [336]. These indicate that there are some factors that overcome the empirical Arrhenius relationship when freezing a solution [337]. Notably, water impurity results in a decrease in the ice melting point (eutectic point); therefore, a liquid phase in the ice grain boundary region can possibly be established if the water is frozen at moderate temperatures [338]. Because the increasing ice crystal repels the impurities, these impurities accumulate in the ice grain boundary region. Ultimately, the concentration of impurities in this region considerably increases, and this effect probably enhances the chemical reaction between reactants [339]. This phenomenon is called the freeze concentration effect. In addition, not only the freezing concentration effect but also the freeze potential effect is suggested to interpret the increasing chemical reaction; however, sufficient studies are still needed to confirm the influence of the phenomenon [340–343]. The scheme for freeze potential affirmed that the reaction can be enhanced by the electrochemical effect that is created by disproportionate ion distribution between ice crystals and liquid-like regions. In addition, the liquid water contents in ice grain boundary region is reduced during the freezing process, and the acid-base equilibrium possibly affects the chemical equilibrium in the brine in the region [344].

This study compared the transformation of Br^- and BrO_3^- in water and ice and attempted to reveal the chemical transformation mechanism using the ion chromatography (IC), UV-vis spectrometer, high-resolution mass spectrometry (HRMS), and inductively coupled plasma mass spectroscopy (ICP-MS). Then, we confirmed the freeze concentration phenomenon in the ice using the Raman spectroscopy. We tested the Br^-/BrO_3^- reaction in various experimental conditions, such as freezing temperature, initial pH, and initial dosage. Finally, we discussed the natural relevance of the frozen Br^-/BrO_3^- system through investigation of O_3 induced Br^- oxidation and the experiment in extremely low reactant concentration conditions. This study demonstrated that the Br^-/BrO_3^- reaction can be accelerated by freezing the solution. Because bromine behavior in polar regions is important, and insufficient attention has focused on the freezing-induced chemical reaction on the bromine explosion phenomenon, our study provides experimental evidence of a novel alternative bromine generation scenario in the Arctic.

Materials and methods

Materials

The following chemicals were used in this study: sodium bromate (Sigma-Aldrich, ≥99%), sodium bromide (Sigma-Aldrich, ≥99%), sodium iodide (Sigma-Aldrich, ≥99%), 2,2-azino-bis(3-ethylbenzothiazoline)-6-sulfonic acid diammonium salt (ABTS, Sigma-Aldrich, ≥98%), hydrochloric acid (Sigma-Aldrich, 35%), perchloric acid (Sigma-Aldrich, 60%), nitric acid (Sigma-Aldrich, 70%), sodium hydroxide (Sigma-Aldrich, 1 N), cresol red (CR, Aldrich, 95%), ^{18}O-labeled H_2O (Sigma-Aldrich, 97%), sodium carbonate (Sigma-Aldrich, ≥99.5%), and sodium bicarbonate (Sigma-Aldrich, ≥99.7%).

All solutions in this study were prepared using deionized water (18.2 MΩ·cm), which was purified using a Barnstead water purification system (Milli-Q Direct 16).

Experimental procedure

The working solution samples of BrO_3^- and Br^- (typically $[BrO_3^-] = 20$ μM, and $[Br^-] = 150$ μM) were prepared by adding aliquots of chemical stock solutions (typically 0.8 mL of 10 mM BrO_3^- and 6 mL of 10 mM Br^-) to 393.2 mL of deionized water in a glass beaker. The initial pH of solution samples was controlled by 60% $HClO_4$ or 1 N NaOH using a Thermo Scientific Orion 2-Star Benchtop pH meter (typically pH 3). Aqueous samples (10 mL) were placed in 15mL VWR centrifuge tubes. These tubes were introduced in the temperature-controlled system using ethanol as a coolant, which was pre-maintained at $-20\,^{\circ}$C. In this study, experiments were conducted at $-20\,^{\circ}$C for reactions in the ice phase and $25\,^{\circ}$C for reactions in the aqueous phase. The time zero was defined as the moment the tubes were placed in the ethanol bath with the reaction temperature maintained constant at $-20\,^{\circ}$C. At pre-determined time points, the frozen centrifuge tubes were withdrawn from the ethanol bath, and a beaker containing lukewarm water at $30\,^{\circ}$C was immediately introduced for 2 min to thaw completely frozen samples before analysis.

Analytical methods

The concentrations of BrO_3^- and Br^- were quantitatively measured using an ion chromatography system (Thermo Fisher Scientific, Dionex Aquion) equipped with a suppressor (AERS 500), a 4-mm column (AS 23), and guard column (AG 23). The eluent solution was a mixture of 0.8 mM sodium bicarbonate ($NaHCO_3$) and 4.5 mM sodium carbonate (Na_2CO_3) with a flow rate of 1 mL min^{-1}. To convert the heights of BrO_3^- and Br^- peaks to their respective concentrations, calibration curves were constructed using six known standard solutions of BrO_3^- and Br^- (200, 100, 50, 25, 12.5, and 6.25 μM).

High-resolution mass spectroscopy (Thermo Fisher Scientific, Q Exactive Focus) with an ^{18}O-water experiment was conducted to confirm the oxygen source. We manually injected the samples into the mass spectrometer using a Hamilton syringe with 5 μL min^{-1} of injection speed. The ionization parameters were changed as follows: a detection range of m/z 94 to 99 for OBr^-, m/z 125 to 135 for BrO_3^-, m/z 232 to 247 for Br_3^-, m/z 180 to 190 for IBr_2^-, a resolution 12500, spray voltage of -2.50 kV, a capillary temperature of 320 °C, sheath gas flow rate of 12 a.u., auxiliary gas flow rate of 1 a.u., auxiliary gas heater temperature of 300 °C, S lens RF level of 50.0, maximum injection time of 100 ms, and an automatic gain control (AGC) target of 1×10^5. The results were analyzed using FreeStyle 1.5 software.

The spatial distribution of BrO_3^- during freezing was visualized using a confocal Raman spectroscope (Renishaw, inVia Qontor) equipped with a microscope stage [345]. An aqueous sample containing 2 mM of BrO_3^-, 2 mM of Br^-, and pH 3 was frozen at -20°C (liquid nitrogen was used as a coolant) by mounting on a temperature-controlled microscope stage (Linkam Scientific, THMS600) at a rate of -2°C min^{-1}. BrO_3^- and HOBr distributions were in-situ scanned by measuring the intensities at 805 and 932 cm^{-1}, respectively. The excitation source was a monochromatic 532 nm laser.

UV-vis spectroscopy (Shimadzu, UV-2600) was used to monitor the presence of hypobromite (BrO^-) in the solution. The absorbance of BrO^- was determined at 329 nm using a 1-cm pathlength UV cuvette, and the concentration was calculated using Beer-Lambert's law: Abs. $= \varepsilon lc$, where $l = 1$ cm and $\varepsilon = 332$ $M^{-1}cm^{-1}$ [346]. The concentration of BrO^- was also double-checked using the ABTS method [347]. Samples (2.5 mL) were placed in 15 mL centrifuge tubes filled with 2 mL of deionized water, 0.25 mL of 1 g L^{-1} ABTS, and 0.25 mL of 0.05 M H_2SO_4. The mixed samples were maintained in the dark for 2 h before analysis. The absorbance values of the samples at 405 nm were measured using a UV-Vis spectrophotometer. The concentration of $ABTS^{\bullet+}$, generated via the reaction between ABTS and BrO^-, was calculated using an absorption coefficient of 31,600 $M^{-1}cm^{-1}$. The concentration of BrO^- was estimated from the corresponding $ABTS^{\bullet+}$ intensity.

The change in pH during freezing was examined using the UV-Vis absorption spectra of cresol red (CR), an acid-base indicator [348, 349]. A 3 mL sample containing 20 μM of BrO_3^-, 150 μM of Br^-, 66.7 μM of CR, and pH 3 was placed in a 4 mL plastic rectangular cuvette. The cuvette was placed in an ethanol bath, pre-maintained at -20°C for 1 h. The frozen cuvette was removed from the ethanol bath, and then UV-Vis absorption spectra were acquired immediately without thawing, using a UV-Vis spectrophotometer. Frozen deionized water was used as a reference.

The total Br content analysis was performed using inductively coupled plasma mass spectroscopy (Thermo Fisher Scientific, iCAP TQe). The Br measurement was carried out in single quadrupole and KED mode: cool gas (Ar) flow 14 L min^{-1}, auxiliary flow 0.8 L min^{-1}, nebulizer flow 1.08 L min^{-1}, collision/reaction gas (He) flow 4.73 L min^{-1} for KED mode.

The bromide speciation analysis was performed using an ion chromatography system (Thermo Scientific, Dionex-2100) coupled to an inductively coupled plasma sector-field mass spectrometer (ICP-SFMS, Thermo Scientific, Element XR). The chromatographic separation was performed using a Dionex Ion AS19 anion exchange column (2 × 250 mm) coupled to a Dionex IonPac AG19 guard column (2 × 50 mm). The column temperature was maintained at 30°C using a thermostatically controlled oven. The sodium hydroxide (NaOH) gradient, generated by an eluent generator at a flow rate of 0.25 mL min^{-1}, used the following protocol: isocratic elution at 0.5 mM from 0 to 6 min, gradient increase from 15 to 45 mM from 6 to 15 min, column clean-out at 45 mM from 15 to 18 min, and equilibration at 15 mM from 18.1 to 25 min. A suppressor (Thermo Scientific, ASRS 600, 2 mm) was used to remove NaOH before the solution entered the ICP-SFMS. Samples (1 mL) were injected manually using a Peak Rheodyne valve with 5 mL plastic syringes. Limits of detection (LODs) were determined to be 4 pg g^{-1} for Br^- and 2 pg g^{-1} for BrO_3^-.

Concentrated O_3 stock solution (approximately 1.3 mM) was prepared by purging O_3 gas into deionized water cooled with an ice bath, while O_3 gas was produced by discharging pure oxygen gas using an O_3 generator (Ozone Tech, LAB-1). The concentration of the O_3 stock solution was spectrophotometrically determined using a molar absorption coefficient of 3200 $M^{-1}cm^{-1}$ at a wavelength of 260 nm.

Result and discussion

Freezing-induced oxidation of Br^- by BrO_3^-

Figure 4.8a and 4.8b show the Br^- and BrO_3^- concentration changes in solution that was either frozen or kept in aqueous condition for 6 h. Under the aqueous condition, there was no concentration change of Br^-. Accordingly, negligible BrO_3^- reduction was also observed in the aqueous condition (data not shown). However, when the solution was frozen, rapid chemical transformation of Br^- and BrO_3^- was found: Br^- removal were 50, 65, 57, 52, and 47%, and BrO_3^- removal were 20, 47, 80, 90, and 100% at 20, 50, 100, 150, and 200 μM of initial Br^- concentration, respectively (note that the initial BrO_3^- concentration was set constantly to 20 μM). The Br^- concentration did not decrease in the absence of BrO_3^-, and vice versa (Figure S1). These results indicate that the reaction between Br^- and BrO_3^- is considerably promoted in ice compared to water, and both reactants are reciprocally responsible for the freezing-induced chemical reaction. According to a previous study, the reaction between Br^- and BrO_3^- is proposed to proceed via the formation of HOBr as follows:

$$\mathrm{BrO_3}^- + \mathrm{Br}^- + 2\,\mathrm{H}^+ \rightarrow \mathrm{HBrO_2} + \mathrm{HOBr} \tag{R29}$$

$$\mathrm{HBrO_2} + \mathrm{Br}^- + \mathrm{H}^+ \rightarrow 2\,\mathrm{HBrO} \tag{R30}$$

$$\mathrm{Overall}\mathrm{BrO_3}^- + \mathrm{Br}^- + 3\,\mathrm{H}^+ \rightarrow 3\,\mathrm{HBrO} \tag{R31}$$

To evaluate the HOBr production, we adjusted the sample pH to 10.50 using NaOH to deprotonate HOBr ($\mathrm{p}K_\mathrm{a} = 8.8$) [331], and monitored the 329 nm light absorbance (Figure 4.8c). Notably, there was negligible HOBr production under aqueous conditions, while the concentration of HOBr rapidly increased as the solution started to freeze, reaching approximately 50 μM at the 150 μM initial Br^- concentration. This trend is similar to the Br^- and $\mathrm{BrO_3^-}$ concentration changes, as shown in Figure 4.8a and 4.8b.

Note that the HOBr generation was also supported by measurements using the ABTS method, and the result was not significantly different from the above (Figure S2). From the stoichiometry in reaction (R31), we can balance the Br^- and $\mathrm{BrO_3^-}$ ratio: one molecule of $\mathrm{BrO_3^-}$ consumes two Br^- molecules and generates three molecules of HOBr. However, we emphasize here that 85 μM Br^- was consumed by the reduction of 18 μM $\mathrm{BrO_3^-}$ to generate 50 μM HOBr; i.e., the $\mathrm{Br}^-/\mathrm{BrO_3^-}$ ratio is 4.72:1, and the $\mathrm{HOBr}/\mathrm{BrO_3^-}$ ratio is 2.77:1.

Considering that HOBr can be hydrolyzed by $\mathrm{H_2O}$ to produce $\mathrm{Br_2}$, as shown in reaction (R32) [350], the discrepancy in the stoichiometry may be explained by further secondary reactions occurring after HOBr formation.

$$\mathrm{Br_2} + \mathrm{H_2O} \rightarrow \mathrm{HOBr} + \mathrm{Br}^- + \mathrm{H}^+ \tag{R32}$$

Note that the equilibrium constant K_eq for reaction (5) is 7.2×10^{-9} M^2 $\left([\mathrm{HOBr}][\mathrm{H}^+][\mathrm{Br}^-]/[\mathrm{Br_2}]\right)$, which empirically means that the rate constant for the forward reaction is lower than that of the backward reaction (i.e., the reaction favors the left-hand side of equation R32)). Therefore, equations (R31) and (R32) can be combined to derive equation (R33).

$$\mathrm{BrO_3}^- + 5\,\mathrm{Br}^- + 6\,\mathrm{H}^+ \rightarrow 3\,\mathrm{Br_2} + 3\,\mathrm{H_2O} \tag{R33}$$

From the stoichiometry of equation (R33), we can balance the Br^- and $\mathrm{BrO_3^-}$ ratio as 5/1, which approximately agrees with the experimentally determined value (4.72/1). We infer that the discrepancy is due to the fact that the intermediate species HOBr remains in the solution (note that the HOBr concentration in the solution is approximately 50 μM).

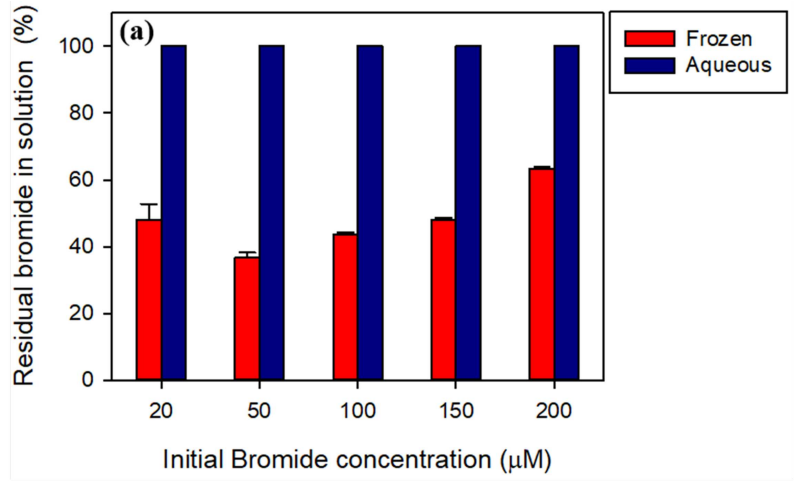

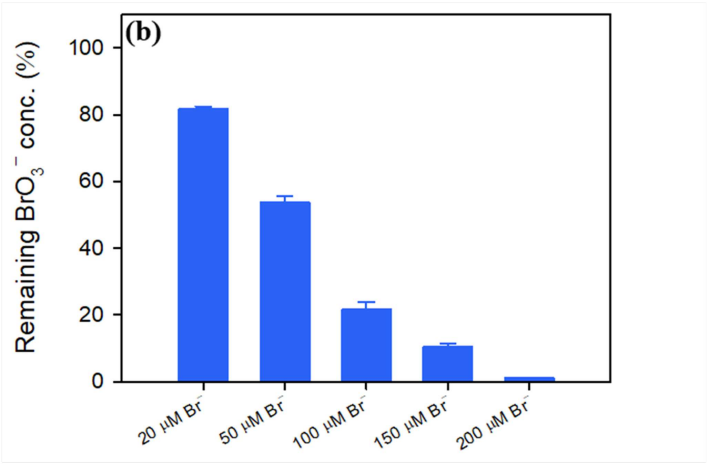

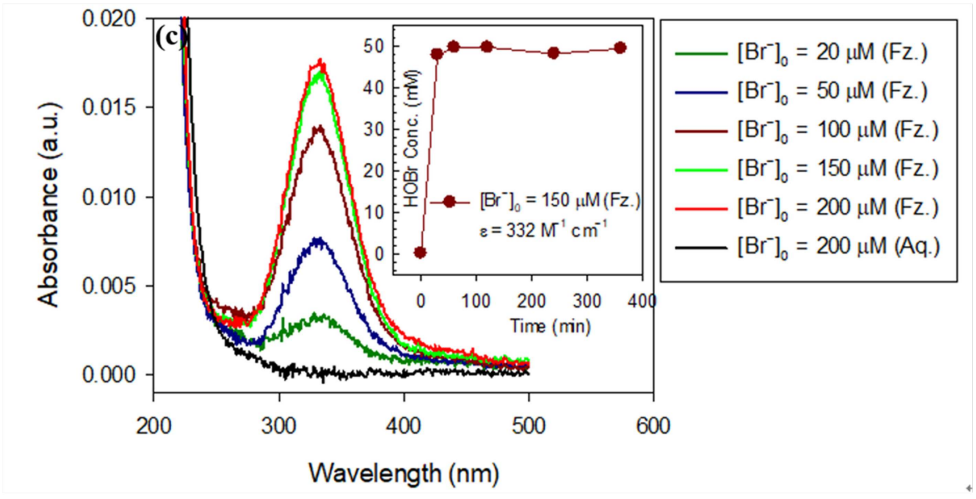

Figure 4.8: (a) Bromide removal in the Br^- / BrO_3^- system. (b) Bromate removal in the frozen Br^- / BrO_3^- system. (c) Hypobromous acid production in the Br^- / BrO_3^- system (inset: HOBr concentration profile at $[Br^-]_0 = 150$ μM during 6 h freezing). The initial Br^- concentration was controlled from 20 to 200 μM. Experimental conditions: $[BrO_3^-]_0 = 20$ μM; $pH_i = 3.0$ (adjusted with $HClO_4$); Temperature = 25°C (aqueous) / −20°C (frozen); Reaction time = 6 h.

Chemical transformation of Br^- and BrO_3^- to Br_2 generation

Equation (R32) describes that Br_2 can be generated via Br^- oxidation by HOBr (in the backward direction). However, the hydrolysis of (dissolved) Br_2 can also generate HOBr in solution (forward direction). Therefore, there are two possible formation pathways for HOBr in solution: the reduction of BrO_3^- and the hydrolysis of Br_2. To identify the oxygen source of HOBr, we conducted high-resolution mass spectrometry (HRMS) using $H_2^{18}O$. The goal was to confirm Br_2 generation in the frozen Br^- / BrO_3^- system. The detection of ^{18}O-labeled HOBr (i.e., $Br^{18}O^-$) would serve as evidence for Br_2 hydrolysis, since HOBr formed from BrO_3^- reduction contains ^{16}O. In the HRMS analysis, HCl was used as the pH-adjusting reagent to avoid spectral interference: $HClO_4$ produces ClO_4^- (m/z 98.9490), which overlaps with the BrO^- detection window (m/z 94–100 in SIM mode). After thawing, the sample pH was adjusted to 10.5 to fully deprotonate HOBr and convert it to BrO^-. As shown in Figure 4.9a, HOBr originated from both the reduction of BrO_3^- and the hydrolysis of Br_2. The detection of $^{79}Br^{18}O$ and $^{81}Br^{18}O$ clearly confirms Br_2 hydrolysis. In our previous study, we demonstrated that OCl^- produced exclusively from Cl_2 hydrolysis yields only $Cl^{18}O$ and not $Cl^{16}O$ species [351]. Thus, we conclude that a portion of the BrO^- in the frozen Br^- / BrO_3^- system was generated via BrO_3^- reduction, while another portion resulted from Br_2 reacting with H_2O (Figure 4.9a).

Secondly, we hypothesize that if dissolved Br_2 is present in the solution, the formation of Br_3^- can be observed due to the equilibrium reaction between Br_2 and Br^-.

$$Br_2 + Br^- \leftrightarrow {Br_3}^- \tag{R34}$$

The equilibrium constant for equation (R34) is 19 M^{-1} at 20°C, which indicates that the $[Br_3^-]$ value is greater than the product of $[Br^-]$ and $[Br_2]$ [350]. As shown in Figure 4.9b, we detected m/z values of 236.7555 for $^{79}Br_3^-$, 238.7535 for $^{79}Br_2{}^{81}Br^-$, 240.7514 for $^{79}Br^{81}Br_2^-$, and 242.7494 for $^{81}Br_3^-$. Furthermore, the m/z signal pattern closely matches the simulated spectrum (Figure S3). Hence, the HRMS results confirm the presence of Br_3^- in the system. Third, we attempted to trap dissolved Br_2 via chemical ionization using 1 mM of I^- addition [352]. In this case, IBr_2^- can be formed, serving as an indicator of Br_2 presence in solution. As shown in Figure 4.9(c), the signal for IBr_2^- was clearly detected by high-resolution mass spectrometry (HRMS). Notably, no IBr_2^- signal appeared when the solution remained in the aqueous condition. This result is consistent with the trend observed for HOBr production: HOBr was only detected under freezing conditions and not in aqueous conditions. Therefore, the HRMS data confirm Br_2 generation in the frozen Br^- / BrO_3^- system.

To demonstrate the volatilization of Br_2 from solution, we monitored the total Br content using inductively coupled plasma mass spectrometry (ICP-MS). As shown in Figure 4.9(d), the total Br concentration ($[Br]_{tot}$) decreased from 170 μM to 120 μM after freezing, while no decrease was observed under aqueous conditions, where the concentration remained at 170 μM. The calculated $[Br]_{tot}$ values ($[BrO_3^-] + [Br^-] + [BrO^-]$) were in good agreement with the ICP-MS data (see inset of Figure 4.9(d)). Initially, $[Br]_{tot}$ was 170 μM (150 μM Br^- and 20 μM BrO_3^-), but approximately 50 μM of Br was lost during freezing. This confirms that Br_2 volatilizes from the ice, although a portion of it re-enters the solution and contributes to HOBr formation, as discussed above.

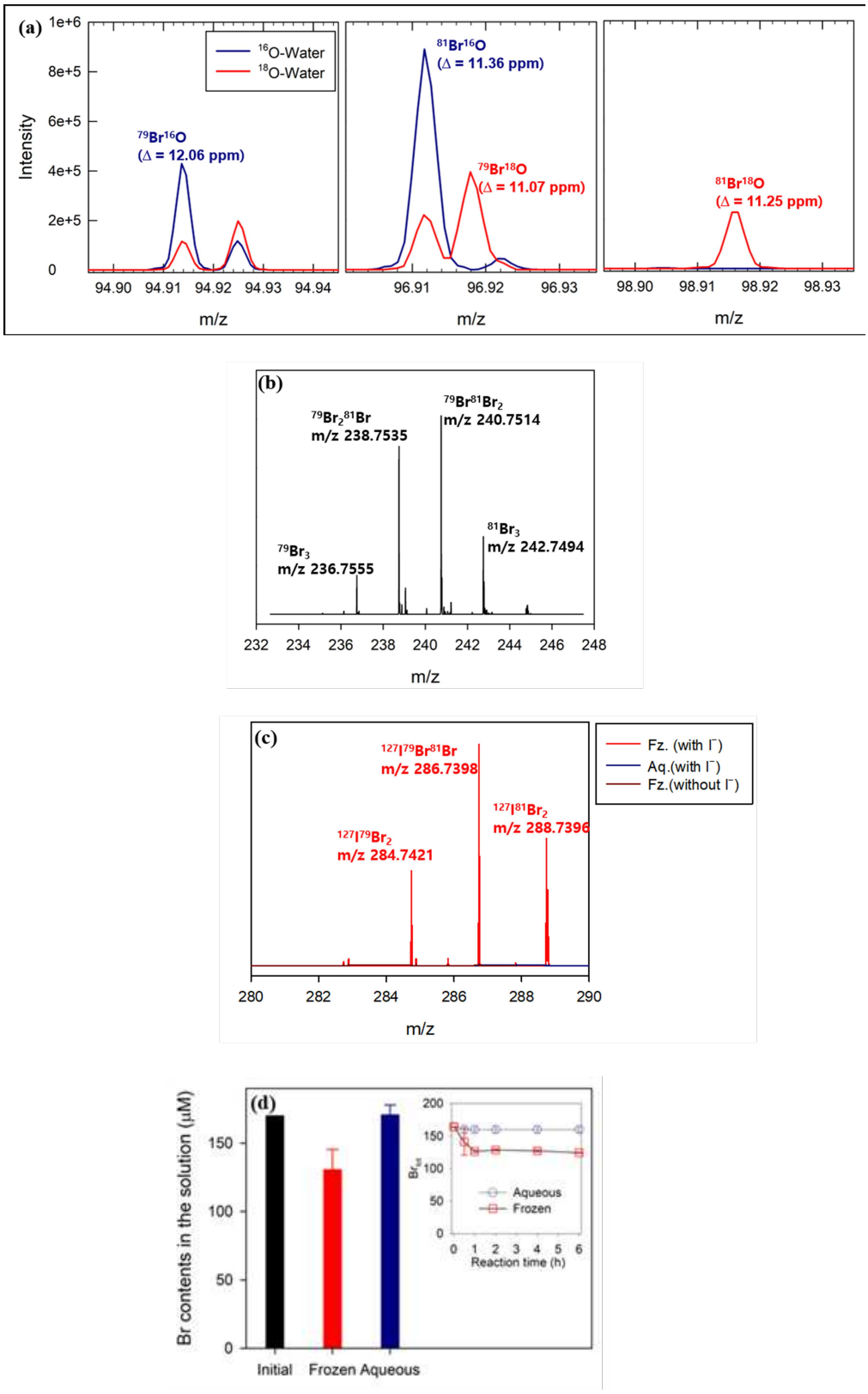

Figure 4.9: High-resolution mass spectra (HRMS) of (a) OBr^-, (b) Br_3^-, and (c) IBr_2^- in the frozen Br^- / BrO_3^- solution. The solution pH was initially adjusted to 3.0 using HCl and then adjusted to 10.50 with NaOH after thawing. (d) ICP-MS results showing the total Br content (inset: time profile of calculated Br_{tot} = $[BrO_3^-]$ + $[Br^-]$ + $[BrO^-]$ in the solution).

Freeze concentration effect

To confirm the increase in freeze concentration during the freezing process, we conducted *in situ* measurements of the ice using a Raman microscope (Figure 4.10). We used a high concentration of reagents (10 mM Br^- and 2 mM BrO_3^-) to acquire sufficiently intense Raman signals of the target species. In the map scan, the red color scale represents the 805 cm^{-1} signal intensity, corresponding to the Br–O vibration of BrO_3^-, while the green color scale represents the 932 cm^{-1} signal intensity, attributed to the Br–O vibration of HOBr (see the Raman spectrum at the bottom). Thus, the spatial distribution of substances in the ice can be visualized. Note that Br^- (monatomic ion) and Br_2 (low polarizability) cannot be visualized via Raman spectroscopy due to the measurement principle. Overall, the intense color signals appear at the center of crystal junctions, whereas black regions correspond to crystal bulk areas. Additionally, as shown in Figure S4, the BrO_3^- signal intensity was significantly decreased when Br^- and BrO_3^- were frozen together, whereas no decrease occurred in the absence of Br^-, and no HOBr-associated Raman peaks appeared. This confirms that Br^--mediated BrO_3^- reduction is an *in situ* reaction within the ice. The estimated thicknesses of the ice grain boundary region and individual ice crystals were less than 5 μm and 50 μm, respectively. This suggests that BrO_3^- dissolved in a few-tenth-millimeter volume becomes concentrated into just a few-micrometer-wide region during the freezing process. Therefore, we estimate that substrate concentrations could reach up to approximately 1000 times ($10 \times 10 \times 10$) higher in ice than in liquid water.

Further, the Br^- oxidation in water was monitored under high Br^- and BrO_3^- concentrations (1000 times higher than the regular experimental condition) to confirm the hypothesis of freezing-induced accumulation (Figure 4.10b). In the aqueous condition, the chemical reaction at pH 3 was negligible, even with elevated reactant concentrations. However, a rapid chemical reaction occurred when the pH was adjusted to 2: approximately 90 mM of 150 mM Br^- and 14 mM of 20 mM BrO_3^- were consumed within 10 minutes. This Br^-/BrO_3^- reaction under high reagent dose and strong acidic conditions is consistent with previously reported kinetic studies [327, 329]. Accordingly, the significance of pH was also confirmed, as shown in Figure S5. When only the pH was decreased from 3 to 1 at 0.15 mM Br^-, only marginal BrO_3^- reduction was observed (Figure S5). Similarly, BrO_3^- reduction was negligible at 1.5 mM Br^- at pH 3. However, at 15 mM Br^-, approximately half of the BrO_3^- was removed within 6 hours of reaction time in water. Additionally, the BrO_3^- reduction efficiency increased with decreasing pH, and complete BrO_3^- removal was achieved by 15 mM Br^- at pH 1 in aqueous conditions.

Also, the proton accumulation in ice was confirmed *in situ* using cresol red (CR) as an acid-base indicator (Figure 4.10c). A peak at 434 nm was observed in the aqueous CR solution, which corresponds to the mono-protonated form of CR (HA^-). The first acid dissociation constant (pK_{a1}) of CR is 1.1 [353]. However, when the solution was frozen for 1 hour, the principal CR peak shifted to approximately 518 nm, corresponding to the di-protonated form (H_2A). For reference spectra of HA^- and H_2A, see Figure S6. Due to the oxidative property of BrO_3^-, CR in ice may undergo oxidation; thus, we did not attempt to estimate the pH in the ice grain boundary using the Henderson–Hasselbalch equation. Nevertheless, the distinct color change of CR strongly indicates that the pH in ice approached 1.1, based on the pK_{a1} of CR. A minor peak appearing near 580 nm may be attributed to brominated CR species. This result supports that the accelerated Br^-/BrO_3^- reaction in ice is driven by the freeze concentration effect. During the freezing of circumneutral solutions, growing ice crystals exclude dissolved species and protons, leading to their accumulation in the ice grain boundary region. Consequently, this region becomes highly concentrated and acidic, which promotes the Br^-/BrO_3^- reaction. This freeze concentration effect must be seriously considered in the context of

environmental chemistry in polar regions and the stratosphere.

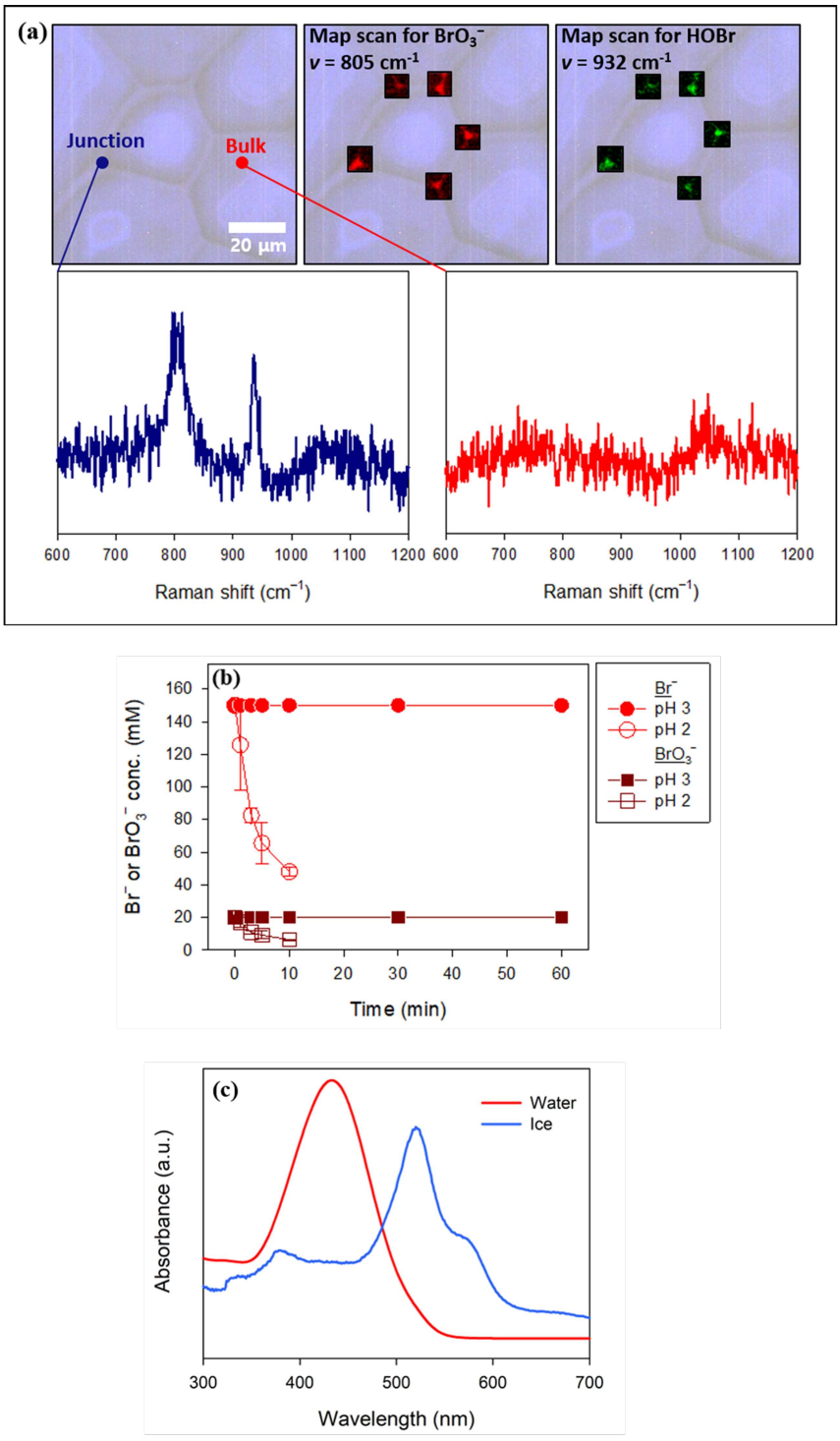

Figure 4.10: (a) Raman microscope image of the frozen Br^- / BrO_3^- solution. Experimental conditions: $[BrO_3^-]_0$ = 2 mM; $[Br^-]_0$ = 10 mM; pH_i = 3.0 (adjusted with $HClO_4$); Temperature = −20°C. (b) Time profile of high reactant concentrations (1000 times higher than the regular condition) in aqueous Br^- / BrO_3^- solution. Experimental conditions: $[BrO_3^-]_0$ = 20 mM; $[Br^-]_0$ = 150 mM; Temperature = 25°C. (c) UV-vis absorption spectra of CR in water and ice. Experimental conditions: $[BrO_3^-]_0$ = 20 μM; $[Br^-]_0$ = 150 μM; $[CR]_0$ = 66.7 μM; pH_i = 3.0 (adjusted with $HClO_4$); Temperature = 25°C (water) / −20°C (ice); Freezing time = 1 h.

Investigation of the Br^-/BrO_3^- reaction at various conditions

Figure 4.11 shows the temperature effect on the Br^- / BrO_3^- system. The BrO_3^- reduction did not progress when the solution was not frozen (25 and 0°C): the solution at 0°C was not frozen during the entire reaction time, although water freezes at 0°C at 101.3 kPa. A significant BrO_3^- decrease was achieved when the solution started to freeze; however, the freezing temperature marginally differed.

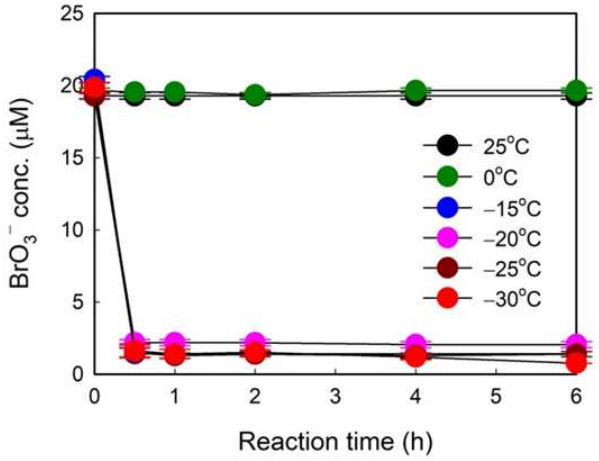

Figure 4.11: The effect of temperature on the Br^-/BrO_3^- reaction. Experimental condition: $[BrO_3^-]_0$ = 20 μM; $[Br^-]_0$ = 150 μM; pH_i = 3.0 ($HClO_4$ adjusted).

The pH effect on the frozen Br^- / BrO_3^- system is shown in Figure 4.12. The reaction was evidently hindered as the initial pH increased. This is because the reaction consumes protons (refer to reaction (R33)). In addition, based on previous studies, the concentration of protons in the ice grain boundary region is 2–3 orders of magnitude higher compared to that in water; therefore, the acid-catalyzed chemical reaction is promoted in the ice grain boundary region, as discussed in the above section [100].

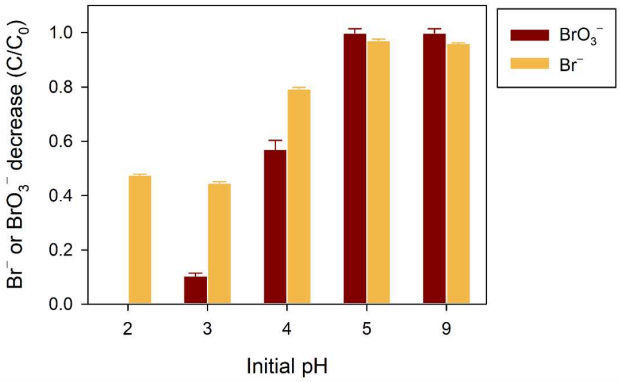

Figure 4.12: The initial pH effect on the frozen Br^-/BrO_3^- system. Experimental condition: $[BrO_3^-]_0$ = 20 μM; $[Br^-]_0$ = 150 μM; Temperature = -20°C; reaction time = 6 h.

We investigated the effect of the initially injected BrO_3^- concentration on the frozen Br^- / BrO_3^- system (Figure 4.13). The reduction efficiency of BrO_3^- decreased with increasing BrO_3^- concentration at 150 μM Br^- (Figure 6a). During the reaction, Br^- was used for BrO_3^- reduction; therefore, a high Br^-/BrO_3^- concentration ratio was preferred for efficient BrO_3^- reduction: the Br^-/BrO_3^- concentration ratios were 15,

7.5, 5, 3.75, and 3 at 10, 20, 30, 40, and 50 μM of the initial BrO_3^- concentration, respectively. Apparently, Br^- consumption ($[Br^-]_0$ – $[Br^-]$) increased with increasing BrO_3^- concentration.

Further, we monitored the HOBr generation by varying the initial BrO_3^- concentrations (Figure 4.13b). The HOBr generation was enhanced by increasing the initial dose of reactants. However, the HOBr generation asymptotically saturated as the initial concentration of BrO_3^- reached 150 μM. The estimated conversion ratio from total Br to HOBr was calculated and presented in Table 4.10. The HOBr generation was likely maximized at approximately 5 for the Br^-/BrO_3^- ratio, which corresponds to the stoichiometry of reaction (R33).

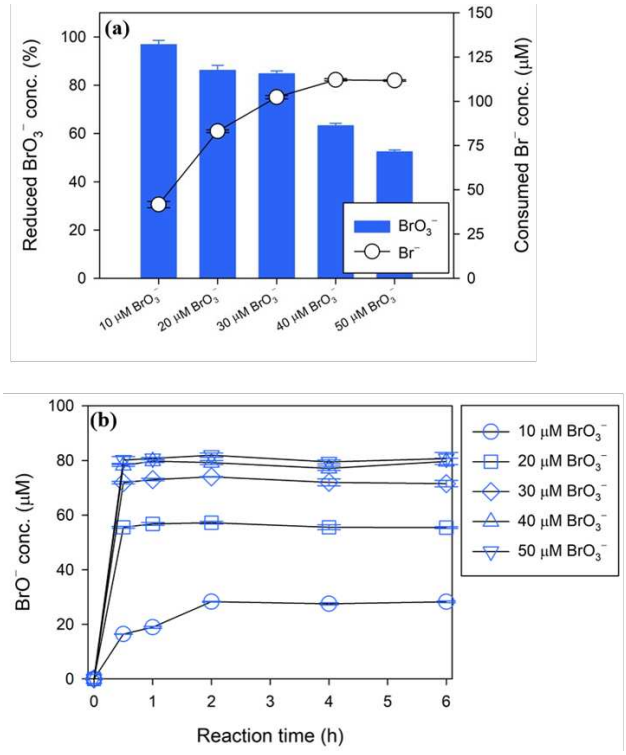

Figure 4.13: (a) The BrO_3^- concentration effect on the frozen Br^- / BrO_3^- system. Experimental condition: $[Br^-]_0$ = 150 μM; pH_i = 3.0 ($HClO_4$ adjusted); Temperature = -20°C; reaction time = 6 h. (b) The HOBr generation at varying BrO_3^- concentrations.

Table 4.10: The values for the Br^- / BrO_3^- system in HOBr generation.

Initial concentration (μM)		Br^- / BrO_3^- ratio	HOBr generation (μM)	HOBr / total Br ratio
Br^-	BrO_3^-			
150	10	15	28.038	0.17
150	20	7.5	55.791	0.33
150	30	5	71.329	0.39
150	40	3.75	79.050	0.41
150	50	3	78.591	0.39
20	20	1	10.316	0.26
50	20	2.5	24.841	0.35
100	20	5	43.924	0.36
150	20	7.5	55.791	0.32
200	20	10	57.215	0.26

The natural relevance of the freezing-induced Br^- and BrO_3^- reaction

According to previous studies, the Br^- concentration in Arctic and Antarctica surface snow samples was approximately 10 ppb range (< 125 nM) [239, 240, 273]. We found no significant concentration of BrO_3^- in the polar region, but we believe that HOBr can be sufficiently produced via Br^- oxidation by O_3 and ·OH, and subsequently, a trace amount of BrO_3^- can exist [284]. To investigate the BrO_3^- generation trend from Br^- oxidation in our regular experimental condition ($[Br^-]_0 = 170\,\mu M$), we monitored the BrO_3^- generation in the O_3-induced Br^- oxidation (Figure 4.14a). The Br^- concentration decreased approximately 20, 50, 80, and 100 μM at 20, 50, 100, and 200 μM O_3 dosage, respectively, at 1 h of reaction time. Accordingly, the BrO_3^- production was approximately 2, 4, 20, and 30 μM, respectively. From this, we know that 100 μM O_3 can produce 20 μM BrO_3^- from 170 μM Br^- (final concentrations: 90 μM Br^- and 20 μM BrO_3^- at 1 h). According to the research, the tropospheric O_3 concentration in the Arctic region is approximately 36 ppbv on average [354], which can be converted to 1.6 nM using the value 22.414 L/mol at 0°C and 101.3 kPa. Hence, we believe that BrO_3^- generation from Br^- oxidation by O_3 cannot be ignored.

We conducted the Br^- / BrO_3^- reaction at extremely low concentration conditions to reveal the environmental relevance of the reaction (Figure 4.14b). Here, the diluted concentrations of Br^- / BrO_3^- (1 nM each) were investigated to confirm the progression of the freezing-induced chemical reaction. In the chromatography, we observed the presence of ^{79}Br of Br^- and ^{79}Br of BrO_3^- in the solution at the retention times of 590 and 730 s, respectively. The signals were well calibrated from 30 to 150 ppt using a Br^- / BrO_3^- solution mixture. The measurement was conducted with a thorough pre-rinse process at every measurement, and the baseline was rigorously monitored to exclude the memory effect on signal acquisition. As shown in Figure 4.14, the BrO_3^- was apparently reduced by freezing: 0.412 and 0.999 nM BrO_3^- were found in the frozen and aqueous solutions, respectively. However, the Br^- concentrations were not notably different in the aqueous and frozen systems. We infer that the comparable Br^- concentration is because the generation of Br^- by BrO_3^- reduction compensated the original Br^- loss in the frozen solution. Consequently, we believe that HOBr, the source of Br_2, is generated from the reduction of BrO_3^-.

As the freezing Br^- / BrO_3^- system is significantly influenced by pH, the environmental acidity can affect the ice chemistry of Br^- oxidation. Hence, acidic ice and snow should be of interest in the present study. Through a literature survey, we found that the pH of snow and ice in polar regions can be slightly acidic [322, 355, 356]; therefore, the freezing-induced Br^- oxidation by BrO_3^- can be naturally relevant. The importance of reactive bromine species has been suggested during the Arctic ozone depletion event. Field campaigns and satellite observations have highlighted high levels of reactive bromine species (such as BrO) in snowpacks and sea ice regions [15, 277, 316, 353]. Reactive bromine species in the atmosphere are generated from the oxidation of Br_2 by oxidants such as nitrous acid and the hydroperoxyl radical, as well as photochemical processes. However, the source of Br_2 has not been clearly elucidated.

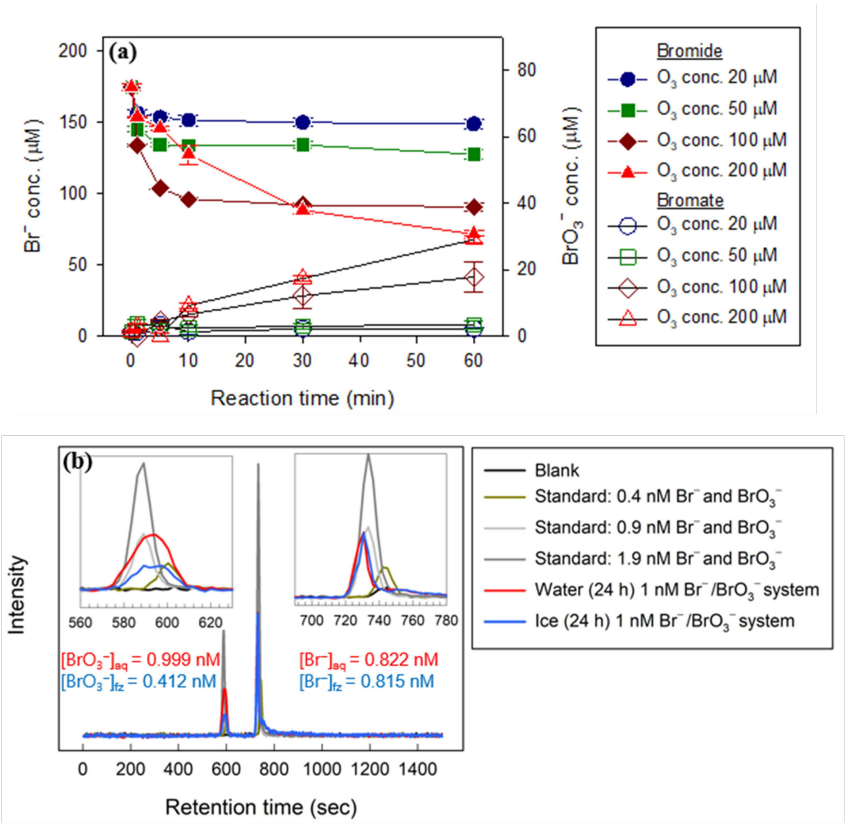

Figure 4.14: (a) Oxidative conversion of bromide to bromate under varying ozone dosage. Experimental condition: $[Br^-]_0$ = 170 M; pH_i = 3.0 ($HClO_4$ adjusted); Temperature = 20°C. (b) The IC-ICP-MS chromatogram of the 1 nM Br^- / BrO_3^- in water and ice after 24 h. Experimental condition: $[BrO_3^-]_0$ = 1 nM; $[Br^-]_0$ = 1 nM; pH_i = 3.0 ($HClO_4$ adjusted); Temperature = 25°C (water) / −20°C (ice); reaction time = 24 h.

Conclusions

In this study, we demonstrated the ice chemistry for Br_2 generation via the reaction between Br^- and BrO_3^-. Experimental studies on HOBr (hydrated Br_2) generation from the Br^- / BrO_3^- reaction were conducted under varying reaction conditions, including freezing temperature, pH, and reactant concentrations. The *in situ* measurement of ice chemistry clearly showed the generation of HOBr from the Br^- / BrO_3^- reaction. We proposed the possible transformation pathways of bromine species based on the experimental results using HRMS and ICP-MS.

The freezing-induced Br^- / BrO_3^- reaction has significant environmental relevance, as it was observed even under naturally relevant low-concentration conditions. Therefore, freezing-induced chemical reactions involving bromine compounds may have a considerable impact on polar environments. We provided experimental evidence for the significance of Br_2 generation in ice and believe that our findings support a novel Br_2 generation pathway in the Arctic.

Acknowledgement

This research was supported by the Korea Polar Research Institute (KOPRI) project (PE25120) and was a part of the project titled "Development of potential antibiotic compounds using polar organism resources (15250103, KOPRI Grant PM24030)", funded by the Ministry of Oceans and Fisheries, Korea. This research was also partly supported by the National Research Foundation of Korea (NRF) grant funded by the Korea government (MSIT) (No. RS-2024-00353764).

CRediT authorship contribution statement

Yong-Yoon Ahn: Conceptualization, Investigation, Writing-original draft. Quoc Anh Nguyen: Conceptualization, Investigation. Andrea Spolaor: Validation, Methodology, Writing–review editing. Stefano Frassati: Methodology, Writing–review editing. Elena Barbaro: Methodology. Giulio Cozzi: Methodology. Clara Turetta: Methodology. Hoon Oh: Methodology. Jaesang Lee: Methodology. Kitae Kim: Validation, Writing–review editing, Supervision.

Supplementary materials

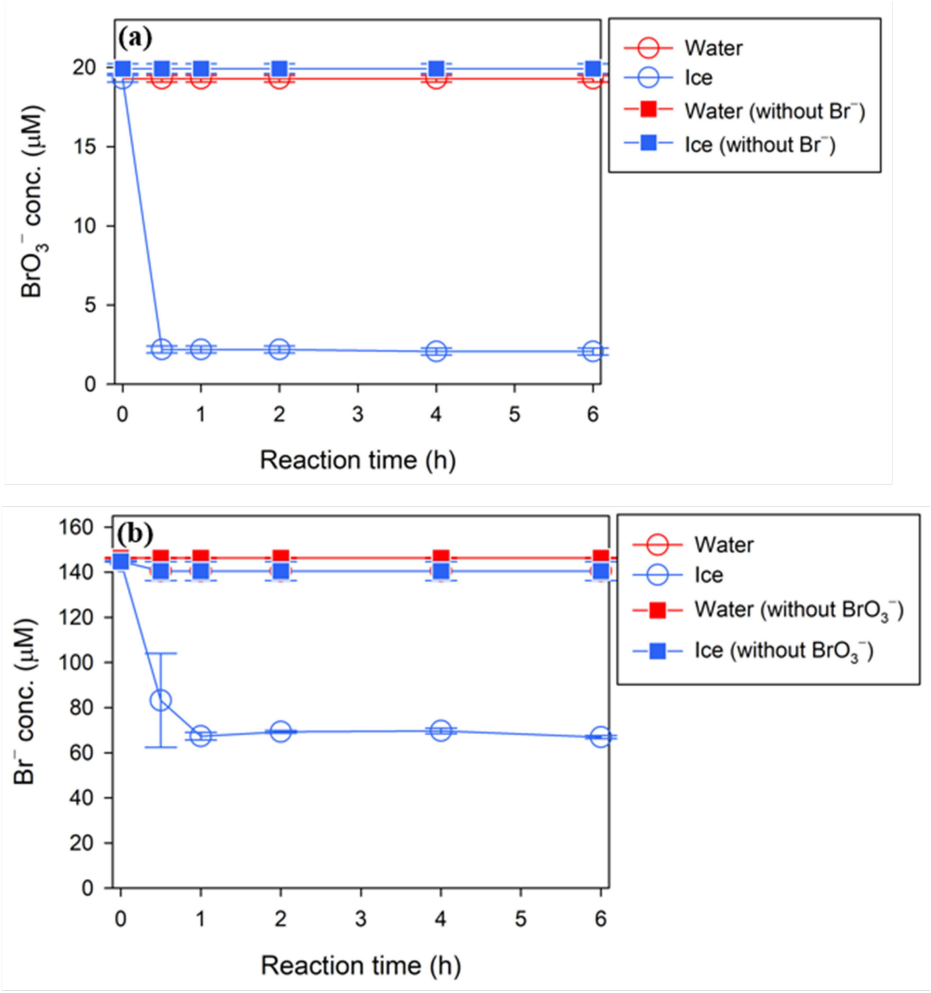

Figure 4.15: Time profile of (a) BrO_3^- and (b) Br^- concentrations. Experimental conditions: $[BrO_3^-]_0$ = 20 μM; $[Br^-]_0$ = 150 μM; pH_i = 3.0 (adjusted with $HClO_4$); Temperature = 25°C (water) / −20°C (ice).

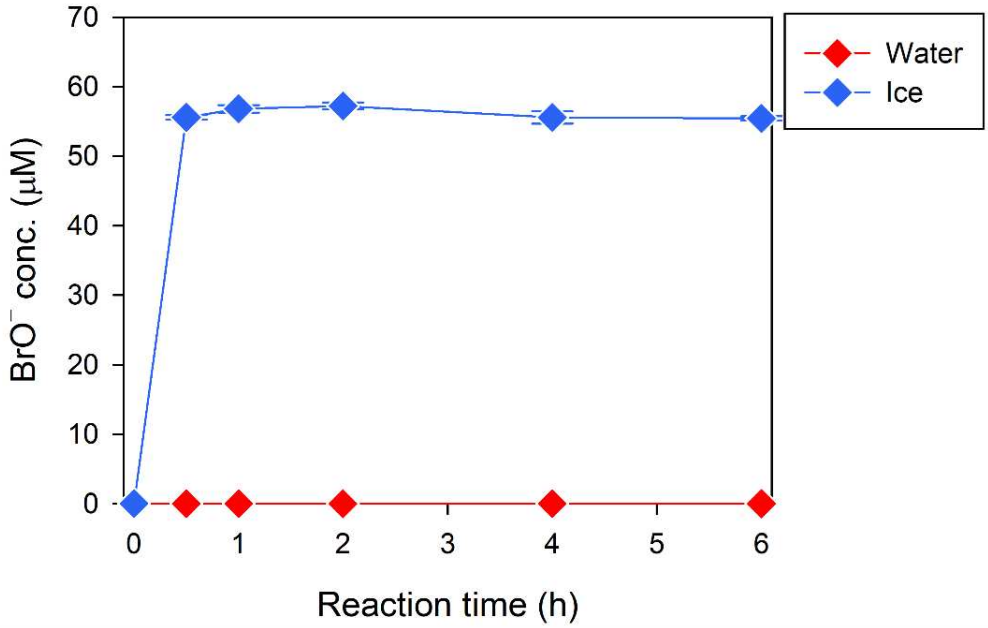

Figure 4.16: Time profile of HOBr concentrations evaluated using the ABTS method. Experimental conditions: $[BrO_3^-]_0 = 20\ \mu M$; $[Br^-]_0 = 150\ \mu M$; $pH_i = 3.0$ (adjusted with $HClO_4$); Temperature = 25°C (water) / −20°C (ice).

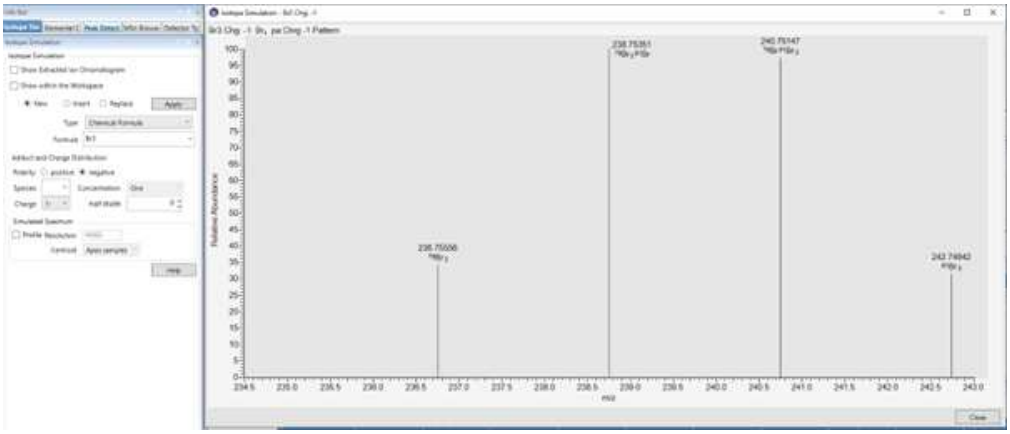

Figure 4.17: The simulated m/z pattern of Br_3^-.

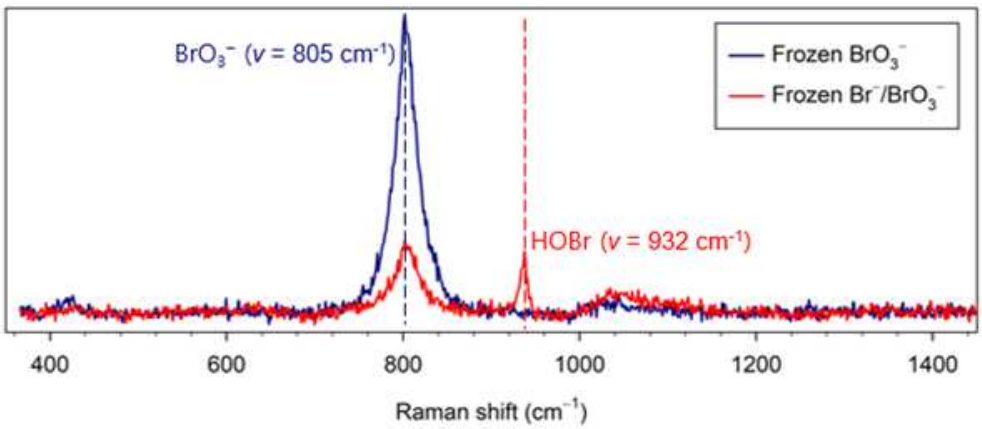

Figure 4.18: The Raman spectrum of the frozen BrO_3^- and Br^- / BrO_3^- solution. Experimental conditions: $[BrO_3^-]_0$ = 2 mM; $[Br^-]_0$ = 10 mM; pH_i = 3.0 (adjusted with $HClO_4$); Temperature = −20°C.

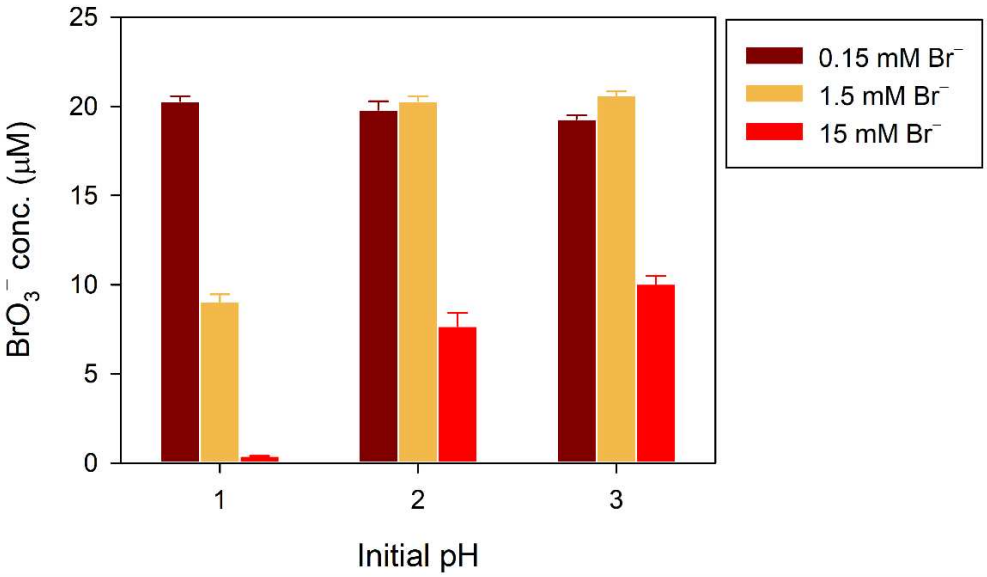

Figure 4.19: Effect of pH and initial Br^- concentration on BrO_3^- reduction in water. Experimental conditions: $[BrO_3^-]_0$ = 20 μM; Temperature = 25°C; reaction time = 6 h.

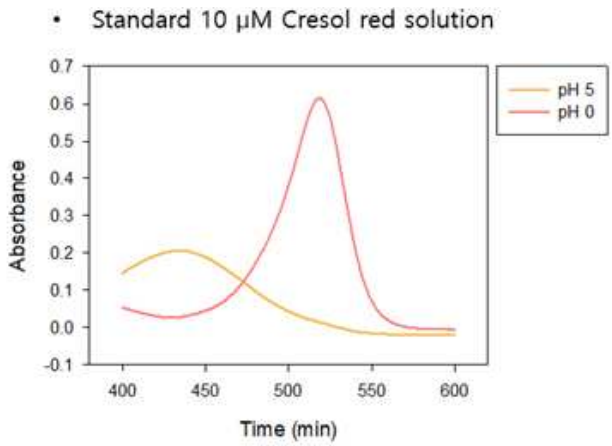

10 μM Cresol red	molar absorptivity
HA^- (434 nm, pH 5)	0.0217
H_2A (520 nm, pH 0)	0.0615

Figure 4.20: UV-vis absorption spectra of CR in pH 0 and pH 5.

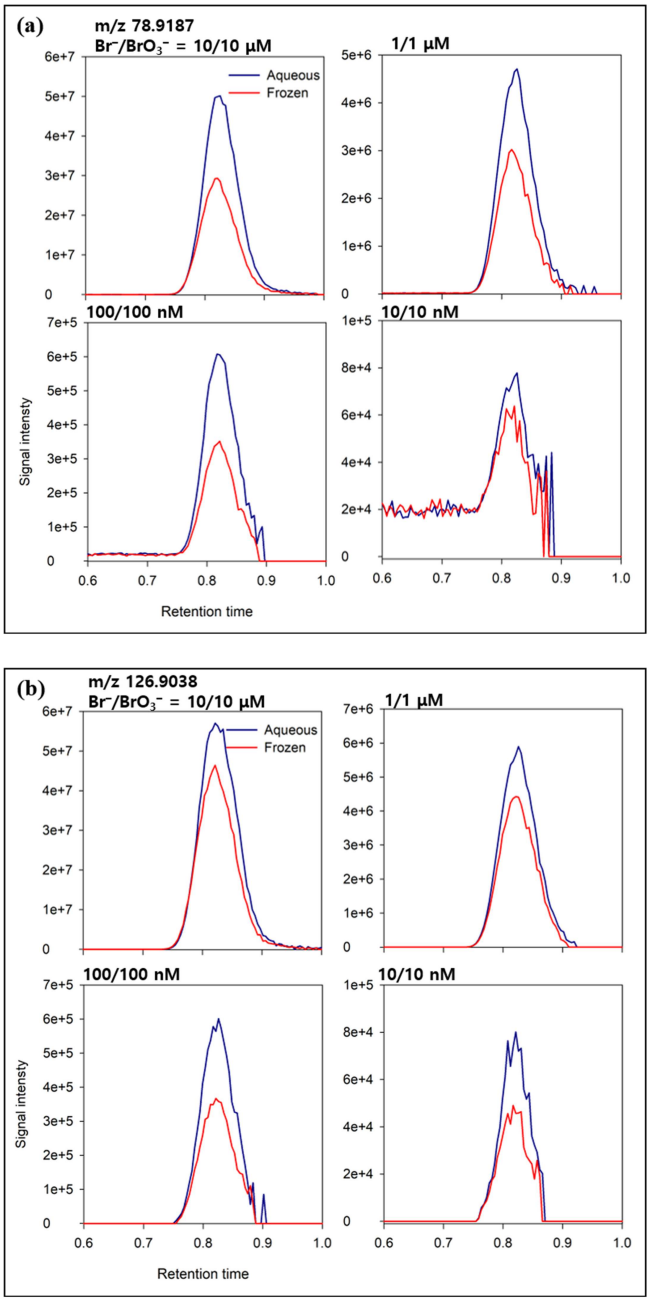

Figure 4.21: The LC-HRMS chromatogram showing (a) Br^- (m/z 78.9187) and (b) BrO_3^- (m/z 126.9038) concentration changes induced by freezing. Experimental conditions: pH_i = 3.0 ($HClO_4$ adjusted); Temperature = 25°C (water) / −20°C (ice); reaction time = 2.5 h.

4.4 Conclusions on bromine

This chapter provides an in-depth analysis of the production and implications of a permanent pool of Br in the form of BrO_3^-. By implementating an innovative analytical method based on IC-ICP-HRMS, we were able to analyze Br speciation in Arctic snow samples at levels as pg g^{-1}

Applying this technique to real snow samples revealed a direct relationship between increased BrO_3^- concentrations and solar radiation intensity, suggesting that photochemical processes may be responsible for the formation of such species. The hypothesis is supported by *in-silico* evaluations, which further reinforce the proposed interpretative framework. However, further studies are needed to fully understand the behaviour of BrO_3^- in frozen environments. A first step in this direction has been taken by analysing the behaviour of BrO_3^- in ice in the presence of Br^-. The results showed that BrO_3^- reduction can occur, leading to a decrease in its concentration. It is important to note that this study refers to ice produced from liquid solutions already containing BrO_3^- and Br^-, so it is possible that the reactions observed are not directly applicable in cases where the former is generated directly on or inside the snow.

Furthermore, future studies should focus on determining the kinetic constants for the photochemical formation of BrO_3^-. These studies should also consider how surrounding environmental chemical-physical parameters influence its formation. Accurately characterizing these factors will be essential for improving the predictive capacity of the models used to study ozone depletion events, as it will allow for a more comprehensive integration of halogen-involving reactions.

Chapter 5

Conclusions and future prospective

This thesis investigates the photochemical behaviour of two species, one organic (BPA) and one inorganic (Br),under conditions representative of cryosphere environments.

Bisphenol A was selected as the organic component because it is frequently found in remote environmental matrices. Classified as an emerging and persistent pollutant, BPA has the potential to impact ecosystems and organisms in polar environments. The main objective of the study was to determine if and to what extent BPA undergoes photochemical degradation within various cryospheric matrices, including synthetic ice, snow and sea ice. First, the degradation kinetics of BPA were determined in each matrix. Subsequently, the degradation products in both snow and ice were analysed to identify potential transformation pathways and assess the environmental implications of the resulting products. The results demonstrated that, despite their chemical similarity, different cryospheric matrices can significantly influence BPA's degradation pathways and the nature of the photochemical products generated. It was found that snow and ice do not necessarily produce the same secondary compounds, which suggests that the physical microstructure and local conditions of the matrices play a crucial role in modulating reactive processes. This finding is particularly relevant in environmental studies, as it implies that when researching the (photo)transformations of contaminants in cold environments, one cannot assume that the products will be similar in snow and ice, even when the same initial species are present.

To date, there are very few, if any, existing photochemical studies of artificial sea ice, especially concerning the degradation of organic contaminants. This represents a significant gap, given that sea ice constitutes a large proportion of ice-covered surfaces in the Arctic and Antarctic. Expanding research in this area is therefore critical to understand the fate of contaminants and their potential ecotoxicological impact in these environments. One possible explanation for this lack of research is the analytical difficulty associated with sea ice. Its complex structure, characterised by the presence of salts, microchannels and concentrated liquid phases (brines), makes sample preparation and analysis particularly challenging. For example, to perform mass spectrometry analysis for identifying degradation products, it is often necessary to remove dissolved salts. This introduces additional preparatory steps that can alter the composition of the sample or reduce analytical sensitivity. These critical issues slow down experimental investigations and help explain the scarcity of currently available data.

To enhance our understanding of photochemical processes in frozen matrices, we need to conduct systematic studies using a wider variety of substrates and experimental conditions. This will help us to assess the influence of key environmental factors, such as salinity, pH and the presence of organic matter, on degradation

mechanisms. Beyond identifying the transformation products, it will be essential to investigate the kinetics of the reactions by accurately determining rate constants under controlled conditions that are representative of the cryospheric environment. Another strategic development would be creating predictive models to estimate the behaviour of pollutants in different cryosphere matrices. Such models, which could be based on estimating half-life times as a function of environmental parameters, would provide valuable support for environmental risk assessment, much like those already provided to study of the fate of pollutants in surface waters.

Regarding the study of Br, a speciation analysis was conducted on Arctic snow samples using IC-ICP-MS. The goalwas to quantify the main forms present: Br^- and BrO_3^-. The results confirmed that BrO_3^- is a significantly more stable species than Br^-, which can be easily oxidized by atmospheric agents. While many of the oxidative mechanisms of Br have already been extensively studied in the context of so-called bromine explosion reactions, including these reactions in predictive Ozone Depletion Events (ODEs) models has often led to an underestimation of the actual extent of ozone depletion observed during daylight hours in the Arctic. This study demonstrated that BrO_3^- can be the final product of complete oxidation of BrO^- by O_3. This process creates a pool of Br in a non-reactive form, removing it from the catalytic cycles of ozone destruction. Including this pathway in atmospheric chemical models could help to bridge the gap between experimental observations and model predictions, improving our ability to accurately simulate the effects of Br cycles on polar tropospheric chemistry.

To improve our understanding of oxidative processes involving Br in polar regions, it is essential to investigate the kinetics of the reactions that lead to the formation of stable species such as BrO_3^-. specifically, it is necessary to determine the reaction rates and identify the environmental factors that either limit or promote their efficiency. This information is essential for refining atmospheric chemical models, making them more accurate and effective in simulating ODEs and the role of reactive Br in Arctic tropospheric chemistry. A better representation of the dynamics between reactive and non-reactive bromine species will bridge the current discrepancies between field observations and model predictions, making a substatial contribution to our understanding of the ozone balance in polar environments.

Chapter 6

Appendices

6.1 Appendix A

This appendix lists the instrumental parameters and snow sampling methods used to quantify bisphenols in alpine snow.

Instrumental analysis

The analysis was performed by high-performance liquid chromatography coupled to tandem mass spectrometry (HPLC-MS/MS), using an HPLC 1100 system (Agilent Technologies) coupled to an API 4000 spectrometer (Sciex). The chromatographic separation was performed using a 50 mm × 4.6 mm Zorbax SB-Aq (Hydro) column with 4 μm particle size. A gradient elution program was set using a binary mixture of ultrapure water (eluent phase A) and methanol (eluent phase B) was used. The chromatographic conditions involved an initial elution at 20 % B phase for the first 3 minutes, followed by a gradient to 100% B between 3 and 5 minutes. The washing phase was maintained isocratic at 100% B from minute 5 to minute 10, while the re-equilibration phase at 20% B phase was conducted between 10 and 13 minutes. The analysis was performed at a constant flow rate of 500 μL min^{-1}, and using an injection volume of 100 μL. A 0.7% ammonia solution (NH_4OH) was used as a post-column reagent, introduced at a flow rate of 50 μL min^{-1}, to improve ESI ionisation efficiency. The source temperature was set at 550 °C

Table 6.1 shows the bisphenols analysed, with their monitored molecular masses and limits of detection (LOD) expressed in pM.

Table 6.1: MS/MS filter parameters for the analysed bisphenols and their LODs.

Compound	Precursor mass	Product ions	LOD (pM)
BPA	227.0	211.9 132.8	3.1
BPAF	335.2	264.9 196.9	2.7
BPAP	289.0	274.1 210.7	6.6

Continued on the next page

Table 6.1 continuation

Compound	Precursor mass (m/z)	Product ions (m/z)	LOD (pM)
BPC	255.1	147.2 240.2	144.1
BPF	199.0	92.7 105.2	74.9
BPFL	349.0	256.4 215.1	31.7
BPM	334.9	330.2 251.1	89.9
BPS	248.9	107.8 91.9	2.4
BPZ	266.9	179.0 223.0	62.9
TMBPA	283.3	161.2 267.1	77.3
2OH-BP	185.0	156.1 117.0	494.0
3Br-Ph	328.9	79.0 81.0	9.0
4Br-BPA	540.9	445.8 446.1	33.1

Chemicals

Standards used in this work include various bisphenols including: BPA, Bisphenol Z (BPZ), Bisphenol AF (BPAF), Bisphenol F (BPF), Bisphenol AP (BPAP), Bisphenol FL (BPFL), Bisphenol S (BPS), Bisphenol M (BPM), Bisphenol C (BPC), Tetrabromobisphenol A (TBBPA), Tetramethyl Bisphenol A (TMBPA), 4,4'-Dihydroxybiphenyl (2OH-BP) and Tribromophenol (3Br-Ph). All compounds were used at or above 99% purity and were supplied by Sigma Aldrich. Methanol (Sigma-Aldrich, gradient grade) and ultrapure water (UPW; 18.2 MΩ·cm resistivity, TOC <10 ppb; Elga LabWater, UK) were used for the HPLC analysis.

Sampling and sample treatment

Samples were collected at 10 cm intervals along a depth profile, starting from the surface, using previously decontaminated 50 mL polypropylene (PP) tubes. The decontamination process consisted of sonication in ultra-pure water (UPW) for 30 minutes. During sample collection, representative field blanks were prepared at each sampling site by exposing an open 50 mL PP tube near the sampling area for the duration of the activity. All samples were stored at -20 °C until analysis. Before analysis, the samples were thawed at room temperature in the original 50 ml tubes.

Sample preparation was conducted in a class 1000 clean room to minimize the risk of contamination. All handling procedures were performed under a laminar flow bench. For analysis, each sample, previously

pre-filtered with a 0.45 μm PTFE membrane serynge filter (25 mm), was spiked with of an internal standard solution (Bisphenol-A-(diphenyl-^{13}C12), Sigma-Aldrich, BPA*).

6.2 Appendix B

This section shows the geometries used to model the species in *in silico* calculations

Gas-Phase Geometries

HOBr

H	-4.56339878248338	0.61366377143180	0.00000095354710
O	-4.03479211049220	1.42161356316199	-0.00000296111266
Br	-2.32014710702442	0.82701966540621	-0.00000099243443

OH radical

H	-4.58280756614227	0.61215733239576	0.00000096883511
O	-4.04336643385772	1.42412166760424	-0.00000296883511

O_3 (singlet)

O	-4.72554561160867	0.60728417278327	0.00000000000000
O	-3.71202267729023	1.32006429244264	0.00000000000000
O	-2.60820571110109	0.75684453477409	0.00000000000000

O_2 (triplet)

O	-2.54351144659346	0.78701380504008	0.00000000000000
O	-3.60042355340654	1.34775219495992	0.00000000000000

BrO radical

O	-2.64303662335973	0.70238881717905	0.00000003762152
Br	-0.93598337664027	0.79345518282095	0.00000096237848

$HOBrO_2$

O	-2.00157394693709	0.62909397668552	-0.50188891569318
Br	-0.97162063251158	1.21438476886531	0.57164587162660
O	0.52515031856212	1.01237958676062	0.05920167922934
O	-1.23130223108643	2.97694435205685	0.41395721101071
H	-1.27734450802700	3.14600131563169	-0.54287184617346

OBrO radical

O	-2.59860960240154	0.59439284538030	-0.00000034432939
Br	-0.89821438370138	1.00552873799089	0.00000175560990
O	0.95900298610292	0.59547841662881	0.00000088871948

BrO_3^-

O	-2.03837094773483	0.21365295106821	0.16698901587912
Br	-1.03901960631261	1.34985044937914	-0.46023089655209
O	0.44971702860737	1.06918112606542	0.16244592100892
O	-1.53556347455992	2.79458047348724	0.13085695966405

BrO_2^-

O	-2.07059451319955	0.02968741072565	-0.00001363201284
Br	-1.05105755623712	1.39931825575706	0.00001534472929
O	0.59448006943668	0.94330333351729	-0.00000471271645

BrO^-

O	0.77538741579370	1.06001318309745	-0.00000273664528
Br	-1.01272441579370	1.30326781690255	0.00001273664528

H_3O^+

H	-2.87484328243496	-1.16082305463108	0.56474807270403
O	-2.03302516988351	-1.65047019307125	0.56474824683131
H	-1.18812373544647	-1.16622260999652	0.56474883599050
H	-2.03677581223506	-2.62434114230114	0.56474784447415

H_2O

H	-2.79875032934446	-1.12449582452816	0.56475248126865
O	-2.03317715614540	-1.70555080499124	0.56474330835697
H	-1.27176151451014	-1.11906737048061	0.56475321037438

Reactant Complex (I step ionic mechanism)

O	1.80838077241837	0.63191765072615	-0.06320541139134
O	0.88723296430994	0.85169662704125	0.74094402998243
O	2.44635265433272	-0.47031589886356	0.07679633577350
Br	-1.37134439106103	-0.22585237890385	-0.18075395436459

Product Complex (I step ionic mechanism)

O	2.04012702257491	0.55232452577495	0.20895686041201
O	0.09811130748811	1.04223294433918	0.53004245865055
O	2.09737073116528	-0.58848323895312	-0.28825588697330
Br	-0.75113706122831	-0.39572423116102	-0.03622943208926

WB97X TS singlet (I step ionic mechanism)

O	0.88777230586337	0.45147437741701	-0.23343793890992
O	-0.41715275318584	0.63004264316998	0.56840838848347
O	1.35650573178651	-0.77239277126027	-0.13139706489668
Br	-1.82712528446405	-0.30912424932673	-0.20357338467689

B3LYP TS singlet (I step ionic mechanism)

O	0.96329736417869	0.40641486359530	-0.27169132766212
O	-0.48450225201379	0.59146424268600	0.57825147271478
O	1.52289476063614	-0.74330971807482	-0.11664717878981
Br	-2.00168987280105	-0.25456938820649	-0.18991296626287

M062X TS singlet (I step ionic mechanism)

```
O   0.89735383204473   0.45499410512733  -0.22063683339984
O  -0.42919065054047   0.64549775508498   0.56388333823004
O   1.32558164000699  -0.77895351944727  -0.14403545669521
Br -1.79374482151126  -0.32153834076506  -0.19921104813501
```

Geometries in Water

HOBr

```
H -4.56876230798488 0.61358325861446 0.00000095624020
O -4.03232647345770 1.42019909327604 -0.00000295572981
Br -2.31724921855741 0.82851464810950 -0.00000100051039
```

OH radical

```
H -4.58335763863539 0.61132936578464 0.00000097285039
O -4.04281636136460 1.42494963421536 -0.00000297285039
```

O_3 (singlet)

```
O -4.72327027091508 0.60687609681350 0.00000000000000
O -3.71209000299307 1.32118506515946 0.00000000000000
O -2.61041372609185 0.75613183802704 0.00000000000000
```

O_2 (triplet)

```
O -2.54371084274094 0.78711959347223 0.00000000000000
O -3.60022415725905 1.34764640652777 0.00000000000000
```

BrO radical

```
O -2.64111033466249 0.70249157912345 0.00000003866505
Br -0.93790966533750 0.79335242087655 0.00000096133495
```

$HOBrO_2$

```
O -2.04710425966101 0.32788642191071 -0.15961789151477
Br -0.95560680654984 1.28798374707466 0.50662132328566
O 0.46806354709357 1.03007439915461 -0.17908184528349
O -1.48685580487334 2.80520794063390 -0.26023221531015
H -0.93518767600937 3.52765149122610 0.09235462882276
```

OBrO radical

```
O -2.18253159600738 0.41685032058942 -0.00000085373551
Br -0.84873813092059 1.34951313613900 0.00000303816389
O 0.49344872692797 0.42903654327158 0.00000011557162
```

BrO_3^-

O -2.02938248820914 0.22569258076212 0.17956247332644
Br -1.03845626254628 1.34741586286595 -0.48812833054845
O 0.43503723917702 1.07250276068417 0.17451606292688
O -1.53043548842159 2.78165379568776 0.13411079429513

BrO_2^-

O -2.03614325023371 0.02462801012567 -0.00001393947304
Br -1.06131864327403 1.42863269476031 0.00001613317048
O 0.57028989350774 0.91904829511402 -0.00000519369743

BrO^-

O 0.77562048883598 1.05998147585378 -0.00000273866216
Br -1.01295748883598 1.30329952414622 0.00001273866216

H_3O^+

H -2.87240801689526 -1.16305679992777 0.56474807307532
O -2.03309062031246 -1.64989451578252 0.56474824397097
H -1.19072827207200 -1.16840217658315 0.56474883419383
H -2.03654109072029 -2.62050350770655 0.56474784875988

H_2O

H -2.79648621805529 -1.12212338107652 0.56475252098209
O -2.03316009629504 -1.71027723585735 0.56474323113791
H -1.27404268564967 -1.11671338306613 0.56475324788000

WB97X TS triplet (I step ionic mechanism)

Br -1.65210616511160 0.70102708792332 -0.20817886925069
O 0.63849521022778 -1.40576014343890 -0.04818114638024
O 0.87642716674358 -0.24793182789885 0.52384517047018
O 0.13718378814024 0.95266388341443 -0.26748515483925

WB97X TS triplet (I step ionic mechanism)

Br -1.16433986863109 -0.47947085900669 3.02314938934362
O 0.36737750970475 0.46237725263970 -0.05761120791655
O -0.61580848351812 0.63520197365425 1.28204753329165
O 0.96153984244446 -0.61802336728726 -0.13428771471872

Early MECP (I step ionic mechanism)

Br -1.17182374102657 0.53653260602714 -0.14572800180178
O 1.48930884163780 -1.75876017603722 0.07070929561655
O 1.65674287360926 -0.60736788804705 0.61925792884059
O 1.32265702577949 0.42090345805712 -0.17743522265536

Late MECP (I step ionic mechanism)

```
Br -0.73334084008927 0.18534127202978 -0.23091965024955
O 1.21318995135563 -1.71688269561053 0.31118195973037
O 1.93206623181912 -0.66845749134983 0.35531050958760
O 0.89471365691451 0.80666491493058 0.02972018093159
```

Bibliography

[1] Bo Su et al. "Cryosphere services and human well-being". In: *Sustainability* 11.16 (2019), p. 4365.

[2] Dahe Qin et al. "Cryospheric science: research framework and disciplinary system". In: *National Science Review* 5.2 (2018), pp. 255–268.

[3] Victor F Petrenko and Robert W Whitworth. *Physics of ice*. OUP Oxford, 1999.

[4] Christopher S Blaszczak-Boxe and Alfonso Saiz-Lopez. "Nitrate photolysis in ice and snow: A critical review of its multiphase chemistry". In: *Atmospheric Environment* 193 (2018), pp. 224–241.

[5] Anne Letréguilly, Niels Reeh, and Philippe Huybrechts. "The Greenland ice sheet through the last glacial-interglacial cycle". In: *Palaeogeography, Palaeoclimatology, Palaeoecology* 90.4 (1991), pp. 385–394.

[6] John Chappell and N_J Shackleton. "Oxygen isotopes and sea level". In: *Nature* 324.6093 (1986), pp. 137–140.

[7] J Oerlemans, M Dyurgerov, and RSW Van de Wal. "Reconstructing the glacier contribution to sea-level rise back to 1850". In: *The Cryosphere* 1.1 (2007), pp. 59–65.

[8] Hans-Otto Pörtner et al. "The ocean and cryosphere in a changing climate". In: *IPCC special report on the ocean and cryosphere in a changing climate* 1155 (2019), pp. 10–1017.

[9] Vanya Miteva et al. "Geochemical and microbiological studies of nitrous oxide variations within the new NEEM Greenland ice core during the last glacial period". In: *Geomicrobiology Journal* 33.8 (2016), pp. 647–660.

[10] David Touchette et al. "Microbial characterization of Arctic glacial ice cores with a semiautomated life detection system". In: *Astrobiology* 23.7 (2023), pp. 756–768.

[11] Amanda M Grannas, Paul B Shepson, and Timothy R Filley. "Photochemistry and nature of organic matter in Arctic and Antarctic snow". In: *Global Biogeochemical Cycles* 18.1 (2004).

[12] Amanda M Grannas et al. "Role of dissolved organic matter in ice photochemistry". In: *Environmental science & technology* 48.18 (2014), pp. 10725–10733.

[13] Florent Domine et al. "Can we model snow photochemistry? Problems with the current approaches". In: *The Journal of Physical Chemistry A* 117.23 (2013), pp. 4733–4749.

[14] TF Kahan and DJ Donaldson. "Photolysis of polycyclic aromatic hydrocarbons on water and ice surfaces". In: *The Journal of Physical Chemistry A* 111.7 (2007), pp. 1277–1285.

[15] Kerri A Pratt et al. "Photochemical production of molecular bromine in Arctic surface snowpacks". In: *Nature Geoscience* 6.5 (2013), pp. 351–356.

[16] William R Simpson et al. "Halogens in the coastal snow pack near Barrow, Alaska: Evidence for active bromine air-snow chemistry during springtime". In: *Geophysical research letters* 32.4 (2005).

[17] Andrea Spolaor et al. "Seasonality of halogen deposition in polar snow and ice". In: *Atmospheric Chemistry and Physics* 14.18 (2014), pp. 9613–9622.

[18] H Gerald Jones. *Snow ecology: an interdisciplinary examination of snow-covered ecosystems*. Cambridge University Press, 2001.

[19] Neville Horner Fletcher. "The chemical physics of ice". In: *The Chemical Physics of Ice* (2009).

[20] Christian Katlein, Marcel Nicolaus, and Chris Petrich. "The anisotropic scattering coefficient of sea ice". In: *Journal of Geophysical Research: Oceans* 119.2 (2014), pp. 842–855.

[21] Ken-ichiro Murata, Ken Nagashima, and Gen Sazaki. "How do ice crystals grow inside quasiliquid layers?" In: *Physical Review Letters* 122.2 (2019), p. 026102.

[22] Clare L Bishop et al. "On thin ice: Surface order and disorder during pre-melting". In: *Faraday discussions* 141 (2009), pp. 277–292.

[23] Hans Helmut Gunter Jellinek. "Liquid-like (transition) layer on ice". In: *Journal of colloid and interface science* 25.2 (1967), pp. 192–205.

[24] JG Dash, AW Rempel, and JS Wettlaufer. "The physics of premelted ice and its geophysical consequences". In: *Reviews of modern physics* 78.3 (2006), pp. 695–741.

[25] George E Ewing. *Thin film water*. 2004.

[26] D Beaglehole and Peter Wilson. "Extrinsic premelting at the ice-glass interface". In: *The Journal of Physical Chemistry* 98.33 (1994), pp. 8096–8100.

[27] JS Wettlaufer. "Impurity effects in the premelting of ice". In: *Physical Review Letters* 82.12 (1999), p. 2516.

[28] Thorsten Bartels-Rausch et al. "Ice structures, patterns, and processes: A view across the icefields". In: *Reviews of Modern Physics* 84.2 (2012), pp. 885–944.

[29] Astrid Döppenschmidt and Hans-Jürgen Butt. "Measuring the thickness of the liquid-like layer on ice surfaces with atomic force microscopy". In: *Langmuir* 16.16 (2000), pp. 6709–6714.

[30] Ignacio Pickering et al. "Grand canonical investigation of the quasi liquid layer of ice: Is it liquid?" In: *The Journal of Physical Chemistry B* 122.18 (2018), pp. 4880–4890.

[31] Julián Gelman Constantin et al. "The quasi-liquid layer of ice revisited: the role of temperature gradients and tip chemistry in AFM studies". In: *Atmospheric Chemistry and Physics* 18.20 (2018), pp. 14965–14978.

[32] Ben Slater and Angelos Michaelides. "Surface premelting of water ice". In: *Nature Reviews Chemistry* 3.3 (2019), pp. 172–188.

[33] Gen Sazaki et al. "How do quasi-liquid layers emerge from ice crystal surfaces?" In: *Crystal growth & design* 13.4 (2013), pp. 1761–1766.

[34] Xing Wei, Paulo B Miranda, and YR Shen. "Surface vibrational spectroscopic study of surface melting of ice". In: *Physical review letters* 86.8 (2001), p. 1554.

[35] H Cho et al. "NMR investigation of the quasi-brine layer in ice/brine mixtures". In: *The Journal of Physical Chemistry B* 106.43 (2002), pp. 11226–11232.

[36] AW Rempel, JS Wettlaufer, and MG Worster. "Interfacial premelting and the thermomolecular force: thermodynamic buoyancy". In: *Physical review letters* 87.8 (2001), p. 088501.

[37] Eric W Wolff, Robert Mulvaney, and K Oates. "The location of impurities in Antarctic ice". In: *Annals of Glaciology* 11 (1988), pp. 194–197.

[38] Eric W Wolff et al. "Factors controlling the electrical conductivity of ice from the polar regions a summary". In: *The Journal of Physical Chemistry B* 101.32 (1997), pp. 6090–6094.

[39] Hans-Werner Jacobi and Birgit Hilker. "A mechanism for the photochemical transformation of nitrate in snow". In: *Journal of Photochemistry and Photobiology A: Chemistry* 185.2-3 (2007), pp. 371–382.

[40] F Domine et al. "Snow physics as relevant to snow photochemistry". In: *Atmospheric chemistry and physics* 8.2 (2008), pp. 171–208.

[41] AM Grannas et al. "An overview of snow photochemistry: evidence, mechanisms and impacts". In: *Atmospheric chemistry and physics* 7.16 (2007), pp. 4329–4373.

[42] Piers RF Barnes and Eric W Wolff. "Distribution of soluble impurities in cold glacial ice". In: *Journal of Glaciology* 50.170 (2004), pp. 311–324.

[43] Emmanuel Thibert and Florent Domine. "Thermodynamics and kinetics of the solid solution of HCl in ice". In: *The Journal of Physical Chemistry B* 101.18 (1997), pp. 3554–3565.

[44] HJ Beine et al. "Surprisingly small HONO emissions from snow surfaces at Browning Pass, Antarctica". In: *Atmospheric Chemistry and Physics* 6.9 (2006), pp. 2569–2580.

[45] Ann Louise Sumner and Paul B Shepson. "Snowpack production of formaldehyde and its effect on the Arctic troposphere". In: *Nature* 398.6724 (1999), pp. 230–233.

[46] Hans-Werner Jacobi, Thompson Annor, and Emmanuel Quansah. "Investigation of the photochemical decomposition of nitrate, hydrogen peroxide, and formaldehyde in artificial snow". In: *Journal of Photochemistry and Photobiology A: Chemistry* 179.3 (2006), pp. 330–338.

[47] Manuel Barret et al. "Formaldehyde in the Alaskan Arctic snowpack: Partitioning and physical processes involved in air-snow exchanges". In: *Journal of Geophysical Research: Atmospheres* 116.D14 (2011).

[48] Manuel Barret, Stephan Houdier, and Florent Domine. "Thermodynamics of the formaldehyde- water and formaldehyde- ice systems for atmospheric applications". In: *The Journal of Physical Chemistry A* 115.3 (2011), pp. 307–317.

[49] Gillian L Daly and Frank Wania. "Simulating the influence of snow on the fate of organic compounds". In: *Environmental science & technology* 38.15 (2004), pp. 4176–4186.

[50] Matt F Simcik et al. "Gas-particle partitioning of PCBs and PAHs in the Chicago urban and adjacent coastal atmosphere: states of equilibrium". In: *Environmental science & technology* 32.2 (1998), pp. 251–257.

[51] Pingqing Fu, Kimitaka Kawamura, and Leonard A Barrie. "Photochemical and other sources of organic compounds in the Canadian high Arctic aerosol pollution during winter- spring". In: *Environmental Science & Technology* 43.2 (2009), pp. 286–292.

[52] Jesse H Kroll and John H Seinfeld. "Chemistry of secondary organic aerosol: Formation and evolution of low-volatility organics in the atmosphere". In: *Atmospheric Environment* 42.16 (2008), pp. 3593–3624.

[53] Fernanda C Bononi et al. “Bathochromic Shift in the UV–visible absorption spectra of phenols at ice surfaces: insights from first-principles calculations”. In: *The Journal of Physical Chemistry A* 124.44 (2020), pp. 9288–9298.

[54] David N Thomas and Gerhard S Dieckmann. “Sea ice: an introduction to its physics, chemistry, biology and geology”. In: (2008).

[55] Stephen G Warren. “Optical properties of ice and snow”. In: *Philosophical Transactions of the Royal Society A* 377.2146 (2019), p. 20180161.

[56] Stephen G Warren and Richard E Brandt. “Optical constants of ice from the ultraviolet to the microwave: A revised compilation”. In: *Journal of Geophysical Research: Atmospheres* 113.D14 (2008).

[57] Eric W Wolff et al. “Modelling photochemical NOx production and nitrate loss in the upper snowpack of Antarctica”. In: *Geophysical Research Letters* 29.20 (2002), pp. 5–1.

[58] Liang Chu and Cort Anastasio. “Quantum yields of hydroxyl radical and nitrogen dioxide from the photolysis of nitrate on ice”. In: *The Journal of Physical Chemistry A* 107.45 (2003), pp. 9594–9602.

[59] Donald K Perovich. “Light reflection and transmission by a temperate snow cover”. In: *Journal of Glaciology* 53.181 (2007), pp. 201–210.

[60] Alexander A Kokhanovsky. “Light penetration in snow layers”. In: *Journal of Quantitative Spectroscopy and Radiative Transfer* 278 (2022), p. 108040.

[61] Luca Teruzzi et al. “An innovative tool for measuring Sunlight propagation through different snowpacks”. In: *EGUsphere* 2024 (2024), pp. 1–30.

[62] John M Wallace and Peter V Hobbs. *Atmospheric science: an introductory survey*. Vol. 92. Elsevier, 2006.

[63] Y Tobo et al. “Organic matter matters for ice nuclei of agricultural soil origin”. In: *Atmospheric Chemistry and Physics* 14.16 (2014), pp. 8521–8531.

[64] Bernd R Pinzer and Martin Schneebeli. “Snow metamorphism under alternating temperature gradients: Morphology and recrystallization in surface snow”. In: *Geophysical research letters* 36.23 (2009).

[65] Florent Domine et al. “Interactions between snow metamorphism and climate: Physical and chemical aspects”. In: *Special Publication-Royal Society of Chemistry* 311 (2006), p. 27.

[66] Desneiges S Murray et al. “Nitrogen wet deposition stoichiometry: the role of organic nitrogen, seasonality, and snow”. In: *Biogeochemistry* 160.3 (2022), pp. 301–314.

[67] Jean Muhlbaier Dasch and Steven H Cadle. “Dry deposition to snow in an urban area”. In: *Water, Air, and Soil Pollution* 29 (1986), pp. 297–308.

[68] Elena Barbaro et al. “Measurement report: Spatial variations in ionic chemistry and water-stable isotopes in the snowpack on glaciers across Svalbard during the 2015–2016 snow accumulation season”. In: *Atmospheric Chemistry and Physics* 21.4 (2021), pp. 3163–3180.

[69] Paolo Gabrielli et al. “Trace elements in winter snow of the Dolomites (Italy): a statistical study of natural and anthropogenic contributions”. In: *Chemosphere* 72.10 (2008), pp. 1504–1509.

[70] Jean-Luc Jaffrezo et al. “Sulfate and MSA in the air and snow on the Greenland ice sheet”. In: *Journal of Geophysical Research: Atmospheres* 99.D1 (1994), pp. 1241–1253.

[71] Marco Vecchiato et al. “The Great Acceleration of fragrances and PAHs archived in an ice core from Elbrus, Caucasus”. In: *Scientific reports* 10.1 (2020), p. 10661.

[72] Warren J Wiscombe and Stephen G Warren. “A model for the spectral albedo of snow. I: Pure snow”. In: *Journal of Atmospheric Sciences* 37.12 (1980), pp. 2712–2733.

[73] Q Libois et al. “Influence of grain shape on light penetration in snow”. In: *The Cryosphere* 7.6 (2013), pp. 1803–1818.

[74] World Meteorological Organization (WMO). *Sea-ice Information and Services*. WMO-No. 574. Available from https://library.wmo.int. Geneva, Switzerland: World Meteorological Organization, 2024. ISBN: 978-92-63-10574-5.

[75] Donald K Perovich. “Sea ice and sunlight”. In: *Sea ice* (2017), pp. 110–137.

[76] Elisa De Laurentiis et al. “Effects of climate change on surface-water photochemistry: a review”. In: *Environmental Science and Pollution Research* 21 (2014), pp. 11770–11780.

[77] Davide Vione et al. “Indirect photochemistry in sunlit surface waters: photoinduced production of reactive transient species”. In: *Chemistry–A European Journal* 20.34 (2014), pp. 10590–10606.

[78] Gurudatta Singh et al. “The fate of organic pollutants and their microbial degradation in water bodies”. In: *Pollutants and water management: resources, strategies and scarcity* (2021), pp. 210–240.

[79] Bhagyashree Tiwari et al. “Review on fate and mechanism of removal of pharmaceutical pollutants from wastewater using biological approach”. In: *Bioresource technology* 224 (2017), pp. 1–12.

[80] Luca Carena et al. “The role of direct photolysis in the photodegradation of the herbicide bentazone in natural surface waters”. In: *Chemosphere* 246 (2020), p. 125705.

[81] Bing Chen, Chun Yang, and Ngoh Khang Goh. “Direct photolysis of nitroaromatic compounds in aqueous solutions”. In: *Journal of Environmental Sciences* 17.4 (2005), pp. 598–604.

[82] Jules C Carlson et al. “Direct UV photolysis of selected pharmaceuticals, personal care products and endocrine disruptors in aqueous solution”. In: *Water Research* 84 (2015), pp. 350–361.

[83] John Mack and James R Bolton. “Photochemistry of nitrite and nitrate in aqueous solution: a review”. In: *Journal of Photochemistry and Photobiology A: Chemistry* 128.1-3 (1999), pp. 1–13.

[84] Andrea A Andrew et al. “Chromophoric dissolved organic matter (CDOM) in the Equatorial Atlantic Ocean: Optical properties and their relation to CDOM structure and source”. In: *Marine Chemistry* 148 (2013), pp. 33–43.

[85] Danning Zhang, Shuwen Yan, and Weihua Song. “Photochemically induced formation of reactive oxygen species (ROS) from effluent organic matter”. In: *Environmental science & technology* 48.21 (2014), pp. 12645–12653.

[86] Zoltán Németh et al. “Analytical methods for investigating the presence, photoisomerisation-, and degradation kinetics of the UV-A filter avobenzone under aqueous conditions to ensure a more realistic environmental measurement”. In: *Journal of Photochemistry and Photobiology A: Chemistry* 439 (2023), p. 114621.

[87] Shuang Luo et al. “UV direct photolysis of sulfamethoxazole and ibuprofen: an experimental and modelling study”. In: *Journal of Hazardous Materials* 343 (2018), pp. 132–139.

[88] Patrick L Brezonik and Jennifer Fulkerson-Brekken. "Nitrate-induced photolysis in natural waters: controls on concentrations of hydroxyl radical photo-intermediates by natural scavenging agents". In: *Environmental Science & Technology* 32.19 (1998), pp. 3004–3010.

[89] Davide Vione et al. "Sources and sinks of hydroxyl radicals upon irradiation of natural water samples". In: *Environmental science & technology* 40.12 (2006), pp. 3775–3781.

[90] Kazuhiko Takeda et al. "Determination of hydroxyl radical photoproduction rates in natural waters". In: *Analytical sciences* 20.1 (2004), pp. 153–158.

[91] Kristopher McNeill and Silvio Canonica. "Triplet state dissolved organic matter in aquatic photochemistry: reaction mechanisms, substrate scope, and photophysical properties". In: *Environmental Science: Processes & Impacts* 18.11 (2016), pp. 1381–1399.

[92] Sarah E Page et al. "Hydroxyl radical formation upon oxidation of reduced humic acids by oxygen in the dark". In: *Environmental science & technology* 46.3 (2012), pp. 1590–1597.

[93] Davide Vione. "A critical view of the application of the APEX software (Aqueous Photochemistry of Environmentally-occurring Xenobiotics) to predict photoreaction kinetics in surface freshwaters". In: *Molecules* 25.1 (2019), p. 9.

[94] Douglas E Latch and Kristopher McNeill. "Microheterogeneity of singlet oxygen distributions in irradiated humic acid solutions". In: *Science* 311.5768 (2006), pp. 1743–1747.

[95] Rachel C Scholes. "Emerging investigator series: contributions of reactive nitrogen species to transformations of organic compounds in water: a critical review". In: *Environmental Science: Processes & Impacts* 24.6 (2022), pp. 851–869.

[96] Hans-Werner Jacobi et al. "Role of nitrite in the photochemical formation of radicals in the snow". In: *Environmental science & technology* 48.1 (2014), pp. 165–172.

[97] Claudio Minero et al. "Photochemincal processes involving nitrite in surface water samples". In: *Aquatic Sciences* 69 (2007), pp. 71–85.

[98] Franck Machado and Pierre Boule. "Photonitration and photonitrosation of phenolic derivatives induced in aqueous solution by excitation of nitrite and nitrate ions". In: *Journal of Photochemistry and Photobiology A: Chemistry* 86.1-3 (1995), pp. 73–80.

[99] Yong-Yoon Ahn, Jungwon Kim, and Kitae Kim. "Catalytic behavior of nitrous acid for acetaminophen transformation during the freezing process". In: *Journal of Hazardous Materials* 456 (2023), p. 131652.

[100] Yong-Yoon Ahn, Jungwon Kim, and Kitae Kim. "Frozen hydrogen peroxide and nitrite solution: The acceleration of benzoic acid oxidation via the decreased pH in ice". In: *Environmental Science & Technology* 56.4 (2021), pp. 2323–2333.

[101] Earl Michael Thurman. *Organic geochemistry of natural waters*. Vol. 2. Springer Science & Business Media, 2012.

[102] Charles M Sharpless and Neil V Blough. "The importance of charge-transfer interactions in determining chromophoric dissolved organic matter (CDOM) optical and photochemical properties". In: *Environmental Science: Processes & Impacts* 16.4 (2014), pp. 654–671.

[103] Richard G Zepp et al. "Singlet oxygen in natural waters". In: *Nature* 267.5610 (1977), pp. 421–423.

[104] Kimberly M Parker and William A Mitch. "Halogen radicals contribute to photooxidation in coastal and estuarine waters". In: *Proceedings of the National Academy of Sciences* 113.21 (2016), pp. 5868–5873.

[105] Jazmín Porras et al. "Humic substances enhance chlorothalonil phototransformation via photoreduction and energy transfer". In: *Environmental science & technology* 48.4 (2014), pp. 2218–2225.

[106] Pratap Reddy Maddigapu et al. "Enhancement by anthraquinone-2-sulphonate of the photonitration of phenol by nitrite: Implication for the photoproduction of nitrogen dioxide by coloured dissolved organic matter in surface waters". In: *Chemosphere* 81.11 (2010), pp. 1401–1406.

[107] Luca Carena et al. "Environmental photodegradation of emerging contaminants: A re-examination of the importance of triplet-sensitised processes, based on the use of 4-carboxybenzophenone as proxy for the chromophoric dissolved organic matter". In: *Chemosphere* 237 (2019), p. 124476.

[108] Ke Zhang and Kimberly M Parker. "Halogen radical oxidants in natural and engineered aquatic systems". In: *Environmental science & technology* 52.17 (2018), pp. 9579–9594.

[109] Peter Wardman. "Reduction potentials of one-electron couples involving free radicals in aqueous solution". In: *Journal of Physical and Chemical Reference Data* 18.4 (1989), pp. 1637–1755.

[110] Tara F Kahan et al. "Anthracene photolysis in aqueous solution and ice: photon flux dependence and comparison of kinetics in bulk ice and at the air- ice interface". In: *Environmental science & technology* 44.4 (2010), pp. 1302–1306.

[111] Stefano Frassati et al. "Photodegradation of bisphenol A in water and ice: identification of products using three photosensitizers". In: *Environmental Science and Pollution Research* (2024), pp. 1–13.

[112] Antonia M Calafat et al. "Exposure to bisphenol A and other phenols in neonatal intensive care unit premature infants". In: *Environmental health perspectives* 117.4 (2009), pp. 639–644.

[113] Xu-Liang Cao, Jeannette Corriveau, and Svetlana Popovic. "Levels of bisphenol A in canned soft drink products in Canadian markets". In: *Journal of Agricultural and Food Chemistry* 57.4 (2009), pp. 1307–1311.

[114] Laura N Vandenberg et al. "Human exposure to bisphenol A (BPA)". In: *Reproductive toxicology* 24.2 (2007), pp. 139–177.

[115] Sarah A Vogel. "The politics of plastics: the making and unmaking of bisphenol a "safety"". In: *American journal of public health* 99.S3 (2009), S559–S566.

[116] Muhammad Faisal Manzoor et al. "An insight into bisphenol A, food exposure and its adverse effects on health: A review". In: *Frontiers in nutrition* 9 (2022), p. 1047827.

[117] D Andrew Crain et al. "An ecological assessment of bisphenol-A: evidence from comparative biology". In: *Reproductive toxicology* 24.2 (2007), pp. 225–239.

[118] Kiyoaki Sone et al. "Effects of 17β-estradiol, nonylphenol, and bisphenol-A on developing Xenopus laevis embryos". In: *General and comparative endocrinology* 138.3 (2004), pp. 228–236.

[119] Shawichi Iwamuro et al. "Teratogenic and anti-metamorphic effects of bisphenol A on embryonic and larval Xenopus laevis". In: *General and comparative endocrinology* 133.2 (2003), pp. 189–198.

[120] Filippo Acconcia, Valentina Pallottini, and Maria Marino. "Molecular mechanisms of action of BPA". In: *Dose-response* 13.4 (2015), p. 1559325815610582.

[121] Beverly S Rubin. "Bisphenol A: an endocrine disruptor with widespread exposure and multiple effects". In: *The Journal of steroid biochemistry and molecular biology* 127.1-2 (2011), pp. 27–34.

[122] Eriko Yamazaki et al. "Bisphenol A and other bisphenol analogues including BPS and BPF in surface water samples from Japan, China, Korea and India". In: *Ecotoxicology and environmental safety* 122 (2015), pp. 565–572.

[123] Hao Wang et al. "Occurrence, spatial distribution, and main source identification of ten bisphenol analogues in the dry season of the Pearl River, South China". In: *Environmental Science and Pollution Research* (2022), pp. 1–14.

[124] Benoit Lalonde and Christine Garron. "Spatial and temporal distribution of BPA in the Canadian freshwater environment". In: *Archives of Environmental Contamination and Toxicology* 78.4 (2020), pp. 568–578.

[125] Marianna D'Amico et al. "Chemicals of Emerging Arctic Concern in north-western Spitsbergen snow: Distribution and sources". In: *Science of The Total Environment* 908 (2024), p. 168401.

[126] Mark L Ferrey et al. "Pharmaceuticals and other anthropogenic chemicals in atmospheric particulates and precipitation". In: *Science of the Total Environment* 612 (2018), pp. 1488–1497.

[127] Sunggyu Lee et al. "Emission of bisphenol analogues including bisphenol A and bisphenol F from wastewater treatment plants in Korea". In: *Chemosphere* 119 (2015), pp. 1000–1006.

[128] Yu Hu et al. "Occurrence, fate and risk assessment of BPA and its substituents in wastewater treatment plant: A review". In: *Environmental Research* 178 (2019), p. 108732.

[129] Iain A Lang et al. "Association of urinary bisphenol A concentration with medical disorders and laboratory abnormalities in adults". In: *Jama* 300.11 (2008), pp. 1303–1310.

[130] Pingqing Fu and Kimitaka Kawamura. "Ubiquity of bisphenol A in the atmosphere". In: *Environmental Pollution* 158.10 (2010), pp. 3138–3143.

[131] Johanna R Rochester. "Bisphenol A and human health: a review of the literature". In: *Reproductive toxicology* 42 (2013), pp. 132–155.

[132] B Senthil Rathi, P Senthil Kumar, and Pau-Loke Show. "A review on effective removal of emerging contaminants from aquatic systems: Current trends and scope for further research". In: *Journal of hazardous materials* 409 (2021), p. 124413.

[133] OP Heemken et al. "The occurrence of xenoestrogens in the Elbe river and the North Sea". In: *Chemosphere* 45.3 (2001), pp. 245–259.

[134] Bich Chau Tran et al. "BPA and phthalate fate in a sewage network and an elementary river of France. Influence of hydroclimatic conditions". In: *Chemosphere* 119 (2015), pp. 43–51.

[135] Rubén Gil-Solsona et al. "A holistic assessment of the sources, prevalence, and distribution of bisphenol A and analogues in water, sediments, biota and plastic litter of the Ebro Delta (Spain)". In: *Environmental pollution* 314 (2022), p. 120310.

[136] Pavel Šauer et al. "Bisphenols emerging in Norwegian and Czech aquatic environments show transthyretin binding potency and other less-studied endocrine-disrupting activities". In: *Science of The Total Environment* 751 (2021), p. 141801.

[137] Joel Sánchez-Piñero et al. "Multi-class organic pollutants in atmospheric particulate matter (PM2. 5) from a Southwestern Europe industrial area: Levels, sources and human health risk". In: *Environmental research* 214 (2022), p. 114195.

[138] Linke Ge et al. "Photochemical degradation of hydroxy PAHs in ice: Implications for the polar areas". In: *Chemosphere* 155 (2016), pp. 375–379.

[139] Caitlin Rering et al. "Comparison of direct and indirect photolysis in imazosulfuron photodegradation". In: *Journal of Agricultural and Food Chemistry* 65.15 (2017), pp. 3103–3108.

[140] JL France, MD King, and J Lee-Taylor. "Hydroxyl (OH) radical production rates in snowpacks from photolysis of hydrogen peroxide (H2O2) and nitrate (NO3-)". In: *Atmospheric Environment* 41.26 (2007), pp. 5502–5509.

[141] Jonathan P Bower and Cort Anastasio. "Degradation of organic pollutants in/on snow and ice by singlet molecular oxygen (1 O* 2) and an organic triplet excited state". In: *Environmental Science: Processes & Impacts* 16.4 (2014), pp. 748–756.

[142] Alexis Fede and Amanda M Grannas. "Photochemical production of singlet oxygen from dissolved organic matter in ice". In: *Environmental Science & Technology* 49.21 (2015), pp. 12808–12815.

[143] Philip PA Malley, Jarod N Grossman, and Tara F Kahan. "Effects of chromophoric dissolved organic matter on anthracene photolysis kinetics in aqueous solution and ice". In: *The Journal of Physical Chemistry A* 121.40 (2017), pp. 7619–7626.

[144] Valter Maurino et al. "Transformation of phenolic compounds upon UVA irradiation of anthraquinone-2-sulfonate". In: *Photochemical & Photobiological Sciences* 7.3 (2008), pp. 321–327.

[145] I Loeff, A Treinin, and Henry Linschitz. "Photochemistry of 9, 10-anthraquinone-2-sulfonate in solution. 1. Intermediates and mechanism". In: *The Journal of Physical Chemistry* 87.14 (1983), pp. 2536–2544.

[146] Rose M Cory, James B Cotner, and Kristopher McNeill. "Quantifying interactions between singlet oxygen and aquatic fulvic acids". In: *Environmental Science & Technology* 43.3 (2009), pp. 718–723.

[147] Rose M Cory et al. "Singlet oxygen in the coupled photochemical and biochemical oxidation of dissolved organic matter". In: *Environmental Science & Technology* 44.10 (2010), pp. 3683–3689.

[148] Andrea Bedini et al. "Phototransformation of anthraquinone-2-sulphonate in aqueous solution". In: *Photochemical & Photobiological Sciences* 11 (2012), pp. 1445–1453.

[149] Jonathan P Bower and Cort Anastasio. "Measuring a 10,000-fold enhancement of singlet molecular oxygen (1O2*) concentration on illuminated ice relative to the corresponding liquid solution". In: *Atmospheric environment* 75 (2013), pp. 188–195.

[150] Josué Bock and Hans-Werner Jacobi. "Development of a mechanism for nitrate photochemistry in snow". In: *The Journal of Physical Chemistry A* 114.4 (2010), pp. 1790–1796.

[151] Luca Carena et al. "Phototransformation of vanillin in artificial snow by direct photolysis and mediated by nitrite". In: *Environmental Science & Technology* 57.23 (2023), pp. 8785–8795.

[152] Davide Vione et al. "Phenol nitration upon oxidation of nitrite by Mn (III, IV)(hydr) oxides". In: *Chemosphere* 55.7 (2004), pp. 941–949.

[153] Hadjira Boucheloukh et al. “Kinetic and analytical study of the photo-induced degradation of monuron by nitrates and nitrites under irradiation or in the dark”. In: *Photochemical & Photobiological Sciences* 11 (2012), pp. 1339–1345.

[154] Davide Vione et al. “Formation of substances with humic-like fluorescence properties, upon photoinduced oligomerization of typical phenolic compounds emitted by biomass burning”. In: *Atmospheric Environment* 206 (2019), pp. 197–207.

[155] Kunal Nepali, Hsueh-Yun Lee, and Jing-Ping Liou. “Nitro-group-containing drugs”. In: *Journal of medicinal chemistry* 62.6 (2018), pp. 2851–2893.

[156] Susan D Richardson and Susana Y Kimura. “Water analysis: emerging contaminants and current issues”. In: *Analytical Chemistry* 92.1 (2019), pp. 473–505.

[157] Roland Kallenborn, Hayley Hung, and Eva Brorström-Lundén. “Atmospheric long-range transport of persistent organic pollutants (POPs) into polar regions”. In: *Comprehensive analytical chemistry*. Vol. 67. Elsevier, 2015, pp. 411–432.

[158] Mohammed A Khairy et al. “Levels, sources and chemical fate of persistent organic pollutants in the atmosphere and snow along the western Antarctic Peninsula”. In: *Environmental pollution* 216 (2016), pp. 304–313.

[159] Kathrin Fenner et al. “Evaluating pesticide degradation in the environment: blind spots and emerging opportunities”. In: *science* 341.6147 (2013), pp. 752–758.

[160] Christina K Remucal. “The role of indirect photochemical degradation in the environmental fate of pesticides: a review”. In: *Environmental Science: Processes & Impacts* 16.4 (2014), pp. 628–653.

[161] Shuwen Yan and Weihua Song. “Photo-transformation of pharmaceutically active compounds in the aqueous environment: a review”. In: *Environmental Science: Processes & Impacts* 16.4 (2014), pp. 697–720.

[162] Elisabeth M-L Janssen, Paul R Erickson, and Kristopher McNeill. “Dual roles of dissolved organic matter as sensitizer and quencher in the photooxidation of tryptophan”. In: *Environmental science & technology* 48.9 (2014), pp. 4916–4924.

[163] Ruchi Bhattacharya and Christopher L Osburn. “Chromophoric dissolved organic matter composition and load from a coastal river system under variable flow regimes”. In: *Science of the Total Environment* 760 (2021), p. 143414.

[164] Erin S Boyle et al. “Optical properties of humic substances and CDOM: relation to structure”. In: *Environmental science & technology* 43.7 (2009), pp. 2262–2268.

[165] N Mladenov et al. “Alpine lake optical properties as sentinels of dust deposition and global change”. In: *Limnology and oceanography* 54.6part2 (2009), pp. 2386–2400.

[166] Hartmut Herrmann et al. “Tropospheric aqueous-phase free-radical chemistry: Radical sources, spectra, reaction kinetics and prediction tools”. In: *ChemPhysChem* 11.18 (2010), pp. 3796–3822.

[167] Ana Kroflič et al. “Underappreciated and complex role of nitrous acid in aromatic nitration under mild environmental conditions: the case of activated methoxyphenols”. In: *Environmental science & technology* 52.23 (2018), pp. 13756–13765.

[168] Shixuan Cui et al. “Natural sunlight-driven aquatic toxicity enhancement of 2, 6-di-tert-butylphenol toward Photobacterium phosphoreum”. In: *Environmental Pollution* 251 (2019), pp. 66–71.

[169] Paul R Erickson et al. "Photochemical formation of brominated dioxins and other products of concern from hydroxylated polybrominated diphenyl ethers (OH-PBDEs)". In: *Environmental science & technology* 46.15 (2012), pp. 8174–8180.

[170] Florent Dominé and Paul B Shepson. "Air-snow interactions and atmospheric chemistry". In: *Science* 297.5586 (2002), pp. 1506–1510.

[171] Amanda M Grannas et al. "The role of the global cryosphere in the fate of organic contaminants". In: *Atmospheric Chemistry and Physics* 13.6 (2013), pp. 3271–3305.

[172] Zhuojuan Li et al. "Effect of fulvic acid concentration levels on the cleavage of piperazinyl and defluorination of ciprofloxacin photodegradation in ice". In: *Environmental Pollution* 307 (2022), p. 119499.

[173] Glenn A Rowland, Alexandra R Bausch, and Amanda M Grannas. "Photochemical processing of aldrin and dieldrin in frozen aqueous solutions under arctic field conditions". In: *Environmental Pollution* 159.5 (2011), pp. 1076–1084.

[174] Sumi N Wren and DJ Donaldson. "Laboratory study of pH at the air–ice interface". In: *The Journal of Physical Chemistry C* 116.18 (2012), pp. 10171–10180.

[175] Ted Hullar et al. "Photodecay of guaiacol is faster in ice, and even more rapid on ice, than in aqueous solution". In: *Environmental Science: Processes & Impacts* 22.8 (2020), pp. 1666–1677.

[176] Kitae Kim et al. "Photoreductive dissolution of iron oxides trapped in ice and its environmental implications". In: *Environmental science & technology* 44.11 (2010), pp. 4142–4148.

[177] Shaochong Liu et al. "Photodegradation of bisphenol A (BPA) in coastal aquaculture waters: Influencing factors, products, and pathways". In: *Chemosphere* 363 (2024), p. 142708.

[178] Yiting Wang et al. "Reaction kinetics and molecular characterization of the compounds formed by photosensitized degradation of the plastic additive bisphenol A in the atmospheric aqueous phase". In: *Scientific Reports* 14.1 (2024), p. 31802.

[179] Edward S Galbavy, Keren Ram, and Cort Anastasio. "2-Nitrobenzaldehyde as a chemical actinometer for solution and ice photochemistry". In: *Journal of Photochemistry and Photobiology A: Chemistry* 209.2-3 (2010), pp. 186–192.

[180] Manuel A Hutterli et al. "Impact of temperature-driven cycling of hydrogen peroxide (H2O2) between air and snow on the planetary boundary layer". In: *Journal of Geophysical Research: Atmospheres* 106.D14 (2001), pp. 15395–15404.

[181] Hans-Werner Jacobi, Bright Kwakye-Awuah, and Otto Schrems. "Photochemical decomposition of hydrogen peroxide (H2O2) and formaldehyde (HCHO) in artificial snow". In: *Annals of glaciology* 39 (2004), pp. 29–33.

[182] Marco Minella et al. "An experimental methodology to measure the reaction rate constants of processes sensitised by the triplet state of 4-carboxybenzophenone as a proxy of the triplet states of chromophoric dissolved organic matter, under steady-state irradiation conditions". In: *Environmental science: processes & impacts* 20.7 (2018), pp. 1007–1019.

[183] Eran Hood et al. "Storage and release of organic carbon from glaciers and ice sheets". In: *Nature geoscience* 8.2 (2015), pp. 91–96.

[184] Yulan Zhang et al. "Dissolved organic carbon in snow cover of the Chinese Altai Mountains, Central Asia: Concentrations, sources and light-absorption properties". In: *Science of the Total Environment* 647 (2019), pp. 1385–1397.

[185] Jacinta Edebeli et al. "Snow heterogeneous reactivity of bromide with ozone lost during snow metamorphism". In: *Atmospheric Chemistry and Physics* 20.21 (2020), pp. 13443–13454.

[186] Elena Barbaro et al. "Col Margherita Observatory: A background site in the Eastern Italian Alps for investigating the chemical composition of atmospheric aerosols". In: *Atmospheric Environment* 221 (2020), p. 117071.

[187] Lara M Schuijt et al. "(Eco) toxicological tests for assessing impacts of chemical stress to aquatic ecosystems: facts, challenges, and future". In: *Science of the total environment* 795 (2021), p. 148776.

[188] K. Mayo-Bean et al. *Methodology Document for the Ecological Structure-Activity Relationship Model (ECOSAR) Class Program*. Technical Report. Version 2012a. U.S. Environmental Protection Agency (US-EPA), 2012.

[189] Julie R Peller, Stephen P Mezyk, and William J Cooper. "Bisphenol A reactions with hydroxyl radicals: diverse pathways determined between deionized water and tertiary treated wastewater solutions". In: *Research on Chemical Intermediates* 35 (2009), pp. 21–34.

[190] Ruiyang Xiao et al. "Mechanistic insight into degradation of endocrine disrupting chemical by hydroxyl radical: an experimental and theoretical approach". In: *Environmental Pollution* 231 (2017), pp. 1446–1452.

[191] Harry Beine and Cort Anastasio. "The photolysis of flash-frozen dilute hydrogen peroxide solutions". In: *Journal of Geophysical Research: Atmospheres* 116.D14 (2011).

[192] Stanislav Lunák and Petr Sedlák. "Photoinitiated reactions of hydrogen peroxide in the liquid phase". In: *Journal of Photochemistry and Photobiology A: Chemistry* 68.1 (1992), pp. 1–33.

[193] Elena Appiani and Kristopher McNeill. "Photochemical production of singlet oxygen from particulate organic matter". In: *Environmental science & technology* 49.6 (2015), pp. 3514–3522.

[194] M Kerbrat et al. "Measuring the specific surface area of snow with X-ray tomography and gas adsorption: comparison and implications for surface smoothness". In: *Atmospheric Chemistry and Physics* 8.5 (2008), pp. 1261–1275.

[195] Jaesang Lee, Urs Von Gunten, and Jae-Hong Kim. "Persulfate-based advanced oxidation: critical assessment of opportunities and roadblocks". In: *Environmental science & technology* 54.6 (2020), pp. 3064–3081.

[196] Wenjie Jin et al. "Insights into generation mechanisms of halogen radicals from excited triplet state of dissolved organic matter". In: *Science of The Total Environment* 834 (2022), p. 155280.

[197] Yu Lei et al. "Rate constants and mechanisms for reactions of bromine radicals with trace organic contaminants". In: *Environmental Science & Technology* 55.15 (2021), pp. 10502–10513.

[198] Emma L Schymanski et al. *Identifying small molecules via high resolution mass spectrometry: communicating confidence*. 2014.

[199] Yanina Barbieri et al. "Photodegradation of bisphenol A and related compounds under natural-like conditions in the presence of riboflavin: Kinetics, mechanism and photoproducts". In: *Chemosphere* 73.4 (2008), pp. 564–571.

[200] Júlio César Cardoso da Silva et al. "Photodegradation of bisphenol A in aqueous medium: Monitoring and identification of by-products by liquid chromatography coupled to high-resolution mass spectrometry". In: *Rapid Communications in Mass Spectrometry* 28.9 (2014), pp. 987–994.

[201] Fernando L Rosario-Ortiz and Julie A Korak. *Oversimplification of dissolved organic matter fluorescence analysis: potential pitfalls of current methods*. 2017.

[202] Jannis Wenk and Silvio Canonica. "Phenolic antioxidants inhibit the triplet-induced transformation of anilines and sulfonamide antibiotics in aqueous solution". In: *Environmental science & technology* 46.10 (2012), pp. 5455–5462.

[203] Peter Reuschenbach et al. "ECOSAR model performance with a large test set of industrial chemicals". In: *Chemosphere* 71.10 (2008), pp. 1986–1995.

[204] Zeyuan Chen and Cort Anastasio. "Concentrations of a triplet excited state are enhanced in illuminated ice". In: *Environmental Science: Processes & Impacts* 19.1 (2017), pp. 12–21.

[205] G. Paolella et al. "Fate of bisphenol A in marine environment: a critical review". In: *Chemical Engineering Journal* 495 (2024), p. 153228.

[206] C. Liao and K. Kannan. "Widespread Occurrence of Bisphenol A in Paper and Paper Products: Implications for Human Exposure". In: *Environmental Science and Technology* 45 (2011), pp. 9372–9379.

[207] R. E. Dodson et al. "Endocrine Disruptors and Asthma-Associated Chemicals in Consumer Products". In: *Environmental Health Perspectives* 120 (2012), pp. 935–943.

[208] Y. Vicente-Martínez, M. Caravaca, and A. Soto-Meca. "Determination of Very Low Concentration of Bisphenol A in Toys and Baby Pacifiers Using Dispersive Liquid–Liquid Microextraction by In Situ Ionic Liquid Formation and High-Performance Liquid Chromatography". In: *Pharmaceuticals* 13 (2020), p. 301.

[209] K. V. Ragavan, N. K. Rastogi, and M. S. Thakur. "Sensors and biosensors for analysis of bisphenol-A". In: *Trends in Analytical Chemistry* 52 (2013), pp. 248–260.

[210] R. U. Halden. "Plastics and Health Risks". In: *Annual Review of Public Health* 31 (2010), pp. 179–194.

[211] H. Kawahata et al. "Endocrine disrupter nonylphenol and bisphenol A contamination in Okinawa and Ishigaki Islands, Japan—within coral reefs and adjacent river mouths". In: *Chemosphere* 55 (2004), pp. 1519–1527.

[212] K. M. Sta. Ana and M. P. Espino. "Occurrence and distribution of hormones and bisphenol A in Laguna Lake, Philippines". In: *Chemosphere* 256 (2020), p. 127122.

[213] J. Xie et al. "Occurrence and partitioning of bisphenol analogues, triclocarban, and triclosan in seawater and sediment from East China Sea". In: *Chemosphere* 287 (2022), p. 132218.

[214] Y. Soltani Nejad et al. "Bisphenol A in fish, seawater, and fishermen's urine: measurement and health risk assessment in southern Iran". In: *International Journal of Environmental Science and Technology* 20 (2023), pp. 3891–3900.

[215] J. Sajiki and J. Yonekubo. "Leaching of bisphenol A (BPA) to seawater from polycarbonate plastic and its degradation by reactive oxygen species". In: *Chemosphere* 51 (2003), pp. 55–62.

[216] X. Liu et al. "Microplastics as Both a Sink and a Source of Bisphenol A in the Marine Environment". In: *Environmental Science and Technology* 53 (2019), pp. 10188–10196.

[217] V. Fauvelle et al. “Organic additive release from plastic to seawater is lower under deep-sea conditions”. In: *Nature Communications* 12 (2021), p. 4426.

[218] T. Artham and M. Doble. “Bisphenol A and metabolites released by biodegradation of polycarbonate in seawater”. In: *Environmental Chemistry Letters* 10 (2012), pp. 29–34.

[219] M. Staniszewska, B. Graca, and I. Nehring. “The fate of bisphenol A, 4-tert-octylphenol and 4-nonylphenol leached from plastic debris into marine water – experimental studies on biodegradation and sorption on suspended particulate matter and nano-TiO2”. In: *Chemosphere* 145 (2016), pp. 535–542.

[220] H. Yamanaka et al. “Efficient Microbial Degradation of Bisphenol A in the Presence of Activated Carbon”. In: *Journal of Bioscience and Bioengineering* 105 (2008), pp. 157–160.

[221] G.-G. Ying and R. S. Kookana. “Degradation of Five Selected Endocrine-Disrupting Chemicals in Seawater and Marine Sediment”. In: *Environmental Science and Technology* 37 (2003), pp. 1256–1260.

[222] S. N. Dimassi et al. “Effect of temperature and sunlight on the leachability potential of BPA and phthalates from plastic litter under marine conditions”. In: *Science of The Total Environment* 894 (2023), p. 164954.

[223] P. Emnet et al. “Personal care products and steroid hormones in the Antarctic coastal environment associated with two Antarctic research stations, McMurdo Station and Scott Base”. In: *Environmental Research* 136 (2015), pp. 331–342.

[224] J. Garnett et al. “Investigating the Uptake and Fate of Poly- and Perfluoroalkylated Substances (PFAS) in Sea Ice Using an Experimental Sea Ice Chamber”. In: *Environmental Science and Technology* 55 (2021), pp. 9601–9608.

[225] J. Garnett et al. “Mechanistic Insight into the Uptake and Fate of Persistent Organic Pollutants in Sea Ice”. In: *Environmental Science and Technology* 53 (2019), pp. 6757–6764.

[226] Stefano Frassati et al. “Photodegradation of bisphenol A and identification of photoproducts in artificial snow under UVA radiation”. In: *Environmental Pollution* (2025), p. 126503.

[227] Katarzyna Polcwiartek, Gary A Stern, and Feiyue Wang. “Incorporation and Distribution of Polycyclic Aromatic Hydrocarbons in Experimental Sea-Ice”. In: *Environmental Science & Technology* 59.14 (2025), pp. 7310–7319.

[228] M. Ewert and J. Deming. “Sea Ice Microorganisms: Environmental Constraints and Extracellular Responses”. In: *Biology* 2 (2013), pp. 603–628.

[229] L. Veselý et al. “Freezing-induced acidification of sea ice brine”. In: *Science of The Total Environment* 946 (2024), p. 174194.

[230] K. Lin, W. Liu, and J. Gan. “Oxidative Removal of Bisphenol A by Manganese Dioxide: Efficacy, Products, and Pathways”. In: *Environmental Science & Technology* 43 (2009), pp. 3860–3864.

[231] J. J. Pignatello, E. Oliveros, and A. MacKay. “Advanced Oxidation Processes for Organic Contaminant Destruction Based on the Fenton Reaction and Related Chemistry”. In: *Critical Reviews in Environmental Science and Technology* 36 (2006), pp. 1–84.

[232] F. J. Millero and S. Sotolongo. “The oxidation of Fe(II) with H_2O_2 in seawater”. In: *Geochimica et Cosmochimica Acta* 53 (1989), pp. 1867–1873.

[233] A. L. Rose and T. D. Waite. "Kinetic Model for Fe(II) Oxidation in Seawater in the Absence and Presence of Natural Organic Matter". In: *Environmental Science & Technology* 36 (2002), pp. 433–444.

[234] D. Price, P. J. Worsfold, and R. F. C. Mantoura. "Hydrogen peroxide in the marine environment: cycling and methods of analysis". In: *TrAC Trends in Analytical Chemistry* 11 (1992), pp. 379–384.

[235] Michel Legrand et al. "Causes of enhanced bromine levels in Alpine ice cores during the 20th century: Implications for bromine in the free European troposphere". In: *Journal of Geophysical Research: Atmospheres* 126.8 (2021), e2020JD034246.

[236] Shuting Zhai et al. "Anthropogenic influence on tropospheric reactive bromine since the pre-industrial: Implications for Arctic ice-core bromine trends". In: *Geophysical Research Letters* 51.5 (2024), e2023GL107733.

[237] Shuting Zhai et al. "Implications of snowpack reactive bromine production for Arctic ice core bromine preservation". In: *Journal of Geophysical Research: Atmospheres* 128.20 (2023), e2023JD039257.

[238] François Burgay et al. "200-year ice core bromine reconstruction at Dome C (Antarctica): observational and modelling results". In: *The Cryosphere* 17.1 (2023), pp. 391–405.

[239] Andrea Spolaor et al. "Diurnal cycle of iodine, bromine, and mercury concentrations in Svalbard surface snow". In: *Atmospheric Chemistry and Physics* 19.20 (2019), pp. 13325–13339.

[240] Niccolò Maffezzoli et al. "Bromine, iodine and sodium in surface snow along the 2013 Talos Dome–GV7 traverse (northern Victoria Land, East Antarctica)". In: *The Cryosphere* 11.2 (2017), pp. 693–705.

[241] Louis Marelle et al. "Improvements to the WRF-Chem 3.5. 1 model for quasi-hemispheric simulations of aerosols and ozone in the Arctic". In: *Geoscientific Model Development* 10.10 (2017), pp. 3661–3677.

[242] K Toyota et al. "Air–snowpack exchange of bromine, ozone and mercury in the springtime Arctic simulated by the 1-D model PHANTAS–Part 1: In-snow bromine activation and its impact on ozone". In: *Atmospheric Chemistry and Physics* 14.8 (2014), pp. 4101–4133.

[243] Stefanie Falk and Björn-Martin Sinnhuber. "Polar boundary layer bromine explosion and ozone depletion events in the chemistry–climate model EMAC v2. 52: Implementation and evaluation of AirSnow algorithm". In: *Geoscientific Model Development* 11.3 (2018), pp. 1115–1131.

[244] Rafael P Fernandez et al. "Modeling the sources and chemistry of polar tropospheric halogens (Cl, Br, and I) using the CAM-Chem global chemistry-climate model". In: *Journal of Advances in Modeling Earth Systems* 11.7 (2019), pp. 2259–2289.

[245] Alfonso Saiz-Lopez et al. "Natural short-lived halogens exert an indirect cooling effect on climate". In: *Nature* 618.7967 (2023), pp. 967–973.

[246] William Robert Simpson et al. "Halogens and their role in polar boundary-layer ozone depletion". In: *Atmospheric Chemistry and Physics* 7.16 (2007), pp. 4375–4418.

[247] Udo Frieß et al. "Iodine monoxide in the Antarctic snowpack". In: *Atmospheric Chemistry and Physics* 10.5 (2010), pp. 2439–2456.

[248] Rainer Vogt et al. "Iodine chemistry and its role in halogen activation and ozone loss in the marine boundary layer: A model study". In: *Journal of Atmospheric Chemistry* 32 (1999), pp. 375–395.

[249] A Saiz-Lopez et al. "On the vertical distribution of boundary layer halogens over coastal Antarctica: implications for O 3, HO x, NO x and the Hg lifetime". In: *Atmospheric Chemistry and Physics* 8.4 (2008), pp. 887–900.

[250] Kitae Kim et al. “Production of molecular iodine and tri-iodide in the frozen solution of iodide: implication for polar atmosphere”. In: *Environmental science & technology* 50.3 (2016), pp. 1280–1287.

[251] Kitae Kim et al. “Production of molecular iodine via a redox reaction between iodate and organic compounds in ice”. In: *The Journal of Physical Chemistry A* 127.12 (2023), pp. 2830–2838.

[252] Alfonso Saiz-Lopez and John MC Plane. “Novel iodine chemistry in the marine boundary layer”. In: *Geophysical research letters* 31.4 (2004).

[253] Colin D O’Dowd et al. “Marine aerosol formation from biogenic iodine emissions”. In: *Nature* 417.6889 (2002), pp. 632–636.

[254] Gordon McFiggans. “Marine aerosols and iodine emissions”. In: *Nature* 433.7026 (2005), E13–E13.

[255] Carlos A Cuevas et al. “Rapid increase in atmospheric iodine levels in the North Atlantic since the mid-20th century”. In: *Nature communications* 9.1 (2018), p. 1452.

[256] Andrea Spolaor et al. “Sea ice dynamics influence halogen deposition to Svalbard”. In: *The Cryosphere* 7.5 (2013), pp. 1645–1658.

[257] RC Tian and E Nicolas. “Iodine speciation in the northwestern Mediterranean Sea, method and vertical profile”. In: *Marine Chemistry* 48.2 (1995), pp. 151–156.

[258] Rosie Chance et al. “The distribution of iodide at the sea surface”. In: *Environmental Science: Processes & Impacts* 16.8 (2014), pp. 1841–1859.

[259] Katrin Bluhm et al. “Distribution of iodide and iodate in the Atlantic sector of the southern ocean during austral summer”. In: *Deep Sea Research Part II: Topical Studies in Oceanography* 58.25-26 (2011), pp. 2733–2748.

[260] Andrea Spolaor et al. “Speciation analysis of iodine and bromine at picogram-per-gram levels in polar ice”. In: *Analytical and bioanalytical chemistry* 405 (2013), pp. 647–654.

[261] Benjamin Silas Gilfedder, Michael Petri, and Harald Biester. “Iodine and bromine speciation in snow and the effect of orographically induced precipitation”. In: *Atmospheric Chemistry and Physics* 7.10 (2007), pp. 2661–2669.

[262] Benjamin S Gilfedder, Michael Petri, and Harald Biester. “Iodine speciation in rain and snow: Implications for the atmospheric iodine sink”. In: *Journal of Geophysical Research: Atmospheres* 112.D7 (2007).

[263] Benjamin Silas Gilfedder et al. “Iodine speciation in rain, snow and aerosols”. In: *Atmospheric Chemistry and Physics* 8.20 (2008), pp. 6069–6084.

[264] Matthew R Jones et al. “Environmental iodine speciation quantification in seawater and snow using ion exchange chromatography and UV spectrophotometric detection”. In: *Analytica Chimica Acta* (2023).

[265] Wanjing Cui et al. “The speciation analysis of iodate and iodide in high salt brine by high performance liquid chromatography and inductively coupled plasma mass spectrometry”. In: *Journal of Analytical Atomic Spectrometry* 34.7 (2019), pp. 1374–1379.

[266] ZuLiang Chen, Mallavarapu Megharaj, and Ravendra Naidu. “Speciation of iodate and iodide in seawater by non-suppressed ion chromatography with inductively coupled plasma mass spectrometry”. In: *Talanta* 72.5 (2007), pp. 1842–1846.

[267] Wei Liu et al. “Determination of bromine and iodine speciation in drinking water using high performance liquid chromatography-inductively coupled plasma-mass spectrometry”. In: *Geostandards and Geoanalytical Research* 35.1 (2011), pp. 69–74.

[268] Kai-en Wang and Shiuh-Jen Jiang. “Determination of iodine and bromine compounds by ion chromatography/dynamic reaction cell inductively coupled plasma mass spectrometry”. In: *Analytical sciences* 24.4 (2008), pp. 509–514.

[269] Di Song and Juan Wang. “Modified resolution factor for asymmetrical peaks in chromatographic separation”. In: *Journal of pharmaceutical and biomedical analysis* 32.6 (2003), pp. 1105–1112.

[270] Elena Barbaro et al. “Domoic acid at trace levels in lagoon waters: assessment of a method using internal standard quantification”. In: *Analytical and bioanalytical chemistry* 405.28 (2013), pp. 9113–9123.

[271] Bogdan K Matuszewski, ML Constanzer, and CM Chavez-Eng. “Strategies for the assessment of matrix effect in quantitative bioanalytical methods based on HPLC- MS/MS”. In: *Analytical chemistry* 75.13 (2003), pp. 3019–3030.

[272] Federico Scoto et al. “Automated observation of physical snowpack properties in Ny-Ålesund”. In: *Frontiers in Earth Science* 11 (2023), p. 1123981.

[273] Andrea Spolaor et al. “Source, timing and dynamics of ionic species mobility in the Svalbard annual snowpack”. In: *Science of the Total Environment* 751 (2021), p. 141640.

[274] Delia Segato et al. “Arctic mercury flux increased through the Last Glacial Termination with a warming climate”. In: *Nature Geoscience* 16.5 (2023), pp. 439–445.

[275] Katarina Abrahamsson et al. “Organic bromine compounds produced in sea ice in Antarctic winter”. In: *Nature Communications* 9.1 (2018), p. 5291.

[276] Paul Vallelonga et al. “Sea-ice reconstructions from bromine and iodine in ice cores”. In: *Quaternary Science Reviews* 269 (2021), p. 107133.

[277] Krishna L Foster et al. “The role of Br2 and BrCl in surface ozone destruction at polar sunrise”. In: *Science* 291.5503 (2001), pp. 471–474.

[278] Xin Yang et al. “Snow-sourced bromine and its implications for polar tropospheric ozone”. In: *Atmospheric Chemistry and Physics* 10.16 (2010), pp. 7763–7773.

[279] T Tang and JC McConnell. “Autocatalytic release of bromine from Arctic snow pack during polar sunrise”. In: *Geophysical Research Letters* 23.19 (1996), pp. 2633–2636.

[280] KD Custard et al. “Production and release of molecular bromine and chlorine from the Arctic coastal snowpack”. In: *ACS Earth and Space Chemistry* 1.3 (2017), pp. 142–151.

[281] Jack E Dibb et al. “Bromide and other ions in the snow, firn air, and atmospheric boundary layer at Summit during GSHOX”. In: *Atmospheric Chemistry and Physics* 10.20 (2010), pp. 9931–9942.

[282] William F Swanson et al. “Comparison of model and ground observations finds snowpack and blowing snow both contribute to Arctic tropospheric reactive bromine”. In: *Atmospheric Chemistry and Physics Discussions* 2022 (2022), pp. 1–38.

[283] Rafael P Fernandez et al. “Arctic halogens reduce ozone in the northern mid-latitudes”. In: *Proceedings of the National Academy of Sciences* 121.39 (2024), e2401975121.

[284] Christina M Morrison et al. “Critical review on bromate formation during ozonation and control options for its minimization”. In: *Environmental Science & Technology* 57.47 (2023), pp. 18393–18409.

[285] Ted Hullar, Theo Tran, and Cort Anastasio. “Nitrate Photolysis at the Air–Ice Interface of Nature-Identical Snow”. In: *ACS Earth and Space Chemistry* 7.9 (2023), pp. 1791–1797.

[286] Liang Chu and Cort Anastasio. “Formation of hydroxyl radical from the photolysis of frozen hydrogen peroxide”. In: *The Journal of Physical Chemistry A* 109.28 (2005), pp. 6264–6271.

[287] Toxicology Excellence for Risk Assessment. *Health Risk Assessment*. US Environmental Protection Agency, 1998.

[288] Mauro Mazzola et al. “Atmospheric observations at the Amundsen-Nobile climate change tower in Ny-Ålesund, Svalbard”. In: *Rendiconti Lincei* 27.Suppl 1 (2016), pp. 7–18.

[289] Yee Jun Tham et al. “Widespread detection of chlorine oxyacids in the Arctic atmosphere”. In: *Nature communications* 14.1 (2023), p. 1769.

[290] CS Boxe and A Saiz-Lopez. “Multiphase modeling of nitrate photochemistry in the quasi-liquid layer (QLL): implications for NO x release from the Arctic and coastal Antarctic snowpack”. In: *Atmospheric Chemistry and Physics* 8.16 (2008), pp. 4855–4864.

[291] Matteo Feltracco et al. “The disinfection by-products are in the air: Aerosol measurements in the urban area of Venice”. In: *Atmospheric Environment* 318 (2024), p. 120224.

[292] Stefano Frassati et al. “Inorganic iodine and bromine speciation in Arctic snow at picogram-per-grams levels by IC-ICP-MS”. In: *Journal of Analytical Science and Technology* 15.1 (2024), p. 49.

[293] Elena Barbaro et al. “Characterization of the water soluble fraction in ultrafine, fine, and coarse atmospheric aerosol”. In: *Science of the Total Environment* 658 (2019), pp. 1423–1439.

[294] Ward Van Pelt et al. “A long-term dataset of climatic mass balance, snow conditions, and runoff in Svalbard (1957–2018)”. In: *The Cryosphere* 13.9 (2019), pp. 2259–2280.

[295] Leonardus van Kampenhout et al. “Improving the representation of polar snow and firn in the Community Earth System Model”. In: *Journal of Advances in Modeling Earth Systems* 9.7 (2017), pp. 2583–2600.

[296] Ida Marie Solbrekke, Asgeir Sorteberg, and Hilde Haakenstad. “The 3 km Norwegian reanalysis (NORA3)–a validation of offshore wind resources in the North Sea and the Norwegian Sea”. In: *Wind Energy Science* 6.6 (2021), pp. 1501–1519.

[297] Frank Neese. “Software update: The ORCA program system—Version 5.0”. In: *Wiley Interdisciplinary Reviews: Computational Molecular Science* 12.5 (2022), e1606.

[298] Frank Neese. “The ORCA program system”. In: *Wiley Interdisciplinary Reviews: Computational Molecular Science* 2.1 (2012), pp. 73–78.

[299] Jeng-Da Chai and Martin Head-Gordon. “Long-range corrected hybrid density functionals with damped atom–atom dispersion corrections”. In: *Physical Chemistry Chemical Physics* 10.44 (2008), pp. 6615–6620.

[300] Stefan Grimme et al. “A consistent and accurate ab initio parametrization of density functional dispersion correction (DFT-D) for the 94 elements H-Pu”. In: *The Journal of chemical physics* 132.15 (2010).

[301] Florian Weigend and Reinhart Ahlrichs. "Balanced basis sets of split valence, triple zeta valence and quadruple zeta valence quality for H to Rn: Design and assessment of accuracy". In: *Physical Chemistry Chemical Physics* 7.18 (2005), pp. 3297–3305.

[302] Vincenzo Barone and Maurizio Cossi. "Quantum calculation of molecular energies and energy gradients in solution by a conductor solvent model". In: *The Journal of Physical Chemistry A* 102.11 (1998), pp. 1995–2001.

[303] Maurizio Cossi et al. "Energies, structures, and electronic properties of molecules in solution with the C-PCM solvation model". In: *Journal of computational chemistry* 24.6 (2003), pp. 669–681.

[304] Elena Barbaro et al. "Dynamics of ionic species in Svalbard annual snow: the effects of rain event and melting". In: *The Cryosphere Discussions* 2019 (2019), pp. 1–27.

[305] Dimitrios G Liakos et al. "Exploring the accuracy limits of local pair natural orbital coupled-cluster theory". In: *Journal of chemical theory and computation* 11.4 (2015), pp. 1525–1539.

[306] Christoph Riplinger and Frank Neese. "An efficient and near linear scaling pair natural orbital based local coupled cluster method". In: *The Journal of chemical physics* 138.3 (2013).

[307] Christoph Riplinger et al. "Sparse maps—A systematic infrastructure for reduced-scaling electronic structure methods. II. Linear scaling domain based pair natural orbital coupled cluster theory". In: *The Journal of chemical physics* 144.2 (2016).

[308] Yan Zhao and Donald G Truhlar. "The M06 suite of density functionals for main group thermochemistry, thermochemical kinetics, noncovalent interactions, excited states, and transition elements: two new functionals and systematic testing of four M06-class functionals and 12 other functionals". In: *Theoretical chemistry accounts* 120.1 (2008), pp. 215–241.

[309] Chengteh Lee, Weitao Yang, and Robert G Parr. "Development of the Colle-Salvetti correlation-energy formula into a functional of the electron density". In: *Physical review B* 37.2 (1988), p. 785.

[310] Axel D Becke. "A new mixing of Hartree-Fock and local density-functional theories". In: *Journal of chemical Physics* 98.2 (1993), pp. 1372–1377.

[311] Seymour H Vosko, Leslie Wilk, and Marwan Nusair. "Accurate spin-dependent electron liquid correlation energies for local spin density calculations: a critical analysis". In: *Canadian Journal of physics* 58.8 (1980), pp. 1200–1211.

[312] Philip J Stephens et al. "Ab initio calculation of vibrational absorption and circular dichroism spectra using density functional force fields". In: *The Journal of physical chemistry* 98.45 (1994), pp. 11623–11627.

[313] Ivan Gladich et al. "Ab initio study of the reaction of ozone with bromide ion". In: *The Journal of Physical Chemistry A* 119.19 (2015), pp. 4482–4488.

[314] Graeme Henkelman and Hannes Jónsson. "Improved tangent estimate in the nudged elastic band method for finding minimum energy paths and saddle points". In: *The Journal of chemical physics* 113.22 (2000), pp. 9978–9985.

[315] William R Simpson et al. "Tropospheric halogen chemistry: Sources, cycling, and impacts". In: *Chemical reviews* 115.10 (2015), pp. 4035–4062.

[316] Paul Wennberg. "Bromine explosion". In: *Nature* 397.6717 (1999), pp. 299–301.

[317] Mark A Kendrick. "Halogens in seawater, marine sediments and the altered oceanic lithosphere". In: *The role of halogens in terrestrial and extraterrestrial geochemical processes: Surface, crust, and mantle*. Springer, 2018, pp. 591–648.

[318] Ronald Fuge. "Sources of halogens in the environment, influences on human and animal health". In: *Environmental Geochemistry and Health* 10.2 (1988), pp. 51–61.

[319] Xin Yang, John A Pyle, and Richard A Cox. "Sea salt aerosol production and bromine release: Role of snow on sea ice". In: *Geophysical Research Letters* 35.16 (2008).

[320] Margaret A Tolbert, Michel J Rossi, and David M Golden. "Antarctic ozone depletion chemistry: Reactions of N2O5 with H2O and HCl on ice surfaces". In: *Science* 240.4855 (1988), pp. 1018–1021.

[321] Daniel O'Sullivan and John R Sodeau. "Freeze-induced reactions: Formation of iodine- bromine interhalogen species from aqueous halide ion solutions". In: *The Journal of Physical Chemistry A* 114.46 (2010), pp. 12208–12215.

[322] Paul O'Driscoll et al. "Freezing halide ion solutions and the release of interhalogens to the atmosphere". In: *The Journal of Physical Chemistry A* 110.14 (2006), pp. 4615–4618.

[323] Paul O'Driscoll et al. "Release of nitric oxide and iodine to the atmosphere from the freezing of sea-salt aerosol components". In: *The Journal of Physical Chemistry A* 112.8 (2008), pp. 1677–1682.

[324] Gordan Grguric, John H Trefry, and Jeffrey J Keaffaber. "Ozonation products of bromine and chlorine in seawater aquaria". In: *Water Research* 28.5 (1994), pp. 1087–1094.

[325] Urs Von Gunten and Juerg Hoigne. "Bromate formation during ozonization of bromide-containing waters: interaction of ozone and hydroxyl radical reactions". In: *Environmental science & technology* 28.7 (1994), pp. 1234–1242.

[326] William C Bray and Herman A Liebhafsky. "The Kinetic Salt Effect in the Fourth Order Reaction BrO3-+ Br-+ 2H+→. Ionization Quotients for HSO4-at 25°". In: *Journal of the American Chemical Society* 57.1 (1935), pp. 51–56.

[327] C. E. S. Côrtes and R. B. Faria. "Kinetics and Mechanism of Bromate–Bromide Reaction Catalyzed by Acetate". In: *Inorganic Chemistry* 43 (2004), pp. 1395–1402.

[328] G. Schmitz. "Kinetics and mechanism of the iodate–iodide reaction and other related reactions". In: *Physical Chemistry Chemical Physics* 1 (1999), pp. 1909–1914.

[329] G. Schmitz. "Kinetics of the bromate–bromide reaction at high bromide concentrations". In: *International Journal of Chemical Kinetics* 39 (2007), pp. 17–21.

[330] Z. Hao et al. "Freezing-Induced Bromate Reduction by Dissolved Organic Matter and the Formation of Organobromine Compounds". In: *Environmental Science & Technology* 54 (2020), pp. 1668–1676.

[331] D. W. Min and W. Choi. "Accelerated Reduction of Bromate in Frozen Solution". In: *Environmental Science & Technology* 51 (2017), pp. 8368–8375.

[332] D. W. Min et al. "Cr(VI) Formation via Oxyhalide-Induced Oxidative Dissolution of Chromium Oxide/Hydroxide in Aqueous and Frozen Solution". In: *Environmental Science & Technology* 54 (2020), pp. 14413–14421.

[333] H. Sun et al. "Degradation of carbamazepine in ice with bromate and nitrite: Role of reactive nitrogen species". In: *Science of The Total Environment* 923 (2024), p. 171376.

[334] H. Sun et al. “Freezing degradation of the anticonvulsant oxcarbazepine by bromate in water ice under sunlight irradiation”. In: *Science of The Total Environment* 894 (2023), p. 165014.

[335] H. Sun et al. “Enhanced freezing-induced carbamazepine degradation by bromate under solar irradiation via the formation of hypobromous acid and hydroxyl radical”. In: *Journal of Hazardous Materials* 457 (2023), p. 131793.

[336] R. O’Concubhair and J. R. Sodeau. “The Effect of Freezing on Reactions with Environmental Impact”. In: *Accounts of Chemical Research* 46 (2013), pp. 2716–2724.

[337] N. Takenaka and H. Bandow. “Chemical Kinetics of Reactions in the Unfrozen Solution of Ice”. In: *The Journal of Physical Chemistry A* 111 (2007), pp. 8780–8786.

[338] H. Fukazawa et al. “Acid ions at triple junction of Antarctic ice observed by Raman scattering”. In: *Geophysical Research Letters* 25 (1998), pp. 2845–2848.

[339] N. Takenaka et al. “Acceleration Mechanism of Chemical Reaction by Freezing: The Reaction of Nitrous Acid with Dissolved Oxygen”. In: *The Journal of Physical Chemistry* 100 (1996), pp. 13874–13884.

[340] E. J. Workman and S. E. Reynolds. “Electrical Phenomena Occurring during the Freezing of Dilute Aqueous Solutions and Their Possible Relationship to Thunderstorm Electricity”. In: *Physical Review* 78 (1950), pp. 254–259.

[341] V. L. Bronshteyn and A. A. Chernov. “Freezing potentials arising on solidification of dilute aqueous solutions of electrolytes”. In: *Journal of Crystal Growth* 112 (1991), pp. 129–145.

[342] P. W. Wilson and A. D. J. Haymet. “WorkmanReynolds Freezing Potential Measurements between Ice and Dilute Salt Solutions for Single Ice Crystal Faces”. In: *The Journal of Physical Chemistry B* 112 (2008), pp. 11750–11755.

[343] A. D. J. Haymet and P. W. Wilson. “The Workman–Reynolds “Freezing Potential”: A new look at the inherent physical process”. In: *Journal of Molecular Liquids* 228 (2017), pp. 243–246.

[344] D. Heger et al. “Beyond pH: Acid/Base Relationships in Frozen and Freeze-Dried Pharmaceuticals”. In: *Principles and Practices of Lyophilization in Product Development and Manufacturing*. Ed. by F. Jameel. Cham: Springer International Publishing, 2023, pp. 39–61.

[345] W. A. Alves and R. B. Faria. “Vibrational investigation of the stretching region of bromate ion in solution”. In: *Spectrochimica Acta Part A: Molecular and Biomolecular Spectroscopy* 58 (2002), pp. 1395–1399.

[346] H. Lei, B. J. Mariñas, and R. A. Minear. “Bromamine Decomposition Kinetics in Aqueous Solutions”. In: *Environmental Science & Technology* 38 (2004), pp. 2111–2119.

[347] U. Pinkernell et al. “Methods for the photometric determination of reactive bromine and chlorine species with ABTS”. In: *Water Research* 34 (2000), pp. 4343–4350.

[348] Ľ. Vetráková, V. Vykoukal, and D. Heger. “Comparing the acidities of aqueous, frozen, and freeze-dried phosphate buffers: Is there a “pH memory” effect?” In: *International Journal of Pharmaceutics* 530 (2017), pp. 316–325.

[349] Ľ. Krausková et al. “Suppression of protein inactivation during freezing by minimizing pH changes using ionic cryoprotectants”. In: *International Journal of Pharmaceutics* 509 (2016), pp. 41–49.

[350] Gábor Lente et al. “One-versus two-electron oxidation with peroxomonosulfate ion: reactions with iron (II), vanadium (IV), halide ions, and photoreaction with cerium (III)”. In: *Inorganic chemistry* 48.4 (2009), pp. 1763–1773.

[351] Yong-Yoon Ahn et al. “Freezing-enhanced degradation of azo dyes in the chloride-peroxymonosulfate system”. In: *Chemosphere* 359 (2024), p. 142261.

[352] J Liao et al. “Observations of inorganic bromine (HOBr, BrO, and Br2) speciation at Barrow, Alaska, in spring 2009”. In: *Journal of Geophysical Research: Atmospheres* 117.D14 (2012).

[353] Dominik Heger, Jana Klánová, and Petr Klán. “Enhanced protonation of cresol red in acidic aqueous solutions caused by freezing”. In: *The Journal of Physical Chemistry B* 110.3 (2006), pp. 1277–1287.

[354] Kathy S Law et al. “Arctic tropospheric ozone trends”. In: *Geophysical Research Letters* 50.22 (2023), e2023GL103096.

[355] P. de Caritat et al. “Chemical composition of arctic snow: concentration levels and regional distribution of major elements”. In: *Science of The Total Environment* 336 (2005), pp. 183–199.

[356] A. P. Nawrot et al. “Chemistry of snow cover and acidic snowfall during a season with a high level of air pollution on the Hans Glacier, Spitsbergen”. In: *Polar Science* 10 (2016), pp. 249–261.